Search for supersymmetry in events with at least one photon and missing transverse momentum in proton-proton collisions at a center-of-mass energy of 13 TeV at the CMS experiment

Von der Fakultät für Mathematik, Informatik und Naturwissenschaften der RWTH Aachen University zur Erlangung des akademischen Grades eines Doktors der Naturwissenschaften genehmigte Dissertation

vorgelegt von

Johannes Schulz, M.Sc. RWTH

aus

Wittlich

Berichter: Prof. Dr. Lutz Feld
Prof. Dr. Michael Krämer

Tag der mündlichen Prüfung: 14. November 2018

Kurzfassung

In dieser Arbeit wird eine Suche nach neuer Physik in Endzuständen mit Photonen und einem signifikanten Ungleichgewicht der transversalen Impulssumme vorgestellt. Es wird ein Datensatz untersucht, der mit dem CMS-Experiment am CERN LHC in Proton-Proton Kollisionen bei einer Schwerpunktsenergie von 13 TeV aufgenommen wurde. Der Datensatz, aufgezeichnet im Jahr 2016, entspricht einer integrierten Luminosität von $35,9\ \text{fb}^{-1}$. Supersymmetrie (SUSY) ist ein vielversprechendes Modell neuer Physik, welches die Existenz bisher unbeobachteter Teilchen vorhersagt und als Motivation dieser Arbeit dient. In den betrachteten Szenarien ist das Gravitino, das supersymmetrische Partnerteilchen des Gravitons, das leichteste SUSY-Teilchen und entkommt der Detektion. Es wird angenommen, dass das zweitleichteste SUSY-Teilchen (NLSP) in sofortigen Zerfällen in das Gravitino und ein Stanardmodell-Boson übergeht, sodass vorwiegend das NLSP die Signatur der Endzustände bestimmt. Das so erzeugte Standardmodell-Boson ist in diesen Modellen mit hoher Wahrscheinlichkeit ein Photon. Die in diesem Dokument vorgestellte Analyse ist die Nachfolgeanalyse einer Suche, die ebenfalls vom Autor während des Doktorstudiums entwickelt und 2016 in Physics Letters B 759 (2016) 479 veröffentlicht wurde [1]. Die Vorgängeranalyse wurde mit $7,4\ \text{fb}^{-1}$ an Daten entwickelt, die bei einer Schwerpunktsenergie von 8 TeV im Jahr 2012 aufgenommen wurden. Die Analyse war eine der ersten SUSY-Suchen in der CMS Kollaboration, welche die elektroschwache Produktion von SUSY-Teilchen untersuchte. In der vorliegenden Analyse wird eine inklusive Ereignisselektion ausgearbeitet, welche auf hohe Sensitivität ungeachtet der zugrundeliegenden Wechselwirkung der Produktion optimiert ist. Den dominanten Standardmodell-Untergrund in der Signalregion bilden Ereignisse in denen ein Z-Boson oder ein $\text{W}^{\pm}$-Boson, insbesondere mit Photonabstrahlung ($\text{V}(\gamma)$), produziert wird und in denen das Z-Boson in zwei Neutrinos oder das $\text{W}^{\pm}$-Boson in ein Neutrino und ein geladenes Lepton zerfällt. Monte-Carlo Simulationen werden genutzt, um die Verteilung dieser Untergründe vorherzusagen. Eine von Standardmodell-Prozessen dominierte Kontrollregion wird definiert, um die Simulationen an die Daten anzupassen und somit Unsicherheiten in ihrer Normierung eliminieren zu können. Umfassende Studien und Validierungen werden durchgeführt, um die systematischen Unsicherheiten, die den gewählten Untergrundbestimmungsmethoden zu Grunde liegen, zu bestimmen. In allen Kontroll- und Validierungsregionen wird eine gute Stabilität der Vorhersage beobachtet. Die Daten werden in der Signalregion mit der Gesamterwartung des Standardmodells verglichen. Es wurde kein Hinweis auf die Existenz neuer Physik gefunden. Zur Interpretation dieses Resultats werden Limits im Rahmen des „general gauge mediation" Modells gesetzt, in welchem Massen des NLSPs je nach Konfiguration bis zu

980 GeV auf 95-prozentigem Vertrauensniveau ausgeschlossen werden können. In zwei vereinfachten Modellen mit elektroschwacher Produktion werden NLSP-Massen unter 780 GeV beziehungsweise 950 GeV ausgeschlossen. Strikte Limits werden außerdem in Modellen gesetzt, die auf der Produktion von SUSY-Teilchen durch die starke Wechselwirkung basieren. In diesen Modellen werden die produzierten Teilchen bis zu einer Masse von 2100 GeV ausgeschlossen. Diese Arbeit setzt die aktuell höchsten Massenlimits in allen betrachteten elektroschwachen Modellen, sowie in Modellen starker Produktion, wenn die Massendifferenz der NLSPs und der produzierten Teilchen klein ist. Die in diesem Dokument vorgestellte Suche wurde 2018 in Physics Letters B 780 (2018) 118 veröffentlicht [2].

Abstract

A search for new physics in final states with photons and a significant imbalance of the transverse momentum sum is presented in this thesis. The data sample of proton-proton collisions at a center-of-mass energy of 13 TeV was collected with the CMS detector at the CERN LHC in 2016 and corresponds to an integrated luminosity of 35.9 fb^{-1}. Supersymmetry (SUSY) is a promising model of new physics predicting the existence of so far unobserved particles and serves as motivation for this thesis. In the considered scenarios the gravitino, which is the supersymmetric partner particle of the graviton, is the lightest SUSY particle and escapes detection. It is assumed that the next-to-lightest SUSY particle (NLSP) decays promptly into a gravitino and a standard model boson, such that the NLSP predominantly determines the signature of the final states. This standard model boson is with high probability a photon. The analysis presented in this document is the successor analysis of a search published in Physics Letters B 759 (2016) 479 [1] in 2016, which was also developed by the author during the doctoral studies. The predecessor analysis was developed using 7.4 fb^{-1} of data, recorded at a center-of-mass energy of 8 TeV in 2012, and was one of the first SUSY searches in the CMS collaboration studying electroweak production of SUSY particles. In this thesis, an inclusive event selection is developed optimized for high sensitivity regardless of the production channel. The dominant standard model background contributions to the signal region originate from events with Z boson or $\text{W}^{\pm}$ boson production, especially if accompanied by photon radiation ($\text{V}(\gamma)$), where the Z boson or $\text{W}^{\pm}$ boson decays into two neutrinos or one neutrino and one charged lepton, respectively. Monte-Carlo simulations are used to predict the shapes of these backgrounds. A control region dominated by standard model processes is defined to fit the simulations to data to eliminate uncertainties in the normalization of these samples. Comprehensive studies and validations are performed to determine the systematic uncertainties arising from the respective background prediction method. Good stability is observed in all control and validation regions. The data are compared to the total standard model expectation in the signal region. No hints for the existence of new physics are found. Limits are set in the context of the general gauge mediation model in which, depeding on the configuration, masses of the NLSP up to 980 GeV are excluded at 95% confidence level. NLSP masses below 780 GeV and 950 GeV are excluded in two simplified models assuming electroweak production of SUSY particles. Stringent limits are set on simplified models based on strong production of SUSY particles, excluding masses of the produced particles up to 2100 GeV. This thesis sets the highest mass limits to date in the studied electroweak models, and in the strong production models if the mass difference between the NLSPs and the produced particles

is small. The search presented in this document was published in Physics Letters B 780 (2018) 118 [2] in 2018.

Contents

Chapter 1

Introduction

"What is now proved was once only imagined."
William Blake.

The theoretical foundation of high-energy physics is the standard model of particle physics (SM) [3–6]. Being very successful at the electroweak (EWK) energy scale along with a high predictive power proven in many experiments, the SM fails to explain several so far unsolved problems such as the smallness of the Higgs boson mass in comparison to the Planck scale, the nature of dark matter, or the origin of neutrino masses. Theoretical extensions of the SM provide approaches how one or more of these shortcomings might be solved. For decades, the most popular extension has been supersymmetry (SUSY) [7] - a theory introducing a symmetry between fermions and bosons. SUSY is able to answer several open questions at once. However, one fundamental insight achieved so far is that SUSY cannot be an exact symmetry, but, compared to the SM particles, supersymmetric partner particles must be heavier.

Nowadays, probing new ideas often requires costly apparatuses and years of development and measurements. At the Large Hadron Collider (LHC) at CERN near Geneva billions of protons are collided every second and nearly at the speed of light. The collider has a circumference of 27 km and lies 100 m underground. The data analyzed in this thesis are recorded by the Compact Muon Solenoid (CMS) detector [8–11], located at the northernmost collision point of the LHC [12]. In 2012, the LHC operated at a center-of-mass energy of 8 TeV, which was upgraded to 13 TeV starting from the data taking in 2015. The CMS detector provides a good hermeticity and a 360° coverage in the plane transverse to the beam axis. Its main components are the tracking system, the electromagnetic and hadronic calorimeter, the superconducting solenoid magnet, and the muon detectors. During the operation, the proton beams are crossed every 25 ns at the four interaction points of the LHC. All signals generated in the active material of the subdetectors during one collision are gathered and unified in one global reconstruction, referred to as the event.

With the advent of the LHC, a significant expansion of the phase space accessible to searches for SUSY is enabled. In recent years, collaborations from LHC experiments have developed and published several analysis strategies and results steadily enlarging the phase space of sufficient sensitivity to discover SUSY. Signal regions are defined to search for deviations with respect to the SM expectation. Proper event selections are needed to reduce the probability that SM processes, throughout the thesis referred to as background, populate these signal regions. Since the data are recorded at a hadron collider, the production of SUSY particles via strong interactions has a much higher probability compared to EWK production of SUSY particles of similar mass. In consequence, SUSY searches predominantly focus on final states with large energy deposits caused by hadrons, reflected by large values of the hadronic activity H_T.

SUSY particles are expected to have masses around the TeV energy scale, which is within the scope of the LHC. To realize the non-degeneracy in mass, SUSY breaking mechanisms are introduced. Gauge-mediated SUSY breaking (GMSB) models often favor SUSY mass hierarchies where the next-to-lightest SUSY particle (NLSP) decays into a photon and a gravitino [13–15], where the gravitino is the SUSY partner particle of the graviton, the so far unobserved gauge boson mediating the gravitational force. To be compatible with current results [6], the NLSP should have a mass of $\mathcal{O}(100\,\text{GeV})$ or higher, generating final states with high-energy photons. In contrast to the photon, the gravitino is expected to not interact with any of the detector components. As the colliding partons only carry a small transverse boost with respect to the proton beam directions, the vectorial momentum sum in the transverse plane ($\vec{p}_T^{\,\text{miss}}$) should almost vanish if all particles produced in the hard scattering are detected. Therefore, the production of gravitinos leads to significant magnitudes of $\vec{p}_T^{\,\text{miss}}$, denoted as p_T^{miss}.

During the first 15 months of the doctoral studies the author accomplished the publication of a search based on a data set recorded by the CMS detector during pp collisions in 2012, corresponding to an integrated luminosity of 7.4 fb^{-1} [1]. In the CMS reference numbering scheme the analysis based on 8 TeV data is denoted as SUS-14-016, which is also used as reference here. The analysis SUS-14-016 was the first SUSY search designed for a special data set, which was recorded during the second half of the 2012 data-taking period with a reconstruction only performed during the Long Shutdown 1 of the LHC. This data set excels in less stringent requirements imposed on events and is part of the so-called "parked data" program [16] initiated to utilize the free storage capacity of the CMS experiment during that time. The accessibility of this new phase space, illustrated in Fig. 1.1 in dependency of H_T, was exploited to develop a SUSY search with significant sensitivity to electroweakly produced SUSY particles with photons in the final state. The analysis strategy was developed by the author from scratch without the guidance of any predecessor analysis. To maintain high signal acceptances, which is essential in EWK searches due to much lower signal cross sections, an event selection designed for the properties of EWK SUSY scenarios was developed. Among others, the analysis SUS-14-016 separated potential signal events from background events by requiring a large "p_T^{miss} significance" - a sophisticated, unitless variable that evaluates the likelihood that the measured p_T^{miss} arises from undetected particles [17]. In the course of the development of SUS-14-016, the author took care of the production of a

GMSB-based EWK signal model, and initiated the production of a further, simplified EWK signal model called "TChiNg", useful for several searches motivated by GMSB SUSY and meanwhile established in the CMS collaboration. At that time, the search SUS-14-016 set the most stringent exclusion limits in all three SUSY scenarios used for the interpretation of the results. Thereby, SUS-14-016 also enhanced the exclusion limit in a SUSY scenario with one photon and one charged lepton in the final state set by the analysis SUS-14-013 [18], which explicitly selected this final state and used almost triple the integrated luminosity. These limits have been the most stringent up to the point in time of the publication of the thesis at hand.

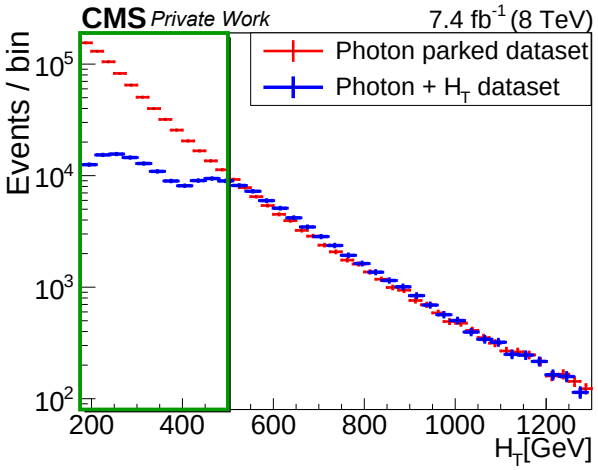

Figure 1.1: Comparison of the H_T distributions of the parked data set used in SUS-14-016 (red) and a data set requiring a photon candidate and $H_T > 500\,\text{GeV}$ (blue) [19]. The parked data set provides a large amount of events with low hadronic activity. The slight difference of these two distributions for $H_T > 500\,\text{GeV}$ is due to differences in the H_T definition of the trigger and the offline selection, and different trigger requirements for the photon candidate and p_T^{miss}.

In between, a preliminary result was published in collaboration with the author under the reference number SUS-16-023 [20] based on the analysis strategy developed in SUS-14-016, but using a data set corresponding to 2.3 fb^{-1} recorded in 2015 at a center-of-mass energy of 13 TeV. The analysis SUS-16-023 was not able to improve on the limits set by SUS-14-016, but also published preliminary exclusion limits in SUSY scenarios with photon final states based on strong production of gluinos, the SUSY partner particles of gluons.

This thesis, corresponding to the CMS reference number SUS-16-046 [2], is developed using the data set recorded by CMS in 2016 in pp collisions at 13 TeV. The data set corrresponds to 35.9 fb^{-1}, and therefore provides a significantly larger amount of data compared to the data set used by the analysis SUS-16-023. One of the key motivations for the development of the analysis was to maximize the generality of the event selection

to achieve sensitivity to a large variety of SUSY scenarios based on both EWK and strong production, and a simultaneous simplification of the event selection to enable the reinterpretability of the results. Therefore, e.g., a suitable, more transparent alternative to the $p_{\mathrm{T}}^{\mathrm{miss}}$ significance is chosen.

This document describes the aspects relevant for the latest analysis corresponding to the CMS reference number SUS-16-046. The thesis is structured as follows: In Chapter 2 and 3, the theoretical foundation motivating the development of the analysis is presented and suitable SUSY signal scenarios are introduced, respectively. Chapter 4 introduces the experimental setup, namely the LHC and the CMS detector. In Chapter 5 the event processing, properties of the data set and the trigger, and the event simulation are described. In the following chapters the reconstruction and identification of high-level objects, e.g., the photon and $p_{\mathrm{T}}^{\mathrm{miss}}$, is explained (Chapter 6), and the event selection, defining the control, validation and signal regions, is introduced (Chapter 7). Chapter 8 describes how the SM background is estimated and validated, together with the determination of the systematic uncertainties arising from these methods, followed by the presentation of the results in Chapter 9. The document concludes with a summary and outlook in Chapter 10.

> "Based only on a proper respect for the power of Nature to surprise us, it seems nearly as obvious that new physics exists in the 16 orders of magnitude in energy between the presently explored territory near the electroweak scale, M_W, and the Planck scale"
> Stephen P. Martin: A Supersymmetry Primer [7].

Comments

Natural units are chosen for the purpose of simplicity [21], where the speed of light c and the reduced Planck constant $\hbar$ are set to unity. Therefore, mass, energy, and momentum, have the same unit and are stated in multiples of eV. Time and length are stated in the metric system. Cross sections and the integrated luminosity are stated in multiples of barn (b) and b^{-1}, respectively, with $1\ \mathrm{b} = 10^{-28}\ \mathrm{m}^2$.

All plots shown in this document that are prepared using data recorded at the CMS experiment or simulations provided by the CMS collaboration are labeled with "**CMS**". If the plots are published in a paper, the plots are labeled with "**CMS**" if they contain CMS data, or with "**CMS** *Simulation*" if they contain CMS simulations only. If the plots are only published as additional material, the label is extended by "*Supplementary*", along with the paper reference number used for the e-print published on the *arxiv.org* webpage. If plots are published as preliminary result but not as a paper the label is extended by "*Preliminary*". All other plots carry the additional label "*Private Work*". Note that plots only showing the background prediction without the distribution of data also do not carry the label "*Simulation*" if at least one of the background processes is estimated using CMS data. A reference is given if a plot was published in another document.

In several figures, distributions of data and simulations are shown in histograms, where the event yield is aggregated for certain intervals with constant or variable widths. These intervals are referred to as "bins". Events with values beyond the shown range are added to the last bin.

Chapter 2

Theoretical foundation

Contents

The elementary particles and their interactions are described by the standard model of particle physics (SM). The great success of the theory has been proven in many independent experiments investigating the interactions of elementary particles. To maintain (chiral) gauge invariance, particles have to acquire masses via the Higgs mechanism. In its minimal realization, the existence of one additional scalar particle, the Higgs boson, is predicted. In 2012, CMS [22] and ATLAS [23] have announced the observation of a new boson with properties consistent with the SM Higgs boson and a mass of about 125 GeV [24, 25]. This discovery, being one of the key motives to build the LHC, completes the picture of how fundamental interactions can be described theoretically consistent with (most) experimental observations and proves the predictive power of the SM. Nevertheless, there are theoretical and phenomenological reasons, why the SM cannot be a fundamental theory. The most commonly explored extension of the SM is supersymmetry (SUSY), solving, depending on its realization, several of these shortcomings of the SM.

In the following, the most important properties and concepts of the SM and its extension by SUSY are outlined, focusing on the aspects relevant for the analysis presented in this thesis. References to more detailed descriptions of the theoretical background are given.

2.1 Standard model of particle physics

The standard model of particle physics [3–6] is a renormalizable quantum field theory describing the elementary interactions of the weak, the electromagnetic, and the strong force. The SM combines the weak and the electromagnetic force into one consistent gauge theory, called the electroweak (EWK) force as proposed by Glashow, Salam, and Weinberg [26–28]. The Lagrangian is obtained by requiring local gauge invariance. The gauge group of the SM

$$SU(3)_C \times SU(2)_L \times U(1)_Y \tag{2.1}$$

combines the $SU(3)_C$ group of the strong interaction and the $SU(2)_L \times U(1)_Y$ group of the EWK interactions, where the indices C, L, and Y indicate the different symmetries in color charge, in transformations of left-handed particles via weak interactions, and in the weak hypercharge, respectively. The corresponding gauge bosons mediating the interactions are the gluons $g^a, a = 1, \ldots, 8$, W bosons $\mathrm{W}^i, i = 0, 1, 2$, and the B boson with the respective gauge couplings g_s, g, and g'. After EWK symmetry breaking, the W^i and B bosons mix to the $\mathrm{W}^\pm$ bosons, the Z boson, and the photon (γ).

The elementary particles can be classified into particles with integer spins (bosons) and half-integer spins (fermions). Elementary fermions, the fundamental constituents of matter, can further be categorized into quarks and leptons. Leptons are composed of electrically charged leptons ($l = \mathrm{e}, \mu, \tau$) and neutral leptons ($\nu = \nu_\mathrm{e}, \nu_\mu, \nu_\tau$), the latter being referred to as neutrinos. Neutrinos only interact via the weak force, while charged leptons can also interact via the electromagnetic force. Quarks ($q = d, u, s, c, b, t$) are the only elementary fermions that also interact strongly.

Leptons and quarks occur in three generations, where related fermions, e.g., the electron, muon, and tau lepton, only differ in mass. Fermions of one generation, e.g., e and ν_e, are arranged in doublets, differing in the third component of the weak isospin I_3 (called flavor: *up*-type, *down*-type). For each fermion there is a corresponding antifermion with opposite charges but same mass. For instance, the relative mass difference between the electron and the positron is measured to be smaller than 10^{-8} [6]. In the following, particles and antiparticles are treated equally and denoted with the name or acronym of the particle, unless otherwise stated. All elementary particles are summarized in Fig. 2.1, including information about the mass, electrical charge and spin.

Quantum Chromodynamics

The quantum gauge field theory describing the interactions of quarks and gluons is quantum chromodynamics (QCD) based on the non-Abelian $SU(3)_C$ gauge group. Generators of non-Abelian groups do not commute, resulting in a self-interaction of the mediators. The charge corresponding to QCD interactions is the color charge, occuring in three different states (N_C) named red, green, and blue, plus their anticolors. The mediators are $N_C^2 - 1 = 8$ massless and electrically neutral gluons g^a, carrying the charge of one color and one anticolor, where the ninth combination forms an $SU(3)$ singlet. This color

neutral singlet would result in an infinite reach of the strong interaction, which is not observed experimentally. Quarks carry one color, while antiquarks carry one anticolor. Interactions of quarks with a gluon gauge field can be interpreted as a rotation in the $SU(3)_C$ space.

The QCD potential is composed of a Coulomb potential-like term proportional to the inverse of the distance ($\propto (-\alpha_s/r)$ and a term with linear proportionality to the distance ($\propto \kappa \cdot r$). The coupling determining the strength of QCD interactions is the strong coupling $\alpha_s = g_s^2/4\pi$. The form of the QCD potential leads to a linear rising potential energy for large distances between two quarks with a constant energy density $\kappa \sim 1\,\mathrm{GeV/fm}$ [30]. This phenomenon is called *linear confinement* and results in the production of a quark-antiquark pair if quarks exceed a certain distance to each other. If the kinetic energy of the quarks is too low to reach the critical distance, the color

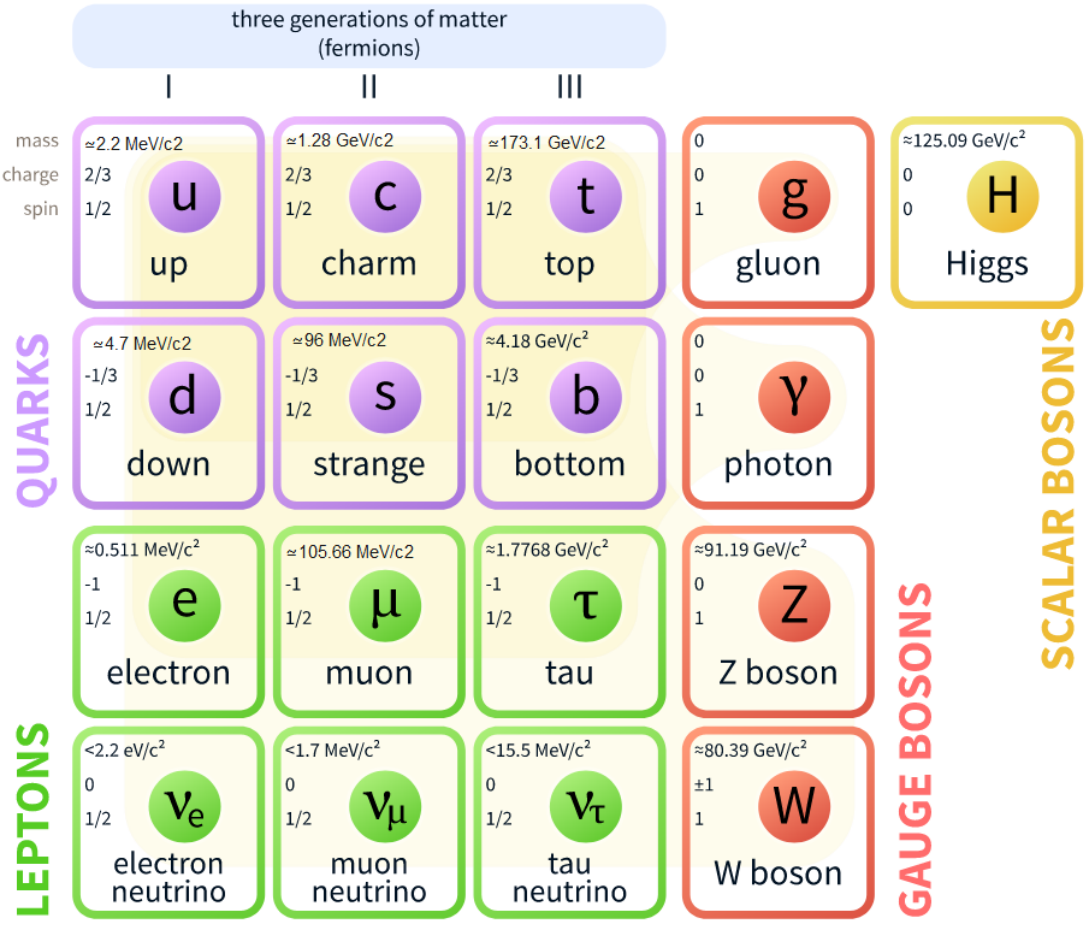

Figure 2.1: Particle content of the standard model [29]. The figure contains all elementary fermions and bosons, including information about the mass, charge, and spin. The charge is normalized to the elementary electric charge. Antifermions are not shown.

charged particles form color singlets in bound states of one quark and one antiquark (mesons) or three quarks or antiquarks, named baryons and antibaryons, respectively. This transition is called *hadronization*. This in turn implies that no free quarks or gluons can be observed [31].

Lattice gauge theory and perturbative expansions allow for the calculation of dynamics and observables to a certain degree of accuracy under specific circumstances. The coupling of the strong force is not a constant and varies depending on the energy scale Q associated with the corresponding interaction. While α_s is large for small energy scales which translates to large distances, its value gets smaller for larger energy scales such that the coupling becomes calculable in perturbative expansions of α_s. In perturbative QCD α_s becomes a function of the renormalization scale μ_R, which generally is chosen to equal the momentum transfer Q of the process. Hence, $\alpha_s(\mu_R^2)$ sets the scale of the strength of the interaction. To first order α_s satisfies the renormalization group equation

$$\alpha_s(\mu_R^2) = \frac{1}{\beta_0 \ln(\mu_R^2/\Lambda_{\text{QCD}}^2)}, \tag{2.2}$$

with β_0 being a constant referred to as 1-loop β-function coefficient. The parameter $\Lambda_{\text{QCD}} \approx 200\,\text{MeV}$ is associated with the energy scale corresponding to the transition of α_s being perturbatively calculable and large values of α_s. This *running* behavior of the coupling results in a low coupling strength for very large momentum transfers, also referred to as "asymptotic freedom". At a momentum transfer equaling the mass of the Z boson, $\alpha_s(m_{\text{Z}}^2)$ is measured to be $\alpha_s(m_{\text{Z}}^2) = 0.1181 \pm 0.0011$ [6], which is larger than the electromagnetic coupling $\alpha_{\text{EM}}^{-1}(m_{\text{Z}}^2) = 127.940 \pm 0.014$ [6], and the weak coupling $\alpha_W = \alpha_{\text{EM}}/\sin^2(\theta_W)$. The angle θ_W is the weak-mixing angle, also referred to as Weinberg angle, with a value of $\sin^2(\theta_W) \approx 0.23$ [6, 32–34] depending on the renormalization scheme.

The proton is composed of two valence u quarks and one valence d quark. Within the proton, these valence quarks are surrounded by gluons and virtual quark-antiquark pairs. The parton density functions (PDFs) of the proton give the fraction of a proton's momentum carried by a certain parton (quark or gluon) as a function of the energy scale of the interaction. PDFs need to be determined from data. The factorization scale μ_F is introduced to define an energy threshold for which emissions with a momentum below this threshold are assumed to be accounted for in the PDFs. This factorization is mandatory due to the non-perturbative nature of QCD for low energy scales.

Both μ_R and μ_F are unphysical and chosen with a certain degree of freedom. If for all calculations an infinite number of terms in the series were considered, dependencies on μ_R and μ_F would cancel. Since de facto calculations can only be carried out to a certain order in perturbation series, uncertainties due to the choice of the scales affect among others Monte-Carlo (MC) simulations. The effect of this dependency on the analysis is estimated by varying the scales up and down by a factor of two and is accounted for as systematic uncertainty, determined for each process based on MC simulation, separately. Further information about how the problem of the non-perturbative character of QCD is approached in MC simulations is given in Section 5.3.

Electroweak unification and the generation of masses

The EWK theory is a gauge theory based on the $SU(2)_L \times U(1)_Y$ symmetry group, unifying the electromagnetic and the weak force. To ensure local gauge invariance of the Lagrangian, the mediators have to be massless. The Dirac Lagrangian in the SM attributes a mass term $-m_f\bar{\psi}\psi$ to all fermions ψ. This mass term is not invariant under the EWK symmetry, precluding the chiral gauge invariance. Therefore, particles are described by quantum field equations for massless particles, contradicting experimental observations. This contradiction is resolved by the spontaneous EWK symmetry breaking of the SM caused by the Higgs field.

The gauge eigenstates of the non-Abelian $SU(2)_L$ group are the W^0, W^1, and W^2 bosons and the gauge eigenstate of the Abelian $U(1)_Y$ group is the B boson. After the spontaneous symmetry breaking, the gauge eigenstates mix to mass eigenstates of the mediators of the weak ($\mathrm{W}^{\pm}$, Z) and electromagnetic (γ) forces according to

$$\begin{pmatrix} \gamma \\ \mathrm{Z} \end{pmatrix} = \begin{pmatrix} \cos(\theta_W) & \sin(\theta_W) \\ -\sin(\theta_W) & \cos(\theta_W) \end{pmatrix} \begin{pmatrix} B \\ \mathrm{W}^0 \end{pmatrix}, \tag{2.3}$$

and

$$\mathrm{W}^{\pm} = \frac{1}{\sqrt{2}}(\mathrm{W}^1 \mp i\mathrm{W}^2). \tag{2.4}$$

The $\mathrm{W}^{\pm}$ bosons only couple to left-handed particles (maximal parity violation), whereas the Z boson also couples to right-handed particles with a different strength (parity violation). The γ only couples to electrically charged particles, and equally to left- and right-handed particles.

The $\mathrm{W}^{\pm}$ bosons have a weak isospin of $\mathrm{I}_3 = \pm 1$. The coupling to a $\mathrm{W}^{\pm}$ boson is the only interaction at tree-level changing the flavor of the participating particles, since all other gauge bosons have $\mathrm{I}_3 = 0$. Therefore, the SM does not allow for flavor changing neutral currents (FCNC) at leading order. Loop contributions to FCNC are strongly suppressed and serve as tests for beyond the SM (BSM) physics [35,36].

The Higgs field, in its simplest realization represented by one complex scalar $SU(2)$ doublet $\Phi \equiv (\Phi^+, \Phi^0)^\intercal$, has the "mexican hat"-shaped potential

$$V(\Phi) = \mu^2 \Phi^\dagger \Phi + \frac{\lambda}{2}\left(\Phi^\dagger \Phi\right)^2. \tag{2.5}$$

This potential causes spontaneous symmetry breaking for a negative μ^2, resulting in a non-vanishing global minimum of the potential, the vacuum expectation value $v \equiv \sqrt{-\mu^2/\lambda} = 246\,\mathrm{GeV}$. Without loss of generality the direction $\langle \Phi^+ \rangle = 0$ and $\langle \Phi^0 \rangle = 1/\sqrt{2}\,(0, v)^\intercal$ can be chosen, which breaks three of the four initial global symmetries induced by the two complex fields. The resulting Goldstone bosons form the longitudinal components of the $\mathrm{W}^{\pm}$ and Z bosons, which are therefore no longer massless. The remaining degree of freedom is a physical field, the Higgs field, and manifests in the

scalar Higgs boson H. The photon remains massless. The elementary boson masses at tree level are given by

$$m_{\mathrm{H}} = \lambda\nu, \;\; m_{\mathrm{W}^{\pm}} = \frac{1}{2}g\nu, \;\; m_{\mathrm{Z}} = \frac{1}{2}\sqrt{g^2 + g'^2}\nu, \;\; m_{\gamma} = 0. \tag{2.6}$$

Charged leptons and quarks acquire masses through their Yukawa coupling with the Higgs field, where the Yukawa coupling describes the interaction between a Dirac and a scalar field. The rough scale of the masses of all elementary particles is set by v and the mass of each particle is proportional to its Yukawa coupling to the Higgs field. So far, it remains unclear how neutrinos acquire masses. It is also possible to introduce a more complex Higgs sector, accompanied by the prediction of additional charged and neutral Higgs bosons [37].

2.2 Motivation for physics beyond the standard model

Based on the wide range of unsolved shortcomings, which are discussed in the following, the SM can be considered as a low-energy effective theory arising from a more fundamental theory. BSM theories, such as SUSY, are designed to address one or several of these problems. Supersymmetry predicts the existence of new particles, e.g., partner particles to all SM particles with a difference in spin of 1/2, providing a basis to address several SM shortcomings.

Gravity

The SM is able to describe the EWK and the strong force. Gravity is disregarded in the SM, since there is no consistent quantum gravitation field theory. So far, gravity is addressed by Einstein's general theory of relativity based on the framework of classical physics. Being negligible at the EWK scale, gravitational interactions become significant at very high energy scales.

Grand unification

The interplay of experimental physics and theory has led to the development of theories of ever-growing comprehension, resulting in, e.g., the unification of the electric and magnetic force to the electromagnetic force, and the subsequent unification with the weak force to the EWK force. The feasibility of subsequent theoretical unifications, possibly up to a "theory of everything", describing all four fundamental forces is conceivable. One of these steps within current reach could be the unification of the strong and the EWK force to one renormalizable field theory, called "grand unified theory" (GUT).

Extensions of the SM, e.g., based on the $SU(5)$ or $SO(10)$ group, enable such a unification where the couplings of the $SU(3)$, $SU(2)$, and $U(1)$ unify at a certain, high, mass scale $M_{\mathrm{GUT}} \sim 10^{16}\,\mathrm{GeV}$. Figure 2.2 illustrates the dependency of the gauge couplings on the energy scale as present in the SM (solid lines) and how the running of the couplings can change in case of SUSY particles with masses around the TeV scale (dashed lines) and a unification at M_{GUT} [6, 7, 38].
GUT models often predict proton decays [6], with the most dominant decay channels being $\mathrm{p} \to \mathrm{e}^+\pi^0$ and $\mathrm{p} \to K^+\nu$. Recent experimental results of proton lifetime measurements [39, 40] are still compatible with most predictions of GUT models but serve as important test [41].

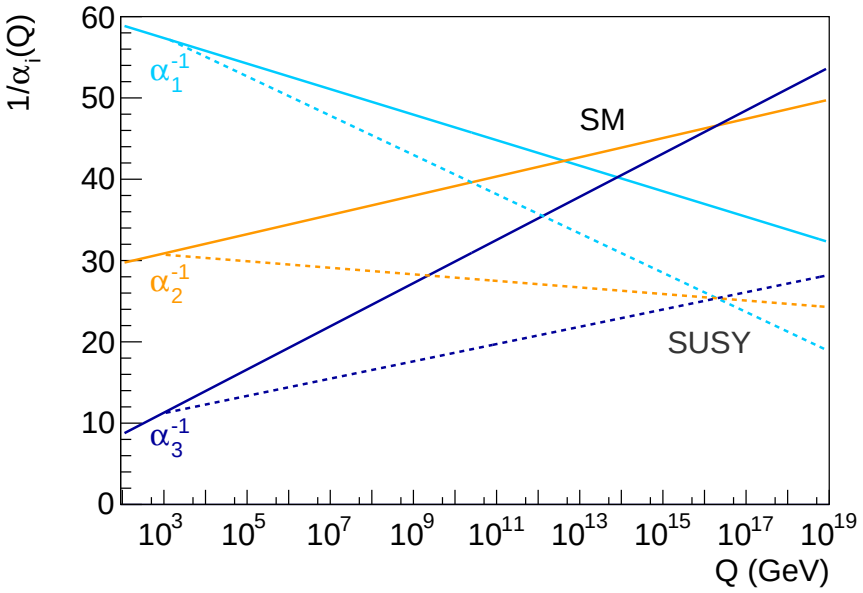

Figure 2.2: Running of the couplings α_i, $i = 1, 2, 3$, corresponding to the $U(1)$, $SU(2)$, and $SU(3)$ gauge groups, respectively, in the SM (solid lines) and a model of SUSY (dashed lines). The couplings α_i follow the relations $\alpha_i = g_i^2/4\pi, g_1 = \sqrt{5/3}g', g_2 = g$, and $g_3 = g_S$ so that $\alpha_1^{-1}(M_Z) \neq \alpha_{\mathrm{EM}}^{-1}(M_Z) \approx 127$. Extrapolating the couplings in the SM, the couplings do not meet at any energy scale. In contrast, several configurations of SUSY are possible that lead to a unification of the gauge couplings. The reciprocals α_i^{-1} are shown that obey the linear relation $\frac{d}{dt}\alpha_i^{-1} = \frac{b_i}{2\pi}$, with $t = \ln(Q/Q_0)$ and b_i being constants depending on the model. The scale Q_0 represents an arbitrary reference scale.

Neutrino masses

Several appearance and disappearance experiments using solar, atmospheric, accelerator, and reactor neutrinos have measured that neutrinos oscillate between different generations [6, 42–45]. Neutrino oscillations are only possible if the mass difference of two generations is non-zero. So far, it is known that at least two of the three neutrinos have finite masses. Since neutrino masses are not included in the SM, a mechanism for their generation has to be added [46]. One possibility is to introduce right-handed, *sterile*, neutrinos. Neutrinos might be their own antiparticles (Majorana particles), possibly resulting in a measurable violation of the lepton number [47]. One mechanism introducing neutrino masses is the seesaw mechanism [48], which provides a picture of how the large mass difference between neutrinos and the other fundamental fermions can be understood. The existence of heavy, right-handed Majorana neutrinos could explain the lepton and baryon asymmetry of the universe.

Dark matter

There is a whole range of evidence for the existence of what is called *dark matter* (DM) [49, 50]. DM summarizes one or more types of massive particles not directly detected so far. Besides gravitational interactions, candidates must only interact weakly, they have to be stable on cosmological time scales, they must have the right relic density, and more than half of the DM should have been cold, i.e., non-relativistic, at the beginning of galaxy formation [51, 52]. One of the most striking evidences for the existence of DM is the measurement of the rotation curves of galaxies via the 21-cm line of neutral hydrogen [53]. In Newtonian dynamics, the rotational velocity $v(r)$, where r is the radius with respect to the galactic center, follows the proportionality $v(r) \propto \sqrt{M(r)/r}$, where $M(r)$ is the mass enclosed by the orbit corresponding to r. Hence, outside the visible mass, where $M(r)$ is constant for increasing r, the velocity is expected to follow $v(r) \propto \sqrt{1/r}$. Observations [53] have shown that the velocity converges to an approximately constant value, implying $M(r) \propto r$ outside the visible mass disk. Therefore, a DM halo is expected to exist outside the visible galaxy mass. DM is measured to represent ∼26.8% of the universe, supplemented by ∼68.3% of *dark energy* [54] and only ∼4.9% of visible matter [55]. There are no particles in the SM that can serve as cold DM candidates, since neutrinos have near-zero masses and move at nearly the speed of light. But, even though SM neutrinos have tiny masses, they are candidates to contribute to the fraction of DM not considered as cold DM [52]. Good candidates for cold DM are the lightest particles of several SUSY scenarios and the lightest Kaluza-Klein excitation in models of extra dimensions [49, 56]. There are also alternative theories, e.g., Modified Newtonian Dynamics, trying to explain phenomena like the observed galaxy rotation velocity, without the introduction of DM particles [53, 57]. However, such a modification is accompanied by a certain degree of arbitrariness and fails in explaining large-scale structure formations [57–59].

The Higgs boson mass

Any massive particle coupling to the Higgs field leads to quantum corrections to the Higgs boson mass proportional to Λ_{UV}^2, where Λ_{UV} is an ultraviolet momentum cut-off of the same order of magnitude as the energy scale up to which the SM is considered to be valid, possibly of the order of $10^{19}\,\text{GeV}$ [7]. These corrections are orders of magnitude larger than the recently measured value of $m_\text{H} \approx 125\,\text{GeV}$ [24, 25]. To agree with the observed Higgs boson mass, unnatural fine tuning between the radiative corrections and the bare mass would be necessary.
Explicitly, if the Higgs field H couples to a Dirac fermion ψ with mass m_f and a Lagrangian term -$\lambda_f H\bar{\psi}\psi$, the corrections to the Higgs mass squared are given by

$$\Delta m_\text{H}^2 = -\frac{\lambda_f^2}{8\pi^2}\Lambda_{UV}^2 + \mathcal{O}\left(m_f^2 \ln(\Lambda_{UV}/m_f)\right), \tag{2.7}$$

where λ_f is the coupling strength of the fermion and the normalization according to [7] is chosen. The largest corrections in the SM are caused by the t quark which has a Yukawa coupling of $\lambda_t \approx 1$, leading to enormous corrections for high values of Λ_{UV}. The observation that the Higgs boson mass is so much smaller than the cut-off scale is referred to as the *hierarchy problem*.

2.3 Supersymmetry

One possible, and since decades the most favored, theoretical extension of the SM is supersymmetry [7], able to solve several of the limitations of the SM. SUSY introduces a symmetry between fermionic and bosonic states, transforming these states into one another by applying the generator Q:

$$Q\,|Boson\rangle = |Fermion\rangle\,, \qquad Q\,|Fermion\rangle = |Boson\rangle\,. \tag{2.8}$$

Hence, the generator Q changes the spin of a particle by 1/2. SM and SUSY particles form chiral and gauge supermultiplets with two degrees of freedom for both the fermionic and bosonic states, connected via the transformation Q. The states of one supermultiplet are denoted as superpartners of each other. Since the operators Q commutes with all operators of gauge transformations and the operator of the mass squared, superpartners only differ in spin.

The names (see also Table 2.1) of the supersymmetric partners of fermions are constructed by prepending an “s”, while the names of the superpartners of SM bosons are built by appending “ino”. All SUSY particles are marked with a tilde, sometimes omitted for neutralinos ($\widetilde{\chi}_i^0$) and charginos ($\widetilde{\chi}_i^\pm$). SUSY particles are often also referred to as sparticles.

The particle content of the minimal supersymmetric extension of the SM (MSSM) is listed in Table 2.1. Besides the SUSY particles generated by Eq. (2.8), the particle

content is extended by the graviton G, the hypothetic gauge boson of the gravitational force, and its superpartner, the gravitino $\widetilde{G}$. The particle content needs to be extended to two complex Higgs chiral supermultiplets, because in the case of only one Higgs supermultiplet, EWK gauge symmetry becomes inconsistent as a quantum theory due to the non-cancellation of gauge anomalies. Also, two Higgs chiral supermultiplets are needed to give masses to all particles, due to the structure of the SUSY theory. The H_u doublet, representing the $SU(2)_L$ doublet with weak hypercharge $Y = +1/2$, consists of two weak isospin components H_u^+ and H_u^0, and gives masses to up-type quarks. The H_d doublet, representing the $SU(2)_L$ doublet with $Y = -1/2$, has the weak isospin components H_d^- and H_d^0, and gives masses to down-type quarks and charged leptons. The two complex doublets add up to eight degrees of freedom. After EWK symmetry breaking five of them manifest in three neutral and two charged mass eigenstates. The SM Higgs boson H and two further neutral Higgs scalar mass eigenstates are a linear combination of H_u^0 and H_d^0, while the two charged Higgs scalar mass eigenstates $H^\pm$ are a mixture of H_u^+ and H_d^-. The remaining three degrees of freedom give masses to the Z and $\mathrm{W}^\pm$ bosons, as already explained in Section 2.1.

Due to EWK symmetry breaking, SUSY partners of the SM gauge bosons mix to mass eigenstates. The neutral gauginos $\widetilde{B}$ and $\widetilde{W}^0$ and the neutral higgsinos $\widetilde{H}_d^0$ and $\widetilde{H}_u^0$ mix to the neutralino mass eigenstates $\widetilde{\chi}_i^0$, $i = 1, \ldots, 4$, via the matrix

$$\mathcal{M}_\mathcal{N} = \begin{pmatrix} M_1 & 0 & -\frac{1}{2}g'v_d & \frac{1}{2}g'v_u \\ 0 & M_2 & \frac{1}{2}gv_d & -\frac{1}{2}gv_u \\ -\frac{1}{2}g'v_d & \frac{1}{2}gv_d & 0 & -\mu \\ \frac{1}{2}g'v_u & -\frac{1}{2}gv_u & -\mu & 0 \end{pmatrix}, \tag{2.9}$$

given in the $(\widetilde{B}, \widetilde{W}^0, \widetilde{H}_d^0, \widetilde{H}_u^0)$ basis. The M_1, M_2, and μ are the bino, wino, and higgsino mass parameters, respectively, and v_d and v_u are the two Higgs vacuum expectation values corresponding to H_d^0 and H_u^0. Note that $v^2 = (246\,\mathrm{GeV})^2 = v_d^2 + v_u^2$. The matrix $\mathcal{M}_\mathcal{N}$ can be rotated to the mass eigenstate basis $(\widetilde{\chi}_1^0, \widetilde{\chi}_2^0, \widetilde{\chi}_3^0, \widetilde{\chi}_4^0)$ using one unitary matrix N with

$$\mathcal{M}_{\mathcal{N},\,\mathrm{diag}} = N^* \mathcal{M}_\mathcal{N} N^\dagger. \tag{2.10}$$

The diagonal element $\mathcal{M}^{ii}_{\mathcal{N},\,\mathrm{diag}}$ then corresponds to the mass of the $\widetilde{\chi}_i^0$.

Similarly, the charged gauginos $\widetilde{W}^\pm$ and the charged higgsinos $\widetilde{H}_u^+$ and $\widetilde{H}_d^-$ mix to chargino mass eigenstates $\widetilde{\chi}_1^\pm$ and $\widetilde{\chi}_2^\pm$ via the matrix

$$\mathcal{M}_\mathcal{C} = \begin{pmatrix} M_2 & \frac{1}{\sqrt{2}}gv_u \\ \frac{1}{\sqrt{2}}gv_d & \mu \end{pmatrix}. \tag{2.11}$$

SUSY models are able to solve, among other shortcomings of the SM, the hierarchy problem. Except for the Higgs boson itself, there are no massive scalar elementary particles in the SM (see Fig. 2.1). By introducing SUSY, scalar superpartners of the SM fermions are generated which aquire masses through their Yukawa coupling to the extended Higgs

Table 2.1: Table of the particle content of the MSSM. For SM bosons and the gaugino superpartners the gauge eigenstates are stated, as well as the mixing of the sfermions and gauginos.

SM particles	**Spin**	**SUSY particles**	**Spin**
Charged leptons l	1/2	Charged sleptons $\widetilde{l}_{L,R}$	0
Neutrinos ν	1/2	Sneutrinos $\widetilde{\nu}$	0
Quarks q	1/2	Squarks $\widetilde{q}_{L,R}$	0
Gluon g	1	Gluino $\widetilde{g}$	1/2
B gauge boson	1	Bino $\widetilde{B}$	1/2
W gauge boson $\mathrm{W}^{0,1,2}$	1	Winos $\widetilde{W}^{0,1,2}$	1/2
Higgs bosons H_u^+, H_u^0, H_d^-, H_d^0	0	Higgsinos $\widetilde{H}_u^+$, $\widetilde{H}_u^0$, $\widetilde{H}_d^-$, $\widetilde{H}_d^0$	1/2
Graviton G	2	Gravitino $\widetilde{G}$	3/2

$\widetilde{W}^{1,2}$, $\widetilde{H}^{\pm}_{u,d}$ mix to chargino mass eigenstates $\widetilde{\chi}_1^{\pm}$, $\widetilde{\chi}_2^{\pm}$
$\widetilde{B}$, $\widetilde{W}^0$, $\widetilde{H}^0_{u,d}$ mix to neutralino mass eigenstates $\widetilde{\chi}_1^0$, $\widetilde{\chi}_2^0$, $\widetilde{\chi}_3^0$, $\widetilde{\chi}_4^0$
$\widetilde{t}_L, \widetilde{t}_R$ $(\widetilde{b}_{L,R}, \widetilde{\tau}_{L,R})$ mix to mass eigenstates $\widetilde{t}_1, \widetilde{t}_2$ $(\widetilde{b}_{1,2}, \widetilde{\tau}_{1,2})$

field. A scalar particle S with mass m_S couples to the Higgs boson via $-\lambda_S|H|^2|S|^2$ and therefore contributes to the correction of m_{H} [7] by

$$\Delta m_{\mathrm{H}}^2 = \frac{\lambda_S}{16\pi^2}\Lambda_{UV}^2 - \mathcal{O}\left(m_S^2 \ln(\Lambda_{UV}/m_S)\right). \tag{2.12}$$

Since spin-1/2 fermions have two degrees of freedom, every SM fermion has two scalar superpartners, leading to an exact cancellation of the quadratic divergences, due to the opposite sign in the contribution, if $\lambda_f^2 = \lambda_S$.
As mentioned above, in unbroken SUSY, superpartners have the same masses, since the operator Q commutes with the operator of the mass squared. However, superpartners with similar masses would have been experimentally accessible, as for instance a selectron with a mass of 511 keV. Since no SUSY particle has been observed so far [60, 61], SUSY must be a broken symmetry. To avoid non-vanishing correction terms $(\lambda_S - \lambda_f^2)\Lambda_{UV}^2$, only soft SUSY breaking terms can be added to the Lagrangian. If m_{soft} is the highest mass scale associated with the soft breaking terms, the correction to m_{H}^2 is of the order of $m_{\mathrm{soft}}^2 \ln(\Lambda_{UV}/m_{\mathrm{soft}})$, and therefore sufficiently small if m_{soft} is of the order of TeV.

The unification of the gauge couplings at the GUT scale can be realized if sparticles indeed exist with masses around the TeV energy scale, many SUSY models provide a candidate for (cold) DM, and, if the lepton number is allowed to be violated, SUSY may also explain neutrino masses [62–64].

R-Parity

In the SM, there are no renormalizable Lagrangian terms that violate the lepton number L or baryon number B [7], in accordance with experimental observations [6]. However, a supersymmetric extension of the SM leads to gauge-invariant and renormalizable terms in the superpotential violating L and B [64]. The terms are given by

$$W_R = \underbrace{\mu_i H_u L_i + \frac{1}{2}\lambda_{ijk} L_i L_j \overline{E}_k + \lambda'_{ijk} L_i Q_j \overline{D}_k}_{\Delta L=1} + \underbrace{\frac{1}{2}\lambda''_{ijk} \overline{U}_i \overline{D}_j \overline{D}_k}_{\Delta B=1}, \tag{2.13}$$

where L and $\bar{E}$ and $Q, \bar{D}$, and $\bar{U}$ are the lepton and quark superfields, respectively. The λ, λ', and λ'' are the Yukawa couplings of the corresponding interactions and $i, j, k \in \{1, 2, 3\}$ represent the generation of the particles. The first three terms violate the lepton number, the last term violates the baryon number.
In SUSY models, a new multiplicative quantum number R_P is introduced as

$$R_P = (-1)^{3(L-B)+2S} = \begin{cases} +1 & \text{for SM particles} \\ -1 & \text{for SUSY particles} \end{cases}, \tag{2.14}$$

where S is the spin of the corresponding particle. In this analysis, R_P is assumed to be conserved, i.e., all terms in Eq. (2.13) are forbidden. This results in crucial features for SUSY events, e.g., SUSY particles have to be produced in pairs and the lightest SUSY particle (LSP) is stable. In many SUSY scenarios with R_P conservation the LSP provides for a viable DM candidate.

Gauge-mediated Superymmetry Breaking

The introduction of the MSSM leads to 105 new free parameters that appear as masses, phases, and mixing angles. This results in an unexplorable multi-dimensional parameter space. Therefore, searches for SUSY are studied in models making assumptions about mass relations and the nature of SUSY breaking and its mediation from a so-called "hidden sector" to the "visible sector", resulting in a handful of remaining free parameters. Besides models where SUSY is broken at energies of the order of the Planck scale and mediated to the visible sector through gravitational interactions only, there are models where SUSY is broken at relatively low energies and mediated by gauge interactions. Since many SUSY scenarios based on gauge-mediated SUSY breaking (GMSB) [13–15] predict final states with high-energy photons, such scenarios determine the analysis strategy developed in this search.

GMSB is a simple and robust theoretical model, automatically suppressing contributions to FCNC and under certain circumstances CP violation, which are both strongly constrained by experimental results [6].
In the minimal model of gauge mediation, only two free parameters are needed to describe all soft breaking terms [65]. However, as a consequence of the observed Higgs mass,

minimal models seem to be ruled out, as these models suppress radiative corrections to the Higgs mass [66], i.e., predict a too light Higgs boson.
Approximately one decade ago, a framework based on GMSB has been developed that encompasses all known GMSB models in a model-unified generalization. This framework is referred to as the general gauge mediation (GGM) framework proposed by Meade, Seiberg, and Shih [67–69], also, among others, used for interpretation in this thesis. The formalism enables the investigation of the entire space of gauge mediation without using a specific model.

In GMSB, the gravitino is always the LSP. Its mass is given by

$$m_{\widetilde{G}} = \frac{F}{\sqrt{3}M'_P} \simeq \left(\frac{\sqrt{F}}{100\,\text{TeV}}\right)^2 \cdot 2.37\ \text{eV}, \tag{2.15}$$

with $M'_P = 2.4{\cdot}10^{18}$ GeV and $\sqrt{F}$ being the reduced Plack mass and the fundamental SUSY breaking scale, respectively. The next-to-lightest SUSY particle (NLSP), significantly responsible for the phenomenology of the SUSY event, is either the lightest neutralino or the lightest slepton. In the following, only scenarios with the former configuration are considered. The NLSP lifetime is given by

$$c\tau_{\text{NLSP}} \equiv \mathcal{A}^{-1} \simeq 0.1\ \text{mm} \left(\frac{\sqrt{F}}{100\,\text{TeV}}\right)^4 \left(\frac{100\,\text{GeV}}{m_{\text{NLSP}}}\right)^5, \tag{2.16}$$

with m_{NLSP} being the NLSP mass. The scale $\sqrt{F}$ is typically of the order of 100 TeV, so that scenarios with prompt decays, displaced vertices or even stable NLSP lifetimes with respect to the detector length scale are possible. In this thesis, only promptly decaying NLSPs are considered.

In general, the neutralino $\widetilde{\chi}_i^0$ is a mixture of bino, wino, and higgsino gauge eigenstates. Therefore, the NLSP can be written as

$$\widetilde{\chi}_1^0 = \sum_{i=1}^{4} N_{1i}\widetilde{\psi}_i^0, \tag{2.17}$$

with $\widetilde{\psi}_i^0 = (\widetilde{B}, \widetilde{W}^0, \widetilde{H}_d^0, \widetilde{H}_u^0)$ and the values N_{1i} of the mass eigenvector. In the case of on-shell Z and H decays, the branching fractions of the NLSP [68] are given by

$$\begin{aligned}
\Gamma(\widetilde{\chi}_1^0 \to \widetilde{G} + \gamma) &= \mid N_{11}c_W + N_{12}s_W \mid^2 \mathcal{A}, \\
\Gamma(\widetilde{\chi}_1^0 \to \widetilde{G} + \text{Z}) &= \left(\mid N_{12}c_W - N_{11}s_W \mid^2 + \frac{1}{2} \mid N_{13}c_\beta - N_{14}s_\beta \mid^2\right) \left(1 - \frac{m_{\text{Z}}^2}{m_{\widetilde{\chi}_1^0}^2}\right)^4 \mathcal{A}, \\
\Gamma(\widetilde{\chi}_1^0 \to \widetilde{G} + \text{H}) &= \frac{1}{2} \mid N_{13}c_\beta + N_{14}s_\beta \mid^2 \left(1 - \frac{m_{\text{H}}^2}{m_{\widetilde{\chi}_1^0}^2}\right)^4 \mathcal{A},
\end{aligned} \tag{2.18}$$

with $s_W \equiv \sin(\theta_W)$ and $c_W \equiv \cos(\theta_W)$, and $s_\beta \equiv \sin(\beta)$ and $c_\beta \equiv \cos(\beta)$, with $\tan(\beta) = v_u/v_d$.
Hence, the nature of the NLSP decay can significantly change with different gauge eigenstate configurations. A natural choice is the assumption $|M_1| < |M_2|, |\mu|$, translating to $N_{11} > N_{12}, N_{13}, N_{14}$ in Eqs. (2.18). In the limit of a pure bino-NLSP composition ($N_{11} \to 1$, and $N_{12}, N_{13}, N_{14} \to 0$), also referred to as "bino-like" NLSP, the probability of the decay $\widetilde{\chi}_1^0 \to \widetilde{G} + \gamma$ is at least c_W^2, with a further enhancement for low NLSP masses where the Z-mass phase space suppression becomes relevant. To embed the results of the analysis in a theoretical context, besides other SUSY scenarios, one GGM scenario is used with the simplified assumption of $\widetilde{\chi}_1^0$ being bino-like and $\widetilde{\chi}_2^0$, $\widetilde{\chi}_1^\pm$ being wino-like. This results in an equivalence of the bino mass M_1 and the mass of $\widetilde{\chi}_1^0$, as well as the wino mass M_2 and the mass of $\widetilde{\chi}_2^0$ and $\widetilde{\chi}_1^\pm$. This benchmark scenario was generated in cooperation with theorists that have developed the GGM framework [67, 70].

Gravitino as dark matter candidate

In GMSB motivated SUSY scenarios, the $\widetilde{G}$ is the LSP. A non-trivial question is whether the $\widetilde{G}$, being the first SUSY particle ever proposed as a DM candidate [71], can still serve as a viable (C)DM candidate.

As shown in Eq. (2.15), the $\widetilde{G}$ has a relatively small mass compared to the remaining SUSY mass spectrum, if gauge mediation is expected to dominate over gravity mediation. In consequence, for a wide range of possible gravitino masses, the $\widetilde{G}$ is considered as warm dark matter, not able to serve as a DM candidate manifested in one single particle species. Since the fundamental SUSY breaking scale $\sqrt{F}$ is directly connected to the gravitino mass, also the lifetime of the NLSP increases with increasing $m_{\widetilde{G}}$, possibly resulting in measurable displaced vertices in collider experiments. However, there are several approaches that reconcile gravitino LSP scenarios with the explanation of DM based on SUSY. One possible realization is a mixed dark matter scenario, where gravitinos as warm DM constituting up to 60% of the thermal relics [72]. This in turn needs a tuning of the reheating temperature. Recent results set lower mass limits on warm dark matter candidates up to 5.1 keV [73].

If one considers R_P violation via bilinear terms in the parity violating potential, first term in Eq. (2.13), gravitino LSP scenarios can be consistent with cosmological constraints, e.g. the Big Bang Nucleosynthesis [74]. In this case, the $\widetilde{G}$ decay is still strongly suppressed intrinsically and its lifetime can exceed the lifetime of the universe. Advantages of such a scenario are that the bilinear R_P violating terms are able to explain neutrino masses under simultaneous consistency with proton lifetime measurements. Still other approaches introduce compressed mass spectra scenarios [75] or extensions or variations of the simplest SUSY extension of the SM [72, 76] able to explain the viability of gravitino LSP scenarios in the context of DM.

Chapter 3

Signal scenarios

Contents

After applying the final event selection the CMS data are compared to the SM expectation. To quantify how much room the results leave for the existence of SUSY, cross section upper limits are calculated for certain SUSY scenarios in dependency of one or two mass parameters. The SUSY scenarios considered in this document, also referred to as signal, are motivated by SUSY based on GMSB, favoring final states with at least one photon and undetectable gravitinos (compare Section 2.3). Two main questions guide the development of analysis strategies: What are the key final state objects the analysis wants to tag as a possible hint for SUSY and how are these objects produced initially? A distinction is made between the production of SUSY particles via EWK and strong interactions, in the following referred to as EWK or strong production.

Electroweak and strong production

In case of strong production, several high-energy jets are expected in the final state, since gluinos and squarks have to decay into quarks and the LSP or intermediate SUSY particles. If the gluinos or squarks and the SUSY particle of the decay products have similar masses, also referred to as compressed-spectrum scenarios, less energy is transferred to the jets.

In contrast, EWK production of charginos and neutralinos leads to final states with bosons (γ, $W^{\pm}$, Z, H) and LSPs, with a significantly lower hadronic activity in the event on average.

Since the strong production of gluinos or squarks has much higher cross sections at the LHC compared to EWK production channels, most SUSY searches investigate final states with large hadronic activity. As limits set on gluino and squark masses are already exceeding the one- and two-TeV threshold in many scenarios, and therefore the production of gluinos and squarks might be inaccessible at the LHC, the interest in electroweakly produced charginos and neutralinos is growing. While searches for heavy SUSY particles especially profit from the increase in the center-of-mass energy due to the large increase of the production cross section, searches for EWK production benefit from a larger data set, as collected by the CMS experiment in 2016 compared to the data set collected in 2015.

Simplified model spectra

Simplified model spectra (SMS) [77] are characterized by a particular sequence of production and decay channels with a handful of SUSY particles being considered as accessible at the LHC, with all other SUSY particles assumed to be too heavy, also denoted as "decoupled". If cascade decays occur in the SMS under consideration, simple assumptions about the branching fractions of these decays are made, usually using branching fractions of 50 or 100%. Therefore, SMS only address a certain phenomenology, in contrast to theoretically motivated models, e.g., the GGM model used in this analysis, where several phenomenologies are combined in one signal point. In the latter scenarios theory parameters are often adjusted to increase the sensitivity of a specific analysis. SMS are more transparent and improve the comparability of the results of different analyses since the same SMS are used by several analyses. However, mass limits set in a specific SMS need to be evaluated in the context of the respective model. Embedded in a theoretical consistent model the mass limits possibly decrease significantly as, e.g., branching fractions to a specific final state are much smaller as assumed in the SMS.

This search is developed to be sensitive especially to EWK production of charginos and neutralinos. An inclusive event selection is elaborated to also provide sensitivity to strong production of gluinos and squarks. Therefore, in total seven signal scenarios are used to interpret the results: one GGM [13, 15, 68, 70, 78–80] scenario dominated by EWK production, as well as two EWK and four strong production SMS.

This chapter describes the phenomenology of the scenarios under consideration and provides an overview over the highest exclusion limits set so far. A profound description of the MC simulation is provided in Section 5.3. The cross sections used to scale the simulated signal samples, as well as the selection acceptances and systematic uncertainties of each signal point are discussed in Section 9.2.

3.1 Electroweak production of charginos and neutralinos

For the simulation of EWK scenarios, the squark and gluino masses are set to a high scale rendering them inaccessible and therefore the strong production as negligible. In this case, the gaugino masses fully determine the properties and the production cross section of the model point under study.

GGM scenario

In the GGM scenario, $\widetilde{\chi}_1^0$ are assumed to be bino-like, while $\widetilde{\chi}_1^\pm$ and $\widetilde{\chi}_2^0$ are assumed to be wino-like. The GGM scenario comprises several production and decay modes depending on the mass configuration of the signal point. The dominant process is shown in Fig. 3.1. The bino and wino masses are varied in the interpretation, while higgsino and slepton masses are decoupled. The branching fractions of the decay modes of the NLSP, compare Eq. (2.18), and the scale of $p_\mathrm{T}^\mathrm{miss}$ and photon p_T are determined by the mass of the bino-like $\widetilde{\chi}_1^0$, while the masses of the wino-like $\widetilde{\chi}_1^\pm$ and $\widetilde{\chi}_2^0$ determine the production cross section. In the GGM framework, where the gauginos are not mass-degenerate by construction, a larger $\widetilde{\chi}_1^\pm - \widetilde{\chi}_1^0$ mass difference increases the hadronic energy in the final state if the Z, H, or $\mathrm{W}^\pm$ bosons decay hadronically. If the $\widetilde{\chi}_1^\pm$ and the $\widetilde{\chi}_1^0$ are nearly mass degenerate, direct chargino-to-gravitino decays via $\widetilde{\chi}_1^\pm \to \mathrm{W}^\pm\widetilde{\mathrm{G}}$ are possible.

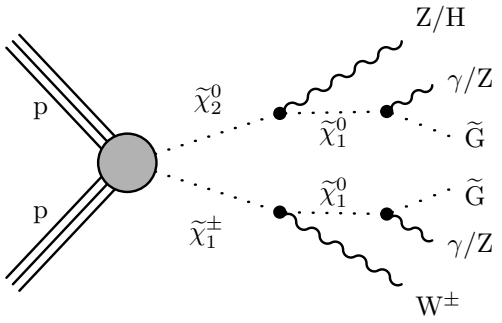

Figure 3.1: Diagram of the dominant process $\widetilde{\chi}_2^0\widetilde{\chi}_1^\pm$ production in the context of the GGM framework. The gaugino decays and the branching fractions depend on the mass configuration under study.

Besides the EWK signal scenario based on the GGM framework comprising all Feynman diagrams accessible with the corresponding configuration, two simplified EWK scenarios are used for the interpretation.

TChiWg scenario

The EWK SMS TChiWg probes the production of mass-degenerate wino-like charginos and neutralinos ($\widetilde{\chi}_1^{\pm}\widetilde{\chi}_1^0$), assuming a 100% branching fraction for the decay modes $\widetilde{\chi}_1^0 \to \gamma\widetilde{\mathrm{G}}$ and $\widetilde{\chi}_1^{\pm} \to \mathrm{W}^{\pm}\widetilde{\mathrm{G}}$. The only free parameter in this scenario is the NLSP mass $\mathrm{m_{NLSP}} \equiv \mathrm{m}_{\widetilde{\chi}_1^{\pm}} = \mathrm{m}_{\widetilde{\chi}_1^0}$. The NLSP mass determines the cross section and cross section upper limits are calculated in dependency of the $\mathrm{m_{NLSP}}$ mass parameter. The diagram of the TChiWg scenario is shown in Fig. 3.2.

Representative for EWK SUSY scenarios, the TChiWg signal point corresponding to an NLSP mass of 700 GeV is chosen as benchmark point. The signal point is chosen to be just not excluded by any other analysis, with the highest NLSP mass limit so far being 680 GeV in the TChiWg scenario. The benchmark signal point is used to illustrate the approximate behavior of the relevant EWK SUSY scenarios for similar masses. Note that significantly different mass configurations result in considerably different kinematical properties. Information on the selection acceptance and the statistical and systematic uncertainties of all mass configurations and signal scenarios under study is provided in Chapter 9.

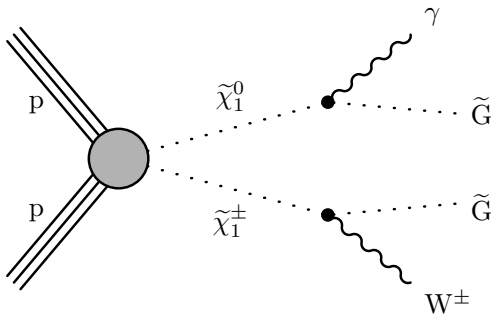

Figure 3.2: Diagram of the TChiWg SMS, where the $\widetilde{\chi}_1^0$ and $\widetilde{\chi}_1^{\pm}$ are assumed to be mass degenerate. The $\widetilde{\chi}_1^0$ decays with 100% probability into a γ and a $\widetilde{\mathrm{G}}$, while the $\widetilde{\chi}_1^{\pm}$ decays with 100% probability into a $\mathrm{W}^{\pm}$ and a $\widetilde{\mathrm{G}}$.

TChiNg scenario

The TChiNg scenario assumes nearly mass-degenerate $\widetilde{\chi}_1^{\pm}$ and $\widetilde{\chi}_1^0$, and considers EWK production of wino-like $\widetilde{\chi}_1^{\pm}\widetilde{\chi}_1^{\mp}$ and $\widetilde{\chi}_1^{\pm}\widetilde{\chi}_1^0$, as shown in Fig. 3.3. In this scenario, the $\widetilde{\chi}_1^{\pm}$ is assumed to have a slightly higher mass than $\widetilde{\chi}_1^0$, and it decays to the $\widetilde{\chi}_1^0$ and low-momentum (soft) particles outside the acceptance of this analysis. The neutralinos are assumed to decay as $\widetilde{\chi}_1^0 \to \gamma\widetilde{\mathrm{G}}$, $\widetilde{\chi}_1^0 \to \mathrm{Z}\widetilde{\mathrm{G}}$, and $\widetilde{\chi}_1^0 \to \mathrm{H}\widetilde{\mathrm{G}}$ with 50, 25, and 25% probability, respectively. The NLSP mass represents the mass of both $\widetilde{\chi}_1^{\pm}$ and $\widetilde{\chi}_1^0$ and is the only free parameter scanned in the TChiNg signal scenario.

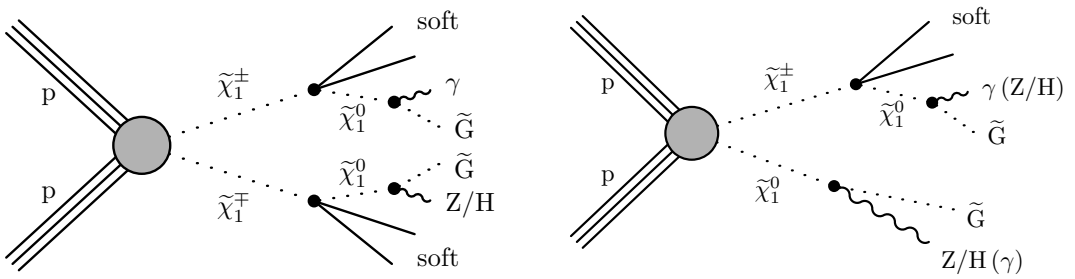

Figure 3.3: The TChiNg model comprises $\widetilde{\chi}_1^{\pm}\widetilde{\chi}_1^{\mp}$ production (left) and $\widetilde{\chi}_1^{\pm}\widetilde{\chi}_1^0$ production (right), where the $\widetilde{\chi}_1^{\pm}$ is slightly heavier than the $\widetilde{\chi}_1^0$, so that only low-momentum (soft) particles appear in the decay of $\widetilde{\chi}_1^{\pm}$ to $\widetilde{\chi}_1^0$. In the TChiNg model, the neutralinos are assumed to decay as $\widetilde{\chi}_1^0 \to \gamma\widetilde{\mathrm{G}}$, $\widetilde{\chi}_1^0 \to \mathrm{Z}\widetilde{\mathrm{G}}$, and $\widetilde{\chi}_1^0 \to \mathrm{H}\widetilde{\mathrm{G}}$ with 50, 25, and 25% probability, respectively.

3.2 Strong production of gluinos and squarks

Four strong production SMS T5gg, T5Wg, T6gg, and T6Wg are used for interpretation. The diagrams are shown in Fig. 3.4, where T5gg and T5Wg are shown in the top row and T6gg and T6Wg are shown in the bottom row of the figure. The T5gg and T5Wg scenarios represent gluino pair production, while the T6gg and T6Wg scenarios assume squark pair production. In all scenarios the neutralino decays as $\widetilde{\chi}_1^0 \to \gamma\widetilde{\mathrm{G}}$, while the chargino decays as $\widetilde{\chi}_1^{\pm} \to \mathrm{W}^{\pm}\widetilde{\mathrm{G}}$. In the T5Wg (T6Wg) scenario, a branching fraction of 50% is assumed for the decays $\widetilde{\mathrm{g}} \to \mathrm{q}\overline{\mathrm{q}}\widetilde{\chi}_1^0$ and $\widetilde{\mathrm{g}} \to \mathrm{q}\overline{\mathrm{q}}\widetilde{\chi}_1^{\pm}$ ($\widetilde{\mathrm{q}} \to \mathrm{q}\widetilde{\chi}_1^0$ and $\widetilde{\mathrm{q}} \to \mathrm{q}\widetilde{\chi}_1^{\pm}$). This results in $\gamma\mathrm{W}^{\pm}$, $\gamma\gamma$, and $\mathrm{W}^{\pm}\mathrm{W}^{\pm}$ final states with a probability of 50, 25, and 25%, respectively. The T5gg (T6gg) scenario assumes a branching fraction of 100% for $\widetilde{\mathrm{g}} \to \mathrm{q}\overline{\mathrm{q}}\widetilde{\chi}_1^0$ ($\widetilde{\mathrm{q}} \to \mathrm{q}\widetilde{\chi}_1^0$). In the T5Wg and T6Wg scenario, the neutralino and chargino are assumed to be degenerate in mass and represent the NLSP. Therefore, in all scenarios two free parameters are scanned - the mass of the gluino or squark and the NLSP mass.

As mentioned above most SUSY searches focus on strong production of SUSY particles and therefore select events with large hadronic activity. This improves the signal-to-background ratio for a large phase space of SUSY particle masses scanned in the respective model. However, if the mass splitting between the initially produced sparticles, e.g. the squarks, and the sparticle of the decay products, e.g. the $\widetilde{\chi}_1^0$, is small, less energy is transferred to the quarks produced in the decay. Therefore, requiring a large hadronic activity in the event selection not only reduces sensitivity to EWK SUSY scenarios but also significantly reduces the signal acceptance of compressed-spectrum scenarios with strong production of gluinos or squarks.

Representative for strong production SUSY scenarios, the T5Wg signal point corre-

sponding to a gluino mass of 1750 GeV and a neutralino mass of 1700 GeV is chosen as benchmark signal point. The strong production benchmark signal point falls within the scope of the compressed spectrum the analysis maximizes its sensitivity for. The signal point is excluded by the recently published analysis SUS-16-047 [81] focusing on strong production of SUSY scenarios with at least one photon in the final state, but has not been excluded by any other analysis before. Like the EWK benchmark signal point, the strong production benchmark signal point is chosen to illustrate the approximate behavior of the strong SUSY scenarios under study with similar mass configurations.

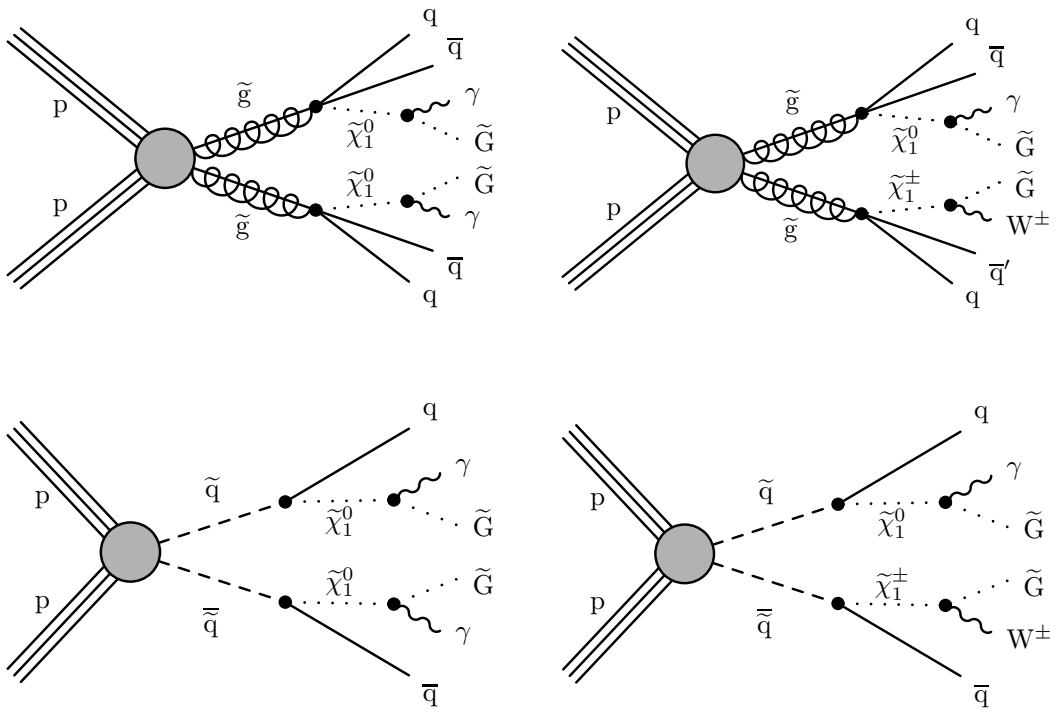

Figure 3.4: For strong gluino pair production the simplified scenarios T5gg (top left) and T5Wg (top right) are used, while for squark pair-production the simplified scenarios T6gg (bottom left) and T6Wg (bottom right) are studied. In the T5Wg (T6Wg) scenario, a branching fraction of 50% is assumed for the decays $\widetilde{g} \to q\bar{q}\widetilde{\chi}_1^{\pm}$ and $\widetilde{g} \to q\bar{q}\widetilde{\chi}_1^0$ ($\widetilde{q} \to q\widetilde{\chi}_1^{\pm}$ and $\widetilde{q} \to q\widetilde{\chi}_1^0$), resulting in final states with zero, one, or two photons.

3.3 Status of exclusion limits

The two papers SUS-14-016 [1] and SUS-16-046 [2] published by the author using 8 TeV and 13 TeV data, respectively, are the most sensitive SUSY searches for electroweak production of gauginos with photons in the final state carried out by CMS and complement other searches for electroweak production of sparticles with different final states [82, 83]. Before the publication of SUS-16-046, the highest mass limits of the three EWK SUSY signal scenarios considered in this search were set by the predecessor analysis SUS-14-016. The only (preliminary) limits for these scenarios set so far using data recorded at 13 TeV are set by SUS-16-023 [20] using 2.3 fb^{-1} of data, not able to improve on the former best limits. In the GGM scenario, SUS-14-016 excludes configurations with a wino-bino mass splitting up to 280 GeV and excludes NLSP masses below 710 GeV at 95% confidence level if the wino and bino have similar masses. In the TChiWg scenario, NLSP masses below 680 GeV are excluded by SUS-14-016, significantly improving on the limit of 540 GeV set by the analysis SUS-14-013 [18], which explicitly selects final states with at least one photon and one charged lepton. The analysis SUS-14-016 excludes NLSP masses below 570 GeV in the TChiNg scenario. Note that different assumptions were made for this version of the TChiNg scenario, disabling the direct comparability.

The most stringent limits for the strong SMS are set by the recently published analysis SUS-16-047 [81], excluding gluino masses up to 2.05 (1.95) TeV and squark masses up to 1.70 (1.55) TeV in the T5gg (T5Wg) and T6gg (T6Wg) scenario, respectively.

The ATLAS collaboration has also searched for indications of SUSY in final states with photons and has recently published a paper combining the results of a single-photon and a di-photon analysis [84]. The ATLAS collaboration interprets the results in four different GGM signal scenarios and sets, in the case of the di-photon analysis, lower limits of 1.06, 1.82, and 2.15 TeV at 95% confidence level on the masses of winos, squarks, and gluinos, respectively, independent of the bino mass. The single-photon analysis excludes gluino masses up to 2.05 TeV with decreasing sensitivity if the mass splitting between gluinos and NLSPs increases. The results are based on data corresponding to 36.1fb^{-1} recorded by the ATLAS detector at a center-of-mass-energy of 13 TeV.

Chapter 4

The experiment

Contents

The Large Hadron Collider (LHC), currently running at a center-of-mass energy of 13 TeV, is operated by the European Organization for Nuclear Research (CERN) located near Geneva. Data recorded in 2016 by the Compact Muon Solenoid (CMS) detector, located at the northernmost interaction point of the LHC, are analyzed in this thesis. In this chapter, the main features and properties of the LHC and the CMS subdetectors, as well as the CMS trigger system are briefly summarized.

4.1 The Large Hadron Collider

With a circumference of 26.7 km and a current center-of-mass energy ($\sqrt{s}$) of 13 TeV, the LHC [12] is the world's largest and most powerful storage ring particle accelerator. In 2010 and 2011, proton-proton (pp) collisions were taken at $\sqrt{s} = 7\,\text{TeV}$, while the center-of-mass energy was upgraded to 8 TeV in 2012. Since 2015, protons are collided at

$\sqrt{s} = 13\,\text{TeV}$. The LHC is supposed to be upgraded to its design center-of-mass energy of 14 TeV by 2021. Besides the pp collisions, also lead nuclei are accelerated and crossed with protons or lead nuclei in separate run eras.

Figure 4.1 shows a sketch of the LHC complex, including the pre-accelerators and the main experiments. The accelerated particles collide at four different interaction points, where the experiments ALICE (A Large Ion Collider Experiment) [85, 86], ATLAS (A Toroidal LHC Apparatus) [87, 88], CMS [8–11], and LHCb (LHC beauty) [89, 90] are located. ALICE is a detector specialized for heavy ion collisions and built to gain insight into quark-gluon plasma, a state expected to have existed shortly after the Big Bang. ATLAS and CMS are multi-purpose detectors built to search for the Higgs boson and new physical phenomena, to perform precision measurements of SM physics, and to analyze lead ion collisions. LHCb is an asymmetric detector only covering the forward region in one direction of the beam axes. The detector is specialized in analyzing the properties of meson decays containing b or c quarks. Main goals of the LHCb collaboration are to investigate CP-violation, to measure rare decays, and to perform SM precision measurements, which also serve as indirect searches for new physics.

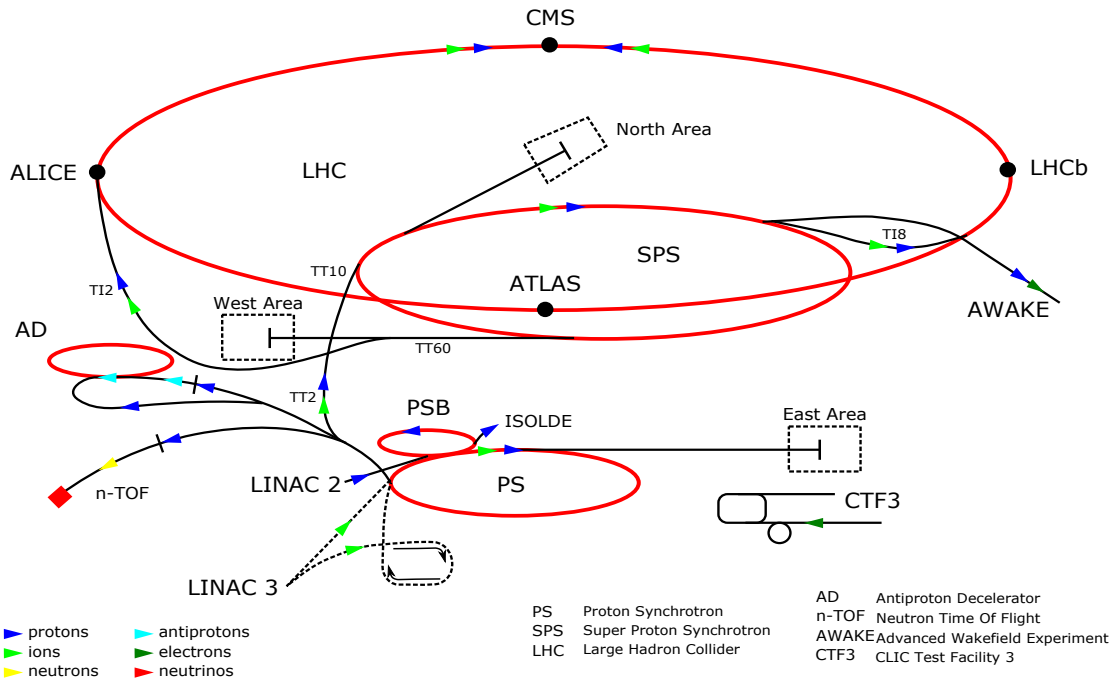

Figure 4.1: Sketch of the LHC complex [91]. Shown are the different pre-accelerators, the LHC storage ring, the four interaction points and several further components. The CMS detector is located at the northernmost interaction point of the LHC.

Before the proton beams are squeezed and collided with almost the speed of light and an energy of 6.5 TeV per proton at one of the crossing points of the LHC, the journey

starts with a bottle of hydrogen gas. The hydrogen atoms are stripped of their electrons by an electric field to obtain protons. These are accelerated by the linear accelerator LINAC 2 to an energy of 50 MeV, before they pass through the acceleration chain of the BOOSTER, the Proton Synchrotron (PS) and the Super Proton Synchrotron (SPS). With an energy of 450 GeV the proton bunches are transferred to the LHC, where their energy is increased to 6.5 TeV. Two beam pipes are used in the LHC to accelerate the bunches in opposite directions. After the LHC system status shows that stable beams have been achieved, the proton bunches are brought to collision. In a typical run, the proton beams are stored in the ring for several hours and the bunches are collided every 25 ns.

A measure of the performance of a collider is given by the instantaneous luminosity

$$\mathcal{L} = N_b^2 n_b f \mathcal{F}/\mathcal{G}, \tag{4.1}$$

Here, N_b is the number of protons in one bunch assuming the same number of protons in each bunch for both beams, n_b is the number of bunches, and f is the revolution frequency.
There are two geometrical factors affecting the magnitude of the luminosity. The beam-related geometrical factor $\mathcal{G}$ characterizes the finite spatial extent of the proton bunches. Most commonly, $\mathcal{G}$ is given by

$$\mathcal{G} = 4\pi\sigma_x\sigma_y = 4\pi\varepsilon_n\beta^*/(\gamma_{\text{rel}}\beta_{\text{rel}}). \tag{4.2}$$

where σ_x and σ_y are the Gaussian widths of a bunch in the plane transverse to the beam direction, assuming equal beams [92]. The less descriptive but more commonly stated values ε_n and β^* are the normalized emittance and the betatron function at the interaction point, respectively [9, 12]. The values γ_{rel} and β_{rel} are the relativistic gamma and beta factors, with $\beta_{\text{rel}} \approx 1$ in very good approximation.
The apparatus-related geometrical factor $\mathcal{F}$ takes the reduction of the luminosity through the deliberate non-zero crossing angle ϕ, as well as an offset of the two beams into account, where the former effect has the largest impact on $\mathcal{F}$ and is given by

$$\mathcal{F} \approx 1/\sqrt{1 + \frac{\gamma_{\text{rel}}\beta_{\text{rel}}(\sigma_s \tan(\phi/2))^2}{\varepsilon_n\beta^*}} \approx 1/\sqrt{1 + \left(\frac{\sigma_s}{\sigma_x}\frac{\phi}{2}\right)^2} < 1, \tag{4.3}$$

where the last step uses the relation $\sigma_x\sigma_y = \varepsilon_n\beta^*/\gamma_{\text{rel}}\beta_{\text{rel}}$ and approximates $\sigma_x \approx \sigma_y$, and $\phi \ll 1$ [92, 93]. The value σ_s represents the bunch length.
Values relevant for the data taken in 2016 are given in Table 4.1 [94].

The instantaneous luminosity decreases with time over a progressing run. Integrating $\mathcal{L}$ over a certain runtime results in a measure for the number of events produced within this data-taking period. The number of events N for a certain process is given by

$$\mathrm{N} = \mathcal{L}_{\text{int}} \cdot \sigma, \quad \text{with} \quad \mathcal{L}_{\text{int}} = \int \mathcal{L}\, dt, \tag{4.4}$$

Table 4.1: LHC beam parameters in 2016 [94].

Parameter	Value in 2016
Betatron function β^*	40 cm
Normalized emittance ε_n	2.2 μm
Crossing angle ϕ	370 / 280 μrad
Number of bunches n_b	2220
Number of protons in one bunch N_b	$1.1{\cdot}10^{11}$
Apparatus-related geometrical factor $\mathcal{F}$	~ 0.65

where σ is the production cross section of the respective process and $\mathcal{L}_{\text{int}}$ the integrated luminosity.

In contrast to the former most powerful particle collider Tevatron [95] at Fermilab near Chicago, which collided protons and antiprotons at $\sqrt{s} = 1.96\,\text{TeV}$, the LHC uses two proton beams to reach much higher luminosities. Since the production of protons is much easier and cheaper compared to the production of antiprotons, N_b and n_b can be increased significantly. Albeit, the usage of two proton beams comes at the cost of the necessity to build two beam pipes instead of one. In 2016, the peak instantaneous luminosity achieved at the LHC was $\mathcal{L} = 1.5{\cdot}10^{34}\,\text{cm}^{-2}\text{s}^{-1}$, almost 40 times higher than the record peak luminosity of the Tevatron [96, 97]. The integrated luminosity delivered by the LHC in 2016 is $\mathcal{L}_{\text{int}} = 40.8\,\text{fb}^{-1}$ [98]. Both the instantaneous and the integrated luminosity for the data-taking period in 2016 are shown in Fig. 4.2 versus day.

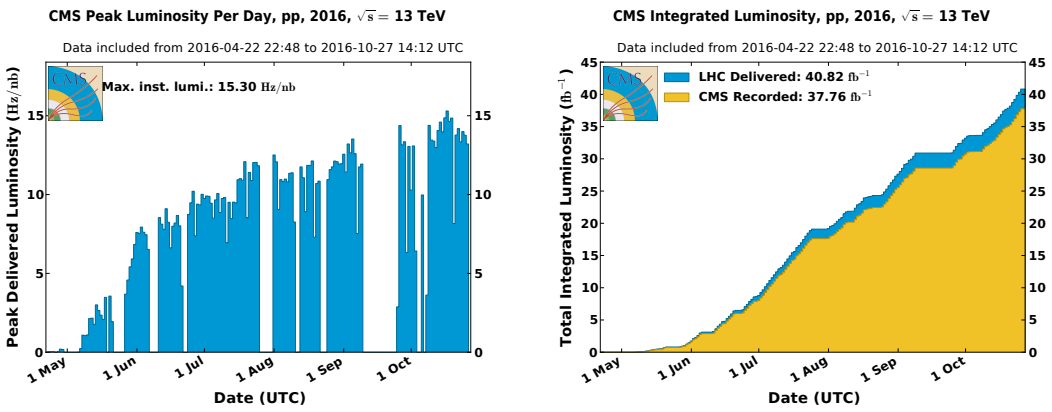

Figure 4.2: Plots of the history of the instantaneous (left) and integrated (right) luminosity for the data-taking period in 2016 versus date [98].

4.2 The Compact Muon Solenoid experiment

The CMS detector has a length of 21.6 m, a diameter of 14.6 m and weighs around 14 kt. The CMS detector is centered around the interaction region and provides a good coverage of the 4π solid angle. To enable a good particle reconstruction and distinction, the CMS detector is composed of a silicon pixel and strip tracking system close to the interaction point, a calorimeter system, consisting of a electromagnetic and a hadron calorimeter, a superconducting solenoid magnet constructed around the calorimeter system and gas-ionization muon chambers as the outermost component. The detector is divided into a barrel and two endcap sections. A sketch of the CMS detector is provided in Fig. 4.3.

In the following, the coordinate system conventionally used for analyses in CMS, the subdetectors and the trigger system of CMS are briefly introduced. Since the analysis investigates final states with photons and large missing transverse moment, the electromagnetic calorimeter is of special importance due to the energy measurement of the photon. The tracker system provides an effective distinction of photons and electrons. All subdetector components are important for a precise global reconstruction of the event and thus for the determination of the momentum imbalance.

4.2.1 The coordinate system and transverse quantities

The right-handed coordinate system conventionally used by CMS analyses has the origin centered at the nominal collision point. The x-axis points radially inward to the center of the LHC, the y-axis is pointing upwards and the z-axis points along the beam axis westwards to the Jura Mountains [99]. A polar coordinate system is chosen, with the azimuthal angle $\phi \in [-\pi, \pi]$ measured in the $x - y$ plane, also referred to as transverse plane, with $\phi = 0$ describing the positive x-axis. The polar angle $\theta \in [0, \pi]$ is measured with respect to the positive z-axis. The radial coordinate in the transverse plane is denoted by r.
The pseudorapidity η is defined by

$$\eta = -\ln\left(\tan\left(\frac{\theta}{2}\right)\right) \tag{4.5}$$

and results in a quantity describing the particle's direction with respect to the beam axis with the property that differences, i.e. $\Delta\eta = \eta_1 - \eta_2$, are invariant against Lorentz boosts along the z-axis in the limit of massless particles.

Since protons consist of quarks with unknown longitudinal momenta, the boost of colliding partons along the beam axis differs for each collision. In contrast to that, the transverse momenta of the incoming partons are expected to be small. The CMS detector completely covers the plane transverse to the beam axis, whereas the coverage along θ is limited by

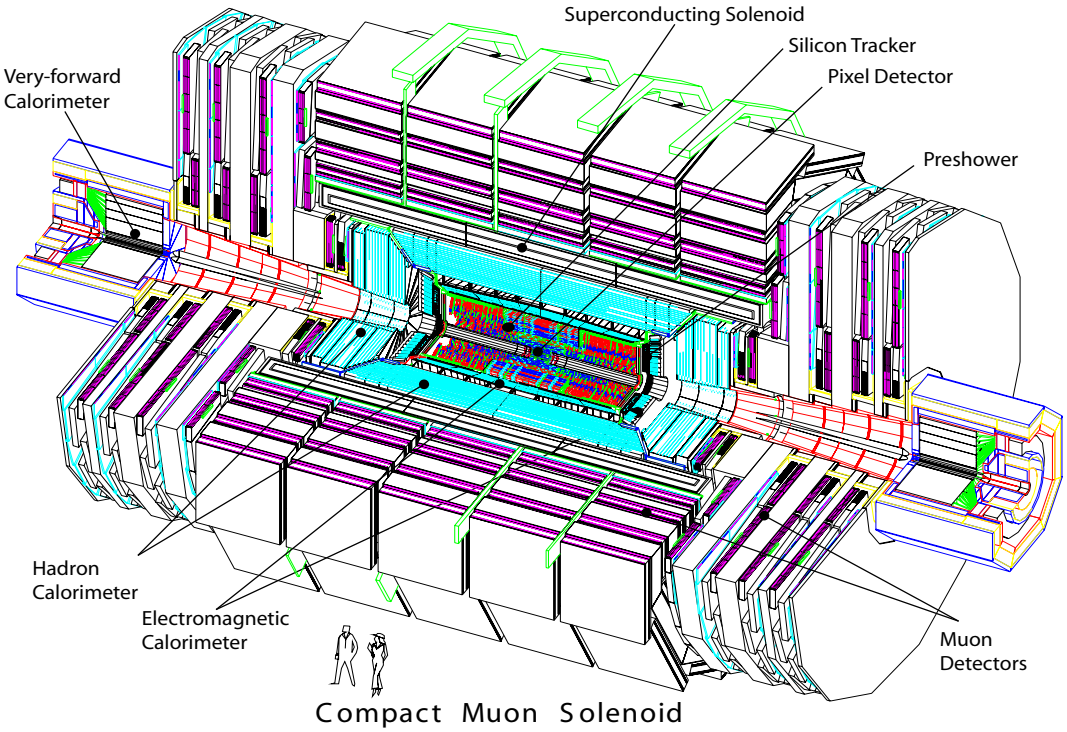

Figure 4.3: Sketch of the CMS detector illustrating all subdetector components [9]. The innermost component is the tracker system composed of a pixel detector and a silicon strip tracker, followed by the electromagnetic and hadronic calorimeter. The magnetic coil is placed behind the hadronic calorimeter (except for the hadron outer calorimeter). The outermost components are the muon detectors.

the beam pipe. For kinematic studies the momenta p of the reconstructed objects are often projected onto the transverse plane by $p_{\mathrm{T}} = p \cdot \sin(\theta) = \sqrt{p_x^2 + p_y^2}$ and similarly for the transverse energy $E_{\mathrm{T}} = E \cdot \sin(\theta)$. These transverse quantities are invariant under Lorentz boost along z.

4.2.2 The tracker system

The silicon tracker system is the innermost component of the CMS detector and is specialized in measuring trajectories of charged particles which are bent due to the magnetic field of 3.8 T in the tracker volume, momenta, and charge signs. Due to the spatial proximity, the tracker is responsible for the identification of primary and displaced vertices, the latter being especially important for a reliable b quark identification.

The tracker system is composed of the inner pixel detector and the outer strip detector. The tracker has a length of 5.8 m and a diameter of about 2.5 m. A schematic cross section of the tracker system, showing the status during the data-taking in 2016, is shown in Fig. 4.4. In the course of the phase-1 CMS upgrade, the pixel detector was upgraded to four barrel layers and three endcap disks for the data-taking period starting in 2017 [100, 101]. The tracker system as present during the data-taking in 2016 is discussed in the following. Statements about resolutions should be understood as reference values, as they depend on several parameters, e.g., the cluster width, the pitch, or the track angle [8, 9, 102, 103].

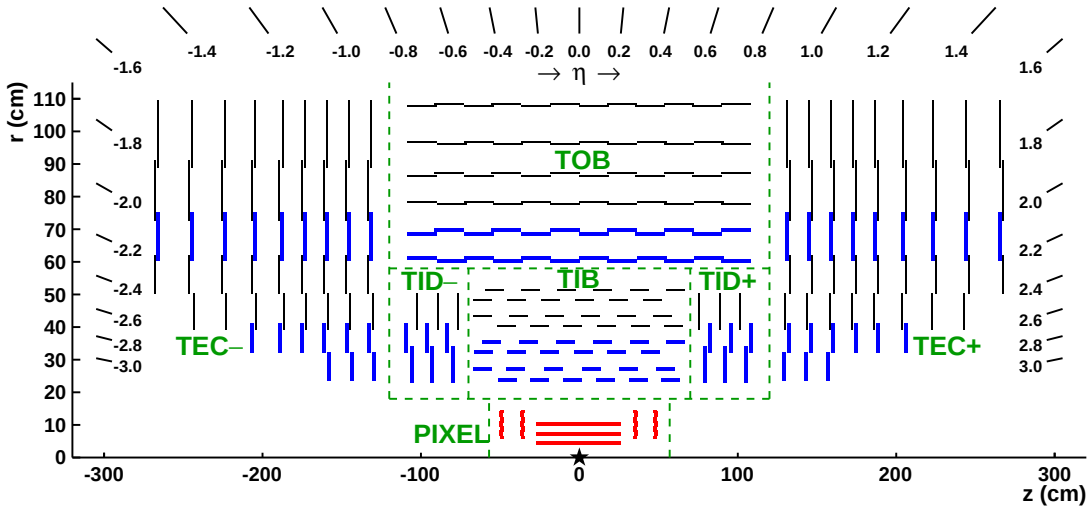

Figure 4.4: Schematic cross section of the CMS tracker system [102]. The innermost component is the silicon pixel detector, composed of three layers in the barrel region and two in each encap. The strip detector consists of the TIB, TOB, TID, and TEC. The spatial extent and values of η are given to illustrate the geometry. Modules sketched in blue and red provide a three-dimensional hit position reconstruction, while those shown in black provide a two-dimensional reconstruction.

The inner pixel detector has three barrel layers at radii of 4.4, 7.3, and 10.2 cm and two endcap disks at each side placed at $z = \pm 34.5$ cm and $z = \pm 46.5$ cm and has a higher granularity compared to the strip detector. One pixel cell has a size of 100×150 μm^2 in $r - \phi \times z$. Due to the analog pulse height read-out and charge-sharing between neighbouring pixels, a position resolution of $\sim$10 μm and $\sim$20 μm is achieved in $r - \phi$ and z direction, respectively. The pixel detector consists of 1440 modules with about 66 million pixels covering the pseudorapidity range $|\eta| < 2.5$. It has a total area of $\sim$1 m^2.

Due to cost reasons and the decreasing particle flux per area with larger radii, the outer region of the tracker is based on strip detector modules. The strip detector is located in the radial region from 20 to 116 cm and is separated into the tracker inner barrel

(TIB), tracker outer barrel (TOB), tracker inner disk (TID), and tracker endcap (TEC), as shown in Fig. 4.4. Details about the geometrical arrangement of the various strip detector subsystems are listed in Table 4.2.

Table 4.2: Geometrical arrangement of the various strip detector subsystems. The number of disks in the TID and TEC refer to one single endcap. The pitch is the distance between the read-out strips.

Subsystem	Layers	Strip pitch	Sensor thickness	Location
TIB	4 barrel layers	$80 - 120\ \mu$m	$320\ \mu$m	$20 < r < 55$ cm
TID	3 disks	$100 - 141\ \mu$m	$320\ \mu$m	$58 < \|z\| < 124$ cm
TOB	6 barrel layers	$122 - 183\ \mu$m	$500\ \mu$m	$55 < r < 116$ cm
TEC	9 disks	$97 - 184\ \mu$m	$320 - 500\ \mu$m	$124 < \|z\| < 282$ cm

Two micro-strip detectors tilted by 100 mrad are mounted back-to-back on the first two layers of the TIB, TID and TOB, as well as on the rings 1, 2, and 5 of the TEC, to provide a measurement of the corresponding second (stereo) coordinate (z or r). In total, the silicon strip detector consists of 15,148 modules with about 9.3 million strips.

Figure 4.5 (right) illustrates the expected number of hits depending on the pseudorapidity achieved by this layout. For $|\eta| \lesssim 2.4$ at least three hits in the pixel and eight hits in the strip detector are expected. The number of hits decrease for very high $|\eta|$. The overall material budget of the tracker ranges from 0.4 to 1.9 radiation lengths with the maximum in the transition region of the barrel and the endcaps [102].

The homogeneous magnetic field of 3.8 T in the tracker system allows for a high momentum resolution. The momentum resolution of the tracker for muons with a p_{T} of 1, 10, and 100 GeV is shown in Fig. 4.6 (left) as a function of η. Figure 4.6 (right) shows the momentum resolution for muons with $|\eta| < 0.9$ (barrel region), $0.9 < |\eta| < 1.4$ (transition region), and $1.4 < |\eta| < 2.5$ (endcap region) in dependency of p_{T}. The momentum resolution is $1 - 3\%$ for muons with $p_{\mathrm{T}} \leq 100$ GeV and $|\eta| \lesssim 1.5$, degrading for higher values of $|\eta|$ and p_{T}. The arrangement of the silicon tracker modules is aligned using tracks generated by cosmic muons and using data from LHC pp collisions [104].

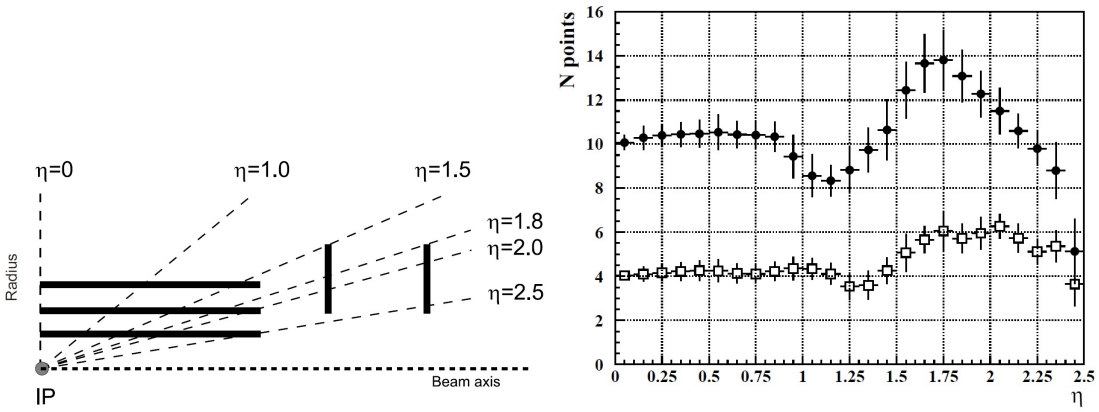

Figure 4.5: Expected number of hits for the silicon pixel detector (left) and the silicon strip detector (right) depending on the pseudorapidity [8]. Except for very high $|\eta|$, three hits in the pixel and about nine hits in the strip detector are expected. In the right plot, the open squares show the number of stereo layers and the filled circles show the full number of measured hits.

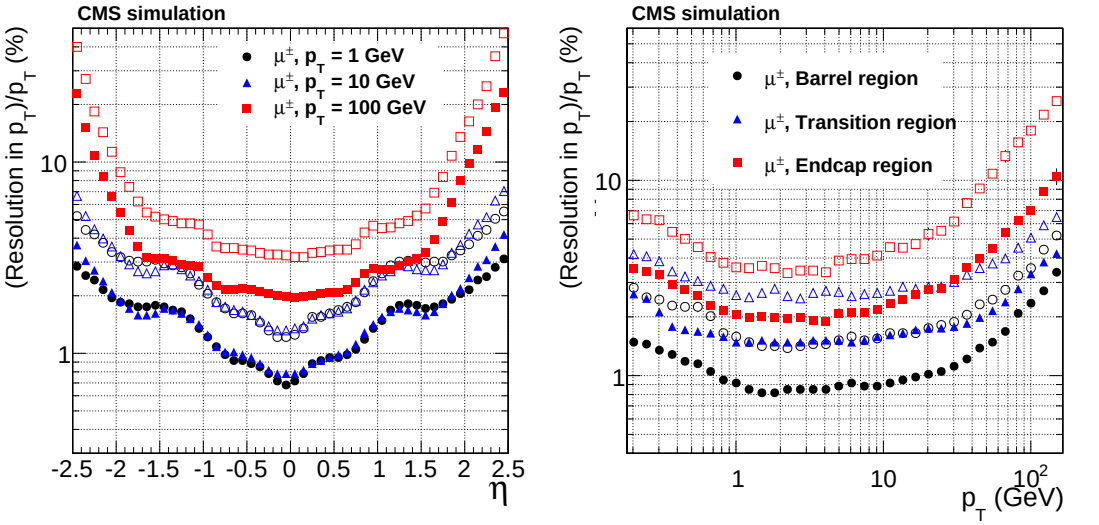

Figure 4.6: Momentum resolution of the CMS tracker depending on η (left) for muons with a p_{T} of 1, 10, and 100 GeV and as a function of p_{T} (right) for muons with $|\eta| < 0.9$ (barrel region), $0.9 < |\eta| < 1.4$ (transition region), and $1.4 < |\eta| < 2.5$ (endcap region), studied using simulated events [102]. The solid (open) markers correspond to the resolution given by the width that contain 68% (90%) of the track residuals. The track residuals are the differences between the reconstructed track parameters and the corresponding parameters of the generated particles.

4.2.3 The electromagnetic calorimeter

The electromagnetic calorimeter (ECAL) is especially responsible for the electron identification and photon energy measurement and is the most important subdetector for the photon identification and characterization. Since electrons and photons share a similar signature in the ECAL, information of the tracker system is needed to distinguish these objects. Similarly to the tracker system, the ECAL is also divided into a barrel and two endcap regions.

The ECAL consists of 75848 lead tungstate ($PbWO_4$) crystals, of which 61200 are mounted in the ECAL barrel ($|\eta| < 1.479$) arranged in a 360- to 170-fold structure in ϕ and η, respectively. Lead tungstate crystals have a high density of 8.28 g/cm^3, a radiation length of 0.89 cm and a Molière radius of 22 mm. The short scintillation decay time ensures the emission of ∼80% of the light in 25 ns, which equals the time of the bunch spacing in the data-taking in 2016. Photodetectors are attached to the $PbWO_4$ crystals to collect the light output, with avalanche photodiodes used in the ECAL barrel and vacuum phototriodes used in the ECAL endcaps. The properties of $PbWO_4$ crystals allow for a fast and compact calorimeter with high granularity, providing an optimal reconstruction of the energy and direction of photons and electrons. The barrel (endcap) crystal volume is 8.14 m^3 (2.90 m^3) with a weight of 67.4 t (24.0 t) with the forefront of the barrel crystals being about 1.29 m away from the nominal interaction point. The endcap envelope has a longitudinal distance to the interaction point of about 3.15 m.

The layout of the ECAL is shown in Fig. 4.7. The crystals in the barrel are grouped in submodules, which are assembled in modules of different types with four of them forming one supermodule. Each ECAL endcap, covering the range $1.479 < |\eta| < 3.0$, consists of two halves, each half containing 3662 crystals. The crystals in the endcap are grouped to 5×5 supercrystal units. Preshower detectors, with a much finer granularity compared to the ECAL, are mounted in front of the ECAL endcaps to identify neutral pions and to improve the position determination of the e/γ candidate. The preshower detectors consist of two layers, with one layer composed of a lead radiator layer followed by silicon strip sensors

The crystals used in the barrel have a cross section at the front of the crystals of 0.0174×0.0174 in $\eta \times \phi$ which corresponds to an area of 22×22 mm^2, chosen to fit the Molière radius of $PbWO_4$. The length of the crystals is 23 cm, corresponding to ∼26 radiation lengths. If photons are required to be measured in the ECAL barrel, the position of the seed has to fulfill $|\eta| < 1.4442$. This value ensures that a 5×5 array of crystals can be spanned around the seed, without exceeding the edge of the ECAL barrel at $|\eta| = 1.479$. The crystals used in the endcap have a front face cross section of 28.6×28.6 mm^2 and a length of 22 cm, corresponding to ∼25 radiation lengths. To avoid crystal borders aligned with particle trajectories, the crystals in the barrel are mounted at an angle of 3° with respect to the vector from the nominal interaction point to the crystals. The crystals in the endcap focus a point 1.3 m away from the interaction point, resulting in $2° - 8°$ angles, varying with η. The preshower detectors mounted in front

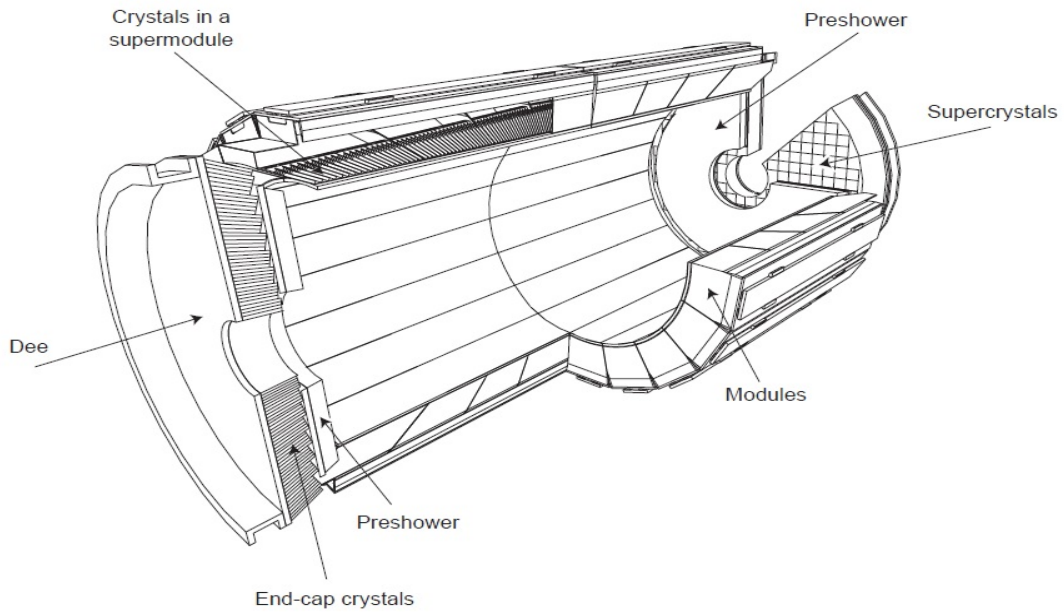

Figure 4.7: Layout of the CMS ECAL [8]. The barrel consists of tilted lead tungstate crystals organized in submodules, modules, and supermodules, as indicated in the figure. Each endcap is divided in two halfs ("Dees") with crystals assembled in 5×5 supercrystals. A preshower detector is mounted in front of the edcaps.

of the crystals in the endcaps range from $1.653 < |\eta| < 2.6$. A schematic section of the ECAL is shown in Fig. 4.8.

The energy resolution of the ECAL [8, 105] for particles with energies below ∼500 GeV can be parametrized by

$$\frac{\sigma_E}{E} = \frac{S}{\sqrt{E/\mathrm{GeV}}} \oplus \frac{N}{E/\mathrm{GeV}} \oplus C, \tag{4.6}$$

where S is the stochastic term related to the number of scintillation photons, resulting in an improvement of the energy resolution with higher energies. N is the noise term caused by electronics, digitization, and noise from multiple pp interactions in one bunch crossing and C is a constant term mainly due to the non-uniformity of the longitudinal light collection, intercalibration errors and rear leakage of energy in the crystal. Using a test beam of electrons with momenta between 20 and 250 GeV, a typical energy resolution of a test barrel supermodule was found to be

$$\frac{\sigma_E}{E} = \frac{2.8\%}{\sqrt{E/\mathrm{GeV}}} \oplus \frac{12\%}{E/\mathrm{GeV}} \oplus 0.3\%, \tag{4.7}$$

as shown in the fit in Fig. 4.9 (left). Since the test was performed using only one fully equipped supermodule, only electron beams with a central impact were used. The energy

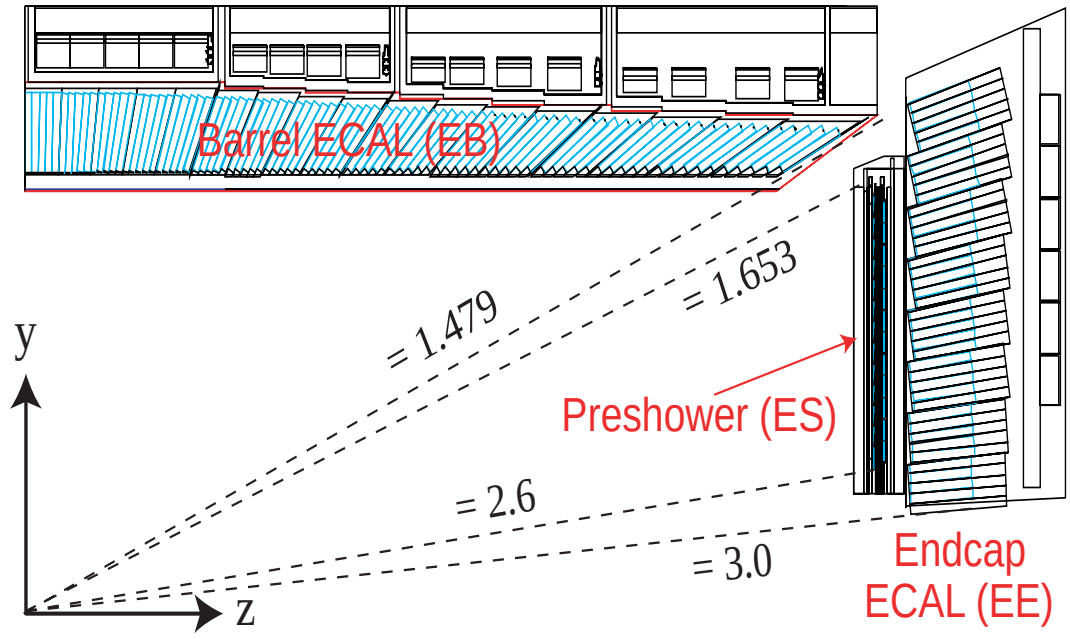

Figure 4.8: Sketch of the CMS ECAL geometry [9]. The barrel covers the area of $|\eta| < 1.479$, the endcaps the region $1.479 < |\eta| < 3.0$. The preshower detectors are mounted in front of the edcaps, covering $1.653 < |\eta| < 2.6$.

was reconstructed from 3×3 crystal matrices.
Energy resolution measurements were also performed with only a loose lateral impact restriction imposed by the trigger. The result for a beam with electron momenta of 120 GeV and an energy reconstruction using a 5×5 crystal cluster is shown in Fig. 4.9 (right), being in good agreement with Eq. 4.7. In this test, a shower containment correction as a function of the incident position was applied.

4.2.4 The hadron calorimeter

The hadron calorimeter (HCAL), located outside the ECAL, is especially important for the energy measurement of hadron jets. In contrast to many SUSY searches, the analysis presented in this thesis uses an inclusive event selection with regard to jets and the overall hadronic activity, reducing the importance of the HCAL for this search. The impact of the HCAL on the resolution of the total transverse momentum imbalance measurement is reduced by using a global event reconstruction exploiting the information provided by all CMS subdetectors. Since final states with jets are not explicitly selected in the analysis, the resolution of the momentum imbalance measurement is better on average compared to analyses selecting events with large hadronic activity.

Similarly to the tracker system and the ECAL, the HCAL is separated into the HCAL barrel (HB), $|\eta| < 1.4$, and the HCAL endcaps (HE), $1.3 < |\eta| < 3.0$. The sampling

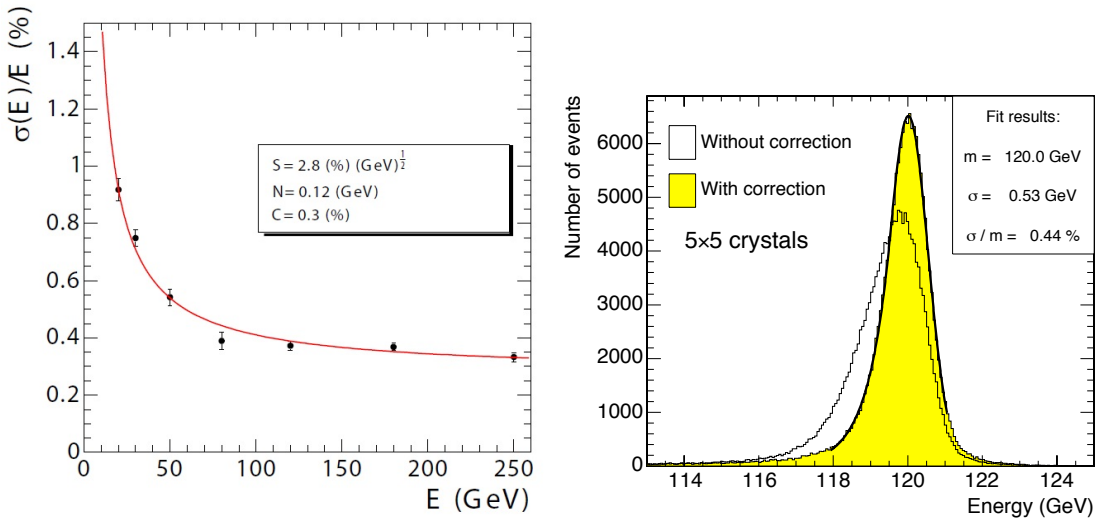

Figure 4.9: A test beam of electrons with a p_{T} between 20 GeV and 250 GeV was used to determine the energy resolution of the ECAL (left) [8], following the parametrization given in Eq. (4.7). In a similar test, an energy resolution of 0.44% for electrons with momenta of 120 GeV was achieved, after the correction for shower containment is applied (right) [8], in good agreement with Eq. (4.7).

calorimeter is made of brass and stainless steel absorbers and plastic scintillators, where the scintillation light is converted by wavelength-shifting fibres and collected by hybrid photodiodes. Additionally, the HCAL system consists of the hadron forward calorimeter (HF), $2.9 < |\eta| < 5$, and the hadron outer (HO) calorimeter, $|\eta| < 1.26$, mounted in the barrel region behind the solenoid. The granularity of the HCAL is $\Delta\eta \times \Delta\phi = 0.087 \times 0.087$ for $|\eta| < 1.6$ and $\Delta\eta \times \Delta\phi \approx 0.17 \times 0.17$ for $|\eta| \geq 1.6$. Figure 4.10 shows a schematic view of the different HCAL components, also indicating the coverage depending on η.

The HB reaches from $r = 1.77$ m to $r = 2.95$ m and is divided into two halves with one half consisting of 18 wedges uniformly arranged in ϕ. Each wedge is further segmented into four sectors and consists of 14 flat brass alloy absorber plates and an innermost and outermost absorber layer made of stainless steel. The plates are aligned parallel to the beam axis. In total, 17 active plastic scintillator tiles are placed between and in front of the absorber layers. The HB wedges are classified into 32 sectors in η to form HCAL towers, such that 16 HCAL towers cover the pseudorapidity range $0 < \eta < 1.392$, as shown in Fig. 4.11. An effective thickness of 5.8 to 10.6 interaction lengths is achieved in the barrel region, increasing with η. The design energy resolution of the HB for single pions with energy E given in GeV is approximately $120\%/\sqrt{E}$. Studies of HCAL test beam data using pions with an energy of $20 - 300$ GeV [106] are in consistency with the design resolution, where

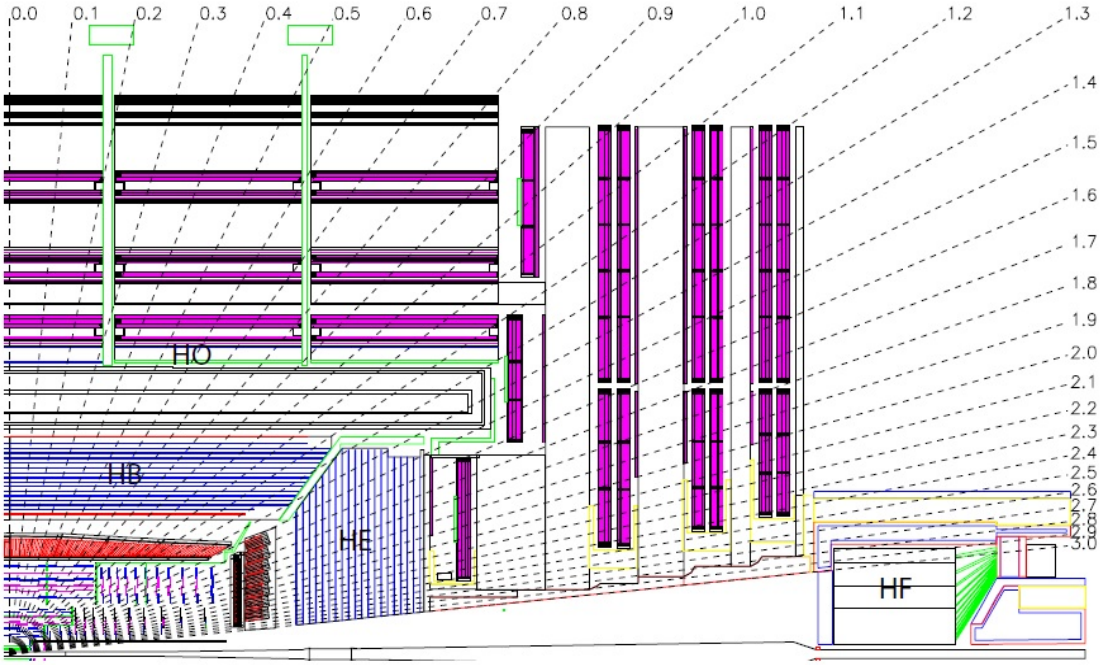

Figure 4.10: Schematic view of the CMS detector, focusing on the HCAL components HB, HE, HO, and HF [8]. The dashed lines illustrate the pseudorapidity coverage.

the resolution was found to follow the relation

$$\frac{\sigma_E}{E} = \frac{115\%}{\sqrt{E/\,\mathrm{GeV}}} \oplus 5.5\%. \tag{4.8}$$

Combining the response of the ECAL and the HCAL, as studied in particle test beams with particle energies varying from 2 to 350 GeV [107], the resolution follows the relation

$$\frac{\sigma_E}{E} = \frac{85\%}{\sqrt{E/\,\mathrm{GeV}}} \oplus 7.4\%. \tag{4.9}$$

The jet momentum resolution in pp collisions, after exploiting information provided by all subdetectors and after applying corrections, is discussed in Section 6.1.3.

In the HE, brass alloy absorber plates with a higher thickness are used with active plastic scintillator layers in between. Per endcap 36 wedges with 14 towers are installed, with one tower overlapping with the HB, as can been seen in Fig. 4.11. The total effective thickness of the HE, including the electromagnetic crystals, is about 10 interaction lengths.

Since especially the HB is limited in size by the magnet and the tracker and ECAL system, the effective thickness realized by the HB is not sufficient. Therefore, the HO detector is mounted outside the solenoid in the barrel region with a layer of scintillators

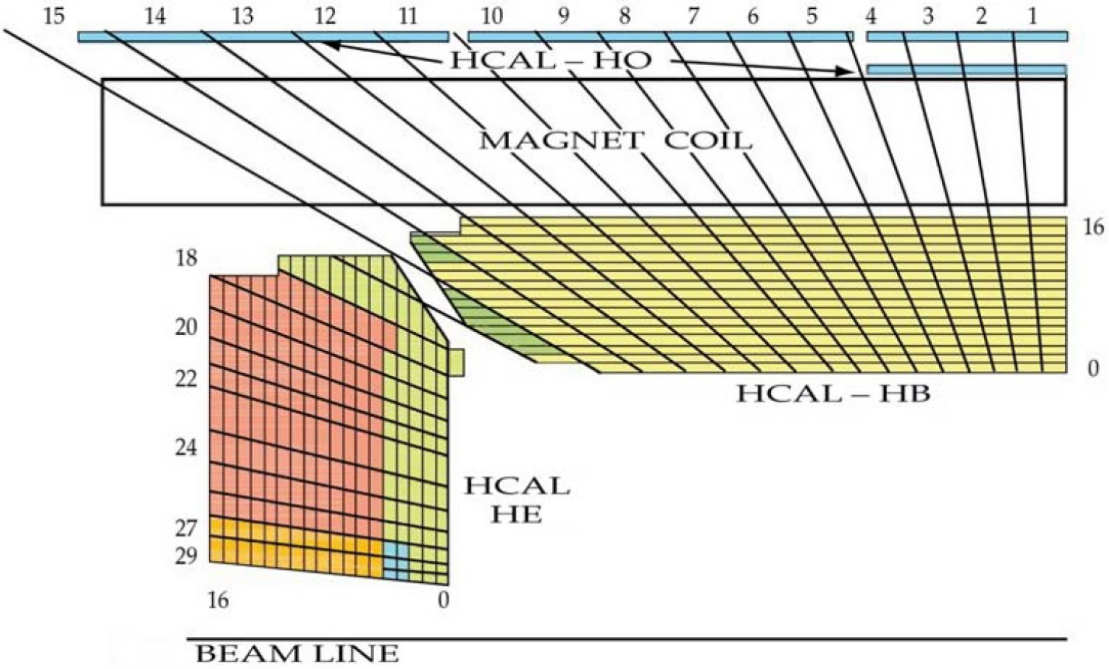

Figure 4.11: Illustration of the HCAL tower segmentation in the HB and the HE [8]. Also shown is the extra HO layer outside the solenoid, extended by a second layer for the most central part of the HCAL. The shading indicates the optical grouping of scintillator layers.

at a radial distance of $r = 4.07$ m. The most central part, covering the first four towers to each side with respect to $\eta = 0$, has an additional HO scintillator layer at $r = 3.82$ m, as shown in Fig 4.11. Combined, the HB, the magnet, and the HO provide an effective thickness of about 10 interaction lengths.

Since the energy deposition in the HF is approximately 8 times larger than the energy deposition in the rest of the detector, one crucial challenge of the HF is high radiation hardness. Therefore, quartz fibres are used as active medium to generate Cerenkov light, which is collected by photomultipliers. Grooved steel plates serve as absorbers. The HF is placed at a distance of $z = 11.2$ m to the interaction point.

4.2.5 The superconducting solenoid magnet

The (relative) momentum resolution of a charged particle in the CMS tracker degrades with the particle's momentum, except for a p_{T} smaller then a few GeV, since the bending radius increases with higher energies. To ensure a good momentum resolution also for high-energy charged particles, a strong magnetic field is needed. The superconducting solenoid used in CMS is placed behind the ECAL and HCAL with respect to the interaction point to avoid additional material in front of the calorimeters. The solenoid

of CMS has a length of 12.5 m, a diameter of 6.3 m, and creates a magnetic field of 3.8 T in the inner volume. The solenoid has a cold mass of 220 t with a four-layer winding of NbTi conductors. The magnet is cooled down to a temperature of 4.5 K using liquid helium. It stores an energy of 2.6 GJ at full current and has an inductance of 14.2 H. The 10000 t heavy iron return yoke of the solenoid ensures a magnetic field in the yoke of about 2 T and consists of five wheels and two endcaps, composed of three disks each, as can be seen in Fig. 4.3.

4.2.6 The muon system

The muon system is the outermost component of the CMS detector. Besides particles not interacting with any of the detector components and punch-through jets, muons are the only particles expected to reach the muon system. The tracker and the muon system provide independent muon momentum measurements, enabling a significant improvement in resolution if information of both subdetectors is combined by a global fit. The impact of the combination is illustrated in Fig. 4.12 as a function of the tranverse momentum of the muon. As the name of the experiment already suggests, the muon identification is of central importance in CMS. Besides the di-photon channel, the $H \to ZZ^* \to \mu^{\pm}\mu^{\mp}\mu^{\pm}\mu^{\mp}$ provided the highest sensitivity in the Higgs boson discovery. In this analysis, the muon identification does only play a minor role. Therefore, the description of the muon system is kept brief. More details can be found in Chapter 7 in [8].

The muon system is divided into the barrel region, $|\eta| < 1.2$, and the overlapping endcaps, $0.9 < |\eta| < 2.4$. The magnetic field within the muon detectors is mostly uniform and the strength is below 0.5 T, except for high $|\eta|$ [108].

In the barrel, drift tube (DT) chambers are used for detection and are interspersed among the layers of the magnetic flux return plates. They are organized into four stations, where the inner three stations consist of 60 chambers composed of two superlayers measuring the $r - \phi$ coordinate and one superlayer measuring the z coordinate, the latter not being measured by the fourth station. The forth station consists of 70 chambers.

Due to the higher rates and the non-uniform magnetic field, cathode strip chambers (CSC) are used in the muon endcaps. Four stations of CSCs, consisting of six layers, are positioned between the return plates in each endcap. The cathode strips of the chambers are aligned radially, providing a precise measurement of the $r - \phi$ coordinate. A measurement of η is enabled by the anode wires readout, running perpendicular to the strips. The DTs and CSCs have a spatial resolution of about $\sim$100 μm.

Resistive plate chambers (RPC) are added in the region $|\eta| < 1.6$ to provide fast and precise muon triggering. Six RPC layers are mounted in the muon barrel and three RPC layers in each endcap.

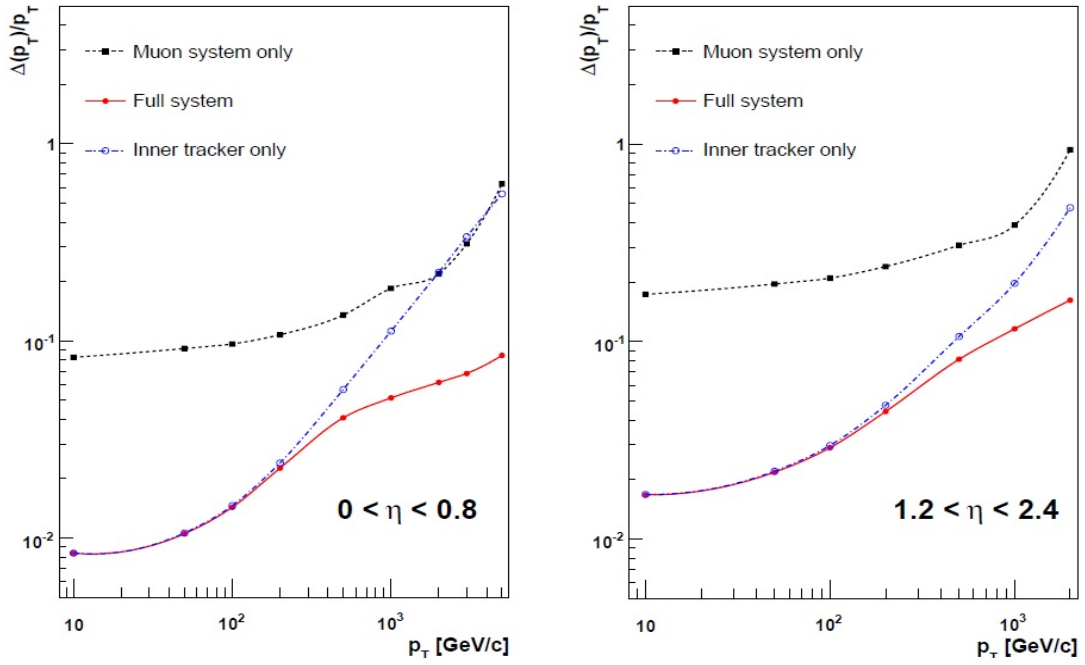

Figure 4.12: Illustration of the muon transverse momentum resolution of the tracker and muon system only and the improvement gained by the combination of both subsystems in dependency of the muon's p_{T} for $|\eta| < 0.8$ (left) and $1.2 < |\eta| < 2.4$ (right) [8].

4.2.7 The trigger system

With instantaneous luminosities of up to $2{\cdot}10^{34}$ cm^{-2}s^{-1} and up to ∼50 simulteaneous pp interactions per bunch crossing, a sophisticated trigger system is needed to guarantee a good performance of the CMS physics program. The trigger system is tuned to make fast physics-driven decisions whether an event is to be selected or rejected. CMS uses a two-fold trigger system to reduce the event rate from 40 MHz to about 1 kHz [109–111]. Before the beginning of the second operation period (Run 2) in 2015, the trigger system was upgraded [112, 113].

In the first step, the hardware based Level-1 (L1) trigger reduces the event rate from 40 MHz to $\mathcal{O}$(100 kHz), using information from the calorimeter trigger towers and the muon system. Since no tracker information is used, photons and electrons cannot be distinguished and are collectively reconstructed as e/γ objects.

The L1 calorimeter trigger is composed of a regional calorimeter trigger providing e/γ candidates and regional transverse energy clusters, and a global calorimeter trigger sorting the e/γ objects together with isolation flags, finding jets and computing global quantities such as $p_{\mathrm{T}}^{\mathrm{miss}}$. Along with the Run 2 upgrade, the clustering has changed from a fixed 4×4 tower granularity to a dynamic clustering to better fit the energy deposit pattern of

a certain object. In the EB, a 5×5 matrix of crystals in $\eta \times \phi$ forms one ECAL tower. In the dynamic clustering, an array of at most 2 towers in η and 5 towers in ϕ is used for the e/γ clustering, with a maximum of 8 towers in total [110]. The isolation of an e/γ object is computed from the 5×9 tower pattern in $\eta \times \phi$ in the ECAL and HCAL, centered around the seed tower. The footprint of the e/γ object (2×5 in the ECAL and 1×2 in the HCAL) is removed from the isolation energy computation. To be flagged as an isolated e/γ object, the isolation energy has to be smaller than a certain threshold that depends on η and the number of simultaneous pp interactions [113].

The L1 muon trigger system uses all three muon detector components, namely the DTs, the CSCs and the RPCs, to provide a maximal η coverage. Information of the muon detector components is processed and sorted in three local track finders divided in η regions, and is subsequently transmitted to the global muon trigger. The global muon trigger merges muons found by more than one component and computes further quality quantities.

In the final step of the L1 trigger more complex variables are computed, a menu of triggers, and a set of selection requirements are implemented. Due to the Run 2 upgrade with optical links running at 10 Gbit/s, the implementation of a total of 512 algorithms at a time is possible, compared to 128 algorithms in the previous setup [112].

Events accepted by the L1 trigger are read out by the Data Acquisition (DAQ) system [114] and made available to the High-Level Trigger (HLT) system, a software-based trigger system with access to the full readout data [111, 115]. The DAQ system assembles information of all subdetector systems, controls the further processing of the data, and is constantly monitored during the data-taking. A back-pressure system is installed which automatically reduces the L1 trigger rates if the system is working at maximum capacity. The HLT hardware is a single processor farm with approximately 26,000 CPU cores [112]. The software has a modular structure with a reconstruction approach similar to the offline implementation. The HLT menu is structured in paths (currently more than 400) with each path being a sequence of reconstruction and filtering modules, arranged according to their complexity to optimize the CPU time. For instantaneous luminosities as present in the data-taking of 2016, average processing times of up to 200 ms are needed for the HLT for one event. The HLT further reduces the event rate to about 1 kHz.

Chapter 5

Event processing and data sets

Contents

The basic concept of searches for BSM physics is to compare the data to the SM expectation in a certain phase space sensitive to new physics. The data are measured and recorded with the CMS detector and its two-level trigger system, as introduced in the previous section. To enable a global and flexible access to data, a central storage and processing network is mandatory. SM and signal processes are generated using the MC simulation method. Data and MC samples are provided centrally and in diverse data formats available to the analyst, where the most suitable data format depends on the need of depth of detail.

In the following chapter, the software and processing infrastructure is introduced. The primary data sets recorded by the HLT and used in the analysis are listed and the measurement of the trigger efficiency is presented. The simulation of background and signal events is described and the MC samples used in the analysis are introduced.

5.1 Data storage and software infrastructure

Events have to pass at least one of the HLT paths to be stored. The storage system of the CMS collaboration is organized in a multi-tier system [116] and made accessible via the Worldwide LHC Computing Grid (WLCG) [117, 118]. The prompt reconstruction and calibration is performed at the Tier-0 at CERN and, since Run 2, at the Tier-1 sites. The Tier-1 sites are used for further reconstruction of data and simulation and the Tier-2 sites predominantly provide data and simulated events to analyses. After passing the HLT, events are stored in a RAW format, the basis for the reconstruction step, with a typical event size of ∼500 kB [116]. For simulation, the first step is the simulation of the kinematic properties of a process and is done by one of the several generators, e.g. MadGraph [119–121] or Pythia [122]. The following key step is the simulation of the detector response, which is the most time-consuming part. After reconstruction, two formats are stored - the Analysis Object Data (AOD) and the Event Summary Data (ESD). The AOD format is used by most analyses, contains all events and in most cases a sufficient depth of detail. The typical AOD event size is ∼300 kB. The ESD data, also referred to as RECO data, contain all information of the RAW sample and the reconstruction. These samples have twice the size of the RAW data and most data sets are only stored temporarily. The primary use of the ESD data is detector commissioning. Starting with Run 2, a further, intermediate file format is centrally provided by CMS - the MiniAOD format - with a further reduction in event size to about 30 kB per event [123, 124]. Based on the MiniAOD format, the data are analyzed individually by small analyst groups or a single analyst to their own preferences. CMS provides a real-time prompt reconstruction of the data, possibly intermediate reconstruction versions, and a final full reconstruction using the most recent alignments, calibrations, and software releases.

This analysis uses the final reconstruction of the 2016 data released on the 3rd of February in 2017 (tag `03Feb2017`). The software used for the reconstruction and further analysis is the CMS software (`CMSSW`) framework [9, 125]. The version used for the reconstruction is `CMSSW_8.0.26_patch1` for data and `CMSSW_8.0.21` or a later version for MC. The version used for the final offline selection is `CMSSW_8.0.26_patch1`. Information about calibrations and alignments is stored in so-called `global tags`. The `global tags` used for data are `80X_dataRun2_2016SeptRepro_v7` and `80X_dataRun2_Prompt_v16`, depending on the time era of the data-taking, while the `global tag` `80X_mcRun2_asymptotic_2016_TrancheIV_v6` is used for MC. The analysis uses a three-level processing framework proceeding from the MiniAOD format. In the first, most CPU-intensive step, the CMS Remote Analysis Builder (`CRAB3`) [126] job submission tool is used to benefit from the resources of the WLCG. The results are locally stored in `ROOT` [127, 128] files and further processed and visualized by self-written `ROOT` and `Python` [129] scripts.

5.2 Data sets and triggers

The analysis uses a variety of data sets and simulated samples based on the MiniAOD format which are stored in several Tier-2 computing centers distributed across the globe. For each sample, several reconstruction versions are available. In the following, the data sets and the triggers used in the analysis are introduced, as well as the efficiency measurement of the trigger chosen to search for new physics, also referred to as signal trigger.

Primary data set

Trigger paths targeting the identification of the same high-level object(s) are grouped together in so-called primary data sets (PDs). Two PDs are used. While the `SinglePhoton` PD is used for the main analysis, i.e., the search for SUSY, the `MET` PD is needed to measure the efficiency of the signal trigger contained in the `SinglePhoton` PD. The PDs are divided into different consecutive run eras "`Run2016X`" and are listed in Table 5.1, together with the paths at which the data samples can be accessed via the CMS data set bookkeeping service (DBS) [130].

Table 5.1: Primary data sets (PDs) used for the main analysis and the trigger efficiency measurement. The DBS paths are similar, only differing in the name of the PD.

PDs	`SinglePhoton`	`MET`
Purpose	Main analysis	Trigger efficiency
DBS paths	/*PD*/Run2016B-03Feb2017_ver2-v2/MINIAOD	
	/*PD*/Run2016C-03Feb2017-v1/MINIAOD	
	/*PD*/Run2016D-03Feb2017-v1/MINIAOD	
	/*PD*/Run2016E-03Feb2017-v1/MINIAOD	
	/*PD*/Run2016F-03Feb2017-v1/MINIAOD	
	/*PD*/Run2016G-03Feb2017-v1/MINIAOD	
	/*PD*/Run2016H-03Feb2017_ver2-v1/MINIAOD	
	/*PD*/Run2016H-03Feb2017_ver3-v1/MINIAOD	

Depending on the status of the detector, events are certified with an appropriate quality flag. The analysis only uses events recorded with the highest possible quality, which are listed in the `JSON` text file
`Cert_271036-284044_13TeV_23Sep2016ReReco_Collisions16_JSON.txt`.
The total integrated luminosity of the combined data sets corresponds to $(35.9 \pm 0.9)\ \mathrm{fb}^{-1}$.

Trigger efficiency measurement

The first selection step of each analysis is determined by the choice of the trigger that has been used to record the data. The signal trigger chosen for this analysis is the `HLT_Photon165_HE10` trigger of the `SinglePhoton` PD. The trigger requires one photon candidate reconstructed by an HLT-optimized algorithm with $p_{\mathrm{T}} > 165\,\mathrm{GeV}$ and $H/E < 0.1$, where H/E is the hadronic-to-electromagnetic energy fraction, as discussed in more detail in Section 6.1.2. No further isolation requirements are imposed on the photon candidate. The signal trigger is seeded in a combination of the following L1 triggers: `L1_SingleEG30`, `L1_SingleEG32`, `L1_SingleEG34`, `L1_SingleEG36`, `L1_SingleEG38`, `L1_SingleEG40`, `L1_SingleJet170`, `L1_SingleJet180`, `L1_SingleJet200`, `L1_SingleTau100er`, `L1_SingleTau120er`. The L1 triggers used as seeds are a combination of triggers requiring one e/γ object with $p_{\mathrm{T}} > 30, 32, 34, 36, 38, 40\,\mathrm{GeV}$, a jet with $p_{\mathrm{T}} > 170, 180, 200\,\mathrm{GeV}$, or a tau lepton with $p_{\mathrm{T}} > 100, 120\,\mathrm{GeV}$. Only the requirements of one of the L1 triggers need to be fulfilled.

To measure the signal trigger efficiency, an independent baseline trigger is used to select the events. The `HLT_PFMET170` trigger of the `MET` PD is chosen for this purpose, as, in contrast to a jet or electron trigger, the $p_{\mathrm{T}}^{\mathrm{miss}}$ trigger efficiency is expected to be independent of the photon identification and energy. The baseline trigger requires $p_{\mathrm{T}}^{\mathrm{miss}} > 170\,\mathrm{GeV}$, where $p_{\mathrm{T}}^{\mathrm{miss}}$ is evaluated by an HLT-optimized algorithm. To determine the trigger efficiency for a phase space as close as possible to the one relevant for the analysis, besides typical event quality requirements, $p_{\mathrm{T}}^{\mathrm{miss}} > 100\,\mathrm{GeV}$ and $\mathrm{M_T}(\vec{p}_{\mathrm{T}}(\gamma), \vec{p}_{\mathrm{T}}^{\,\mathrm{miss}}) > 100\,\mathrm{GeV}$ is required, as these criteria are applied for all control, validation, and signal regions. The variable $\mathrm{M_T}(\vec{p}_{\mathrm{T}}(\gamma), \vec{p}_{\mathrm{T}}^{\,\mathrm{miss}})$ is the transverse mass of the highest-energy photon and $p_{\mathrm{T}}^{\mathrm{miss}}$ and is discussed in more detail in Section 7.2. Using a baseline trigger already selecting high-$p_{\mathrm{T}}^{\mathrm{miss}}$ events provides a higher statistical precision as, e.g., a muon trigger.

The trigger efficiency is measured by dividing the number of events satisfying the event selection and that pass the signal and the baseline trigger by the number of events that at least pass the latter trigger. The efficiency represents the probability that an event fulfilling the offline selection for a certain phase space is also accepted by the trigger under study. The result of the measurement is shown in Fig. 5.1 in dependency of $p_{\mathrm{T}}(\gamma)$ to identify the p_{T} threshold for which the efficiency reaches a constant value. Due to differences in the online and offline determination of $p_{\mathrm{T}}(\gamma)$, the efficiency shows a finite slope around the online threshold, also referred to as efficiency turn-on. The trigger efficiency is found to be constant for $p_{\mathrm{T}}(\gamma) > 180\,\mathrm{GeV}$ and is measured to be

$$\varepsilon_{\text{signal trigger}} = (94.3 \pm 0.4)\%, \tag{5.1}$$

where the uncertainty is of statistical origin only and calculated from a 68% confidence level Clopper-Pearson interval.
All SM background and signal MC samples are scaled to this efficiency.

The trigger efficiency is also measured in dependency of other variables used in the event selection to ensure that no systematic effects are introduced by imposing further

selection requirements. In all cases, the efficiency is found to be constant, as shown in Appendix A.

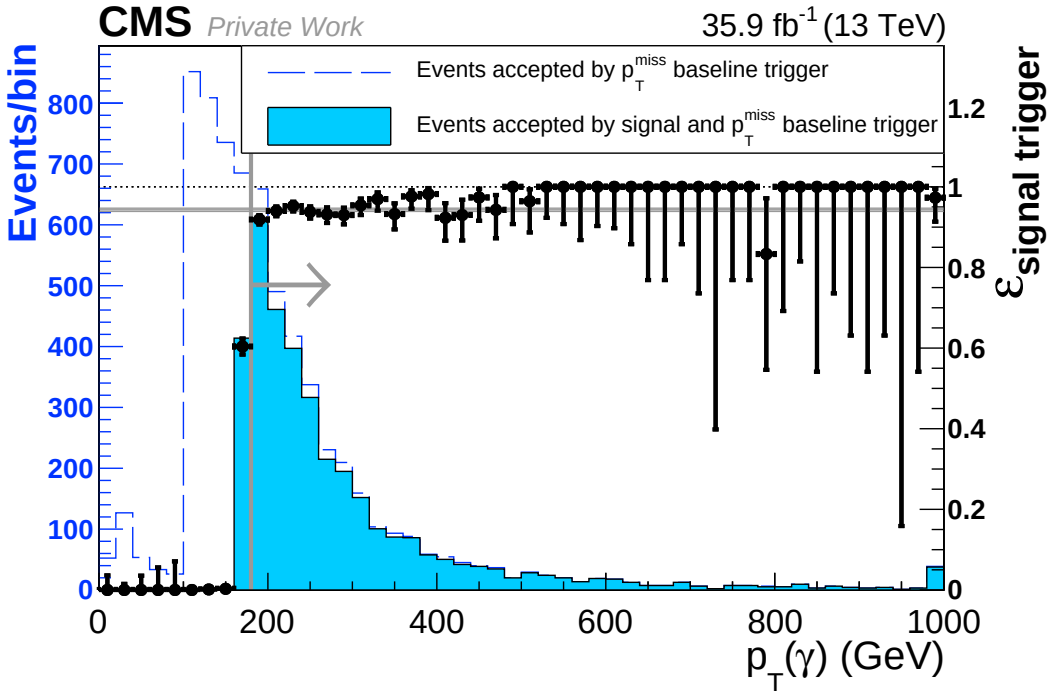

Figure 5.1: Measurement of the efficiency of the `HLT_Photon165_HE10` signal trigger as a function of $p_{\mathrm{T}}(\gamma)$. The measurement is performed using the `HLT_PFMET170` baseline trigger in the phase space defined by requiring $p_{\mathrm{T}}^{\mathrm{miss}}$ and $\mathrm{M_T}(\vec{p}_{\mathrm{T}}(\gamma), \vec{p}_{\mathrm{T}}^{\,\mathrm{miss}}) > 100\,\mathrm{GeV}$. The efficiency is constant for $p_{\mathrm{T}}(\gamma) > 180\,\mathrm{GeV}$ and is measured to be $(94.3 \pm 0.4)\%$, as indicated by the horizontal gray line.

5.3 Background and signal Monte-Carlo simulation

The MC simulation of SM and BSM processes can be divided into several generation steps, starting from the short distance scale up to the scale where partons form color-charge singlets (hadrons) that may undergo further decays. In contrast to the very short distance scales, where QCD interactions are rather weak and generators can compute the physics exploiting perturbation theory, QCD-inspired phenomenological models need to be used at larger distances. Due to this circumstance, it can be useful to use different generators for different generation steps, which are connected by introducing a well-defined transition criterion (Q_{cut}).

Short distance event simulation

At short distances, soft- and collinear-safe observables, e.g. the inclusive cross section, can be reliably computed to a certain order using QCD perturbation theory. The Kinoshita-Lee-Nauenberg (KLN) theorem [131–133] ensures that logarithmic divergences arising from soft (low-energy) emission and final state collinear (small-angle) parton splittings cancel against virtual corrections to the inclusive cross section at any order in perturbation theory. In addition, initial-state collinear singularities can be factorized into the PDFs, following the factorization theorem. Therefore, the leading order (LO) cross section calculation of a process has to be considered as an estimate for the LO cross section of the process under consideration accompanied by an arbitrary number of collinear and soft gluons, and not a specific "$AB \to XY$" production. However, other, less inclusive observables can receive large corrections due to infrared and collinear singularities in QCD. These corrections are of the order of $\alpha_s(Q)\ln(Q/\Lambda_{\text{had}})$, where Q is the momentum scale of the primary process and Λ_{had} is the hadronic scale, typically $\mathcal{O}(100\,\text{MeV})$. Since $\alpha_s(Q) \propto 1/\ln(Q/\Lambda_{\text{had}})$, this results in corrections of the order of unity. In general-purpose MC generators like Pythia, which can be used to generate the whole physics from very short distance scales to the hadronization, shower algorithms are used to compute the cross section including all leading-logarithmic corrections. Starting from the dynamics of the basic process, the generation is followed by a variety of shower splittings with a corresponding probability. The total cross section is then given by the sum of all partial cross sections. Initial-state radiation (ISR) arising from (color-)charged initial-state particles is evolved backwards in time following an algorithm formulated by Sjöstrand [134]. Electrically charged leptons and quarks can emit bremsstrahlung photons leading to further corrections of the order of $\alpha_{\text{em}}(\text{Q})\ln(Q/m)$, with m being the mass of the radiating particle. In the shower algorithm, the photon radiation is cut off below a certain energy, typically of the order of the mass of the radiating particle. During the development of the shower, color information is tracked, meaning that (anti-)quarks are represented by a line and a direction of the color flow, while gluons are represented by a pair of colors with opposite directions. Color information is used for several models, e.g., hadronization models.

One disadvantage of shower algorithms is that they are tuned for collinear and soft dynamics, lacking in accuracy in high-energy, wide-angle emissions. Therefore, general-purpose generators like Pythia include Matrix Element Corrections (MEC) [135, 136], which correct the highest-energy jet at wide emission angles. This procedure can be expanded up to arbitrary jet multiplicities and over the whole phase space, as proposed in [137]. Beside the direct incorporation of MEC into the general-purpose MC generators, the method of Matrix Elements and Parton Shower (ME+PS) or the next-to-leading order (NLO) calculation and Parton Shower (NLO+PS) matching can be used. In the ME+PS method [138] tree-level LO matrix elements are generated for the basic process, e.g., by MadGraph5_aMC@NLO in LO mode, accompanied by a certain number of partons. A criterion, e.g., that the relative p_{T} in any pair of partons is larger than Q_{cut}, is imposed to determine the transition to the application of the parton shower algorithm, which then covers the generation of the kinematic properties below Q_{cut}. Using the ME+PS

method with one additional parton results in the same accuracy as using the MEC, with the difference that for MEC no transition criterion needs to be defined. In the NLO+PS method [139], one additional parton radiation at tree-level accuracy and NLO virtual corrections are included, e.g., as used by MadGraph5_aMC@NLO in NLO mode. Double counting of the partons generated with MadGraph5_aMC@NLO and those with Pythia in the parton showering is removed using the MLM [121] and FXFX [140] matching schemes, in the LO and NLO samples, respectively.

Depending on the complexity of the basic process and the number of additional high-p_{T} wide-angle jets, different methods result in the most accurate description for different processes. Since BSM searches often investigate phase spaces with a high multiplicity of well-isolated high-p_{T} jets, ME+PS or NLO+PS methods often result in superior accuracy compared to only using general-purpose MC generators.

The ME partonic event configuration for SM and SUSY processes is interfaced to the general-purpose MC generators for showering using the Les Houches Event (LHE) [141] and the Supersymmetry Les Houches Accord (SLHA) [142] file format, respectively.

Hadronization and parton distribution functions

Color-charged particles produced in the parton shower of a process have to hadronize to color-singlet hadrons. The non-perturbative character of the linear confinement disables the computation of the process using perturbation theory. Therefore, phenomenological models are employed, which are applied to the simulated event after a certain infrared cutoff criterion is met in the parton showering. The modeling of the hadronization is realized using the Pythia 8 program, which is based on the Lund model [143] following the string fragmentation model [122]. Such a model is based on the linear confinement connecting a quark and antiquark with opposite color-charge by a string with tension $\kappa \approx 1\,\mathrm{GeV/fm} \approx 0.2\,\mathrm{GeV}^2$ and the potential $V(r) = \kappa \cdot r$, neglecting the Coulomb potential-like term. As the distance increases, also the energy in the string increases. When a certain energy is reached, the string breaks and a quark-antiquark pair is created. The probability of a breakup depends on the mass of the produced quarks (m_q) and their transverse (defined with respect to the string axis) momentum $p_{\perp q}$ and is based on quantum mechanical tunneling:

$$P(\text{breakup}) \propto \exp\left(\frac{-\pi m_q^2}{\kappa}\right) \exp\left(\frac{-\pi p_{\perp q}^2}{\kappa}\right). \tag{5.2}$$

Baryon production is realized by allowing a string break to create two *diquarks*. Quarks of masses larger than the strange quark are not produced in the fragmentation.
Instead of using the string fragmentation model, as incorporated, e.g., in the Pythia framework, some generators use the so-called cluster model [144] to implement the hadronization. Such generators are not used in the analysis.

These algorithms, the underlying event, and the pileup events are tuned to data from pp collisions at 7 TeV recorded by CMS and proton-antiproton ($p\bar{p}$) collisions recorded by the CDF experiment, incorporated in the CUETP8M1 generator tune [145].

All MC samples incorporate the NNPDF 3.0 [146] parton distribution functions. These PDF sets are based on LO, NLO, and next-to-NLO (NNLO) QCD theory, also incorporating electroweak corrections. A large variety of data sets are used, among others data recorded at the HERA (ep), the Tevatron ($p\bar{p}$) and the LHC (pp) accelerator. The data sets used in NNPDF 3.0 have a kinematical coverage from $\mathcal{O}(1\,\text{GeV}^2)$ to $\mathcal{O}(10^6\,\text{GeV}^2)$ in Q^2 and from $\mathcal{O}(10^{-5})$ to $\mathcal{O}(1)$ in x.

Detector simulation

Two procedures are used to simulate the detector response to the events generated by the MC generators as described above. The GEANT4 ("GEometry ANd Tracking") [147] package is used to model the detector and the detector response for SM processes, while the CMS fast simulation [148, 149] is used for signal samples to reduce simulation time.

The GEANT4 toolkit provides a comprehensive platform for a detailed simulation of the CMS detector and its response to particles traversing some or all subdetector systems. The program takes into account the different geometries and materials of the detector components, the decay properties of the primary and secondary particles, the movement of these particles through the detector under the influence of the magnetic field, as well as their interactions with the detector material and the response of sensitive detector components to these interactions. The toolkit provides an extensive list of physics processes relevant for particles with energies from 250 eV up to the TeV scale to model the realistic behaviour of the particles being moved step-by-step through the detector. The complex simulation based on GEANT4 is also referred to as "full simulation".

In certain cases, some loss of accuracy in the detector simulation is acceptable in order to reduce the simulation time. Examples are processes with very large cross sections or BSM scenarios that are scanned over a large parameter space. A fast MC simulation of the CMS detector has been developed, reducing the time for simulation of the same number of events by a factor of about $500 - 1000$. This makes the complete event production, where most of the production time is consumed by the reconstruction step, about 100 times faster compared to the full, GEANT4-based, simulation. The input and output format is the same as for the full simulation. Particles and possible decay products are propagated through the detector considering the magnetic field and known decay properties. Interactions taken into account in the fast simulation comprise electron bremsstrahlung, photon conversion, charged particle multiple scattering, and energy loss by ionization, as well as nuclear interactions for particles crossing the tracker, and electron, photon, and hadron showering for the transition of the calorimeters. Several simplifications are incorporated in the fast simulation, e.g., the simulation of the detector components is simplified by reducing the complexity of the geometry and approximating

the detector material by sensitive and non-sensitive material. The energy response for hadrons is derived from full simulation and tabulated in dependency of energy and η, and their mean and RMS values are used as input for the simplified fast simulation. Overall, very good agreement is observed between both the fast and full simulation and data [149], albeit the agreement should be checked if more sophisticated, detector-detail sensitive quantities or algorithms are used in the analysis, as for instance explicitly done for the $p_{\mathrm{T}}^{\mathrm{miss}}$ significance used in SUS-14-016 [1].

For events generated with fast simulation, a veto is applied if a jet with $|\eta| < 2.5$, $p_{\mathrm{T}} > 20\,\mathrm{GeV}$, and a charged hadron fraction of less than 10% cannot be matched to any generated jet within a cone with a radius of $\Delta R = \sqrt{(\Delta\phi)^2 + (\Delta\eta)^2} = 0.3$. This procedure is recommended by the CMS SUSY group. The effect of this veto is studied and found to reduce the signal acceptance by 0.3% for the analysis.

Simulated data sets

The QCD multijet and photon-plus-jets (γ + jets), as well as the Z and $\mathrm{W}^{\pm}$ samples are generated with the MadGraph5_aMC@NLO [119–121] event generator at LO in bins of H_{T} computed at generator level. The $\mathrm{Z}\gamma$ and $\mathrm{W}^{\pm}\gamma$ samples are generated with MadGraph5_aMC@NLO at LO in one inclusive bin for $p_{\mathrm{T}}(\gamma) > 130\,\mathrm{GeV}$. The top pair production processes with and without photon radiation, $\mathrm{t\bar{t}}(\gamma)$, are generated with MadGraph5_aMC@NLO in NLO [119, 140]. The $\mathrm{W}^{\pm}\mathrm{W}^{\mp}$ diboson production is generated with Powheg v2 [150–154], while $\mathrm{W}^{\pm}\mathrm{Z}$ and ZZ diboson productions are generated using Pythia 8 [122]. The $\mathrm{W}^{\pm}\mathrm{W}^{\mp}$, $\mathrm{W}^{\pm}\mathrm{Z}$, and ZZ processes are collectively denoted as "diboson" processes in the following.

The $\mathrm{Z}\gamma$ samples are scaled with $p_{\mathrm{T}}(\gamma)$ dependent next-to-next-to-leading logarithm (NNLL) K-factors [155], which are listed in Table 5.2 and are of the order of 1.3 for $p_{\mathrm{T}}(\gamma) > 175\,\mathrm{GeV}$. A constant NNLO K-factor of 1.34, calculated for $p_{\mathrm{T}}(\gamma) > 175\,\mathrm{GeV}$, is applied to the $\mathrm{W}^{\pm}\gamma$ production cross section [155], and NLO K-factors of the order of 1.2 are applied to the $\mathrm{W}^{\pm}$ and $\mathrm{Z}(\to \nu\nu)$ production cross sections (see Table 5.2). The diboson production cross sections are available at NLO ($\mathrm{W}^{\pm}\mathrm{Z}, \mathrm{ZZ}$) and NNLO ($\mathrm{W}^{\pm}\mathrm{W}^{\mp}$) precision [156]. The $\mathrm{W}^{\pm}\gamma$ and $\mathrm{Z}\gamma$ processes, collectively denoted as $\mathrm{V}\gamma$, are the dominant backgrounds in the signal region. A data sideband region is used to obtain additional scale factors for the $\mathrm{V}(\gamma)$ and γ + jets samples, where $\mathrm{V}(\gamma)$ comprises the $\mathrm{W}^{\pm}$ and Z boson production, with and without photon radiation, as comprehensively presented in Section 8.4.

All SM background MC samples as introduced above are listed in Table B.1 in the appendix, along with the DBS path and the corresponding cross section.

The GGM signal scan is generated with Pythia 8, while the SMS signal scans are generated with MadGraph5_aMC@NLO at LO. The signal samples are scaled by cross sections calculated at NLO and NLO+NLL accuracy [157–165] for the GGM and the SMS scans,

Table 5.2: Higher-order K-factors for the $Z\gamma$, $W^{\pm}\gamma$, $W^{\pm}$, and Z processes. The $Z\gamma$ NNLL K-factors are calculated in five bins of $p_T(\gamma)$.

Process	$p_T(\gamma)$ in GeV	Order	K-factor
$Z\gamma$	$175 - 190$	NNLL	1.39
	$190 - 250$	NNLL	1.35
	$250 - 400$	NNLL	1.30
	$400 - 700$	NNLL	1.23
	> 700	NNLL	1.23
$W^{\pm}\gamma$	> 175	NNLO	1.34
$W^{\pm}$	inclusive	NLO	1.21
Z	inclusive	NLO	1.23

respectively, with all unconsidered sparticles assumed to be decoupled. For the EWK models, the cross sections are computed in a limit of mass-degenerate wino $\widetilde{\chi}_2^0$ and $\widetilde{\chi}_1^{\pm}$. The signal cross sections are further discussed in Section 9.2.1.

All SMS scans are provided centrally and their DBS paths are listed in Table B.2 in the appendix. The GGM signal scan was generated privately for the 13 TeV results of the 2015 data set and the 8 TeV results. For the interpretation of the results of the 2016 data set a central production of the GGM scan is provided, also listed in Table B.2.

MC samples are generated with a finite number of events $N_{\text{events}}^{\text{gen}}$, where the amount of $N_{\text{events}}^{\text{gen}}$ is guided by the magnitude of the cross section of the (sub)process and the phase space the sample has to cover. Given the cross section σ of the respective process, the MC samples are weighted by the factor

$$w = \frac{\mathcal{L}_{\text{int}} \cdot \sigma}{N_{\text{events}}^{\text{gen}}} \tag{5.3}$$

to fit the total integrated luminosity corresponding to the data.

Additional pp interactions during one bunch-crossing are considered in the simulation. To match the distribution of the number of simultaneous pp interactions observed in data, all simulated samples are weighted on an event-by-event basis. To account for overlaps in the detector readout due to the high collision frequency of 40 MHz, previous and subsequent collisions are also included in the simulation.

Chapter 6

Object reconstruction and object definition

Contents

In this chapter, the reconstruction of the objects relevant for the analysis is introduced. Most of the particles produced in the hard scattering of the protons traverse at least a part of the CMS detector and generate electrical signals in one or more subdetector systems [166]. These signals are used to reconstruct the initial particles at a certain confidence level. This signal-to-object translation has been studied and optimized by the CMS collaboration and is used in this analysis [167]. The reconstruction of the global event, including the missing transverse momentum, and the calculation of the isolation energies are based on the PF algorithm [168], which combines information of all detector components.

6.1 Object reconstruction

The PF algorithm combines the signals of all CMS subdetectors and categorizes these into photons, electrons, muons, as well as neutral and charged hadrons.

Tracks

The reconstruction of tracks caused by charged particles is based on a combinatorial track finder sequence based on Kalman filtering [169]. For electrons, a different approach is used as described below. The combinatorial track finder consists of three stages: the initial seed generation, the trajectory building, and the final fit determining the kinematic track properties. In the PF reconstruction, this sequence is iteratively applied in ten successive steps, each targeting a different category of tracks with different quality criteria to increase the overall tracking efficiency.

Calorimeter clustering

A clustering algorithm uses the signals generated in the ECAL, the HCAL, and the preshower detectors and its main purpose is the measurement of the energy and position of neutral particles, as well as the improvement in the energy measurement of and the separation from charged particles. The clustering is performed separately in the ECAL and HCAL barrel and endcaps, and the two preshower layers. In a first step, cluster seeds are determined by scanning the calorimeter cells for energy maxima with respect to the closest four or eight cells that exceed a certain energy threshold. Then, topological clusters are built by attaching neighbouring cells that fulfill a certain energy criterion. For the ECAL barrel, e.g., the energy maximum of the seed applies with respect to the closest eight cells and has to exceed an energy of 230 MeV. Cells considered in the subsequent topological cluster building have to exceed an energy of 80 MeV. In a next step, energy clusters are formed within the topological clusters by applying an expectation-maximization algorithm based on a Gaussian-mixture model. This Gaussian-mixture model postulates that the energy deposits in the cells of the topological cluster actually arise from a fixed number of Gaussian energy deposits. In the ECAL, superclusters are formed by combining nearby clusters in a narrow η-window and a wider ϕ-window to collect energy from bremsstrahlung and photon conversions. The ECAL and HCAL energy measurements need to be calibrated based on the energy deposits in the respective calorimeter and the position in η. For the energy measurement of hadrons, also the energy deposit in the ECAL, as well as the non-linearity of the calorimeter response has to be taken into account.

Electrons

For the electron seeding, an ECAL-based approach is applied, where ECAL superclusters determine the energy and position of the electron candidate. This information is then used to infer the position of the hits in the tracker system. If this approach fails, a tracker-based approach is applied. A preselection based on the number of hits in the tracker and the χ^2-value of the track fit is applied to the track candidate. These candidates then are fit again with a Gaussian-sum filter (GSF) [170] with five components, which is more suited for electrons as it allows for significant and punctual energy losses along the

track, i.e., emission of bremsstrahlung photons. In a final step, the tracks are required to fulfill a certain threshold of a boosted-decision-tree classifier. Then, the electron seeds obtained by both approaches are combined and the final electron tracking with twelve GSF components is applied.

Muons

For the muon tracking, information provided by the muon spectrometer and the tracker system is used. Three different types of muon tracks are reconstructed. Standalone muon tracks are reconstructed using only hits in the muon chambers. Each track in the inner tracker with $p_{\mathrm{T}} > 0.5\,\mathrm{GeV}$ and $p > 2.5\,\mathrm{GeV}$ that can be extrapolated to fit at least one muon segment in the muon chambers is called a tracker muon track. Finally, if a standalone muon track is matched to a track in the inner tracker under certain quality criteria, the muon candidate is called a global muon. Since in addition to muons only the remnants of high-energy hadronic showers, also referred to as "punch through", can generate signals in the muon chambers, the purity of the muon reconstruction is very high.

Particle-flow blocks

The reconstructed tracks and energy clusters form PF elements. In a next step, a linking algorithm is applied. The PF elements are sorted in the $\eta - \phi$ plane and only neighbouring elements are considered by the link algorithm to prevent the computing time from growing quadratically with the number of PF elements. If a pair of elements fulfills the linking criteria, the distance of these two elements is determined. The distance is defined as the difference in η and ϕ between the cluster position and the position of the extrapolated track. If several elements of the same type are linked to the same element of another type, e.g., if several tracks are linked to the same ECAL cluster, or multiple ECAL clusters are linked to the same preshower cluster, only the pair with the smallest distance is kept. Elements with a direct link or an indirect link through a shared element, e.g., an HCAL cluster and a track that are linked to the same ECAL cluster, form one PF block.

Particle-flow candidates

Due to the high muon purity in the muon chambers, the muon identification is the first step in the sequence of object identifications. Muons are selected and categorized by different selection criteria. If a muon is reconstructed in a block, the respective PF elements are removed from the collection.

In consequence of the tracker thickness, electrons emit bremsstrahlung photons with a high probability and photons often convert to electron-positron pairs, which again can emit bremsstrahlung photons. Therefore, electrons and isolated photons are identified in the

same sequence step, after the muon elements are removed from the PF blocks. Electrons are seeded from a GSF track linked to an ECAL cluster which is not also linked to at least three additional tracks. Photons are seeded from a high-energy supercluster that is not linked to a GSF track. Electron and photon candidates have to fulfill quality and isolation requirements, where the electron identification is based on a boosted-decision-tree classifier. Also, the energy deposit in HCAL cells close to the ECAL supercluster has to be small compared to the supercluster energy. The position of the photon is given by the position of the supercluster, whereas the position of the electron is given by that of the GSF track. Elements fulfilling the electron or photon reconstruction are again removed from the PF block.

In the subsequent steps hadrons, non-isolated photons, and secondary particles are reconstructed. A post-processing algorithm is applied to check and correct each event for large artificial $p_{\mathrm{T}}^{\mathrm{miss}}$.

Based on studies of simulated H$\rightarrow \gamma\gamma$ events, $20 - 60\%$ of the photons convert to an electron-positron pair before the last three layers of the tracker, depending on the tracker material budget, and therefore the pseudorapidity [171]. Photon conversions are recovered by the PF algorithm and are included in the set of photon candidates.

The set of particles identified by the PF algorithm provides the basis for the global event description and the subsequent particle identification, the latter increasing the purity of certain objects by applying stricter quality requirements. This step is discussed in the following for objects relevant for the analysis.

6.1.1 Missing transverse momentum

The PF missing transverse momentum ($\vec{p}_{\mathrm{T}}^{\,\mathrm{miss}}$) represents the imbalance of the momenta of all reconstructed PF objects ($N_{\mathrm{PF\ obj.}}$) projected onto the transverse plane of the detector. It's uncorrected value is given by

$$\vec{p}_{\mathrm{T}}^{\,\mathrm{miss,\ uncorr}} = -\sum_{i}^{N_{\mathrm{PF\ obj.}}} \vec{p}_{\mathrm{T},i}. \tag{6.1}$$

The non-linearity of the response of the calorimeter for hadronic particles, as well as lower energy thresholds and inefficiencies in the tracker can lead to a bias using $\vec{p}_{\mathrm{T}}^{\,\mathrm{miss,\ uncorr}}$, especially for events with a large hadronic activity. To reduce this bias, jet energy corrections [172] are propagated to $\vec{p}_{\mathrm{T}}^{\,\mathrm{miss}}$ by

$$\vec{p}_{\mathrm{T}}^{\,\mathrm{miss}} = \vec{p}_{\mathrm{T}}^{\,\mathrm{miss,\ uncorr}} - \sum_{i}^{N_{\mathrm{jets}}} (\vec{p}_{\mathrm{T,\ jet}_i}^{\,\mathrm{corr}} - \vec{p}_{\mathrm{T,\ jet}_i}), \tag{6.2}$$

where all corrected jets with $p_{\mathrm{T}} > 15\,\mathrm{GeV}$ and an ECAL energy deposit fraction of less than 90% are used, collectively denoted as N_{jets}. The magnitude of the vector $\vec{p}_{\mathrm{T}}^{\,\mathrm{miss}}$ is referred to as $p_{\mathrm{T}}^{\mathrm{miss}}$.

Limited momentum and direction resolutions are sources for increased values of $p_{\mathrm{T}}^{\mathrm{miss}}$, as well as the presence of particles not interacting with the detector, e.g. neutrinos or neutral LSPs. The $p_{\mathrm{T}}^{\mathrm{miss}}$ is a powerful variable for many SUSY searches, especially in separating SM and SUSY processes. In this analysis, $p_{\mathrm{T}}^{\mathrm{miss}}$ is used to define the control and signal regions.

6.1.2 Photons

Photons are required to have a minimal transverse momentum of 15 GeV. This requirement ensures a high identification efficiency and reduces the contribution of low-energy photons produced within a jet or π^0 decays. Only photons reconstructed in the ECAL barrel are used. More complex identification requirements are listed in the following and their thresholds are recommended by the CMS collaboration [173] if not stated otherwise. The requirements are optimized for photons reconstructed in the ECAL barrel and have a photon identification efficiency of 91%, while 83% of non-photon background is rejected.

- **Hadronic-to-electromagnetic energy fraction $H/E < 0.0597$**
  The ratio of the energy deposit H induced in the HCAL tower closest to the photon's ECAL supercluster seed has to be less than 5.97% of the energy E measured in the ECAL. Only the single HCAL tower closest to the supercluster seed is used to be less sensitive to pileup. The H/E requirement significantly suppresses jets that are misidentified as photons.

- **ECAL shower shape $\sigma_{i\eta i\eta} < 0.01031$**
  The variable $\sigma_{i\eta i\eta}$ is a measure for the shape of the electromagnetic shower in the ECAL with respect to the extent in η and is defined as

$$\sigma_{i\eta i\eta}^2 = \frac{\sum_i^{5\times5} w_i(\eta_i - \eta_{\mathrm{seed}})^2}{\sum_i^{5\times5} w_i}. \tag{6.3}$$

  The weight $w_i = \max(0, 4.7 + \ln(E_i/E_{5\times5}))$ is used to weight the η differences of the i-th crystal in the 5×5 crystal array spanned in the $\eta - \phi$ plane around the supercluster seed to the η value of the seed (η_{seed}), according to the energy deposit in the i-th crystal. The value $E_{5\times5}$ is the energy sum of all crystals in the 5×5 crystal array around the seed. The maximum condition ensures that all ECAL crystals considered in the summation over i carry roughly at least 1% of $E_{5\times5}$. Since the energy shower is spread in ϕ direction due to the magnetic field being parallel to the beam axis, only the width in η is used to classify the shower shape. Jets misidentified as photons and high-energy photons originating from neutral pion decays are suppressed by this requirement, since a shower shape composed of more than one particle is expected to be broadened also in η, leading to higher values of $\sigma_{i\eta i\eta}$.

- **Photon isolation energies**
  Photon isolation energies are calculated from the information provided by the

PF algorithm. Three categories of isolation energies are defined: charged hadron isolation ($\text{Iso}_{h^\pm}$), neutral hadron isolation (Iso_{h^0}), and photon isolation (Iso_γ). The isolation energies are calculated by summing the transverse momenta of the PF objects of the respective category within a cone with an outer radius of 0.3 in ΔR around the photon candidate. The PF algorithm ensures that no double counting of energy entries arises in the isolation energy calculation. Nevertheless, besides the exclusion of the energy entries assigned to the photon candidate, certain geometrical requirements are imposed to remove a possible contribution of the photon to the isolation energy. These requirements differ depending on the isolation category. The isolation energy is corrected for the contribution of pileup. While charged hadrons can be assigned to their vertex with good reliability, only an averaged pileup contribution can be calculated for the neutral hadron and photon isolation energies. The pileup correction is calculated multiplying an event-dependent average pileup energy density per unit area in the $\eta - \phi$ plane with an η-dependent effective area, which is computed separately for each isolation type [174]. In total, seven effective area sections are defined in dependency of $|\eta|$, whereof two fall in the range $|\eta| < 1.44$. The values of the effective area for these two sections are given in Table 6.1. If the pileup correction is greater than the isolation energy, the latter is set to zero. As shown in Fig. 6.1, the dependency of the uncorrected neutral hadron and photon isolation energy to the number of reconstructed primary vertices is removed by applying the pileup correction. To be considered as an isolated photon in the analysis, the candidate has to meet the criteria:

- $\text{Iso}_{h^\pm} < 1.295\,\text{GeV}$,
- $\text{Iso}_{h^0} < (10.910\,\text{GeV} + 0.0148 \cdot p_\text{T} + 0.000017\,\text{GeV}^{-1} \cdot p_\text{T}^2)$,
- $\text{Iso}_\gamma < (3.630\,\text{GeV} + 0.0047 \cdot p_\text{T})$.

The isolation requirements suppress photons originating from jets, typically consisting of multiple particles within the isolation cone. Photon reconstructions from π^0 decays are suppressed especially by the photon isolation requirement.

Table 6.1: Effective areas of charged hadrons ($h^\pm$), neutral hadrons (h^0), and photons depending on η [173].

η section	$h^\pm$ effective area	h^0 effective area	γ effective area
$\lvert\eta\rvert < 1.0$	0.0360	0.0597	0.1210
$\lvert\eta\rvert < 1.44$	0.0377	0.0807	0.1107

- **Number of pixel seeds $N_{\text{pixel seed}} < 1$**
  In the PF track reconstruction, several seeding configurations are used. If the track is reconstructed with two or three hits in consecutive layers in the pixel detector, the track fulfills the criteria of a pixel seed. For the photon identification it is required that there is no reconstructed track that is seeded in the pixel detector

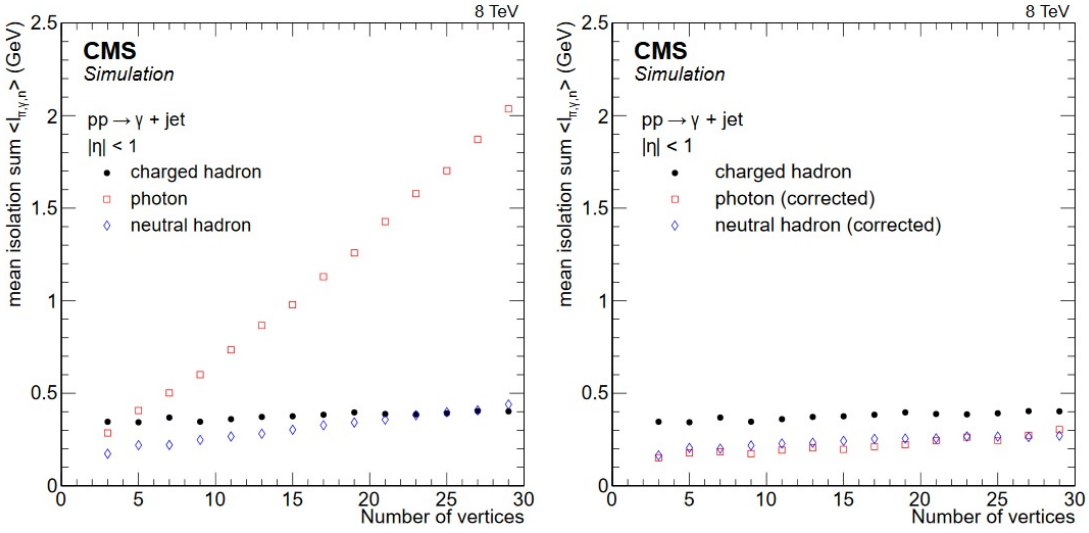

Figure 6.1: Charged hadron, neutral hadron, and photon isolation energies depending on the number of reconstructed vertices in γ+jet events with photons with $p_{\mathrm{T}} > 50\,\mathrm{GeV}$ and $|\eta| < 1.0$ before (left) and after (right) applying the pileup corrections [171].

whose extrapolation matches the position of the primary vertex and the position of the ECAL shower. This pixel seed veto, or another comparable criterion evaluating the geometrical consistency of tracks and ECAL showers, is essential to distinguish between electrons and photons.

- **Seed crystal energy E_{seed} divided by $p_{\mathrm{T}} > 0.3$**
  Through detailed studies of the photon properties in the course of the analysis it was found that some photons receive anomalously high a posteriori energy corrections in data. As a consequence, these photons predominantly populate the (highest) signal region bins and are not covered by the background prediction. Further studies have shown that the energy superclusters of the affected photons seem to consist of two high-energy subclusters without associated tracks, indicating that this subcluster structure does not arise from photon conversion. However, these photons seem to point to gaps in the ECAL, intrinsically causing the application of large corrections to their energy. Figure 6.2 shows the ratio of the photon p_{T} after the correction to the uncorrected momentum $p_{\mathrm{T,\,uncorrected}}$ against the ratio $E_{\mathrm{seed}}/p_{\mathrm{T}}$ (left) and R_9 (right) for events populating the highest signal region bin in data. The variable R_9 is defined as the ratio of the energy deposited in the 3×3 cluster around the seed crystal to the energy deposited in the full supercluster. Unlike typical correction factors of the order of unity, some photons have a corrected p_{T} three times as large as the initial p_{T}. This translates to absolute corrections of $\mathcal{O}(1\,\mathrm{TeV})$. Figure 6.2 illustrates that the quantity $E_{\mathrm{seed}}/p_{\mathrm{T}}$ provides a good discrimination for these pathological photons. To prevent the analysis from misinterpreting the final data-to-background comparison, a conservative criterion is applied, requiring

that the seed crystal of the photon carries at least 30% of the photon's p_T. This criterion was discussed with and confirmed by the photon reconstruction group within CMS. Figure 6.3 shows the distribution of E_{seed}/p_T in two different phase spaces used in the analysis. The bottom row shows the distribution in the signal region, so that the data are not shown for $E_{seed}/p_T > 0.3$. The right figures are each an enlarged illustration of the critical region $E_{seed}/p_T < 0.35$ with linear y-axis scale. The figures show that a background prediction for these pathological data events is missing, illustrating the importance of this photon quality criterion. The signal sensitivity is not affected by requiring $E_{seed}/p_T > 0.3$.

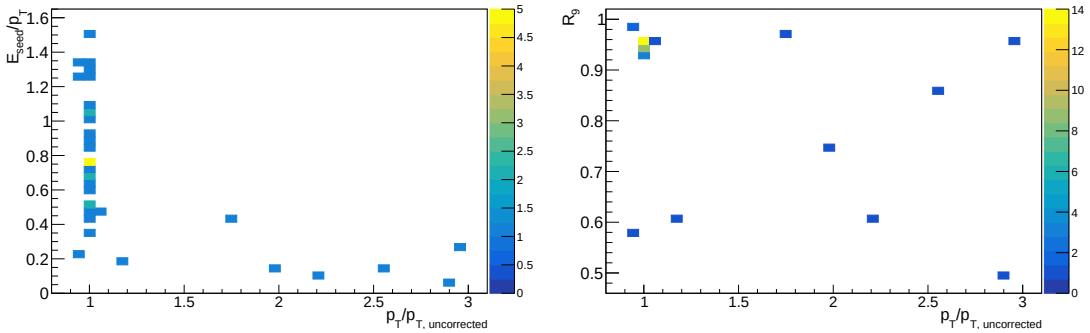

Figure 6.2: The value E_{seed}/p_T (left) and R_9 (right) against the ratio of the photon's p_T after the momentum correction to the uncorrected p_T ($p_{T,\,uncorrected}$) for data events populating a phase space with high values of $p_T(\gamma)$, p_T^{miss}, and $M_T(\vec{p}_T(\gamma), \vec{p}_T^{\,miss})$, see text for the definition of R_9. Some photons receive p_T corrections leading to a corrected p_T value three times as large as the initial p_T. These anomalously high corrections are in violent contrast to typical correction factors of the order of unity. The quantity E_{seed}/p_T provides a good separation for these critical events.

Studies have shown that ECAL spikes generated by spontaneous discharges of the avalanche photodiodes can be reconstructed as a photon candidate. Such unphysical energy entries in the ECAL can lead to the reconstruction of nongenuine p_T^{miss} pointing to the opposite direction with respect to the ECAL spike. This increases the probability that the event is selected applying the signal selection, as the back-to-back topology additionally leads to large values of $M_T(\vec{p}_T(\gamma), \vec{p}_T^{\,miss})$. In contrast to such unphysical candidates, real photons are expected to have a finite ECAL shower width. Therefore, photon candidates are required to fulfill $\sigma_{i\eta i\eta} > 0.001$ and $\sigma_{i\phi i\phi} > 0.001$, where $\sigma_{i\phi i\phi}$ is defined in the same way as $\sigma_{i\eta i\eta}$ using the ϕ-direction.

All photon identification requirements are summarized in Table 6.2.

All photon identification variables are compared with simulation using final-state radiation photons of $Z \to \mu\mu\gamma$ events [171,175]. Sufficient agreement is observed. Data-to-simulation

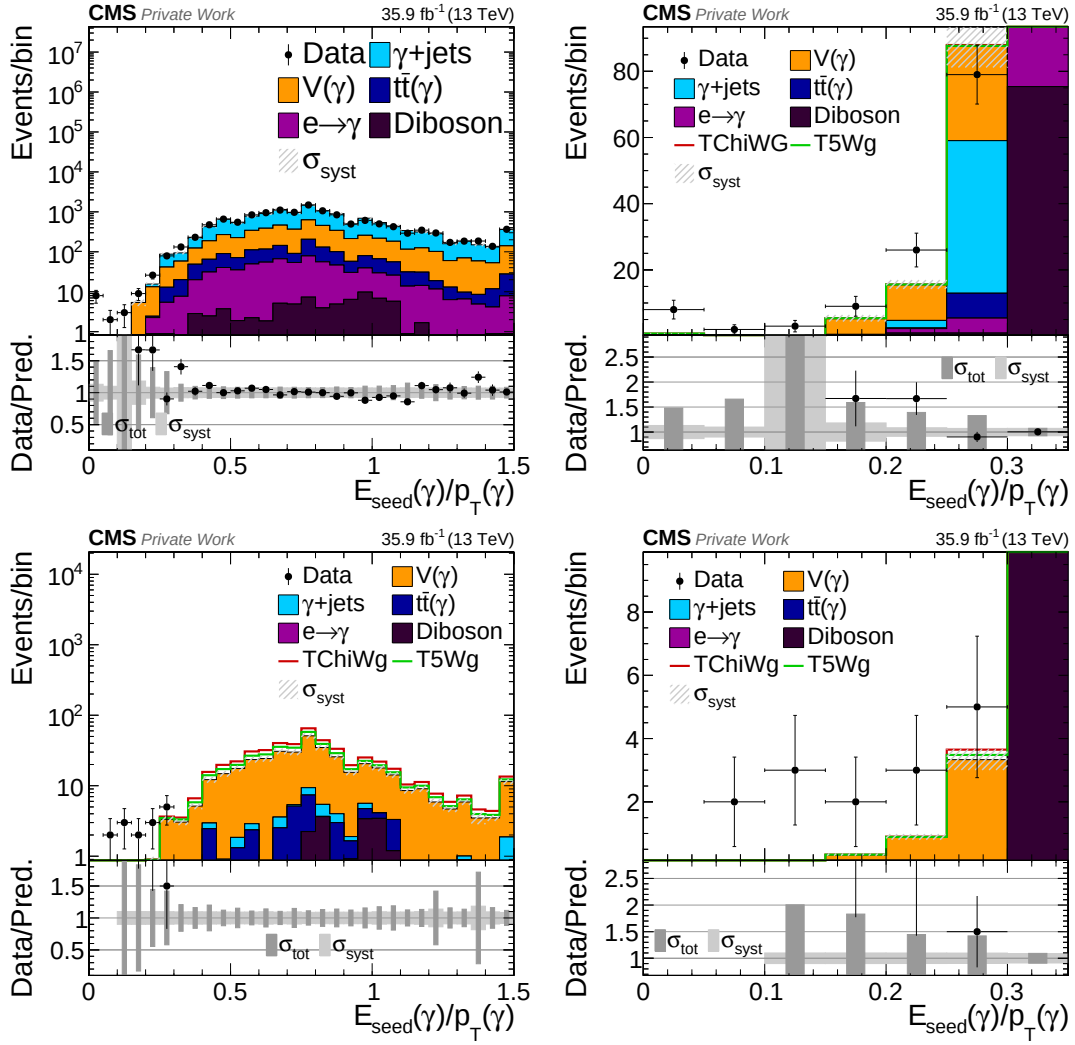

Figure 6.3: Distribution of the photon $E_{\text{seed}}/p_{\text{T}}$ in two different phase spaces used in the analysis. The bottom row shows the distribution in the signal region, so that the data are not shown for $E_{\text{seed}}/p_{\text{T}} > 0.3$, as a certain signal sensitivity is expected for larger values. The right figures show an enlarged illustration of the critical region $E_{\text{seed}}/p_{\text{T}} < 0.35$ with linear y-axis scale. No SM background prediction is available for events with low values of $E_{\text{seed}}/p_{\text{T}}$ and no signal sensitivity loss is induced by requiring $E_{\text{seed}}/p_{\text{T}} > 0.3$.

efficiency ratios are determined depending on $p_{\text{T}}(\gamma)$ and η. The analysis selects photons with $p_{\text{T}} > 180\,\text{GeV}$. The data-to-simulation efficiency ratio for these photons is close to unity. Therefore, no additional scale factor is applied and an efficiency ratio uncertainty of 2% is considered to cover deviations from unity [175].

Table 6.2: Identification criteria for photons reconstructed in the ECAL barrel [173].

Identification variable		Value
p_{T}	$>$	15 GeV
$\lvert\eta\rvert$	$<$	1.44
H/E	$<$	0.0597
$\sigma_{i\eta i\eta}$	$<$	0.01031
$\sigma_{i\eta i\eta}$, $\sigma_{i\phi i\phi}$	$>$	0.001
$\mathrm{Iso}_{h^{\pm}}$	$<$	1.295 GeV
Iso_{h^0}	$<$	$10.910\,\mathrm{GeV} + 0.0148 \cdot p_{\mathrm{T}} + 0.000017\,\mathrm{GeV}^{-1} \cdot p_{\mathrm{T}}^2$
Iso_{γ}	$<$	$3.630\,\mathrm{GeV} + 0.0047 \cdot p_{\mathrm{T}}$
$N_{\text{pixel seed}}$	$<$	1
$E_{\text{seed}}/p_{\mathrm{T}}$	$>$	0.3

6.1.3 Further objects

One key feature of the analysis is the inclusive event selection, enabling high sensitivity to a large variety of SUSY scenarios. The analysis exhausts the information given by the photons and $p_{\mathrm{T}}^{\mathrm{miss}}$, avoiding to discard certain scenarios by requiring or excluding objects like jets or charged leptons. These objects have almost no effect on the analysis results and are therefore only briefly summarized in the following section.

Jets and hadronic activity

Jets are reconstructed from PF candidates with the anti-k_{T} clustering algorithm [176] as implemented in the FastJet [177] package. A distance parameter of 0.4 is used. Jet momentum is determined as the vectorial sum of all particle momenta in the jet. Tracks identified to be originating from pileup vertices are discarded. An offset correction is applied to correct for remaining pileup contributions. Energy corrections [174, 178] are derived from MC simulation, and are confirmed with measurements of the energy balance in dijet, γ+jet, Z + jet, and multijet events. A jet candidate has to fulfill $p_{\mathrm{T}} > 30\,\mathrm{GeV}$ and $|\eta| < 3$ with a geometrical isolation from reconstructed photons, electrons, and muons. Loose identification requirements are imposed as recommended by the CMS collaboration [179].

The jet momentum resolution can be parametrized by

$$\frac{\sigma_{p_{\mathrm{T}}}}{p_{\mathrm{T}}} = \frac{N}{p_{\mathrm{T}}} \oplus \frac{S}{\sqrt{p_{\mathrm{T}}}} \oplus C. \tag{6.4}$$

Figure 6.4 (left) shows the jet energy resolution depending on p_{T} and for different intervals of number of pp interactions μ based on simulation studies. The extraction of the parameters N, S, and C of Eq. (6.4) is summarized in Figure 6.4 (right) for the

pseudorapidity range $|\eta| < 1.3$. The parameters are determined in dependency of $\mu \times A$, where $A = \pi R^2$ is the jet area with R being the distance parameter used for the jet clustering. The constant term C is of the order of 4%, also depending on the jet flavor. The stochastic term S is about 0.9 $\sqrt{\text{GeV}}$. The noise term N is highly sensitive to pileup, varying from 1 to 10 GeV for $0 < \mu \times A < 100$. Charged hadrons generate tracks in the inner tracker that can be extrapolated to the HCAL, so that charged hadrons originating from other pp interactions of the same bunch crossing (in-time pileup) can be excluded from the jet clustering. If this charged hadron subtraction (CHS) is applied, about 50% of the in-time pileup can be removed within the tracker coverage and the dependency on pileup is significantly reduced.

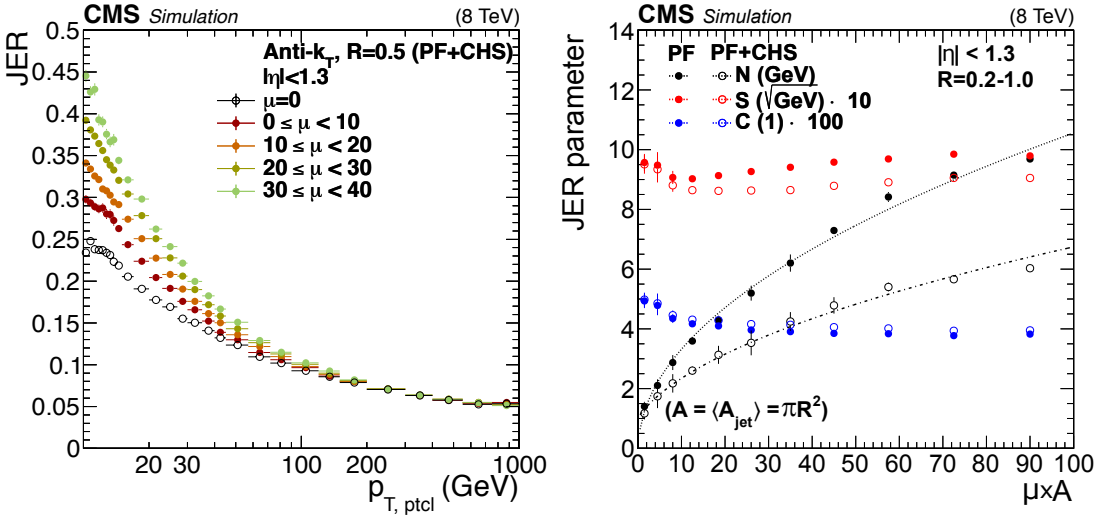

Figure 6.4: Jet energy resolution (JER) based on simulation studies [172]. The left plot shows the JER depending on the p_T of the jet for different pileup intervals. The energy resolution follows the parametrization given in Eq. (6.4). The right plot shows the results of the extraction of the parameters N, S, and C of Eq. (6.4) in dependency of the number of pp interactions in one bunch crossing times jet area $\mu \times A$. The results are determined for $|\eta| < 1.3$ and with (open symbols) and without (solid symbols) applying the charged hadron subtraction (CHS). The right plot has slightly been adapted to improve comprehension.

A well-suited measure for the hadronic activity in an event is the scalar sum of the transverse momenta of all jets:

$$\mathrm{H_T} = \sum_{i}^{N_{\text{jets}}} p_{\mathrm{T}}(\text{jet}_i), \tag{6.5}$$

where $\mathrm{N_{jets}}$ is the number of jets fulfilling the criteria listed above. Large values of $\mathrm{H_T}$ can be a hint for events produced via strong production. Requiring large $\mathrm{H_T}$ in the event selection would eliminate, e.g., sensitivity to electroweak production of gauginos, as in these events no or only a few jets are produced in the decay chains.

Charged leptons

Electrons and muons are not used in the event selection and are only considered for validation studies. Electron-like objects are used to define an electron control region to estimate the background from electrons misidentified as photons ($e \to \gamma$). Tau leptons are not explicitly used.

Electrons and muons are reconstructed from PF candidates fulfilling stricter identification and quality requirements. These criteria follow the recommendations of the CMS collaboration [180, 181], optimized in detailed studies.

Electron-like objects used to estimate the $e \to \gamma$ background fulfill the same identification requirements as photons, but with inverted pixel seed veto, compare Table 6.2.

Chapter 7

Event selection

Contents

One key part of the analysis is the event selection. Compared to the total inelastic pp cross section, processes of new physics have production cross sections orders of magnitude lower, making it impossible to discover any kind of new phenomena in the recorded data set without a significant reduction of SM background events. A first reduction of events is carried out by the trigger system as described in Section 4.2.7. In a subsequent selection step, this subset of data has to fulfill common quality requirements, reducing for instance events with high detector noise or non-collision events. A preselection is applied to serve as a basis for all control regions (CRs), the validation region (VR), and the signal region (SR). These regions are defined to develop and validate the estimation of the contributing SM backgrounds (CR and VR) and to maximize the sensitivity to new physics (SR), exploiting the knowledge about the expected phenomenology of SM processes and the SUSY scenarios of interest. The event selection was developed blindly, i.e., without comparing data to prediction in the signal region to avoid biasing the event selection with regard to the outcome.

7.1 Preselection

The reconstructed event vertex of the hard scattering, the primary vertex, is given by the vertex with the largest value of summed physics-object p_{T}^2. Here, physics objects are the objects defined by the anti-k_{T} jet finding algorithm [11, 176, 182] applied to all tracks associated with the respective vertex, all remaining single tracks, and the corresponding associated $p_{\mathrm{T}}^{\mathrm{miss}}$.

The missing transverse momentum, as introduced in Section 6.1.1, is a variable calculated using information of all subdetectors. As it represents the vectorial sum of the transverse momenta of all final state objects of the event, the magnitude is highly sensitive to any kind of detector noise or signatures unrelated to the hard process of the collision event. Artificial energy measurements and limited energy resolution, as well as the failure of measuring energy deposits lead to anomalous $p_{\mathrm{T}}^{\mathrm{miss}}$. Such a spurious imbalance can be caused by protons interacting with gas molecules in the beam pipe, beam halo muons, electronics noise, and dead cells in the ECAL or noise in the HCAL hybrid photodiodes and readout box electronics. Also low-quality muons, which do not pass the indentification requirements of the PF algorithm can lead to spurious $p_{\mathrm{T}}^{\mathrm{miss}}$. Various algorithms correct or reject such events utilizing for instance topological and timing based information [183]. Figure 7.1 illustrates the effect of applying these filter algorithms to data.

A single-photon signal trigger was chosen for this analysis, as described in detail in Section 5.2. To prevent the analysis from systematic turn-on effects in data, at least one well identified photon with $p_{\mathrm{T}} > 180\,\mathrm{GeV}$ is required in the offline selection. The triggering object is matched to a photon passing the offline identification. Photons are required to have a spherical distance to the nearest jet of at least 0.5 in ΔR. To ensure that the $p_{\mathrm{T}}^{\mathrm{miss}}$ is not predominantly caused by a mismeasured jet, a minimal distance of 0.3 in $\Delta\phi$ is required between $p_{\mathrm{T}}^{\mathrm{miss}}$ and all jets with $p_{\mathrm{T}} > 100\,\mathrm{GeV}$. This preselection is applied to all control, validation, and signal regions, and is summarized in Table 7.1.

7.2 Variable definitions

On the one hand, searches for new physics need to develop an event selection that separates SUSY events of a certain scenario from SM background events to enable the observation of differences between measurement and prediction. On the other hand, the larger the variety of SUSY scenarios the selected phase space is sensitive to, the more the discovery potential increases. A good balance between a scenario specific and the best possible inclusive selection should be achieved. Therefore, the event selection is enriched by further, more complex variables based on the properties of photons and $p_{\mathrm{T}}^{\mathrm{miss}}$.

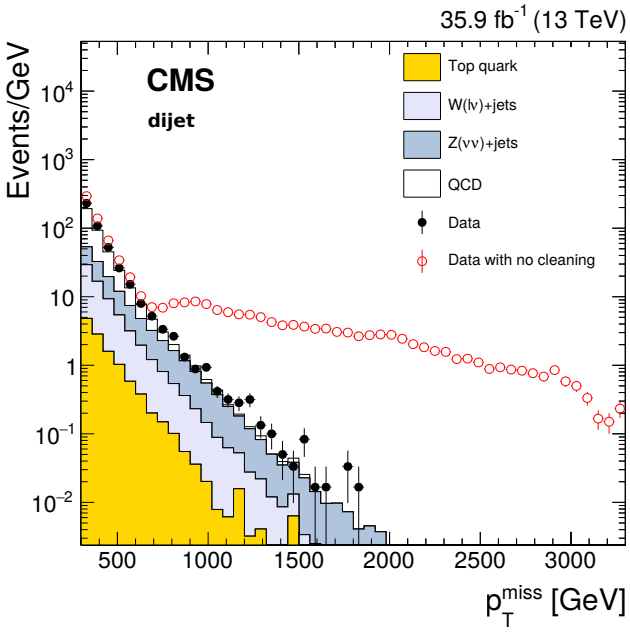

Figure 7.1: Data-to-simuation comparison in a phase space defined by requiring $p_{\mathrm{T}}^{\mathrm{miss}} > 250\,\mathrm{GeV}$ and requiring the presence of two jets, where the first (second) jet has to exceed $p_{\mathrm{T}} > 500(200)\,\mathrm{GeV}$, before (open red circles) and after (black dots) applying the $p_{\mathrm{T}}^{\mathrm{miss}}$ filters [183].

7.2.1 The transverse mass $\mathrm{M_T}$

The signal and fit control region are defined in the two-dimensional phase space of $p_{\mathrm{T}}^{\mathrm{miss}}$ and $\mathrm{M_T}(\vec{p}_{\mathrm{T}}(\gamma), \vec{p}_{\mathrm{T}}^{\,\mathrm{miss}})$. The variable $\mathrm{M_T}(\vec{p}_{\mathrm{T}}(\gamma), \vec{p}_{\mathrm{T}}^{\,\mathrm{miss}})$, in the following referred to as $\mathrm{M_T}$, is the transverse mass of the leading photon and $\vec{p}_{\mathrm{T}}^{\,\mathrm{miss}}$, and it is defined as the invariant mass only using the transverse components of the four-vector:

$$\mathrm{M_T} \equiv \mathrm{M_T}(\vec{p}_{\mathrm{T}}(\gamma), \vec{p}_{\mathrm{T}}^{\,\mathrm{miss}}) = \sqrt{2 \cdot p_{\mathrm{T}}^{\mathrm{miss}} \cdot p_{\mathrm{T}}(\gamma)[1 - \cos(\Delta\phi(\vec{p}_{\mathrm{T}}(\gamma), \vec{p}_{\mathrm{T}}^{\,\mathrm{miss}}))]}. \tag{7.1}$$

It can be regarded as an approach to reconstruct the mass of a particle that decays into a detected and an undetected particle, like the $\mathrm{W}^{\pm} \to l^{\pm}\nu$ decay. The transverse mass is shown in Fig. 7.2 (top left) for several SM processes and the two benchmark signal points. The event samples are normalized to unity and plotted after applying the preselection. In all SUSY scenarios considered in the analysis, the $\widetilde{\chi}_1^0$ can decay according to $\widetilde{\chi}_1^0 \to \gamma\widetilde{\mathrm{G}}$. R-parity is assumed to be conserved, resulting in the pair production of sparticles, and therefore the presence of two gravitinos in one SUSY event. Hence, $\mathrm{M_T}$ roughly represents the $\widetilde{\chi}_1^0$ mass in SUSY events, washed out by the presence of the second $\widetilde{\mathrm{G}}$, as can be seen for the TChiWg benchmark signal point with a $\widetilde{\chi}_1^0$ mass of 700 GeV. The $\widetilde{\chi}_1^0$ mass of the T5Wg signal point is 1700 GeV and almost all events are gathered in the last bin. Besides selecting SUSY events with high $\widetilde{\chi}_1^0$ masses, large $\mathrm{M_T}$ values also

Table 7.1: Selection criteria applied in the preselection and for the fit control, the validation, and the signal region.

Region	Selection
Preselection	$p_{\mathrm{T}}^{\mathrm{miss}}$ filters
	At least one reconstructed vertex
	At least one photon with $p_{\mathrm{T}} > 180\,\mathrm{GeV}$
	Triggering object matched to reconstructed photon
	$\Delta R(\gamma, \mathrm{jet}) > 0.5$
	$\lvert\Delta\phi(\vec{p}_{\mathrm{T}}^{\,\mathrm{miss}}, \mathrm{jet})\rvert > 0.3$, if $p_{\mathrm{T}}(\mathrm{jet}) > 100\,\mathrm{GeV}$
Fit control region	Preselection
	$p_{\mathrm{T}}^{\mathrm{miss}} > 100\,\mathrm{GeV}$
	$\mathrm{M_T} > 100\,\mathrm{GeV}$
	$p_{\mathrm{T}}^{\mathrm{miss}} < 300\,\mathrm{GeV}$ or $\mathrm{M_T} < 300\,\mathrm{GeV}$
Validation region	Preselection
	$p_{\mathrm{T}}^{\mathrm{miss}} > 300\,\mathrm{GeV}$
	$\mathrm{M_T} > 300\,\mathrm{GeV}$
	$\mathrm{S_T^\gamma} < 600\,\mathrm{GeV}$
Signal region	Preselection
	$p_{\mathrm{T}}^{\mathrm{miss}} > 300\,\mathrm{GeV}$
	$\mathrm{M_T} > 300\,\mathrm{GeV}$
	$\mathrm{S_T^\gamma} > 600\,\mathrm{GeV}$

suppress SM background events, especially with $\mathrm{W}^{\pm} \to \mathrm{e}^{\pm}\nu$ decays, where the electron is misidentified as photon, or events where the photon and $p_{\mathrm{T}}^{\mathrm{miss}}$ are uncorrelated, as present in the $\gamma +$ jets background.

7.2.2 The $\mathrm{S_T^\gamma}$ variable

To maximize the separation of the SM background and possible SUSY events, the variable $\mathrm{S_T^\gamma}$, defined as

$$\mathrm{S_T^\gamma} = \sum_{i}^{N_\gamma} \mathrm{p_T}(\gamma_i) + p_{\mathrm{T}}^{\mathrm{miss}}, \tag{7.2}$$

is introduced, where N_γ represents all photons fulfilling the requirements listed in Table 6.2. In SM processes, photon and neutrino production are not correlated. In the SUSY scenarios considered in the analysis, photons and gravitinos are always produced in the same event. Furthermore, two gravitinos are produced in all cases and some SUSY scenarios can lead to the production of more than one high-energy photon. As can be seen in Fig. 7.2 (top right), SUSY events populate much higher $\mathrm{S_T^\gamma}$ values compared to SM events. Especially for EWK SUSY scenarios, $\mathrm{S_T^\gamma}$ exploits the kinematical differences

compared to SM processes, as solely using $p_{\mathrm{T}}^{\mathrm{miss}}$ or $p_{\mathrm{T}}(\gamma)$, shown in Fig. 7.2 (bottom row), provides less separation power.

7.3 Signal region

The definition of the SR is optimized for sensitivity to a variety of SUSY signal scenarios based on both EWK and strong production. In SUSY scenarios with R-Parity conservation, one key feature is the pair production of sparticles, which decay into stable LSPs and certain SM particles. In the SUSY scenarios considered in this analysis, the LSP is the neutral $\widetilde{\mathrm{G}}$. The $\widetilde{\mathrm{G}}$ leaves the detector undetected, leading to a significant amount of $p_{\mathrm{T}}^{\mathrm{miss}}$. In SM processes, $p_{\mathrm{T}}^{\mathrm{miss}}$ only arises from neutrinos and imperfect energy measurements. The lightest neutralino predominantly decays into a photon and a gravitino, leading to a large invariant mass of these two objects. In contrast to that, there is no SM process where a particle decays into a photon and a neutrino, enabling a high separation power of SM and SUSY processes using $\mathrm{M_T}$.
The SR is defined by requiring

- $p_{\mathrm{T}}^{\mathrm{miss}} > 300\,\mathrm{GeV}$,
- $\mathrm{M_T} > 300\,\mathrm{GeV}$, and
- $\mathrm{S_T^{\gamma}} > 600\,\mathrm{GeV}$.

Hence, the signal selection only exploits properties of photons and $p_{\mathrm{T}}^{\mathrm{miss}}$, ensuring a large degree of generality. Also, no explicit jet requirement is used. The four $\mathrm{S_T^{\gamma}}$ regions $600 - 800$, $800 - 1000$, $1000 - 1300$, and $> 1300\,\mathrm{GeV}$ define exclusive bins that are simultaneously interpreted in a multichannel counting experiment for best sensitivity.

7.4 Control and validation regions

The control regions are optimized to enable a data-based background prediction with high accuracy and to perform first cross checks of these methods. The CRs and VR are defined orthogonally to the SR to use a statistically independent subset of data. The VR is used to test the full background prediction for consistency.

7.4.1 Fit control region

The main SM background contributing to the SR is $\mathrm{V}(\gamma)$, which constitutes around three quarters of all backgrounds. Therefore, one CR is optimized to normalize the MC simulation of the $\mathrm{V}(\gamma)$ processes to data in a χ^2-fit, simultaneously with the simulation of

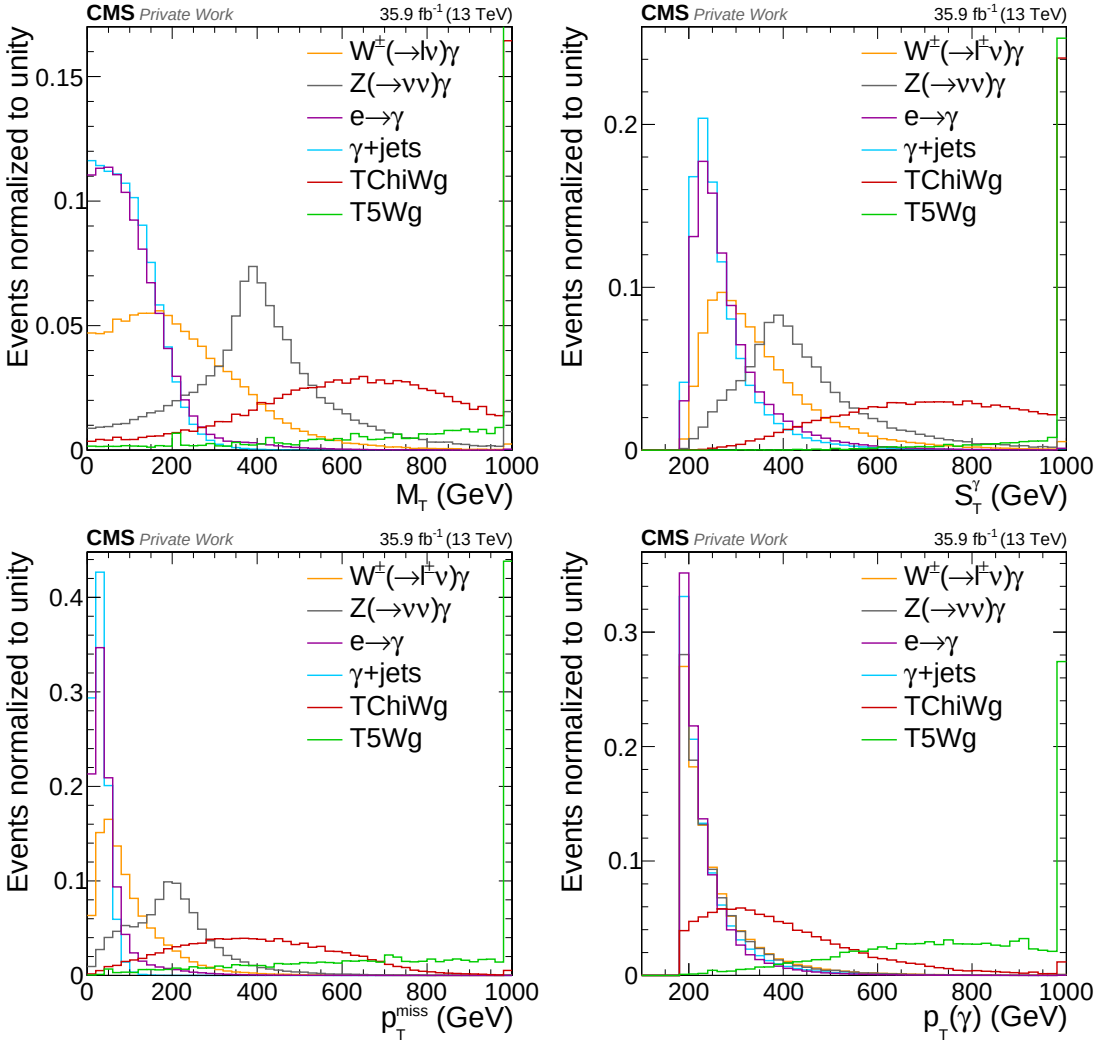

Figure 7.2: Distributions of M_T (top left), S_T^γ (top right), p_T^{miss} (bottom left), and $p_T(\gamma)$ (bottom right) for several SM background processes and the benchmark signal points after applying the preselection. The event samples are normalized to unity. Events with values beyond the shown range are included in the last bin. The peak-like structure of the process $Z(\to \nu\nu)\gamma$ in the distributions of M_T, S_T^γ, and p_T^{miss} is a consequence of the requirement $p_T(\gamma) > 180\,\text{GeV}$ applied in the preselection. The ISR photon boosts the Z boson, and therefore the neutrinos, in opposite direction with respect to the photon with the same amount of momentum, resulting in peaks at $p_T^{miss} \approx 180\,\text{GeV}$, $M_T \approx \sqrt{2 \cdot p_T^{miss} \cdot p_T(\gamma)[1-\cos(\pi)]} \approx 2{\cdot}180\,\text{GeV} = 360\,\text{GeV}$, and $S_T^\gamma \approx p_T(\gamma) + p_T^{miss} \approx 360\,\text{GeV}$. The kinematic properties of the process are overlayed by further selection requriements, and reconstruction and radiation effects.

γ + jets, as presented in Section 8.4. To get reliable χ^2-fit values with small uncertainties, the fit CR has to fulfill several requirements. On the one hand, a large amount of SM background events with floating normalization are needed to get a small statistical uncertainty in the fit results. On the other hand, all remaining backgrounds contributing to this CR should be small to minimize the influence of the uncertainties in their normalization. Possible signal contamination, i.e., the ratio of expected signal events to expected SM background events, should be small to not overestimate the scale factors in the case of a presence of SUSY in data and to preserve signal sensitivity in the SR. The control region used to perform the fit is defined by

- $p_{\mathrm{T}}^{\mathrm{miss}} > 100\,\mathrm{GeV}$,
- $\mathrm{M_T} > 100\,\mathrm{GeV}$, and
- $p_{\mathrm{T}}^{\mathrm{miss}} < 300\,\mathrm{GeV}$ or $\mathrm{M_T} < 300\,\mathrm{GeV}$.

7.4.2 Electron control region

For the data-driven background estimation of electrons that are misidentified as photons, electron CRs are used. For these CRs the same selection criteria are applied as for phase space the background estimation is needed for, but requiring at least one pixel seed for the photon candidate, i.e., the photon is replaced by an electron-like object. To estimate the contribution of electrons misidentified as photons, the distributions in these CRs are scaled by the electron-to-photon misidentification probability, as described in Section 8.3.

7.4.3 Validation region

A VR is introduced to test all background estimation methods in a phase space close to the SR, but with negligible signal contamination. In this region the full background prediction is validated before performing data-to-background comparisons in the SR. The VR has the same selection criteria as the SR, but requiring $\mathrm{S_T^\gamma} < 600\,\mathrm{GeV}$. Since this selection comprises the requirement of at least one photon with $p_{\mathrm{T}} > 180\,\mathrm{GeV}$ and $p_{\mathrm{T}}^{\mathrm{miss}} > 300\,\mathrm{GeV}$, the VR lies in the phase space $480\,\mathrm{GeV} < \mathrm{S_T^\gamma} < 600\,\mathrm{GeV}$.
The definitions of the fit control, the validation, and the signal region are summarized in Table 7.1.

Figure 7.3 (upper left) shows a sketch illustrating the definition of the signal and fit control region, as well as the approximate phase space of the VR, which is not exclusively defined in the $p_{\mathrm{T}}^{\mathrm{miss}} - \mathrm{M_T}$ phase space. Figure 7.3 (upper right) shows the distribution of the total SM background in the $p_{\mathrm{T}}^{\mathrm{miss}} - \mathrm{M_T}$ phase space after applying the preselection, while the plots on the bottom left and right show the distribution for the T5Wg and TChiWg benchmark signal points in the same phase space, respectively. These plots illustrate the high separation power between background and signal. The number of signal events in the fit CR is far below 1% compared to the SM background contribution for both benchmark

points. 91% and 64% of the preselected events of the T5Wg and TChiWg benchmark signal points, respectively, fulfill the SR requirements.

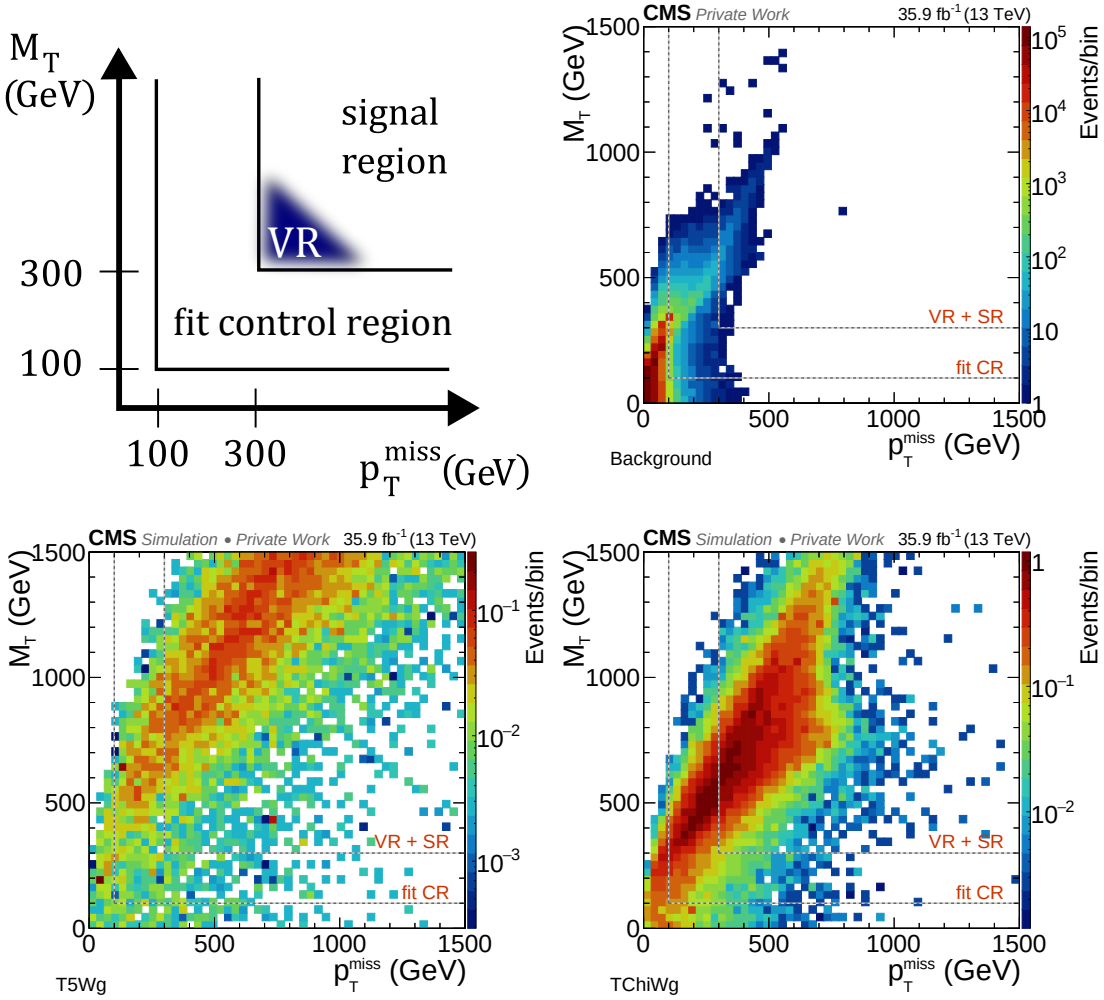

Figure 7.3: Sketch of the definition of the signal and the fit control region (upper left). The validation region (VR) is not solely defined in the $p_{\mathrm{T}}^{\mathrm{miss}} - \mathrm{M_T}$ space, but the corresponding phase space is indicated by the blue area. The upper right plot shows the distribution of the SM background in the $p_{\mathrm{T}}^{\mathrm{miss}} - \mathrm{M_T}$ phase space, while the bottom row shows the distribution for the T5Wg (left) and TChiWg (right) benchmark signal points. The signal contamination of both benchmark signal points is below 1% in the fit control region.

Chapter 8

Background estimation methods

Contents

The goal of this thesis is to develop an analysis that is able to probe a so far unexplored phase space for physics beyond the SM. The basis to do so is the elaboration of the expectation based on our current knowledge of physics. There are three main categories of how the contribution of SM processes can be estimated. Most of the SM processes can be estimated to a good precision using MC simulation scaled according to higher-order cross section calculations. Often, the precision of the simulation can be improved by comparing and adjusting the simulation to data in a suitable CR. For some processes a fully data-driven method can provide a suitable approach. All of these methods are used in the analysis.

8.1 Background overview

The analysis selects final states with high-energy photons and a significant amount of missing transverse momentum. An inclusive event selection is applied without any requirements on the presence or absence of jets or charged leptons. The main background contributing to the SR is the production of a vector boson in association with a high-energy photon ($V\gamma$). Control regions are used to develop estimation methods for all relevant SM backgrounds which can then be applied to the SR. Since different processes have different kinematical properties, the relative amount of events of a certain process can change between control, validation, and signal region. The focus lies on those backgrounds that have the largest contribution to the SR. To elaborate reliable prediction methods, also a precise knowledge of the backgrounds relevant for the CRs is needed.

Figure 8.1 shows the contribution of all backgrounds to the fit CR, the VR, and the SR as a function of S_T^γ. In the fit CR (top row), the two dominant backgrounds are $V(\gamma)$ and $\gamma + \text{jets}$, where the top right plot is the same as the left plot with a logarithmic y-axis scale to improve visualization of the negligible signal contribution. In the VR (bottom left), $V(\gamma)$ has the largest contribution. The relative amount of $V(\gamma)$ events is even larger in the SR (bottom right). The contribution of $\gamma + \text{jets}$ to the validation and signal region is almost negligible because p_T^{miss} only arises from jet mismeasurements, for which the amount of the vectorial sum rarely exceeds 300 GeV. In addition, the $|\Delta\phi(\vec{p}_T^{\,\text{miss}},\ \text{jet})| > 0.3$ requirement for jets with $p_T > 100\,\text{GeV}$ imposed in the preselection further suppresses events where p_T^{miss} is dominated by the mismeasurement of a high-energy jet. Subdominant backgrounds are $t\bar{t}(\gamma)$, electrons that are misidentified as photons, and in extremely rare cases diboson production with leptonic decays. The contribution from QCD multijet events is found to be negligible. In all plots also the expected contribution of the two benchmark signal points is shown.

8.2 Top pair and diboson production

Top pair and diboson production only have a small contribution to all regions defined in the analysis. Therefore, these backgrounds are estimated using MC simulation and are scaled by (N)NLO cross sections, as described in Section 5.3.

Top pair production

Top pair production is an important background for many analyses. The decay products result in several high-level objects guiding many event selections, especially in BSM searches. Each top quark decays nearly immediately and almost exclusively into a $W^\pm$ boson and a b quark. The $W^\pm$ boson decays hadronically in two thirds of the cases and into a charged lepton and a neutrino in all other cases. Therefore, $t\bar{t}$ production

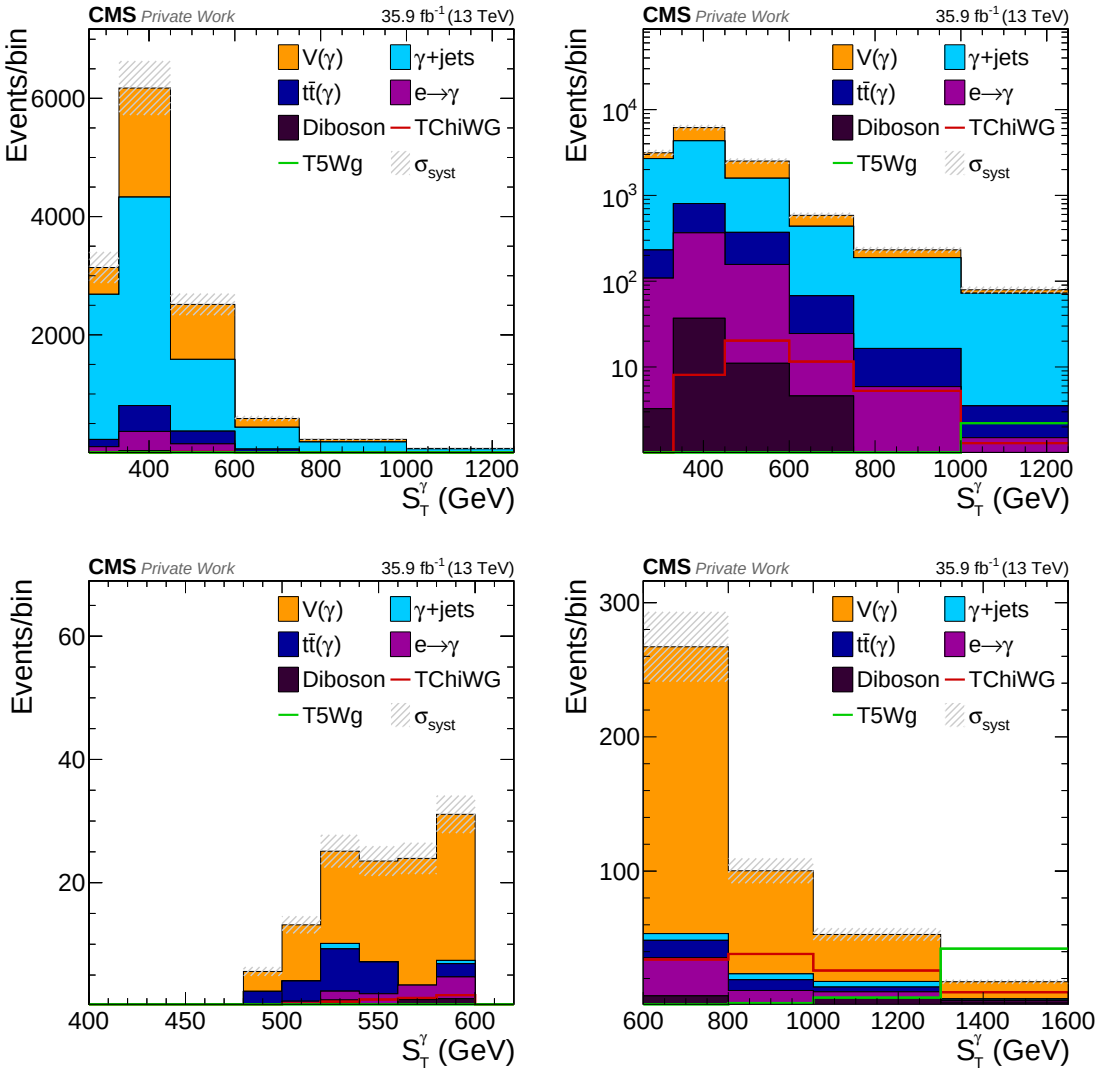

Figure 8.1: Plots showing the contribution of all relevant standard model backgrounds and the benchmark signal points to the fit control (top row), the validation (bottom left), and signal region (bottom right).

can result in final states with jets, genuine $p_{\mathrm{T}}^{\mathrm{miss}}$, and charged leptons. Photons may be reconstructed due to photon initial or final state radiation, or electron or jet misidentifications. Studies have shown that the largest contribution comes from initial-state photon radiation, if the photon is required to have a p_{T} larger than 180 GeV. Events from $\mathrm{t\bar{t}}(\gamma)$ production that would contribute due to misidentified electrons are estimated by a data-driven approach as described in Section 8.3 and are excluded from the simulation.

Diboson production

The diboson background comprises $W^{\pm}W^{\mp}$, $W^{\pm}Z$, and ZZ production. Similarly to $t\bar{t}(\gamma)$, the dibson background contributes due to initial or final state photon radiation or misidentified electrons or jets. Additionally, $W^{\pm} \to l^{\pm}\nu$ and $Z \to \nu\bar{\nu}$ decays lead to large values of $p_{\mathrm{T}}^{\mathrm{miss}}$. Likewise, diboson events where electrons are misidentified as photons are estimated using the data-driven technique introduced in Section 8.3. Since the cross section of diboson production is relatively small, its contribution to all regions is almost negligible.

8.3 Electrons misidentified as photons

Electrons and photons, often collectively denoted as e/γ objects, have a similar signature in the electromagnetic calorimeter. To be able to distinguish whether the e/γ shower originates from a photon or an electron, additional information provided by the inner tracking system is needed. The only difference between an electron and an unconverted photon in terms of detector signature is the presence of a track generated by the electrically charged electron, connecting the interaction point and the ECAL shower. The discriminant deciding on the nature of the e/γ object is the pixel seed, as introduced in Chapter 6.

8.3.1 Electron-to-photon misidentification rate extraction from data

Photons do not couple to the electrically neutral Z boson. This provides the opportunity to measure the electron-to-photon misidentification rate with high precision using $Z \to e^{+}e^{-}$ decays. If the invariant mass of an electron and a photon candidate equals the mass of the Z boson, it is almost certain that the object reconstructed as photon actually is an electron. Such an approach is called a "tag-and-probe" method [184].

For the *tag*, a well-identified electron is selected. At least one *probe* object is required that fulfills all identification requirements of a photon, but without any requirement on the presence or absence of pixel seeds. By this definition, both electrons and photons are selected as *probes*. If the invariant mass of the *tag* and the *probe* object matches the Z mass, the combination is counted as N_{ee}^{Z} event if the *probe* has at least one pixel seed, and as $N_{e\gamma}^{Z}$ event if not. The contribution of Z boson decays is extracted by fitting the *tag*-and-*probe* invariant mass distribution by a combination of a signal and background shape. The signal shape is taken from MC simulation, where the *tag* and *probe* objects both originate from the Z boson decay, and is convolved with a Gaussian distribution to take differences between MC simulation and data into account. The combinatorial background shape is given by the invariant mass distribution of an electron-muon pair, smeared by a kernel density estimator with Gaussian cores [185] to reduce the impact of

fluctuations. The procedure is developed in [186] for data recorded at 13 TeV and the result is used here.
Since only one of the two electrons of the $Z \to e^+e^-$ decay has to be misidentified as a photon to contribute to $N^Z_{e\gamma}$, $N^Z_{e\gamma}$ is given by

$$N^Z_{e\gamma} = 2 \cdot f \cdot N^Z, \tag{8.1}$$

where f is the true $e \to \gamma$ misidentification probability and N^Z is the true number of $Z \to e^+e^-$ decays. To contribute to N^Z_{ee}, both electrons must not be misidentified, so that

$$N^Z_{ee} = (1-f)^2 \cdot N^Z. \tag{8.2}$$

For simplicity the approximation

$$R_{\gamma/e} = \frac{N^Z_{e\gamma}}{N^{Z,\,\text{count}}_{ee}} = \frac{N^Z_{e\gamma}}{2 \cdot N^Z_{ee}} = \frac{2 \cdot f \cdot N^Z}{2 \cdot (1-f)^2 \cdot N^Z} = \frac{f}{(1-f)^2} \overset{f \ll 1}{\approx} f \tag{8.3}$$

is used as $e \to \gamma$ misidentification probability. The value $N^{Z,\,\text{count}}_{ee} = 2 \cdot N^Z_{ee}$ is the number of reconstructed electron-electron events entering the calculation of $R_{\gamma/e}$, where the factor of 2 arises from the double-counting of N^Z_{ee} events since both reconstructed electrons serve as *tag* and as *probe* object. The measurement yields

$$R_{\gamma/e} = 0.027 \pm 0.014, \tag{8.4}$$

where the uncertainty already comprises the systematic uncertainty.
In general, the electron-to-photon misidentification probability is not constant and depends on several kinematic and geometric variables, as well as the event activity. Furthermore, systematic uncertainties in the fit method have to be considered. A conservative systematic uncertainty of 50% is assigned to $R_{\gamma/e}$ that covers all dependencies and systematic uncertainties arising from the method. Since the $e \to \gamma$ background has only a small contribution to all analyzed regions, this simplification is bearable. The statistical uncertainty in $R_{\gamma/e}$ is negligible compared to the systematic uncertainty.

To estimate the $e \to \gamma$ contribution, electron CRs are selected with the exact same selection requirements as the regions of interest, but inverting the pixel seed veto for the leading photon candidate. These regions are then scaled by $R_{\gamma/e}$ to serve as $e \to \gamma$ estimate.

8.3.2 Validation of the prediction method for misidentified electrons

To validate the method, the same procedure is performed using MC simulation. The resulting electron-to-photon misidentification probability for simulation is

$$R^{\text{sim}}_{\gamma/e} = 0.015 \pm 0.008. \tag{8.5}$$

The large difference between $R_{\gamma/\mathrm{e}}$ and $R^{\mathrm{sim}}_{\gamma/\mathrm{e}}$ highlights the importance of using a data-driven method to predict the $\mathrm{e} \to \gamma$ contribution. The uncertainty reflects the uncertainty of the measurement in data and is chosen to be 50%. MC generator information, often also denoted as MC truth information, is also used to determine $\mathrm{N}^{\mathrm{Z}}_{\mathrm{e}\gamma}$ and $\mathrm{N}^{\mathrm{Z}}_{\mathrm{ee}}$, resulting in a similar value for $R^{\mathrm{sim}}_{\gamma/\mathrm{e}}$.

Electron CRs are selected and scaled by $R^{\mathrm{sim}}_{\gamma/\mathrm{e}}$ to provide $\mathrm{e} \to \gamma$ predictions ("predicted $\mathrm{e} \to \gamma$"). The predictions are compared to distributions obtained by matching the reconstructed γ to the generated electron $\mathrm{e}_{\mathrm{gen.}}$ ("gen. matched $\mathrm{e} \to \gamma$"). The criteria for the reconstructed-to-generated object matching are given by

$$\Delta p_{\mathrm{T}} \equiv \left| \frac{p_{\mathrm{T}}(\gamma) - p_{\mathrm{T}}(\mathrm{e}_{\mathrm{gen.}})}{p_{\mathrm{T}}(\gamma)} \right| < 0.5 \quad \text{and} \quad \Delta R(\gamma, \mathrm{e}_{\mathrm{gen.}}) < 0.1. \tag{8.6}$$

The MC samples used for this cross check are top pair, $\mathrm{W}^{\pm}$ boson, and dibson production, as these processes are the ones with electrons in the final state that are relevant for the analysis. Figure 8.2 shows validation plots for three different regions as a function of $\mathrm{S}^{\gamma}_{\mathrm{T}}$. Figure 8.2 (top left) shows $\mathrm{S}^{\gamma}_{\mathrm{T}}$ applying the preselection but requiring $p_{\mathrm{T}}(\gamma) > 100\,\mathrm{GeV}$ instead of $p_{\mathrm{T}}(\gamma) > 180\,\mathrm{GeV}$ to increase the statistical precision. For the top right plot of Fig. 8.2 additionally $p^{\mathrm{miss}}_{\mathrm{T}} > 50\,\mathrm{GeV}$ and $\mathrm{M_T} > 50\,\mathrm{GeV}$ is required. The bottom plot shows the comparison in the fit CR.

The validation plots show good agreement between prediction and the matching using MC truth information within the uncertainties. In most cases the statistical uncertainty of the prediction is small since the yields and statistical uncertainties in the electron CRs are scaled by $R^{\mathrm{sim}}_{\gamma/\mathrm{e}} \ll 1$. The statistical uncertainties in the distributions obtained by matching the reconstructed photon to a generated electron depend on the contribution of the different MC samples to a certain bin. Bins with a large statistical uncertainty contain simulated events with large weights.
Validation plots for $p^{\mathrm{miss}}_{\mathrm{T}}$, $\mathrm{M_T}$, and $p_{\mathrm{T}}(\gamma)$ using the same selections are provided in Appendix C.

8.4 Vector boson and photon-plus-jets production

As shown in Fig. 8.1, the most important background of the analysis is $\mathrm{V}(\gamma)$, where $\mathrm{V}(\gamma)$ represents the composition of $\mathrm{W}^{\pm}$ boson and Z boson production, with and without photon radiation, the latter having a significantly smaller contribution. The ratio of $\mathrm{Z}\gamma \to \nu\bar{\nu}\gamma$ to $\mathrm{W}^{\pm}\gamma \to \mathrm{l}^{\pm}\nu\gamma$ events in the SR is approximately 3:2. For Z boson production, only the $\mathrm{Z} \to \nu\bar{\nu}$, while for $\mathrm{W}^{\pm}$ boson production only the $\mathrm{W}^{\pm} \to \mathrm{l}^{\pm}\nu$ decay channels contribute due to the neutrino(s) causing a significant amount of $p^{\mathrm{miss}}_{\mathrm{T}}$. To increase the precision in the prediction, the MC simulations of these processes are fitted to data in the fit control region defined in Section 7.4.1. Since $\gamma +$ jets also has a large contribution to

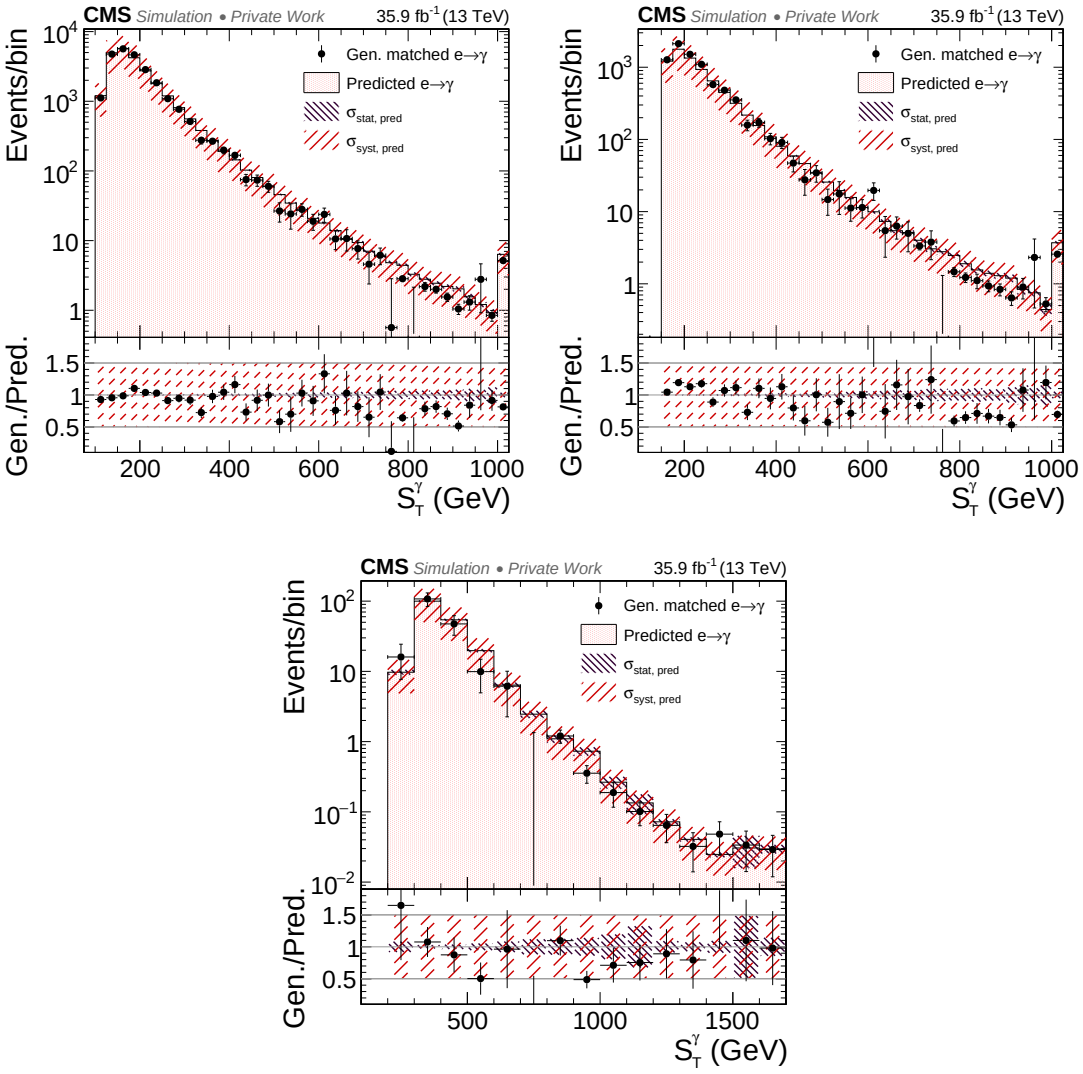

Figure 8.2: Validation plots for the e $\rightarrow \gamma$ background estimation method as a function of S_T^γ applying the preselection, but requiring $p_T(\gamma) > 100\,\text{GeV}$ (top left), additionally requiring $p_T^{\text{miss}} > 50\,\text{GeV}$ and $M_T > 50\,\text{GeV}$ (top right), and in the fit control region (bottom).

the fit control region, V(γ) and γ+jets are fitted simultaneously, predominantly to reduce the uncertainty in the scale factor determined for V(γ).

8.4.1 Estimation from Monte-Carlo simulation normalized to data

The fit control region is defined by applying the preselection and additionally requiring $p_{\mathrm{T}}^{\mathrm{miss}} > 100\,\mathrm{GeV}$ and $\mathrm{M_T} > 100\,\mathrm{GeV}$, but excluding the validation and signal region. These criteria are chosen to meet the following aspects:

- The precision of the scale factor is limited by the statistical precision of the fit sample and the systematic uncertainties in the shape predicted by the MC simulation. The systematic uncertainties in the shape cannot be decreased, but the statistical uncertainty can be reduced by a large data set in the fit CR.
- In the fit, the overall normalization is fixed. Since two backgrounds are fitted simultaneously, both fit components should have a statistically significant and balanced contribution to the fit sample to reliably determine both scale factors.
- The remaining, non-floating backgrounds should aggregate a small relative amount of events in the fit sample to ensure a small influence of the uncertainty in the fixed backgrounds on the fit result.
- In the case of presence of SUSY in data, the scale factors for the floating backgrounds would be overestimated by the fit if the signal has a significant contribution to the fit CR. Therefore, the phase space should be chosen such that the amount of expected SUSY events is small compared to the total SM background.

The two floating backgrounds in the fit are $\mathrm{V}(\gamma)$ and $\gamma+\mathrm{jets}$, while the fixed background is composed of $\mathrm{t\bar{t}}(\gamma)$, $\mathrm{e} \to \gamma$, and diboson production. There are 12,752 data events in the fit CR ensuring a high statistical precision of the fit. Prior to the fit, the floating backgrounds $\mathrm{V}(\gamma)$ and γ+jets constitute 3940 and 4265 events to the fit CR, while the fixed backgrounds only add up to 1493 events. Hence, a good balance of $\mathrm{V}(\gamma)$ and γ+jets events is achieved and the fixed backgrounds only make up for 18% of the pre-fit background contribution and only 12% of the post-fit integral.

The template variable, i.e., the variable used for the fit, is $|\Delta\phi(\vec{p}_{\mathrm{T}}^{\,\mathrm{miss}}, \text{nearest jet}/\gamma)|$ and is shown in Fig. 8.3 for data, $\gamma+\mathrm{jets}$ (blue line), and $\mathrm{V}(\gamma)$ (orange line), as well as the TChiWg benchmark signal point. In this distribution, the main backgrounds $\gamma+\mathrm{jets}$ and $\mathrm{V}(\gamma)$ have different shapes. In $\gamma+\mathrm{jets}$ events no genuine $p_{\mathrm{T}}^{\mathrm{miss}}$ is expected. To populate the fit CR, at least one jet has to be significantly mismeasured. Therefore, in $\gamma+\mathrm{jets}$ events $p_{\mathrm{T}}^{\mathrm{miss}}$ tends to be aligned with a jet. Furthermore, besides the presence of a reconstructed photon, a higher jet activity is expected. This increases the probability that one object close to the direction of $p_{\mathrm{T}}^{\mathrm{miss}}$ is found. In contrast to that, the $\mathrm{V}(\gamma)$ events show a rather uniform distribution, with a slight tendency towards a back-to-back signature in $|\Delta\phi(\vec{p}_{\mathrm{T}}^{\,\mathrm{miss}}, \text{nearest jet}/\gamma)|$. In those events, where the $p_{\mathrm{T}}^{\mathrm{miss}}$ is back-to-back to the nearest object, no jet is reconstructed and the photon from ISR boosts the system containing the neutrinos (genuine $p_{\mathrm{T}}^{\mathrm{miss}}$) in the opposite direction in the ϕ-plane due to momentum balance. A different shape of the floating backgrounds is essential and ensures that scaling one background cannot compensate the other.

The expected contribution of the TChiWg benchmark signal point, which has a larger contribution to the fit CR compared to the T5Wg benchmark point, see also Fig. 7.3, is shown in Fig. 8.3, where the right plot equals the left plot but with a logarithmic y-axis scale to improve visualization. The plot illustrates that the scale factors determined for V(γ) and γ + jets would not be affected by the presence of the benchmark signal point. Signal scenarios with small sparticle masses can have similar kinematic properties compared to SM background processes leading to an increase of the signal contamination. For the calculation of the SUSY upper cross section limits the amount of overestimated V(γ) and γ + jets events in case of presence of the respective SUSY scenario in data is subtracted from the expected signal yield.

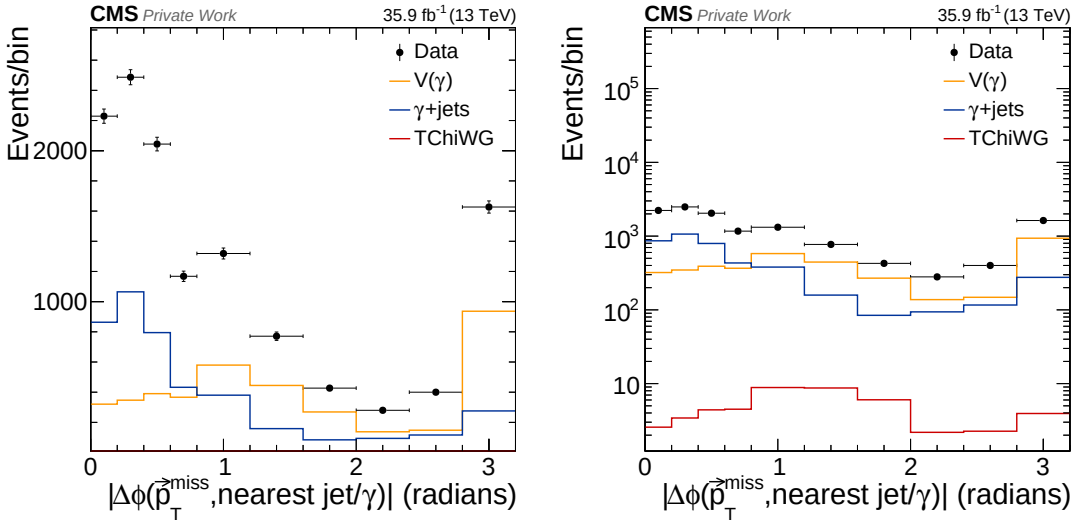

Figure 8.3: Pre-fit distributions of the data, V(γ) (orange line), γ + jets (blue line), and the TChiWg benchmark signal point (red line) for $|\Delta\phi(\vec{p}_{\mathrm{T}}^{\,\mathrm{miss}}, \text{nearest jet}/\gamma)|$ in the fit control region. The right plot shows the left plot with logarithmic y-axis scale to better illustrate the small contribution of a possible SUSY signal.

A χ^2-fit is performed to derive scale factors for the two floating background components. The fit is constrained to a fixed total scale determined by the integral of measured events in the fit CR, reducing the complexity of the fit to one dimension. Under this constraint, varying the scale factor for one floating background determines the scale factor of the other.

Let n_{data}, n_{fixed}, $n_{\mathrm{V}(\gamma)}^{\mathrm{before}}$, and $n_{\gamma+\mathrm{jets}}^{\mathrm{before}}$ be the number of measured events and the pre-fit integrals of the fixed, the V(γ), and the γ + jets background in the fit CR, respectively. Then, the total scale factor $\mathcal{SF}_{\mathrm{total}}$ is given by

$$\mathcal{SF}_{\mathrm{total}} = \frac{n_{\mathrm{data}} - n_{\mathrm{fixed}}}{n_{\mathrm{V}(\gamma)}^{\mathrm{before}} + n_{\gamma+\mathrm{jets}}^{\mathrm{before}}}. \tag{8.7}$$

Let V(γ) be the background component for which its scale factor $\mathcal{SF}_{\mathrm{V}(\gamma)}$ is iteratively varied. Then, the scale factor for $\gamma+\mathrm{jets}$ is given by

$$\mathcal{SF}_{\gamma+\mathrm{jets}} = \frac{\mathcal{SF}_{\mathrm{total}} \cdot (n^{\mathrm{before}}_{\mathrm{V}(\gamma)} + n^{\mathrm{before}}_{\gamma+\mathrm{jets}}) - \mathcal{SF}_{\mathrm{V}(\gamma)} \cdot n^{\mathrm{before}}_{\mathrm{V}(\gamma)}}{n^{\mathrm{before}}_{\gamma+\mathrm{jets}}}. \tag{8.8}$$

By this definition, the total number of predicted events always equals the integral of measured events in the fit CR, but due to the different shapes of the floating backgrounds, the bin-by-bin deviation between prediction and data varies.

The scale factor for V(γ) is varied in steps of 0.02 and for each combination of scale factors all background components are added up and a bin-wise χ^2-test is performed between the data histogram and the background prediction. For the χ^2-test calculation, the `ROOT` routine `Chi2Test` is used [187]. The χ^2-values for all combinations are plotted against $\mathcal{SF}_{\mathrm{V}(\gamma)}$. The resulting distribution is fitted by a parabola, as shown in Fig. 8.4 (left). The minimum of the parabola determines the best fit scale factor for V(γ). The absolute statistical uncertainty of the best fit value is given by the range corresponding to the χ^2-value of the minimum increased by unity projected onto the $\mathcal{SF}_{\mathrm{V}(\gamma)}$-axis, as illustrated in Fig. 8.4.

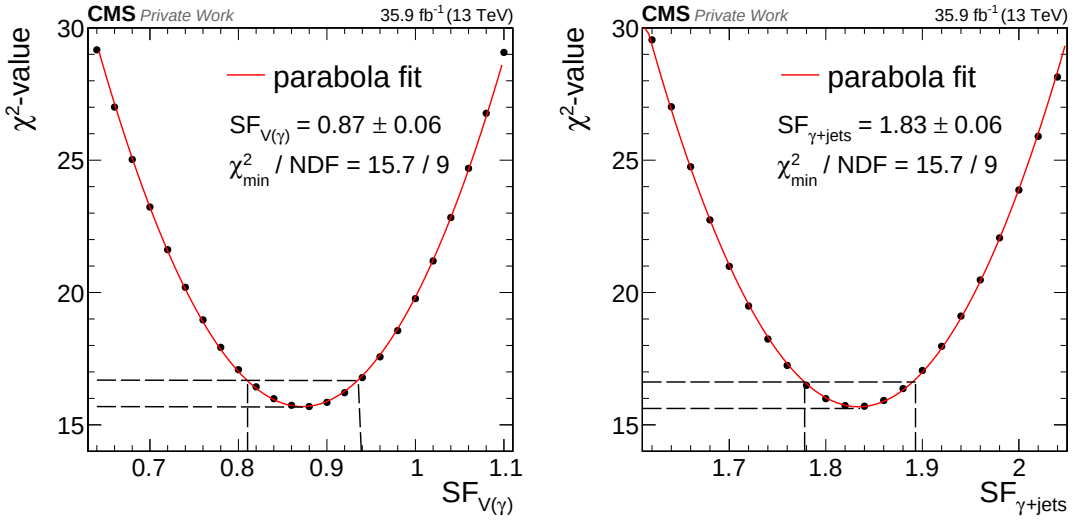

Figure 8.4: Resulting χ^2-values of the fit iteratively varying $\mathcal{SF}_{\mathrm{V}(\gamma)}$ (left) and $\mathcal{SF}_{\gamma+\mathrm{jets}}$ (right) in steps of 0.02. The best fit value is determined by minimizing the parabola fitted to the χ^2-distribution. The statistical uncertainty of the fit value is given by the range projected onto the scale factor axis that corresponds to the χ^2-value of the best fit value increased by unity.

The same procedure is repeated iteratively varying $\mathcal{SF}_{\gamma+\mathrm{jets}}$ in steps of 0.02. While the best fit value for $\mathcal{SF}_{\gamma+\mathrm{jets}}$ is already determined by the best fit value of $\mathcal{SF}_{\mathrm{V}(\gamma)}$, compare Eq. (8.8), a second iteration is performed to ensure a similar precision in the parabola fit, i.e., the determination of the best fit value.

The number of degrees of freedom (NDF) is given by the number of comparisons between the measurement and prediction, reduced by the number of estimators in the fit. Since the only free parameter in the fit is the ratio of $\mathcal{SF}_{\mathrm{V}(\gamma)}$ to $\mathcal{SF}_{\gamma+\mathrm{jets}}$, NDF is given by the number of bins used in the fit reduced by unity. The best fit values correspond to $\chi^2/\mathrm{NDF} = 15.7/9$ and result in the scale factors

$$\begin{aligned} \mathcal{SF}_{\mathrm{V}(\gamma)} &= 0.87 \pm 0.06 \text{ and} \\ \mathcal{SF}_{\gamma+\mathrm{jets}} &= 1.83 \pm 0.06, \end{aligned} \tag{8.9}$$

where the uncertainties are of statistical origin only. In the subsequent analysis, the statistical fit errors enter as systematic uncertainties. As shown in Fig. 8.1, the contribution of $\gamma + \mathrm{jets}$ to the signal region is almost negligible. Studies have shown that varying the correlation of the fit uncertainties between $\mathrm{V}\gamma$ and $\gamma + \mathrm{jets}$ from uncorrelated to 100% anti-correlated has no impact on the final results. Therefore, the uncertainties are treated as uncorrelated for simplicity.

The fit results meet the expectation. As introduced in Section 5.3, the $\mathrm{V}\gamma$ samples are scaled to their NNLO cross sections, while the $\mathrm{W}^{\pm} \to \mathrm{l}^{\pm}\nu$ and $\mathrm{Z} \to \nu\bar{\nu}$ samples are scaled to NLO prior to the fit, where the higher orders are corrections in QCD. EWK higher-order corrections are expected to lower the signal cross section. Therefore, a scale factor close to, but smaller than unity is expected. The $\gamma + \mathrm{jets}$ sample is only scaled to LO cross section, so large corrections that might increase the cross section by a factor of two or more are expected, as also discussed in the first paragraph of Section 9.2.4 in [6]. The predecessor analysis obtained comparable results using a similar phase space [1].

Figure 8.5 shows the post-fit distribution in the fit CR. Besides the data, the total fit result (red line) and the individual components of the fit, $\mathrm{V}(\gamma)$ (orange line), $\gamma+\mathrm{jets}$ (blue line), and the fixed background (magenta area), are shown. The total fit shows a good description of the measured distribution. The ratio (Data-Fit)/σ_{stat} in the bottom panel of the plot only relates the deviations to the statistical uncertainty, where some bins show variations up to a factor of two. Eventhough these variations are not significant, studies of the systematic uncertainties in the shape of the MC simulations were performed and found to cover these deviations, as reported in the next section.

8.4.2 Systematic uncertainties in the shape

All uncertainties that would affect the normalization of the $\mathrm{V}(\gamma)$ and $\gamma+\mathrm{jets}$ backgrounds are eliminated by the MC normalization method. Systematic uncertainties in these backgrounds arise only from the simulated shape.

Jet energy scale

Although jets are not a central feature of the event selection, the analysis is affected by the propagation of the jet energy scale (JES) to $p_{\mathrm{T}}^{\mathrm{miss}}$. The resulting uncertainty in the

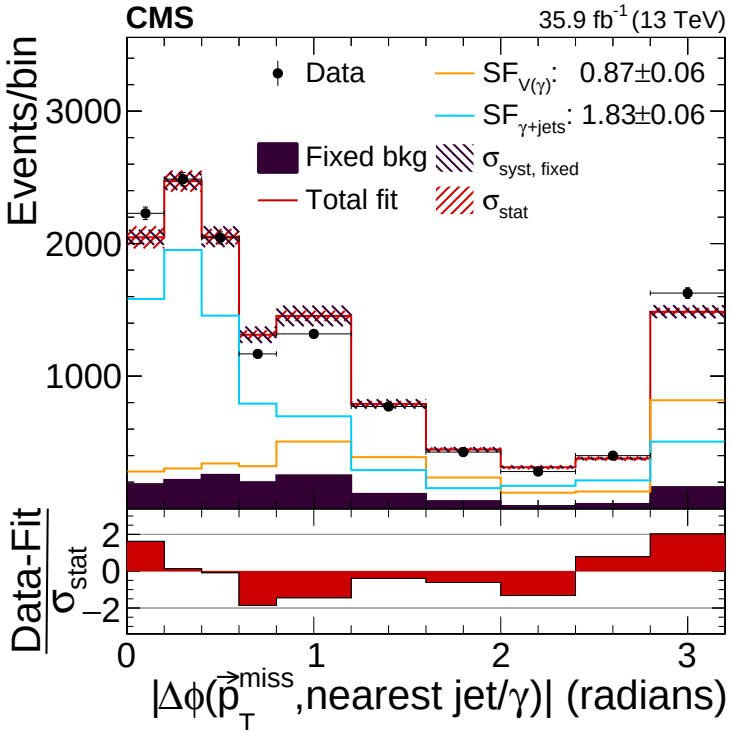

Figure 8.5: Post-fit distributions for γ+jets (blue line) and V(γ) (orange line) together with the fixed background (magenta area) and the total fit distribution (red line). The statistical uncertainty of the post-fit distribution is shown in the red hatched area and the systematic uncertainty of the fixed background is indicated by the magenta hatched area. The values in the legend are the resulting best fit values for $\mathcal{SF}_{\mathrm{V}(\gamma)}$ and $\mathcal{SF}_{\gamma+\mathrm{jets}}$. The total fit shows a good agreement between measurement and prediction. The ratio plot shows the difference of the data and the post-fit yields normalized to their combined statistical uncertainty only.

background prediction in the SR is determined by propagating a shifted JES to $p_{\mathrm{T}}^{\mathrm{miss}}$ and repeating the analysis. The shift is given by shifting the JES upwards and downwards by its uncertainty. To study the effect of the uncertainty, the whole event selection is applied using the shifted $p_{\mathrm{T}}^{\mathrm{miss}}$, new scale factors are derived for the V(γ) and $\gamma+$jets background in the fit CR, and the new background prediction is compared to the nominal prediction in the $\mathrm{S}_{\mathrm{T}}^{\gamma}$ distribution in the SR bin-by-bin, as shown in Fig. 8.6. The determination of the new scale factors ensures that the uncertainty in the normalization is canceled. The scale factors fitted using the nominal and the shifted JES are listed in Table 8.1, while the absolute and relative deviations from the nominal predictions are shown in Table 8.2 for each bin in the SR separately. The largest deviation in the prediction of the respective bin is taken as symmetric systematic uncertainty and varies from $5.0-5.9\%$ for V(γ) and $0.9-32.3\%$ for $\gamma+$jets. The large deviation of 32.3% for $\gamma+$jets affects the highest

bin in S_T^γ, where only approximately one γ + jets event is expected, so that compared to a total of approximately 18 expected SM background events the absolute effect on the uncertainty in the background prediction is small.

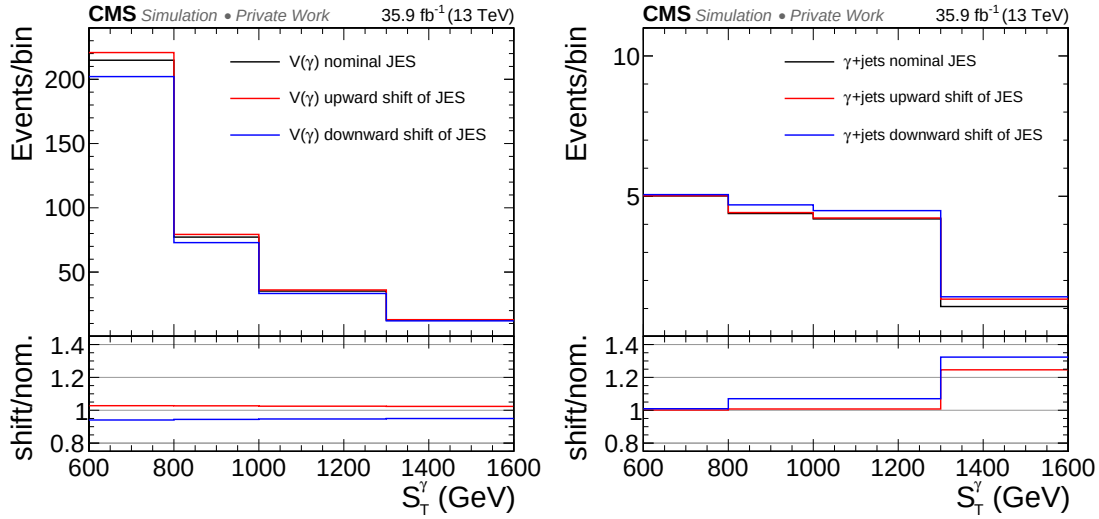

Figure 8.6: Illustration of the effect on the prediction of S_T^γ in the signal region for V(γ) (left) and γ + jets (right) shifting the jet energy scale (JES) up and down by its uncertainty and its propagation to p_T^{miss}.

Table 8.1: Nominal scale factor fit results for the V(γ) and γ + jets backgrounds together with the scale factors determined by shifting the JES down and up by its uncertainty.

JES	$\mathcal{SF}_{\text{V}(\gamma)}$	$\mathcal{SF}_{\gamma+\text{jets}}$
nominal	0.87	1.83
down	0.89	1.85
up	0.83	1.96

Table 8.2: Absolute (abs.) and relative (rel.) deviations from the nominal prediction for V(γ) and γ + jets in the four signal region bins shifting the JES down and up by its uncertainty.

		S_T^γ :							
		600 − 800 GeV		800 − 1000 GeV		1000 − 1300 GeV		> 1300 GeV	
	JES	abs.	rel.	abs.	rel.	abs.	rel.	abs.	rel.
V(γ)	down	5.97	2.8%	2.08	2.7%	0.87	2.5%	0.30	2.3%
	up	-12.74	-5.9%	-4.30	-5.6%	-1.87	-5.3%	-0.64	-5.0%
γ + jets	down	0.01	0.1%	0.03	0.8%	0.03	0.8%	0.26	24.6%
	up	0.05	0.9%	0.31	7.0%	0.29	7.0%	0.35	32.3%

Renormalization and factorization scales

The shape uncertainty due to the choice of the renormalization and factorization scales μ_R and μ_F is determined by varying these scales in different combinations of the factors 0.5, 1, and 2 and refitting the V(γ) and $\gamma+$jets backgrounds with the same procedure as described above. The scale factors fitted for each combination are listed in Table 8.3. The deviations from the nominal scale factors indicate the magnitude of the uncertainty that arise from the uncertainty in the normalization of the simulated sample. The prediction for each combination is compared in the four signal region bins for both backgrounds separately and bin-by-bin and the results are given in Table 8.4 and Table 8.5 for the V(γ) and $\gamma+$jets background, respectively. The relative deviations from the nominal prediction are illustrated in Fig. 8.7. For V(γ), the variation in μ_F has a larger impact compared to the variation in μ_R, whereas the impact is of similar magnitude for $\gamma+$jets. The largest deviation in the respective bin is taken as systematic uncertainty and varies between $3.8-9.0\%$ and $2.8-7.1\%$ for V(γ) and $\gamma+$jets, respectively.

Table 8.3: Nominal scale factor fit results for the V(γ) and $\gamma+$jets backgrounds, indicated by the combination (1,1), together with the scale factors determined using renormalization (μ_R) and factorization (μ_F) scales varied by combinations of the factors 0.5, 1, and 2.

Factors (μ_R,μ_F)	$\mathcal{SF}_{\mathrm{V}(\gamma)}$	$\mathcal{SF}_{\gamma+\mathrm{jets}}$
(1,1)	0.87	1.83
(1,2)	0.89	1.95
(1,0.5)	0.85	1.72
(2,1)	0.89	2.03
(2,2)	0.91	2.16
(2,0.5)	0.88	1.89
(0.5,1)	0.84	1.65
(0.5,2)	0.86	1.75
(0.5,0.5)	0.83	1.55

Parton distribution functions

A similar procedure is used to determine the shape uncertainty due to the choice of the PDFs, where 100 replicas of each PDF are used to rescale the MC simulation [188]. The standard deviation with respect to the mean prediction of all 100 variations is determined bin-by-bin in the signal region and is taken as systematic uncertainty, varying between $1.6-3.8\%$ for V(γ) and $1.9-8.2\%$ for $\gamma+$jets. The results are illustrated in Fig. 8.8. Table 8.6 shows the absolute and relative deviations with respect to the mean determined based on the 100 replicas of the PDFs for V(γ) and $\gamma+$jets. Detailed tables showing the respective scale factors and deviations from the nominal prediction can be found in Tables D.1−D.6 in the appendix for each PDF replica.

Table 8.4: Absolute (abs.) and relative (rel.) deviations from the nominal prediction for V(γ) in the four signal region bins using renormalization (μ_R) and factorization (μ_F) scales varied by combinations of the factors 0.5, 1, and 2.

	S_T^γ :							
V(γ)	600 − 800 GeV		800 − 1000 GeV		1000 − 1300 GeV		> 1300 GeV	
Factors (μ_R,μ_F)	abs.	rel.	abs.	rel.	abs.	rel.	abs.	rel.
(1,2)	-6.71	-3.1%	-3.37	-4.4%	-1.84	-5.2%	-0.83	-6.6%
(1,0.5)	7.90	3.7%	3.99	5.2%	2.20	6.3%	1.00	7.9%
(2,1)	-0.18	-0.1%	0.15	0.2%	0.08	0.2%	0.12	1.0%
(2,2)	-6.94	-3.2%	-3.25	-4.2%	-1.77	-5.1%	-0.72	-5.7%
(2,0.5)	7.80	3.6%	4.19	5.5%	2.30	6.6%	1.14	9.0%
(0.5,1)	0.35	0.2%	-0.14	-0.2%	-0.08	-0.2%	-0.13	-1.1%
(0.5,2)	-6.25	-2.9%	-3.45	-4.5%	-1.89	-5.4%	-0.94	-7.5%
(0.5,0.5)	8.12	3.8%	3.79	4.9%	2.09	6.0%	0.84	6.7%

Table 8.5: Absolute (abs.) and relative (rel.) deviations from the nominal prediction for γ + jets in the four signal region bins using renormalization (μ_R) and factorization (μ_F) scales varied by combinations of the factors 0.5, 1, and 2.

	S_T^γ :							
γ + jets	600 − 800 GeV		800 − 1000 GeV		1000 − 1300 GeV		> 1300 GeV	
Factors (μ_R,μ_F)	abs.	rel.	abs.	rel.	abs.	rel.	abs.	rel.
(1,2)	-0.15	-3.1%	-0.04	-0.9%	-0.10	-2.5%	-0.04	-4.1%
(1,0.5)	0.18	3.7%	0.04	1.0%	0.11	2.7%	0.05	4.6%
(2,1)	0.08	1.6%	0.07	1.7%	0.11	2.7%	0.03	2.5%
(2,2)	-0.08	-1.6%	0.03	0.7%	0.01	0.2%	-0.02	-1.6%
(2,0.5)	0.26	5.2%	0.11	2.5%	0.22	5.3%	0.08	7.1%
(0.5,1)	-0.07	-1.3%	-0.07	-1.6%	-0.11	-2.7%	-0.03	-2.6%
(0.5,2)	-0.23	-4.7%	-0.12	-2.8%	-0.23	-5.5%	-0.07	-6.9%
(0.5,0.5)	0.13	2.7%	-0.01	-0.2%	0.02	0.4%	0.03	2.4%

8.4.3 Validation of the normalization method

To increase confidence in the background estimation method, especially for the most dominant background V(γ), several validation studies are performed. The binning of the template distribution $|\Delta\phi(\vec{p}_{\mathrm{T}}^{\,\mathrm{miss}}, \text{nearest jet}/\gamma)|$ in the fit CR is varied using both different number of bins and different bin widths. Furthermore, different template variables are used for the fit, as well as altering fit CR definitions.

Since V(γ) and γ + jets are the dominant backgrounds in the fit CR, checking the agreement between the total SM background prediction and the data for several kinemat-

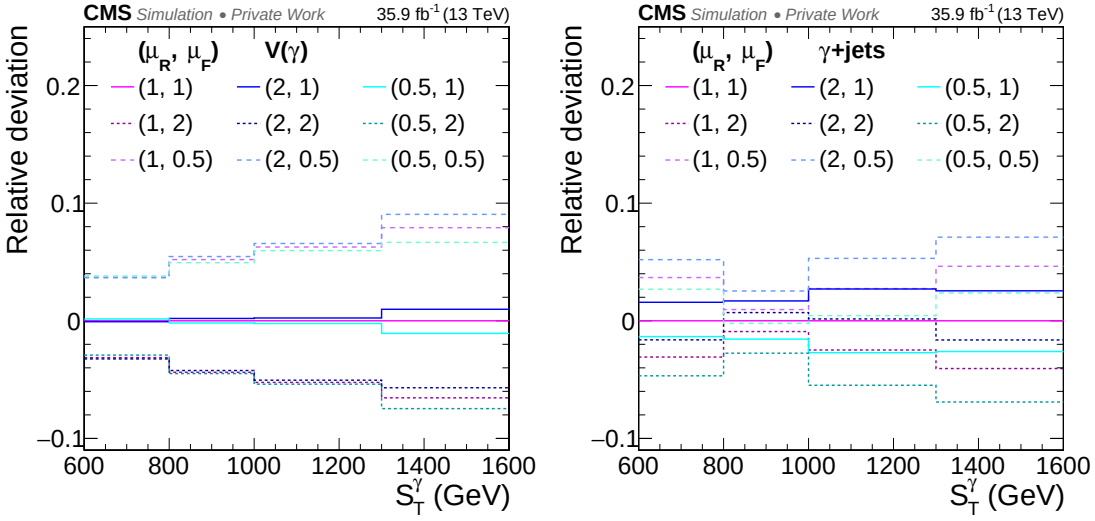

Figure 8.7: Relative deviation in the predicted yields as a function of S_T^γ in the signal region for V(γ) (left) and γ + jets (right) using different combinations of the renormalization scale (μ_R) and the factorization scale (μ_F) varied by the factors 0.5, 1, and 2.

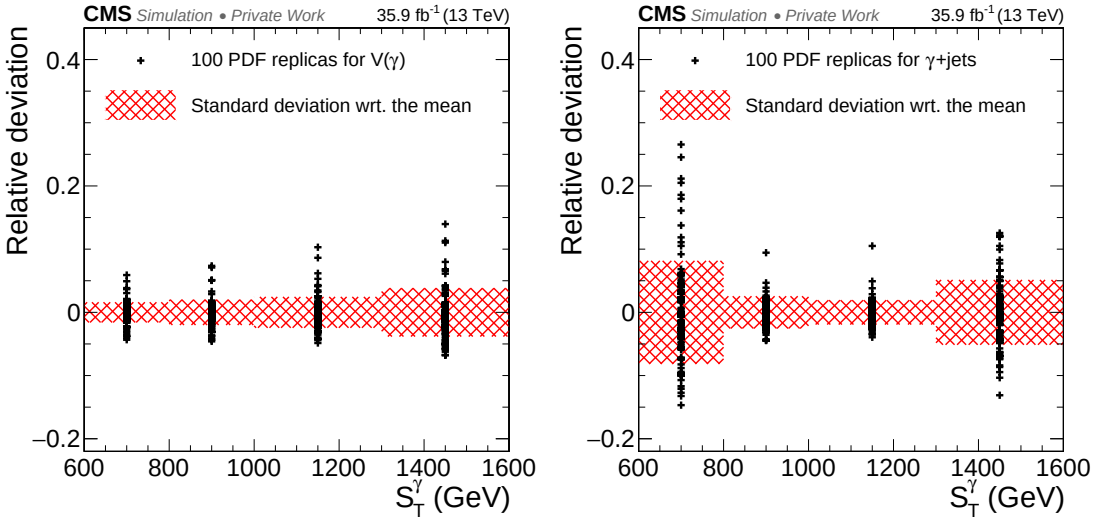

Figure 8.8: Relative deviations in the predicted yields as a function of S_T^γ in the signal region bins for V(γ) (left) and γ + jets (right) using 100 different replicas of the PDFs (black points) and their standard deviations (red area) with respect to the mean of the variations.

ically independent variables is an important test for the stability of the normalization method. This and background-to-data comparisons in the VR, where V(γ) has the largest contribution of all backgrounds, is presented in Section 8.5.

Table 8.6: Absolute (abs.) and relative (rel.) deviations from the predictions of V(γ) and γ + jets in the four signal region bins with respect to the standard deviation of the variations using 100 replicas of the PDFs.

	S_T^γ :							
	600 − 800 GeV		800 − 1000 GeV		1000 − 1300 GeV		> 1300 GeV	
	abs.	rel.	abs.	rel.	abs.	rel.	abs.	rel.
V(γ)	3.41	1.6%	1.54	2.0%	0.86	2.4%	0.48	3.8%
γ + jets	0.41	8.2%	0.11	2.6%	0.08	1.9%	0.05	5.1%

Varied binning of the fit template variable

Besides the systematic uncertainties due to the shape prediction of the simulated samples, the fit results of the MC normalization method underlie statistical fluctuations. To validate that these fluctuations are covered by the statistical uncertainty determined in the fit, the binning of the template variable is altered, varying both the number of bins and the bin widths. Thus, the population of events per bin is varied. The result of these variations is summarized in Fig. 8.9. The lines and darker, inner error bands correspond to the nominal fit values used in the analysis and their uncertainties, respectively. The lighter, outer error bands correspond to the squared sum of the fit uncertainty and the systematic shape uncertainties discussed in the previous section. The systematic uncertainties are chosen to equal the systematic uncertainties determined for the lowest S_T^γ bin of the SR, since this bin has the best statistical precision and the phase space is closest to the fit CR and the VR. The number of bins used for the fit is shown in the left column, together with the interval borders in $|\Delta\phi(\vec{p}_T^{\,\text{miss}}, \text{nearest jet}/\gamma)|$ with same bin widths stated in the curved brackets and the corresponding bin widths stated in the squared brackets. Thus, the first row "20 bins: {0, 0.8, 3.2}, [0.1, 0.2]" means that in total 20 bins are used in the fit, where a bin width of 0.1 is used between 0.0 and 0.8 in $|\Delta\phi(\vec{p}_T^{\,\text{miss}}, \text{nearest jet}/\gamma)|$, and a bin width of 0.2 is used between 0.8 and 3.2. The studies show that the scale factors agree well within the statistical uncertainties regardless of the chosen binning.

Altering template variables and fit control regions

The scale factors for V(γ) and γ + jets are determined in the fit CR using the template variable $|\Delta\phi(\vec{p}_T^{\,\text{miss}}, \text{nearest jet}/\gamma)|$. To check the stability of the method, the phase space used for the fit is altered by changing the lower and upper bounds in M_T and p_T^{miss} defining the fit CR, or imposing an additional requirement on the nominal fit CR. By this, several different, partially overlapping phase spaces are used to determine scale factors for the V(γ) and γ + jets simulation. Also, different template variables are used for the fit. The results are summarized in Fig. 8.10.

The first column of Fig. 8.10 shows the definition of the CR and the template variable used for the fit. The requirements are in addition to the preselection. In all cases,

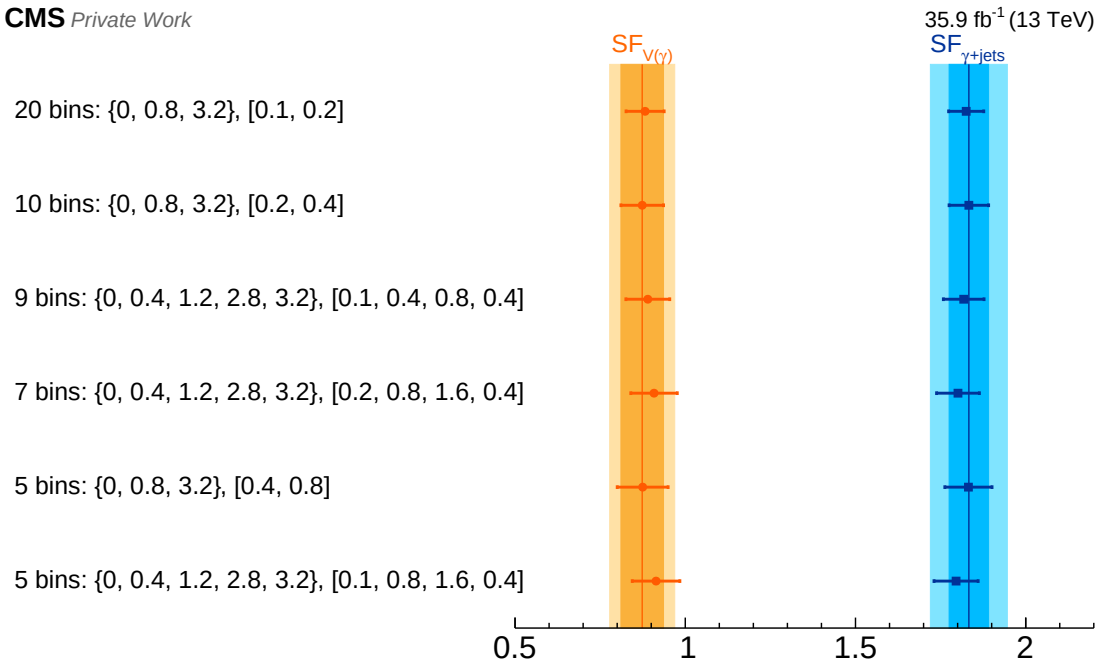

Figure 8.9: Fit results for different binnings of the template variable $|\Delta\phi(\vec{p}_{\mathrm{T}}^{\,\mathrm{miss}}, \text{nearest jet}/\gamma)|$ in the fit control region. The lines and darker, inner error bands correspond to the nominal fit results, the lighter, outer error bands correspond to the squared sum of the fit uncertainty and all other systematic uncertainties arising from the variation of the factorization and renormalization scales, using different PDF weights and shifting the JES by its uncertainty, as described in Section 8.4.2. The notation used in the left column is explained in the text.

the first and second requirement states the lower bound on $p_{\mathrm{T}}^{\mathrm{miss}}$ and $\mathrm{M_T}$, respectively. The third requirement represents the two dimensional definition in the $\mathrm{M_T}$-$p_{\mathrm{T}}^{\mathrm{miss}}$ phase space, similarly to the definition illustrated in Fig. 7.3. In some cases there is a fourth selection requirement stated as "$\mathrm{N_{jets}} < 3$", "$\mathrm{N_{e,\mu}} = 1$", or "$\mathrm{N_{b\ jet}} = 0$", representing the additional requirement of "number of jets lower than three", "exactly one electron or muon", or "zero b jets", respectively. The notation "JES down" or "JES up" means that $p_{\mathrm{T}}^{\mathrm{miss}}$ calculated with a jet energy scale shifted by its uncertainty is used. Behind the colon, the template variable is stated. In several cases $|\Delta\phi(\vec{p}_{\mathrm{T}}^{\,\mathrm{miss}}, \mathrm{jet_1})|$ is used as cross check template variable, as this distribution was used as fit variable in the analysis SUS-16-023. For all cross checks, sufficient agreement is observed within the uncertainties.

The largest deviation is observed in the phase space where the presence of exactly one electron or muon is required. Several aspects may result in this deviation: For one, the requirement of the presence of one e or μ significantly changes the subset of data populating the new fit CR and especially the relation of the contributing backgrounds.

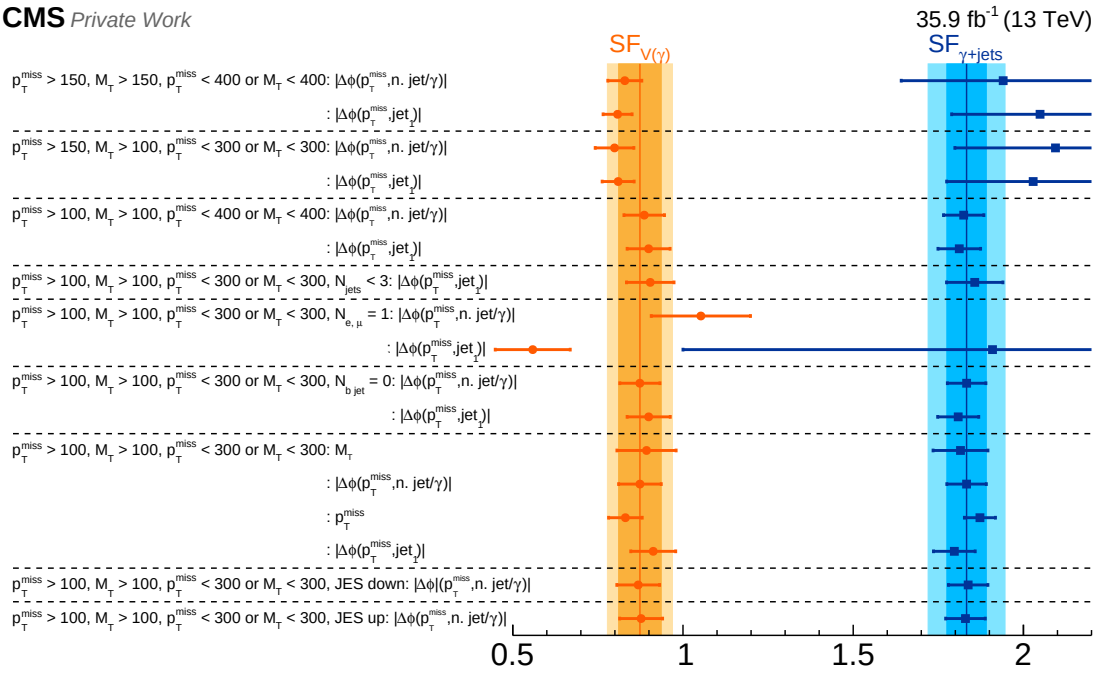

Figure 8.10: Fit results for different control region definitions and different template variables, sorted by the corresponding selections. The lines and darker, inner error bands correspond to the nominal fit results, the lighter, outer error bands correspond to the squared sum of the fit uncertainty and all other systematic uncertainties arising from the variation of the factorization and renormalization scale, using different PDF weights and shifting the JES by its uncertainty, as described in Section 8.4.2. In the region where one electron or muon is required especially the scale factor for $\gamma+$jets cannot be determined reliably and the visualization of the fit results for these cases are adjusted in the plot to improve the readability. See text for more details. All values for $p_{\mathrm{T}}^{\mathrm{miss}}$ and $\mathrm{M_T}$ are given in GeV.

The nominal fit CR and fit variable are tuned to determine scale factors for the V(γ) and $\gamma+$jets backgrounds. Requiring one charged lepton, the $\gamma+$jets background is almost completely eliminated (see Fig. 8.11). The fixed background, which is very subdominant in the nominal fit CR, becomes almost as significant as the V(γ) background. To determine a reliable scale factor in this phase space, the fixed background would have to be allowed to vary, too. In addition, the fixed and the V(γ) background have almost the same shape using $|\Delta\phi(\vec{p}_{\mathrm{T}}^{\,\mathrm{miss}}, \text{nearest jet}/\gamma)|$ or $|\Delta\phi(\vec{p}_{\mathrm{T}}^{\,\mathrm{miss}}, \mathrm{jet}_1)|$, which disables the reliable determination of the V(γ) scale factor. Because of the constraint of a fixed total scale, the two fitted scale factors behave anti-correlated. If the fixed background was allowed to vary, an increase of the V(γ) scale factor would result in a decrease of the scale factor for the fixed background, especially because of the similar shapes of those two background categories. This would result in a small variation of the χ^2-value over a

larger variation of scale factors, leading to much larger uncertainties in the minimum of the χ^2-distribution, i.e., the respective scale factor. Therefore, also the determined uncertainties for the fits in this region are underestimated.

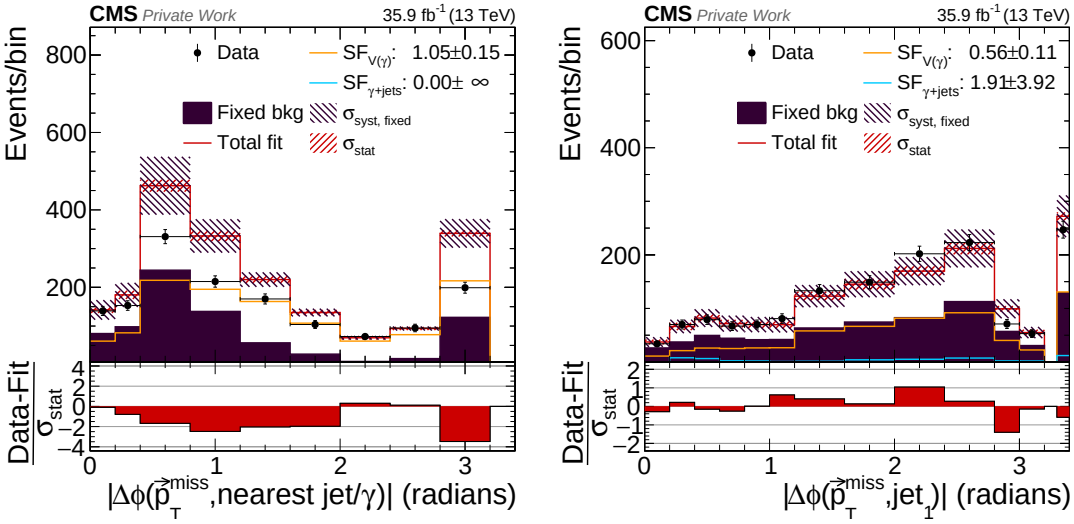

Figure 8.11: Post-fit distributions for γ + jets (blue line), V(γ) (orange line), and the fixed background (magenta area), as well as the total fit distribution (red line) for $|\Delta\phi(\vec{p}_{\mathrm{T}}^{\,\mathrm{miss}}, \text{nearest jet}/\gamma)|$ (left) and $|\Delta\phi(\vec{p}_{\mathrm{T}}^{\,\mathrm{miss}}, \mathrm{jet}_1)|$ (right) applying the selection of the nominal fit control region and additionally requiring exactly one electron or muon. The last bin in $|\Delta\phi(\vec{p}_{\mathrm{T}}^{\,\mathrm{miss}}, \mathrm{jet}_1)|$ is filled by events without any reconstructed jet, also included in the fit. The contribution of γ + jets is negligible, whereas the fixed background is almost as dominant as the V(γ) background. Applying the nominal fit procedure in this phase space leads to unreliable fit results.

8.5 Validation of the total standard model background prediction

After all background components and their estimation methods have been introduced, the total SM background estimation is applied to different distributions in the fit CR and the VR. The VR has the same selection criteria as the SR, but requiring $S_{\mathrm{T}}^{\gamma} < 600\,\mathrm{GeV}$, as this phase space is not sensitive to signal and to ensure the orthogonality to the SR.

Figure 8.12 compares the total SM background prediction to the measurement in the fit CR in the distributions $|\Delta\phi(\vec{p}_{\mathrm{T}}^{\,\mathrm{miss}}, \text{nearest jet}/\gamma)|$ (top left), M_{T} (top right), $p_{\mathrm{T}}(\gamma)$ (bottom left), and $p_{\mathrm{T}}^{\mathrm{miss}}$ (bottom right). All distributions show good agreement and indicate the stability of the prediction.

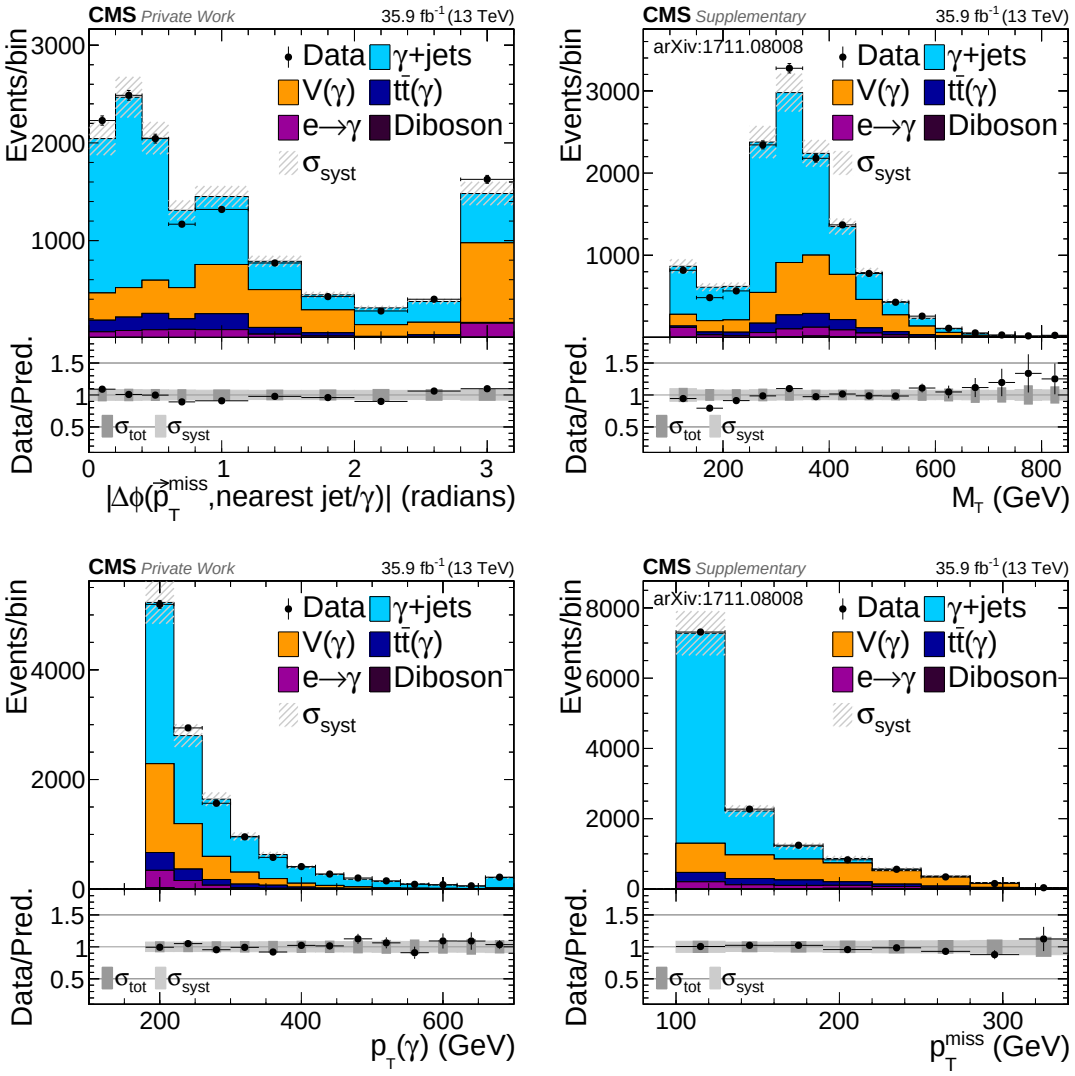

Figure 8.12: Data-to-prediction comparisons in the fit control region. The template fit variable $|\Delta\phi(\vec{p}_{\mathrm{T}}^{\,\mathrm{miss}}, \text{nearest jet}/\gamma)|$ is shown in the top left plot, $\mathrm{M_T}$ and $p_{\mathrm{T}}(\gamma)$ in the top right and bottom left, respectively, and $p_{\mathrm{T}}^{\mathrm{miss}}$ is shown in the bottom right plot. The absolute number of events in data and total standard model background match by definition in this phase space.

Figure 8.13 shows $\mathrm{S_T^\gamma}$, the variable used for the final interpretation of the results in the SR, applying three different selections. The top left plot shows $\mathrm{S_T^\gamma}$ in the fit CR. For the top right plot the same selection is used as for the fit CR, but also requiring $|\Delta\phi(\vec{p}_{\mathrm{T}}^{\,\mathrm{miss}}, \text{nearest jet}/\gamma)| > 1$ to reduce the contribution of γ + jets simultaneously enhancing the relative amount of $\mathrm{V}(\gamma)$ events. The bottom plot shows

S_T^γ in the VR. All three distributions show good agreement between prediction and data.

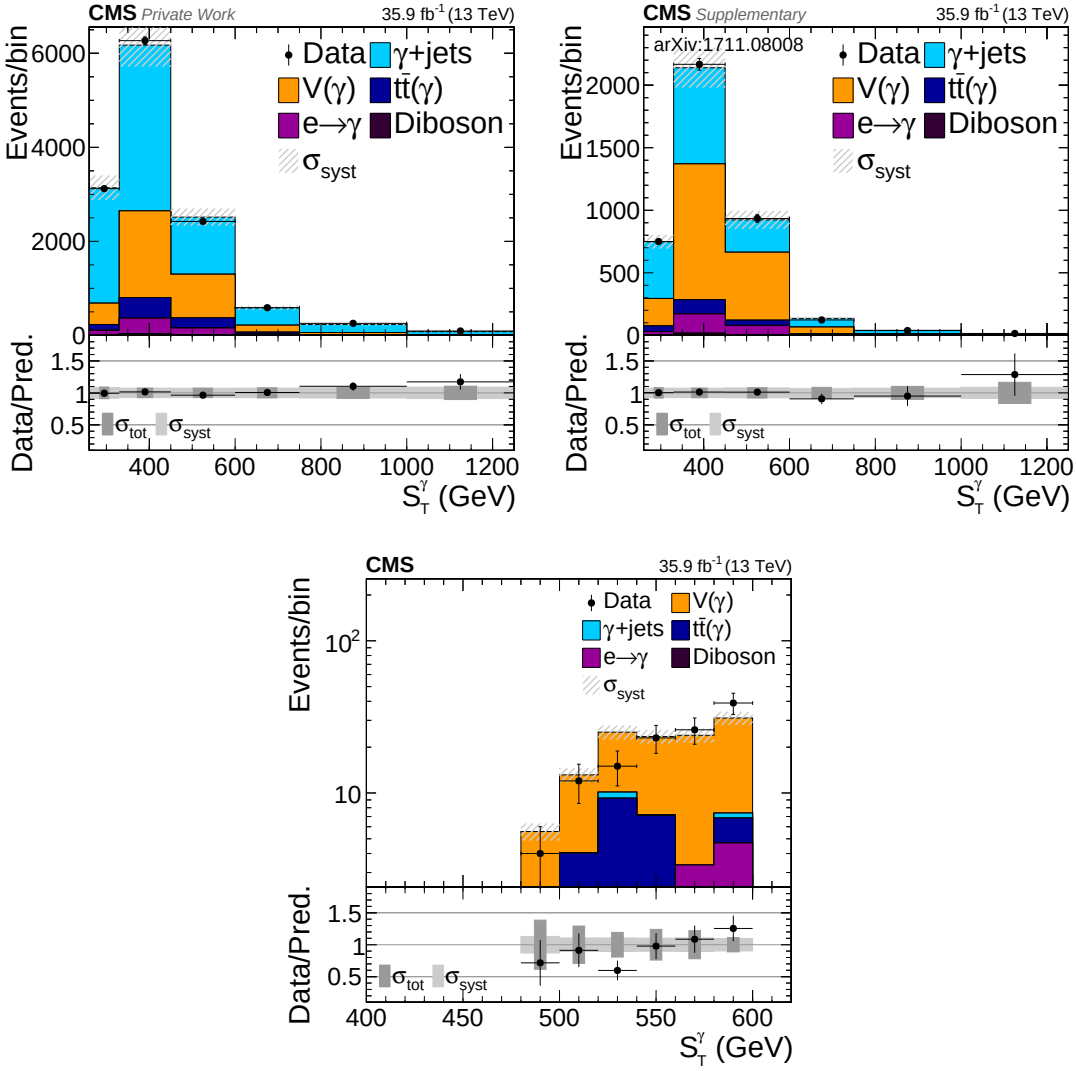

Figure 8.13: Data-to-prediction comparison for S_T^γ in the fit control region (top left), in the fit control region additionally requiring $|\Delta\phi(\vec{p}_T^{\,\text{miss}}, \text{nearest jet}/\gamma)| > 1$ to enhance the relative contribution of V(γ) (top right), and in the validation region (bottom).

Figure 8.14 shows the data-to-prediction comparisons for $|\Delta\phi(\vec{p}_T^{\,\text{miss}}, \text{nearest jet}/\gamma)|$ (top left), M_T (top right), $p_T(\gamma)$ (bottom left), and p_T^{miss} (bottom right) in the VR. As this region only covers the phase space 480 GeV $< S_T^\gamma <$ 600 GeV, the statistical precision of this phase space is small, but still a statement about the agreement of shape and normalization can be made. The plots show that the total SM background prediction

provides a good description of the measurement in the VR. In total, 122 events are measured in the VR, compared to 123 events expected by the total SM background prediction.

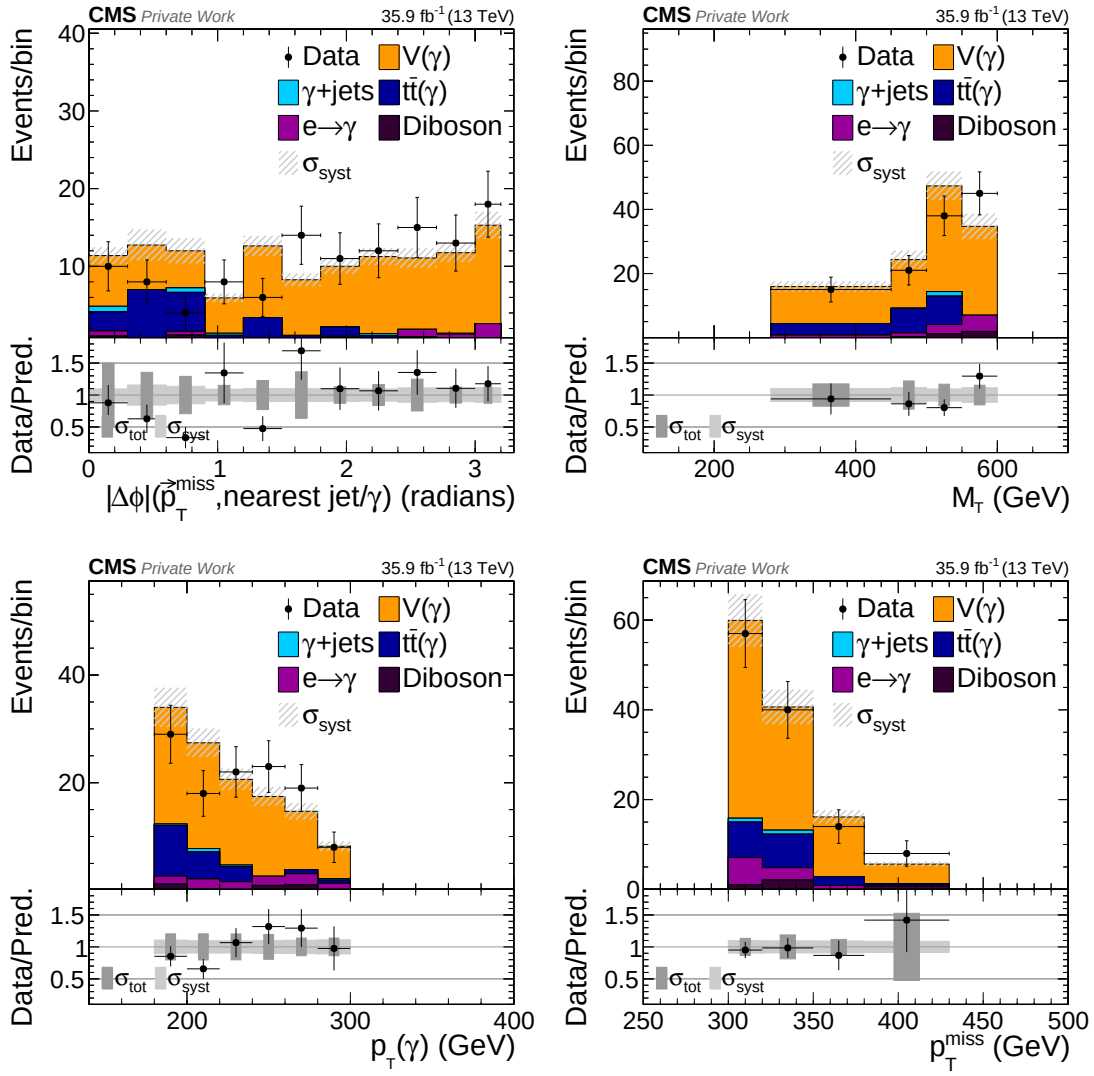

Figure 8.14: Data-to-prediction comparison of several analysis relevant variables in the validation region. The template fit variable $|\Delta\phi(\vec{p}_{\mathrm{T}}^{\,\mathrm{miss}}, \text{nearest jet}/\gamma)|$ is shown in the top left plot, the transverse mass and $p_{\mathrm{T}}(\gamma)$ are shown in the top right and bottom left plot, respectively, and $p_{\mathrm{T}}^{\mathrm{miss}}$ is shown in the bottom right plot. Both the normalization and the shape of the data are well described by the SM background prediction.

Chapter 9

Results and interpretation

Contents

In the previous chapters, the basis of the data reconstruction and global event description is provided, an event selection maximizing the sensitivity to EWK and strong production of SUSY processes is implemented, and a stable background prediction including thorough studies of the systematic uncertainties is developed and validated. All steps are developed without using the data populating the signal region. As all analysis steps are considered as finalized, the measurement is now "unblinded", i.e., compared to the SM background prediction in the signal region in official agreement with the CMS collaboration. The results and their interpretation in the context of different SUSY scenarios are presented in this chapter.

9.1 Results

The signal region comprises four exclusive intervals defined in dependency of S_T^γ. The CMS measurement is compared to the SM background prediction in Fig. 9.1 and the

corresponding yields are given in Table 9.1 for each bin, showing both the separate contributions of the individual background components and the total yields. Uncertainties are provided for each background and bin. The statistical uncertainty in the e $\rightarrow \gamma$ background is caused by the limited size of the collected data sample and is significantly lower compared to its systematic uncertainty in each bin. All other statistical uncertainties are due to the limited number of simulated events. The sources of the systematic uncertainties are discussed in Chapter 8 and summarized in Table 9.2. The total systematic uncertainty results from the quadratic sum of the systematic uncertainties of each background component. Good agreement is observed between data and SM

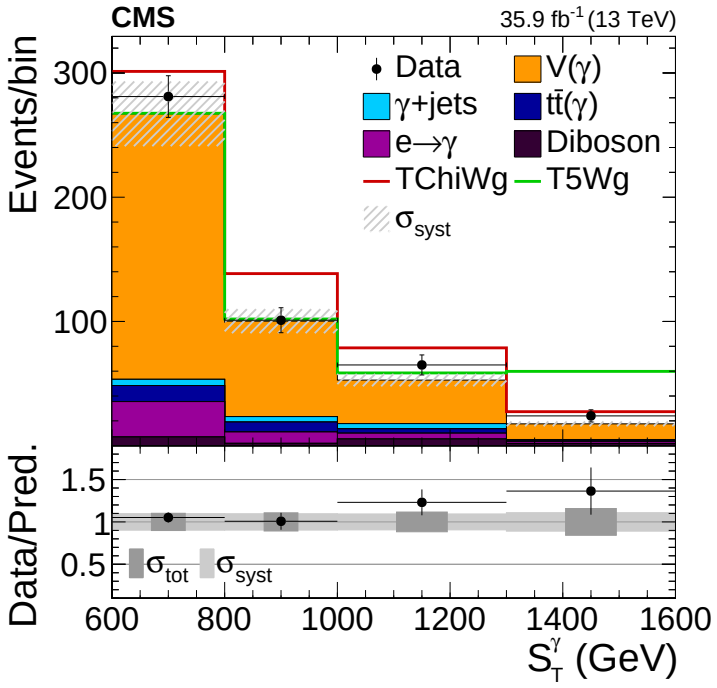

Figure 9.1: Comparison of the measurement and prediction in the signal region in four exclusive bins of S_T^γ. Two SUSY benchmark signal points are stacked onto the SM background prediction, where the TChiWg signal point corresponds to an NLSP mass of 700 GeV and the T5Wg signal point corresponds to a gluino mass of 1750 GeV and an NLSP mass of 1700 GeV. Events with values of S_T^γ beyond the shown range are included in the last bin. The hatched light gray band in the upper panel, as well as the solid light gray band in the lower panel represent the total systematic uncertainty (σ_{syst}). The dark gray band in the lower panel indicates the quadratic sum of the statistical and systematic uncertainties (σ_{tot}).

background prediction, without any indication for the presence of new physics. A small excess of measured events for high S_T^γ is observed, but with a discrepancy of 1.6 standard deviations for $S_T^\gamma > 1$ TeV the deviation is not considered as significant and is reflected in weaker observed limit compared to the expected limit on SUSY signal scenarios

Table 9.1: Expected standard model background and measured data yields, as well as the statistical and systematic uncertainties for the separate signal region bins defined in S_T^γ. For the total background uncertainty the uncertainties of the individual background components are summed quadratically.

S_T^γ: 600−800 GeV

	Yield	σ_{stat}	σ_{syst}
$V(\gamma)$	213	4.4	21.3
γ + jets	5	1.1	0.5
$t\bar{t}(\gamma)$	13	5.7	3.9
$e \to \gamma$	29	0.9	14.2
Diboson	7	2.8	2.1
Total	267	7.9	26.0
Data	281		

S_T^γ: 800−1000 GeV

	Yield	σ_{stat}	σ_{syst}
$V(\gamma)$	76.8	1.9	8.1
γ + jets	4.4	1.2	0.4
$t\bar{t}(\gamma)$	8.0	3.8	2.4
$e \to \gamma$	9.2	0.5	4.6
Diboson	1.9	1.7	0.6
Total	100.2	4.7	9.7
Data	101		

S_T^γ: 1000−1300 GeV

	Yield	σ_{stat}	σ_{syst}
$V(\gamma)$	35.0	1.3	3.9
γ + jets	4.2	1.3	0.4
$t\bar{t}(\gamma)$	3.5	0.9	1.1
$e \to \gamma$	4.7	0.4	2.3
Diboson	5.4	3.0	1.6
Total	52.8	3.6	5.0
Data	65		

S_T^γ: >1300 GeV

	Yield	σ_{stat}	σ_{syst}
$V(\gamma)$	12.6	0.7	1.6
γ + jets	1.1	0.5	0.4
$t\bar{t}(\gamma)$	0.7	0.5	0.2
$e \to \gamma$	1.5	0.2	0.8
Diboson	1.7	1.7	0.5
Total	17.6	2.0	1.9
Data	24		

(Section 9.3). The most dominant background in the SR is $V(\gamma)$, which constitutes about 77% of the total expected SM background. Representative for the EWK and strong production of SUSY events with photons in the final state, the expected number of additional events in the case of the presence of a signal point of the TChiWg (red line) and T5Wg (green line) scenario is shown in Fig. 9.1, stacked onto the SM background prediction. For the EWK scenario TChiWg, the benchmark signal point corresponding to an NLSP mass of 700 GeV is chosen, while the T5Wg signal point representing the strong production corresponds to a gluino mass of 1750 GeV and an NLSP mass of 1700 GeV. The distribution of these events already indicates that all four signal regions are important to provide sensitivity to both types of SUSY scenarios. While for the T5Wg signal point only the last bin provides significant sensitivity, sensitivity to the TChiWg signal point was small if the first three bins were not considered. Both signal points are excluded by this analysis. These two signal points are only of illustrative character, as the distribution of events changes along with the variety of signal scenarios and mass configurations.

Table 9.2: Systematic uncertainties in the standard model background prediction in the signal region in percent.

	V(γ)	γ+jets	e $\rightarrow \gamma$	t$\bar{\text{t}}(\gamma)$	Diboson
Fit uncert. of statistical origin	6.9	3.3	–	–	–
Scale uncertainty in shape	3.8−9.0	2.8−7.1	–	–	–
PDF uncertainty in shape	1.6−3.8	1.9−8.2	–	–	–
JES uncertainty in shape	5.0−5.9	0.9−32	–	–	–
Misidentification scale factor	–	–	50	–	–
Cross section, PDF, scales	–	–	–	30	30
Integrated luminosity	–	–	–	2.5	2.5
Photon efficiency scale factor	–	–	–	2.0	2.0
Trigger efficiency	–	–	–	0.4	0.4

9.2 Signal properties and uncertainties

To quantify what the measurement in the SR means in terms of the existence of SUSY, suitable SUSY scenarios are studied and brought into context with the data and the SM background prediction. The SUSY scenarios considered for this interpretation are introduced in Chapter 3 and their simulation is described in Section 5.3. To be able to calculate reliable mass limits on SUSY particles, the event yields expected by a certain SUSY model are weighted by the according signal cross section and the acceptance of the event selection. Studies are performed to determine the sources and the magnitude of systematic uncertainties in the signal simulation.

9.2.1 Signal cross sections

As the data are recorded in pp collisions at the LHC, the production cross section of squarks and gluinos is much larger compared to the cross section of sparticles produced via EWK interactions, making it much more challenging to probe EWK SUSY scenarios. For instance, the pair production cross section of gluinos with a mass of 1000 GeV is about 0.33 pb, which is more than 500 times the production cross section of a wino-like chargino pair of similar mass. The cross section depends on the mass of the initially produced sparticles and in case of gauginos on their gauge eigenstates.

All SUSY production cross sections used in this analysis are shown in Fig 9.2 as a function of the wino mass $m_{\widetilde{W}}$ along with their theoretical uncertainties. The EWK production cross sections are shown on the left, while the cross sections of gluino and squark pair production are shown on the right. The cross sections of the EWK GGM scenarios are calculated at NLO accuracy using PROSPINO, while the cross section for all exclusive production channels, as used for all SMS, are computed at NLO+NLL precision [157–165]. For the EWK production channels, the cross sections are computed in the limit of mass-degenerate wino-like gauginos with decoupled gluinos and squarks,

while for the computation of the gluino (squark) pair-production cross sections, squarks (gluinos) are decoupled. Since the EWK GGM scenario represents a full model in the sense that several processes contribute to the scenario, the cross sections differ from the ones used for the SMS. The theory uncertainties shown in Fig 9.2 contain uncertainties arising from the choice of the PDF sets and the renormalization and the factorization scale, except for the uncertainty in the GGM EWK cross section, which only reflects the statistical accuracy of the numerical methods applied by PROSPINO. As motivated in Chapter 3, the TChiWg scenario is weighted by the $\chi_1^0\chi_1^\pm$ production cross section, while the TChiNg scenario is weighted by the sum of the $\chi_1^0\chi_1^\pm$ and $\chi_1^\pm\chi_1^\mp$ production cross sections. For the computation of the squark pair production, a ten-times squark mass degeneracy is assumed, i.e., $\widetilde{d}$, $\widetilde{u}$, $\widetilde{s}$, $\widetilde{c}$, and $\widetilde{b}$ quarks are assumed to have the same masses, while top squarks are assumed to be decoupled.

9.2.2 Event selection acceptances

The acceptance of the event selection for a certain SUSY scenario is defined as the ratio of the number of events contributing to the SR, i.e., the number of events passing all selection criteria including reconstruction efficiencies, to the number of events initially produced, without applying any selection.

The selection acceptances of the SUSY scenarios considered in this analysis are shown in

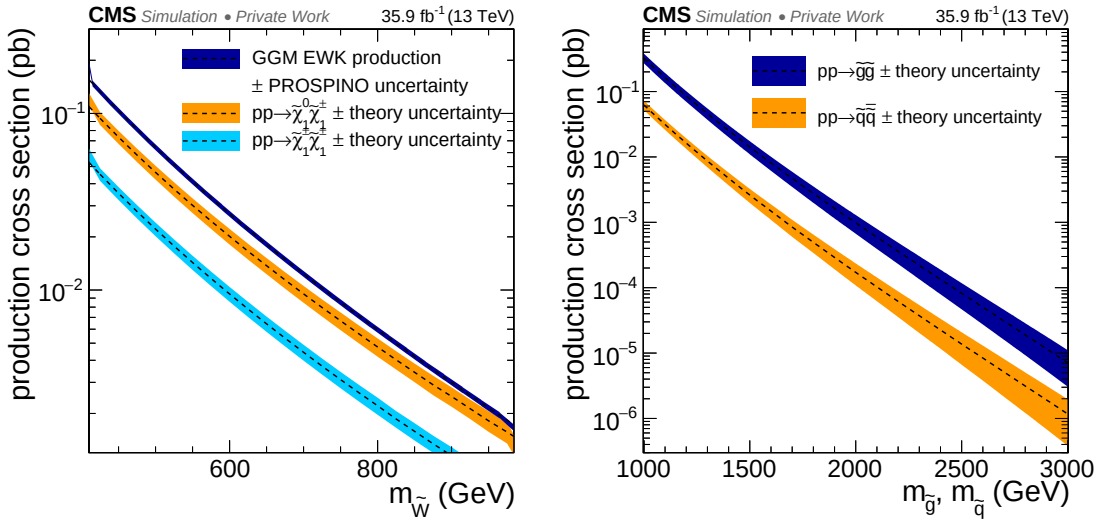

Figure 9.2: Production cross sections of several SUSY channels produced via EWK (left) and strong (right) interactions depending on the masses of the initally produced sparticles. The EWK cross sections are given in dependency of the wino mass $m_{\widetilde{W}}$, as for all EWK scenarios it is assumed that wino-like gauginos are produced.

Fig 9.3. The top row shows the acceptances of the EWK SMS TChiWg and TChiNg (left) and the EWK GGM scenario (right), followed by the acceptances of the T5gg (middle left), T5Wg (middle right), T6gg (bottom left), and T6Wg (bottom right) SMS.

The acceptances of all scenarios increase with a higher mass of the produced sparticles in the majority of the phase space, as the overall energy scale of the event is higher. As a consequence, also the chance of an event to pass the selection criteria increases. The effect is smaller in the phase space shown for the strong SMS, as only gluinos and squarks with masses already above 1 TeV are considered. The acceptance significantly increases with larger NLSP masses in all scenarios, since it determines the energy scale of the photons and the gravitinos (and therefore $p_{\mathrm{T}}^{\mathrm{miss}}$), which are the most important objects in the event selection. In the case of the EWK SMS, the NLSP mass is similar to the mass of the gauginos produced in the hard scattering. For a fixed mass of the initally produced sparticles, the acceptances decrease with a larger mass splitting to the NLSP, as more energy is transferred to the intermediate decay products, which are mostly jets.

For the TChiNg scenario, the neutralinos are assumed to decay as $\widetilde{\chi}_1^0 \to \gamma\widetilde{\mathrm{G}}$, $\widetilde{\chi}_1^0 \to \mathrm{Z}\widetilde{\mathrm{G}}$, and $\widetilde{\chi}_1^0 \to \mathrm{H}\widetilde{\mathrm{G}}$ with 50, 25, and 25% probability, respectively, whereas a simplified branching fraction of 100% is assumed for the $\widetilde{\chi}_1^0 \to \gamma\widetilde{\mathrm{G}}$ decay in the TChiWg scenario. Therefore, only in 75% of the TChiNg events at least one photon is produced, which roughly represents the TChiNg-to-TChiWg acceptance ratio for high NLSP masses. With a probability of 25% two $\widetilde{\chi}_1^0 \to \gamma\widetilde{\mathrm{G}}$ decays occur in the TChiNg scenario, significantly increasing the chance to fulfill the event selection, especially for low NLSP masses. Therefore, for NLSP masses below 550 GeV, the acceptance of the TChiNg scenario is higher than the acceptance for the TChiWg scenario.

In the GGM scenario, the NLSP is assumed to be bino-like. Therefore, $\widetilde{\chi}_1^0 \to \gamma\widetilde{\mathrm{G}}$ and $\widetilde{\chi}_1^0 \to \mathrm{Z}\widetilde{\mathrm{G}}$ decays occur with a probability of approximately 77 and 23%, respectively, as explained in Section 2.3. Thus, about one in two events has two photons in the final state, whereas in roughly 5% of the events no high-energy photons are present in the final state.

In the T5gg and T6gg SMS, a branching fraction of 100% is assumed for the $\widetilde{\mathrm{g}} \to \mathrm{q}\bar{\mathrm{q}}\widetilde{\chi}_1^0$ and $\widetilde{\mathrm{q}} \to \mathrm{q}\widetilde{\chi}_1^0$ decays, while a branching fraction of 50% is assumed for the decays $\widetilde{\mathrm{g}} \to \mathrm{q}\bar{\mathrm{q}}\widetilde{\chi}_1^0$ and $\widetilde{\mathrm{g}} \to \mathrm{q}\bar{\mathrm{q}}\widetilde{\chi}_1^{\pm}$ ($\widetilde{\mathrm{q}} \to \mathrm{q}\widetilde{\chi}_1^0$ and $\widetilde{\mathrm{q}} \to \mathrm{q}\widetilde{\chi}_1^{\pm}$) in the T5Wg (T6Wg) scenario. Thus, only 75% of the events in the latter two scenarios have photons in the final state. Furthermore, there is always a second photon in the final states of the T5gg and T6gg scenarios. The acceptance for a signal point with squark pair production is higher as the acceptance for a signal point with gluino pair production with similar mass configuration, as the squarks decay via two-body decays into a gaugino and a quark, while the gluinos decay via three-body decays into a gaugino and two quarks, increasing the jet activity and decreasing the energy of the gauginos in the T5gg (T5Wg) scenario compared to the T6gg (T6Wg) scenario.

As described in Section 5.3, fast simulation events are vetoed if generated jets fail certain quality requirements. The acceptance of the SUSY scenarios is reduced by up to 0.3% appyling this cleaning veto.

Exemplary for an EWK and and a strong production SUSY scenario, cutflow tables are provided in Table 9.3 and 9.4 for the TChiWg benchmark signal point with an NLSP mass of 700 GeV and the T5Wg benchmark signal point with a gluino mass of 1750 GeV and an NLSP mass of 1700 GeV, respectively, which are the two signal points also shown in Fig. 9.1.

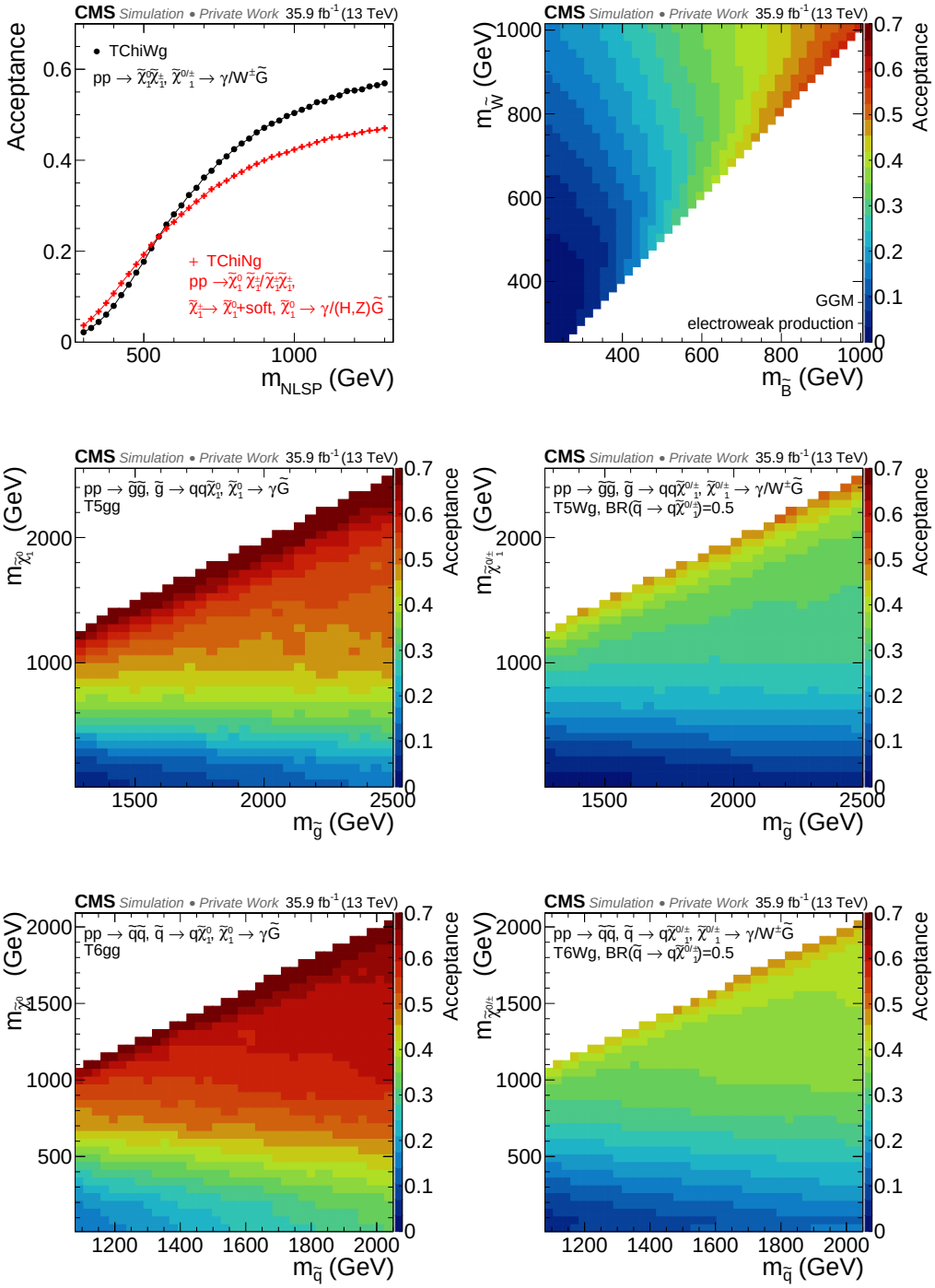

Figure 9.3: Acceptances of the TChiWg and TChiNg (top left), GGM (top right), T5gg (middle left), T5Wg (middle right), T6gg (bottom left), and T6Wg (bottom right) SUSY scenario.

Table 9.3: Cutflow of the TChiWg benchmark signal point with a wino NLSP with a mass of 700 GeV. The preselection cut comprises the requirement of at least one isolated photon with $p_{\mathrm{T}} > 180\,\mathrm{GeV}$, which was accepted by the trigger. For the photon a minimal distance in ΔR of 0.5 is required with respect to the nearest jet. Also $\Delta\phi(p_{\mathrm{T}}^{\mathrm{miss}},\ \mathrm{jet}) > 0.3$ is required for all jets with $p_{\mathrm{T}} > 100\,\mathrm{GeV}$. The yields correspond to a center-of-mass energy of 13 TeV and an integrated luminosity of $35.9\,\mathrm{fb}^{-1}$.

Selection	Number of events	Fraction wrt. inital number of events
Before selection	321.8	(100%)
Preselection	181.4	(56%)
$p_{\mathrm{T}}^{\mathrm{miss}} > 300\,\mathrm{GeV}$	123.7	(38%)
$\mathrm{M_T} > 300\,\mathrm{GeV}$	121.5	(38%)
$\mathrm{S_T^\gamma} > 600\,\mathrm{GeV}$	115.8	(36%)
$600\,\mathrm{GeV} < \mathrm{S_T^\gamma} < 800\,\mathrm{GeV}$	36.5	(11%)
$800\,\mathrm{GeV} < \mathrm{S_T^\gamma} < 1000\,\mathrm{GeV}$	40.9	(13%)
$1000\,\mathrm{GeV} < \mathrm{S_T^\gamma} < 1300\,\mathrm{GeV}$	27.8	(9%)
$\mathrm{S_T^\gamma} > 1300\,\mathrm{GeV}$	10.6	(3%)

Table 9.4: Cutflow of the T5Wg benchmark signal point with a gluino mass of 1750 GeV and a gaugino mass of 1700 GeV. The preselection cut comprises the requirement of at least one isolated photon with $p_{\mathrm{T}} > 180\,\mathrm{GeV}$, which was accepted by the trigger. For the photon a minimal distance in ΔR of 0.5 is required wrt. to the nearest jet. Also $\Delta\phi(p_{\mathrm{T}}^{\mathrm{miss}},\ \mathrm{jet}) > 0.3$ is required for all jets with $p_{\mathrm{T}} > 100\,\mathrm{GeV}$. The yields correspond to a center-of-mass energy of 13 TeV and an integrated luminosity of $35.9\,\mathrm{fb}^{-1}$.

Selection	Number of events	Fraction wrt. inital number of events
Before selection	121.8	(100%)
Preselection	60.3	(50%)
$p_{\mathrm{T}}^{\mathrm{miss}} > 300\,\mathrm{GeV}$	55.4	(46%)
$\mathrm{M_T} > 300\,\mathrm{GeV}$	54.9	(45%)
$\mathrm{S_T^\gamma} > 600\,\mathrm{GeV}$	54.9	(45%)
$600\,\mathrm{GeV} < \mathrm{S_T^\gamma} < 800\,\mathrm{GeV}$	0.5	(0%)
$800\,\mathrm{GeV} < \mathrm{S_T^\gamma} < 1000\,\mathrm{GeV}$	1.8	(1%)
$1000\,\mathrm{GeV} < \mathrm{S_T^\gamma} < 1300\,\mathrm{GeV}$	6.1	(5%)
$\mathrm{S_T^\gamma} > 1300\,\mathrm{GeV}$	46.5	(38%)

9.2.3 Systematic uncertainties

There are three sources of systematic uncertainties that are equal and constant for all SUSY scenarios and also all SM backgrounds that are estimated directly from simulation.

The MC samples are scaled by a weight factor to fit the integrated luminosity recorded by CMS, compare Eq. (5.3). The uncertainty of the measurement of $\mathcal{L}_{\text{int}}$ is estimated to be 2.5% [189]. A further uncertainty of 2% arises from the determination of the data-to-simulation efficiency ratio for the photon identification, as described in Section 6.1.2. The third systematic uncertainty is given by the uncertainty in the trigger efficiency. As described in Section 5.2, all MC samples are scaled by the trigger efficiency of (94.3±0.4)%, resulting in an additional systematic uncertainty of 0.4%.
All of these three systematic uncertainties are treated as fully correlated among the search region bins.

There are several sources of uncertainties in the signal simulation that partially have to be determined for each signal point of the one- or two-dimensional signal scan grid separately.

Signal scans are requested and used only by a few analysis teams. To save computing time, signal scans are generated using the fast simulation method described in Section 5.3. Especially the signal acceptance for analyses imposing requirements on $p_{\text{T}}^{\text{miss}}$ can be affected by the simplified simulation of the CMS detector. Therefore, the whole event selection is repeated using the missing transverse momentum computed at generator level ($p_{\text{T}}^{\text{miss, gen}}$) instead of using the PF $p_{\text{T}}^{\text{miss}}$. The signal yield entering the statistical interpretation is then given by the average of the two resulting signal yields. The associated systematic uncertainty is computed for all SUSY scenarios and for each signal region bin separately, and is given by half of the difference in the yields obtained using PF $p_{\text{T}}^{\text{miss}}$ and $p_{\text{T}}^{\text{miss, gen}}$. The systematic uncertainty due to fast simulation of the CMS detector varies in the range of $< 0.1-5\%$ and $< 0.1-25\%$ for the EWK and strong production SUSY scenarios, respectively. The fast simulation $p_{\text{T}}^{\text{miss}}$ uncertainty is illustrated in the top row of Fig. 9.4 for the EWK SMS for each signal point and signal region bin. Representative for the strong production SUSY models, the uncertainty is shown for each signal point and signal region bin for the T5Wg scenario in Fig. 9.5. Similar illustrations are provided in Appendix E for all other SUSY scenarios.

The MadGraph modeling of initial-state radiation, which affects the total transverse momentum $p_{\text{T}}^{\text{ISR}}$ of the system of the gauginos, is improved by reweighting the $p_{\text{T}}^{\text{ISR}}$ distribution of MC SUSY events. This reweighting procedure is based on studies of the p_{T} of Z boson events [190]. The reweighting factors range between 1.18 at $p_{\text{T}}^{\text{ISR}} = 125\,\text{GeV}$ and 0.78 for $p_{\text{T}}^{\text{ISR}} > 600\,\text{GeV}$. A constant factor is computed for each affected SUSY model separately to ensure that the overall normalization is unchanged. The full deviation from unity is taken as the systematic uncertainty in the reweighting procedure. The resulting systematic uncertainty is shown in the middle row of Fig. 9.4 for the EWK SMS for each mass point and signal region bin separately and is found to be 0.6−3.0%.

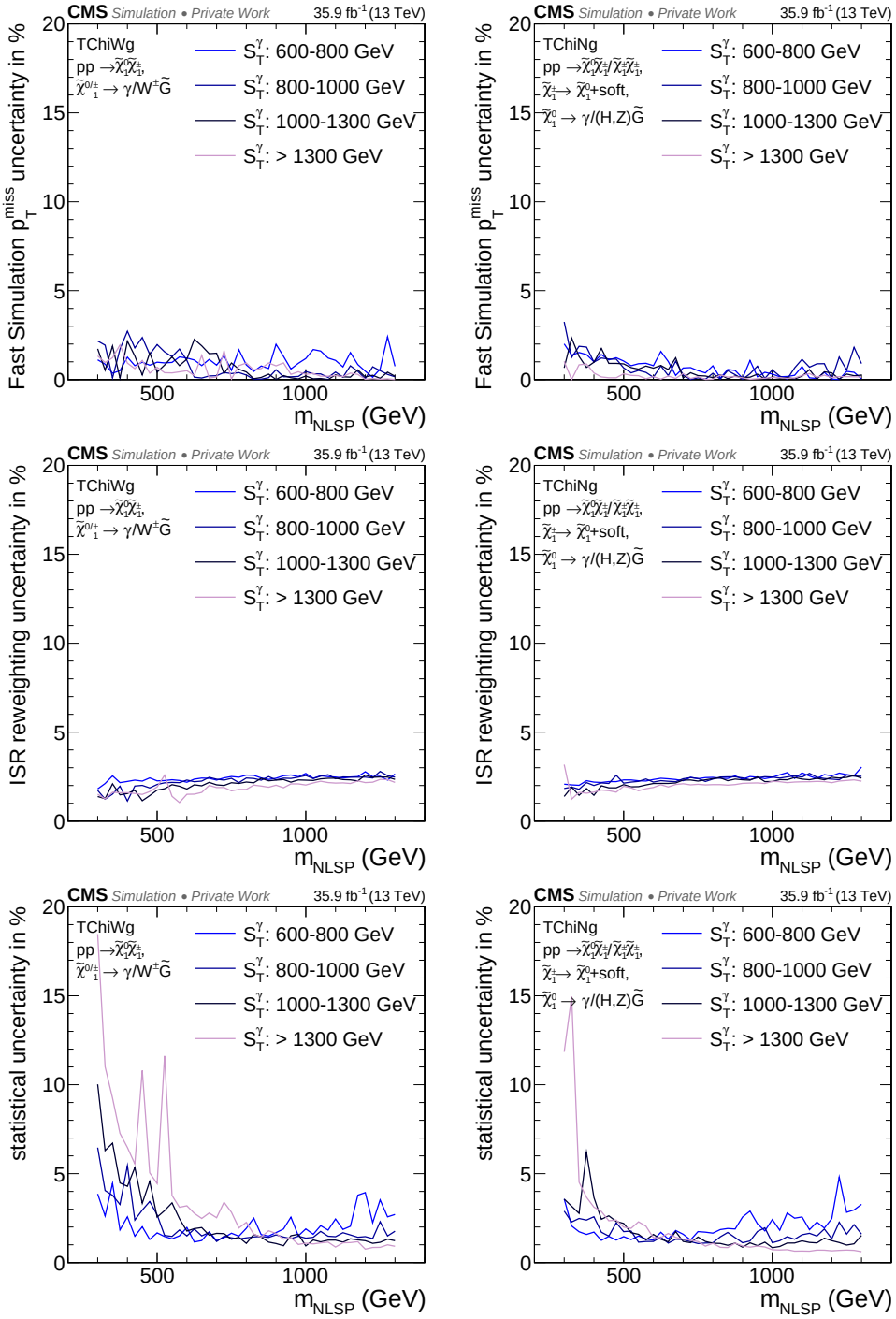

Figure 9.4: Systematic uncertainties arising from $p_{\mathrm{T}}^{\mathrm{miss}}$ mismodelling due to the fast simulation of the CMS detector (top row), the ISR reweighting of the $p_{\mathrm{T}}^{\mathrm{ISR}}$ distribution (middle row), and the statistical uncertainty (bottom row) for the EWK SMS TChiWg (left) and TChiNg (right), for each mass point and signal region bin. See text for more details about how the uncertainties are estimated.

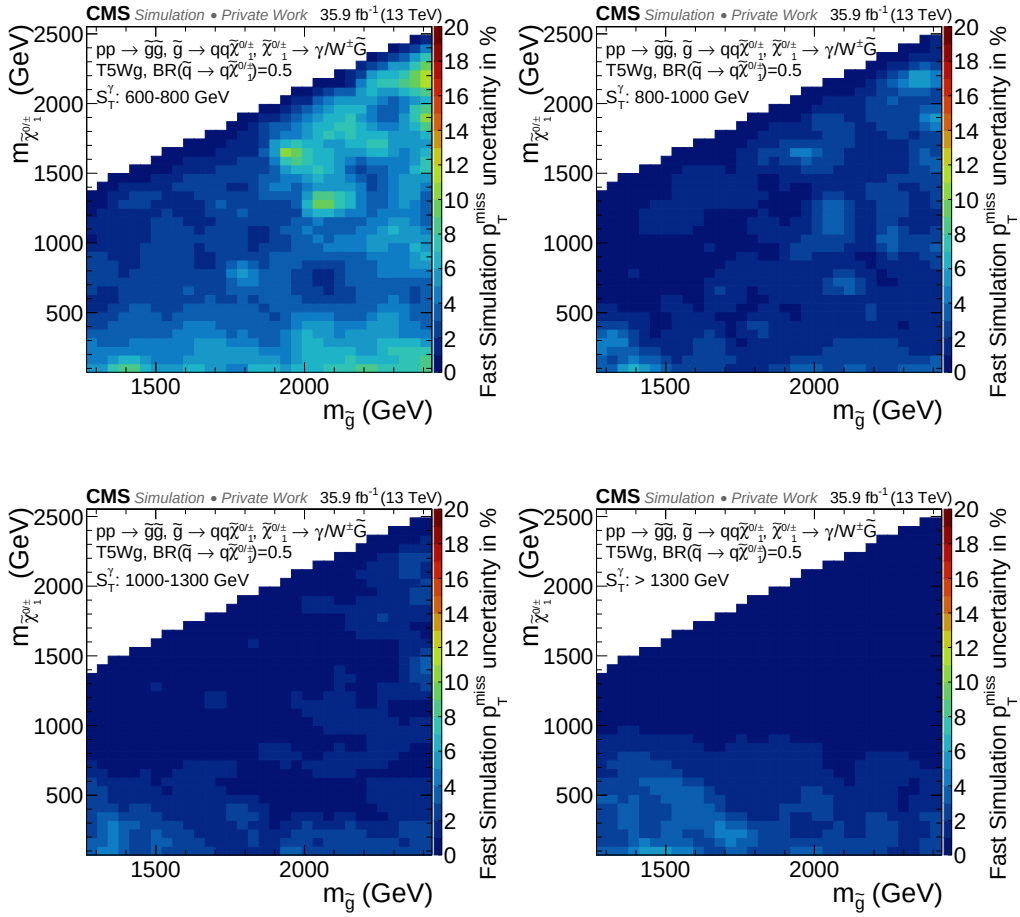

Figure 9.5: Systematic uncertainties arising from $p_{\mathrm{T}}^{\mathrm{miss}}$ mismodelling due to the fast simulation of the CMS detector for the T5Wg strong production SMS for the four signal region bins in S_{T}^{γ} with $600-800\,\mathrm{GeV}$ (top left), $800-1000\,\mathrm{GeV}$ (top right), $1000-1300\,\mathrm{GeV}$ (bottom left), and more than $1300\,\mathrm{GeV}$ (bottom right).

Different choices of the PDFs and the factorization and renormalization scales can affect both the normalization and the kinematic properties of the signal scenario, where the effect on the former is expected to be larger. The uncertainty affecting the normalization is accounted for in the theory uncertainty in the cross section, see also Section 9.2.1. Since PROSPINO does not provide these uncertainties, the theory uncertainty for the GGM scan is estimated by using the added up uncertainty of the combination of $\widetilde{\chi}_1^0\widetilde{\chi}_1^\pm$ and $\widetilde{\chi}_1^\pm\widetilde{\chi}_1^\mp$ production, providing an estimate in good approximation. The remaining effect on the shape due the choice of the PDFs is found to be negligible. The systematic uncertainty in the shape arising from different choices of the factorization and renormalization scales is studied and found to be small, varying in the range of $< 0.1{-}1.8\%$ ($< 0.1{-}1.2\%$) for the EWK (strong) production SUSY scenarios. The uncertainties are illustrated for the EWK SMS (left) and the T5Wg model (right) in Fig. 9.6, whereas the plots of the remaining SUSY models can be found in the Appendix E.

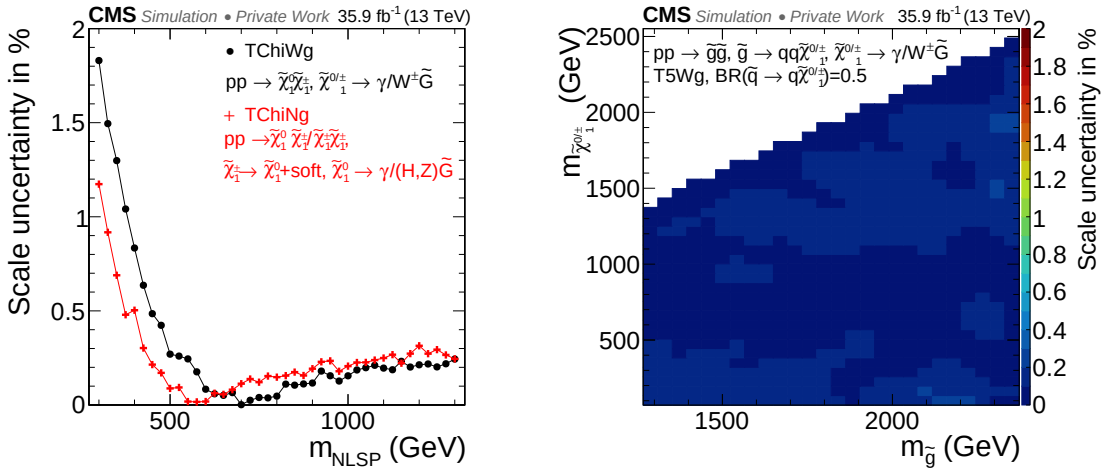

Figure 9.6: Systematic uncertainty in the shape arising from the choice of the factorization and renormalization scales for the EWK SMS (left) and the T5Wg strong production SMS (right).

A possible systematic effect of the pileup simulation is studied by dividing the signal events into a low-pileup and high-pileup category, where events belong to the low-pileup category if the number of reconstructed vertices is lower than 17, and to the high-pileup category otherwise. The full deviation of the change in acceptance for the low- and high-pileup categories with respect to the combined sample is taken as systematic uncertainty and varies between $< 0.1{-}0.4\%$ and $< 0.1{-}2.1\%$ for the EWK and strong production SUSY scenarios, respectively.

The finite number of events generated for the signal scans leads to statistical uncertainties that vary across the different models and signal points. The statistical uncertainty is determined for each signal region bin separately. The bottom row of Fig. 9.4 shows the statistical uncertainty of the EWK SMS, while Fig. 9.7 shows the respective statistical

uncertainty for the T5Wg model for each signal region bin. Similar plots for the remaining signal scenarios can be found in Appendix E.
All uncertainties affecting the MC signal simulation are summarized in Table 9.5.

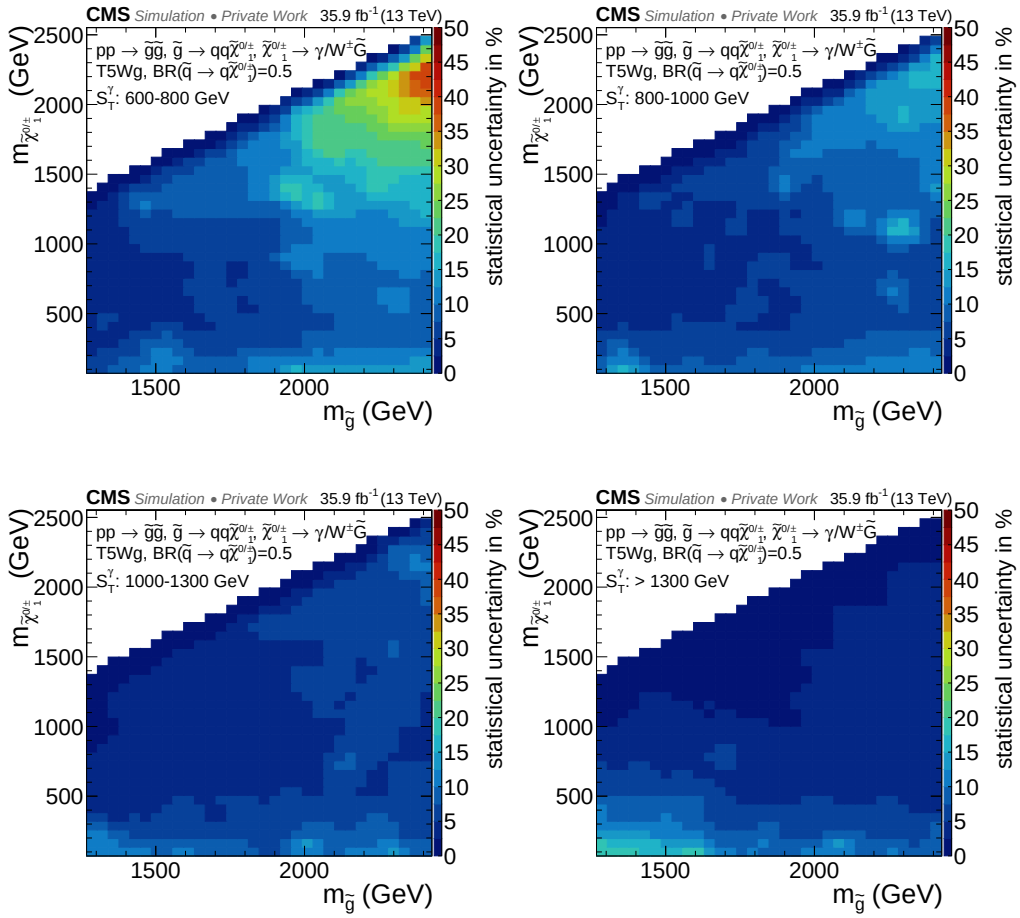

Figure 9.7: Statistical uncertainty arising from the finite number of generated events in the signal MC simulation for the T5Wg strong production SMS for the four signal region bins in S_T^γ with $600-800$ GeV (top left), $800-1000$ GeV (top right), $1000-1300$ GeV (bottom left), and more than 1300 GeV (bottom right).

Table 9.5: Summary of uncertainties relevant for the electroweak (middle column) and strong production (right column) signal models stated in percent.

	Signal scenario	
Source	Electroweak	Strong production
Statistical MC precision per signal region	1−28	2−50
Fast simulation uncertainty in $p_{\mathrm{T}}^{\mathrm{miss}}$	< 0.1−5	< 0.1−25
Scale uncertainty in shape	< 0.1−1.8	< 0.1−1.2
Integrated luminosity	2.5	2.5
Trigger efficiency	0.4	0.4
Photon scale factor	2.0	2.0
Pileup	< 0.1−0.4	< 0.1−2.1
ISR reweighting	0.6−3.0	–

9.3 Signal cross section and exclusion limits

Expected and observed upper cross section and mass exclusion limits are calculated in one- and two-dimensional parameter spaces for the EWK and strong production SUSY models introduced in Chapter 3. The limits are calculated at 95% confidence level (CL) using a modified frequentist $\mathrm{CL_s}$ approach [191–193] with a profile likelihood test statistic and asymptotic formulae [194]. The limit setting procedure and the notations are explained in the following.

A likelihood function needs to be defined using the yields of the SM background prediction $b(\theta)$, the measurement (data), the expected signal yields $s(\theta)$, and the systematic uncertainties evaluated for background and signal which enter as nuisance parameters θ. The likelihood function is defined by

$$\mathcal{L}(\mathrm{data}|\mu,\theta) = \mathrm{Poisson}(\mathrm{data}|\mu \cdot s(\theta) + b(\theta)) \cdot \rho(\hat{\theta}|\theta), \tag{9.1}$$

where μ is the signal strength modifier proportional to the signal cross section, and $\rho(\hat{\theta}|\theta)$ is the nuisance probability density function (pdf) with $\hat{\theta}$ being the best estimate of the nuisance parameters. Different choices of the parametrization of $\rho(\hat{\theta}|\theta)$ can be made. Here, the log-normal pdf

$$\rho(\hat{\theta}|\theta) = \frac{1}{\sqrt{2\pi}\ln(\kappa)} \exp\left(-\frac{(ln(\theta/\hat{\theta}))^2}{2(\ln(\kappa))^2})\right) \cdot \frac{1}{\theta} \tag{9.2}$$

is used, with the parameter κ characterizing the width of the log-normal distribution. In contrast to the Gaussian pdf, which is not suited for positively defined parameters like the signal cross section, the log-normal pdf goes to zero at $\theta = 0$, without the need of truncation.

In the statistical interpretation of the analysis, the four SR bins are combined to calculate the final limit. Therefore, the expression Poisson(data|$\mu \cdot s(\theta)+b(\theta)$) of Eq. (9.1) represents the product of Poisson probabilities,

$$\prod_{i=1}^{4} \frac{(\mu \cdot s_i + b_i)^{n_i}}{n_i!} e^{-(\mu \cdot s_i + b_i)}, \tag{9.3}$$

to observe n_i events in the i-th bin.

A test statistic $\widetilde{q}_\mu$ is defined to compare the compatibility of the measurement with the signal + background ($\mu \cdot s + b$) and the background-only (b) hypotheses. By the Neyman-Pearson Lemma [195], a likelihood ratio is the most powerful discriminator for statistical hypotheses. The classical frequentist approach is formulated without consideration of systematic uncertainties. Therefore, a modified frequentist approach based on the quantity CL_s is chosen using the one-sided profile likelihood test statistic

$$\widetilde{q}_\mu = -2 \ln \frac{\mathcal{L}(\text{data}|\mu, \hat{\theta}_\mu)}{\mathcal{L}(\text{data}|\hat{\mu}, \hat{\theta})}, \text{ with } 0 \leq \hat{\mu} \leq \mu. \tag{9.4}$$

The parameter $\hat{\theta}_\mu$ is the maximum likelihood estimator of θ given μ, while $\hat{\mu}$ and $\hat{\theta}$ correspond to the global maximum of the likelihood function. The tilde of $\widetilde{q}_\mu$ serves the distinction against the test statistic used for instance at LEP or Tevatron. The constraint $0 \leq \hat{\mu}$ takes into account that only positive signal rates are expected, while the constraint $\hat{\mu} \leq \mu$ ensures that a $\hat{\mu}$ value larger than the expected signal strength cannot be considered as evidence against the signal hypothesis, resulting in one-sided confidence intervals. Considering the data yields in the signal region bins, the observed values $\widetilde{q}_\mu^{\text{obs}}$ and $\hat{\theta}_\mu^{\text{obs}}$ corresponding to the signal strength modifier under test, as well as $\hat{q}_0^{\text{obs}}$ can be calculated.

The "confidence level" is defined by

$$\mathrm{CL}_s = \frac{\mathrm{CL}_{s+b}}{\mathrm{CL}_b} = \frac{p_\mu}{1 - p_b}, \tag{9.5}$$

where p_μ and p_b represent the p-values of the signal + background and the background-only hypothesis, respectively. The p-values are defined and computed by

$$p_\mu = P(\widetilde{q}_\mu \geq \widetilde{q}_\mu^{\text{obs}} | \text{signal + background}) = \int_{\widetilde{q}_\mu^{\text{obs}}}^{\infty} f(\widetilde{q}_\mu | \mu, \hat{\theta}_\mu^{\text{obs}}) d\widetilde{q}_\mu, \tag{9.6}$$

and

$$1 - p_b = P(\widetilde{q}_\mu \geq \widetilde{q}_\mu^{\text{obs}} | \text{background-only}) = \int_{\widetilde{q}_0^{\text{obs}}}^{\infty} f(\widetilde{q}_\mu | 0, \hat{\theta}_0^{\text{obs}}) d\widetilde{q}_\mu. \tag{9.7}$$

Here, $f(\widetilde{q}_\mu|\mu)$ represents the pdf of the test statistic defined in Eq. (9.4) for a certain value μ. Assuming the validity of the Wald approximation [196] $\widetilde{q}_\mu$ can be written as

$$\widetilde{q}_\mu = \frac{(\mu - \hat{\mu})^2}{\sigma^2}, \quad 0 \leq \hat{\mu} \leq \mu, \tag{9.8}$$

which is valied to $\mathcal{O}(1/\sqrt{N})$, with N being the data sample size. Using the approximation of Eq. (9.8), where $\hat{\mu}$ follows a Gaussian distribution with standard deviation σ, $f(\widetilde{q}_\mu|\mu)$ can be parametrized by

$$f(\widetilde{q}_\mu|\mu) = \frac{1}{2}\delta(\widetilde{q}_\mu) + \begin{cases} \frac{1}{2\sqrt{2\pi\widetilde{q}_\mu}} \exp\left[-\widetilde{q}_\mu/2\right], & 0 < \widetilde{q}_\mu \leq \mu^2/\sigma^2, \\ \frac{1}{(2\mu/\sigma)\sqrt{2\pi}} \exp\left[-\frac{(\widetilde{q}_\mu+\mu^2/\sigma^2)^2}{2(2\mu/\sigma)^2}\right], & \widetilde{q}_\mu > \mu^2/\sigma^2, \end{cases} \tag{9.9}$$

where $\delta(\widetilde{q}_\mu)$ is the Dirac delta function. The asymptotic formulae become exact in the large sample limit. In the case of a very small data sample, MC simulation can be used.

To calculate the 95% CL upper limit on the signal cross section, the signal strength modifier μ is varied until CL_s equals $\alpha = 0.05$. The exclusion limit is determined by $\mu = 1$, where all signal points are excluded that fulfill $\mathrm{CL}_s \leq 0.05$.

Expected median upper cross section limits and ± 1 and ± 2 uncertainty bands are computed by generating background-only pseudo-data which are considered as "data" in the procedure described above. To save computing time one exploits that the distribution of the test statistic does not depend on the pseudo-data, so that the p-value for each μ under study has to be computed only once. Expected limits are useful, e.g., to maximize the experimental sensitivity and to evaluate possible fluctuations in data. The expected median upper limit and the corresponding uncertainty bands are computed by

$$\mu_{\mathrm{up},\pm m\sigma} = \sigma(\Phi^{-1}(1 - \alpha\Phi(m)) \pm m), \tag{9.10}$$

where m represents the order of the uncertainty σ, Φ^{-1} is the inverse of the cumulative distribution of the standard Gaussian distribution, and $1 - \alpha$ represents the CL. The case $m = 0$ gives the expected median upper limit.
Furthermore, the median exclusion significance

$$\mathrm{med}[Z_\mu|0] = \sqrt{\widetilde{q}_{\mu,\mathrm{A}}}, \tag{9.11}$$

assuming pseudo-data distributed according to $\mu = 0$, as well as the observed significance

$$Z_{\mathrm{obs}} = \sqrt{\widetilde{q}_\mu^{\mathrm{obs}}} \tag{9.12}$$

are calculated. The index "A" in Eq. (9.11) indicates that the so-called "Asimov data set", which suppresses statistical fluctuations, is used as pseudo-data.

Using the CL_s criterion as defined in Eq. (9.5) results in a more conservative exclusion limit than simply using the also well-motivated criterion $p_\mu \leq \alpha$, because the denominator of Eq. (9.5) is always less than or equal to unity. This procedure avoids excluding scenarios with very low experimental sensitivity if less data are measured than expected, because in this case not only p_μ, but also the denominator $1 - p_b$ decreases.

9.3.1 Limits on electroweak production of charginos and neutralinos

Three different SUSY models are used to interpret the results in terms of EWK production of charginos and neutralinos. The 95% CL observed upper cross section limit, as well as the expected and observed exclusion contours, are shown in Fig. 9.8 for the EWK GGM signal scan. The limits are presented in the wino-bino mass plane, where the wino mass $m_{\widetilde{W}}$ represents the mass of $\widetilde{\chi}_2^0$ and $\widetilde{\chi}_1^\pm$, while the bino mass $m_{\widetilde{B}}$ represents the mass of $\widetilde{\chi}_1^0$. The analysis reaches the highest sensitivity for nearly degenerate wino and bino masses. In this case, the analysis excludes wino and bino masses up to 980 GeV at 95% CL, improving on the former best limit of 710 GeV [1] based on data recorded at 8 TeV. The sensitivity decreases with a larger wino-bino mass splitting since on average the energy of the photons and gravitinos decreases, while more energy is transferred to the decay products of the $\widetilde{\chi}_1^\pm$ and $\widetilde{\chi}_2^0$. Figure 9.9 compares the expected (dashed) and observed (solid) exclusion contour of this analysis (black) to the limits set by SUS-14-016 (red) and SUS-16-023 (yellow). An expansion of the excluded phase space is achieved for the whole wino-bino mass plane compared to the former highest exclusion limit, except for very low bino masses due to the much higher threshold on $p_T(\gamma)$ in the event selection.

The expected (dashed red line) and observed (solid black line) limits for the EWK TChiWg (left) and TChiNg (right) simplified models are shown as a function of the NLSP mass (m_{NLSP}) in Fig. 9.10 together with the theoretical cross section (blue lines).
The analysis excludes NLSP masses below 780 GeV at 95% CL in the TChiWg scenario and below 950 GeV in the TChiNg scenario. Due to the slight excess observed with respect to the SM background prediction especially in the highest S_T^γ bins, the observed limits are weaker compared to the expected exclusion limits of 920 (1070) GeV for the TChiWg (TChiNg) scenario. The former highest observed (expected) limit in the TChiWg scenario of 680 (620) GeV [1] set by the predecessor analysis SUS-14-016 is improved by 100 (300) GeV, as shown in Fig. 9.11 (left), where the upper cross section limits set by SUS-14-016 need to be compared to the signal cross section at 8 TeV (green lines). Figure 9.11 (left) also shows the expected and observed upper cross section limits set by SUS-16-023 using 2.3 fb^{-1} of data recorded at $\sqrt{s} = 13$ TeV (yellow lines). A version of the TChiNg scenario was used by SUS-14-016 for interpretation [1] but with different assumptions made about the signal cross section and the signal generation, disabling direct comparability.

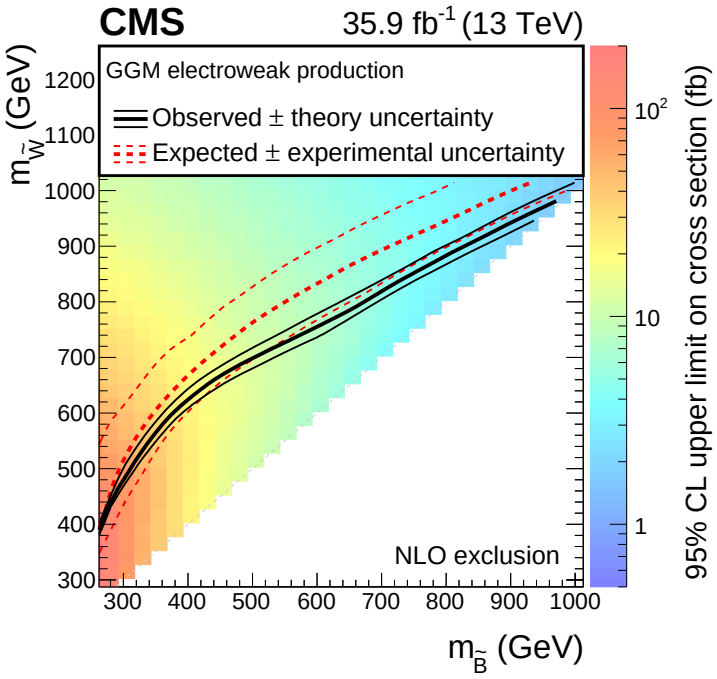

Figure 9.8: Observed upper cross section limit at 95% CL for the EWK GGM signal in the wino-bino mass plane. The thick lines represent the observed (black) and expected (red) exclusion contours, where the phase space closer to the diagonal is excluded by the analysis. The thin dotted red curves indicate the region containing 68% of the distribution of limits expected under the background-only hypothesis. The thin solid black curves show the change in the observed limit due to variation of the signal cross sections within their theoretical uncertainties.

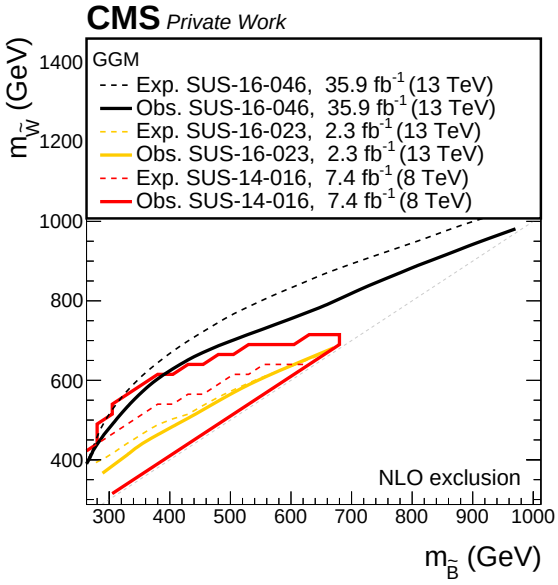

Figure 9.9: Expected (dashed) and observed (solid) exclusion limits for the EWK GGM signal in the wino-bino mass plane set by the analyses SUS-16-046 (black), SUS-16-023 (yellow), and SUS-14-016 (red). The analysis at hand significantly improves the limits set by the predecessor analyses.

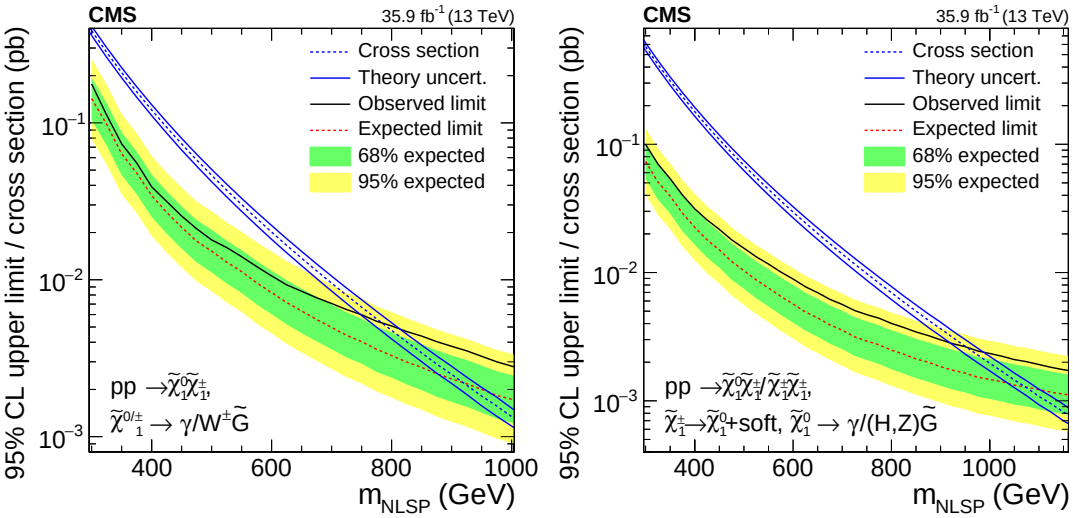

Figure 9.10: Observed (black) and expected (red) upper cross section limits as a function of the NLSP mass (m_{NLSP}) for the TChiWg (left) and TChiNg (right) model together with the corresponding theoretical cross section (dashed blue). The inner (green) band and the outer (yellow) band indicate the regions containing 68 and 95%, respectively, of the distribution of limits expected under the background-only hypothesis. The solid blue lines represent the theoretical uncertainty in the signal cross section.

Figure 9.11 (right) compares the expected (dashed) and observed (solid) cross section limit in the TChiWg scenario set by the single photon analysis SUS-16-047 [81] to the result of this analysis. The upper cross section limits set by SUS-16-047 (pink) fluctuate around the nominal signal cross sections, highlighting the advantage of the analysis SUS-16-046 especially in the EWK SUSY sector.

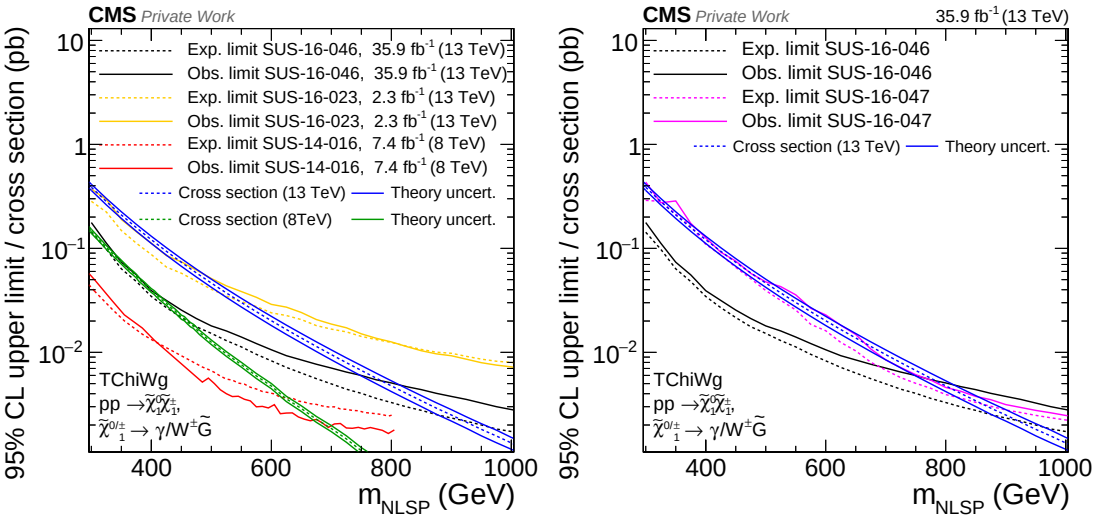

Figure 9.11: Expected (dashed) and observed (solid) upper cross section limits at 95% CL in the TChiWg scenario of the analysis SUS-16-046 (black) compared to the two predecessor analyses SUS-14-016 (red) and SUS-16-023 (yellow) on the left and compared to the single photon analysis SUS-16-47 (pink) on the right, together with the signal cross section at 13 TeV (blue). To evaluate the limit set by SUS-14-016, also the 8 TeV signal cross section is shown in the plot on the left (green).

9.3.2 Limits on strong production of gluinos and squarks

The results are also interpreted in simplified models of strong production scenarios. The two scenarios T5gg and T5Wg are based on gluino pair-production. The former scenario represents final states with two photons, while the latter represents a mixture of two photons, one photon and one $W^{\pm}$ boson, and two $W^{\pm}$ bosons in the final state. The cross section upper limits and exclusion contours are shown in Fig. 9.12 (top row) in the $\tilde{g} - \tilde{\chi}_1^0/\tilde{\chi}_1^{\pm}$ mass plane. This search can exclude gluino masses of up to 2100 (2000) GeV in the T5gg (T5Wg) scenario, where the highest mass limits correspond to scenarios with small $\tilde{g} - \tilde{\chi}_1^0/\tilde{\chi}_1^{\pm}$ mass splittings. The exclusion limit gets weaker at low NLSP masses because of the acceptance loss, which mostly arises from the lower energy of the photons and the gravitinos accompanied by larger hadronic activity in the event.

Similar scenarios, T6gg and T6Wg, based on squark pair-production are also used for

interpretation and are shown in Fig. 9.12 (bottom row). Here, squark masses up to 1750 (1650) GeV are excluded in the T6gg (T6Wg) scenario. Again, the highest mass limits are achieved for small $\tilde{q} - \tilde{\chi}_1^0/\tilde{\chi}_1^\pm$ mass splittings.

The mass limits on squarks are weaker compared to those on gluinos due to the lower production cross section for same sparticle masses, compare Fig. 9.2. However, in case of squark production the hadronic activity in the event is lower on average compared to gluino production and the ratio of energy transferred to photons and gravitinos is larger, slightly reducing the dependency of the exclusion limit on the $\tilde{q} - \tilde{\chi}_1^0/\tilde{\chi}_1^\pm$ mass difference. The higher sensitivity in the T5gg and T6gg models compared to the T5Wg and T6Wg models is due to the assumption of a branching fraction of 100% for $\tilde{\chi}_1^0 \to \tilde{G}\gamma$ and two photons in the final state contributing to S_T^γ, increasing the separation power between signal and SM background.

Figure 9.13 shows the comparison of the expected (dashed lines) and observed (solid lines) limits set by this analysis (black) and the analysis SUS-16-047 (red) in the T5gg (top left), T5Wg (top right), T6gg (bottom left), and the T6Wg (bottom right) scenario. The color scale encodes the observed upper cross section limit set by SUS-16-046. The analysis SUS-16-047, which is developed with focus on strong production SUSY models with photon final states, sets the highest mass limits for a wide range of the $\tilde{g}/\tilde{q} - \tilde{\chi}_1^0/\tilde{\chi}_1^\pm$ phase space in these models. For mass splittings with $m_{\tilde{g}/\tilde{q}} - m_{\tilde{\chi}_1^0/\tilde{\chi}_1^\pm} \lesssim 450\,\text{GeV}$, however, this analysis exceeds the sensitivity to strong production SUSY models compared to SUS-16-047 and sets the currently highest mass limits for these scenarios in this phase space.

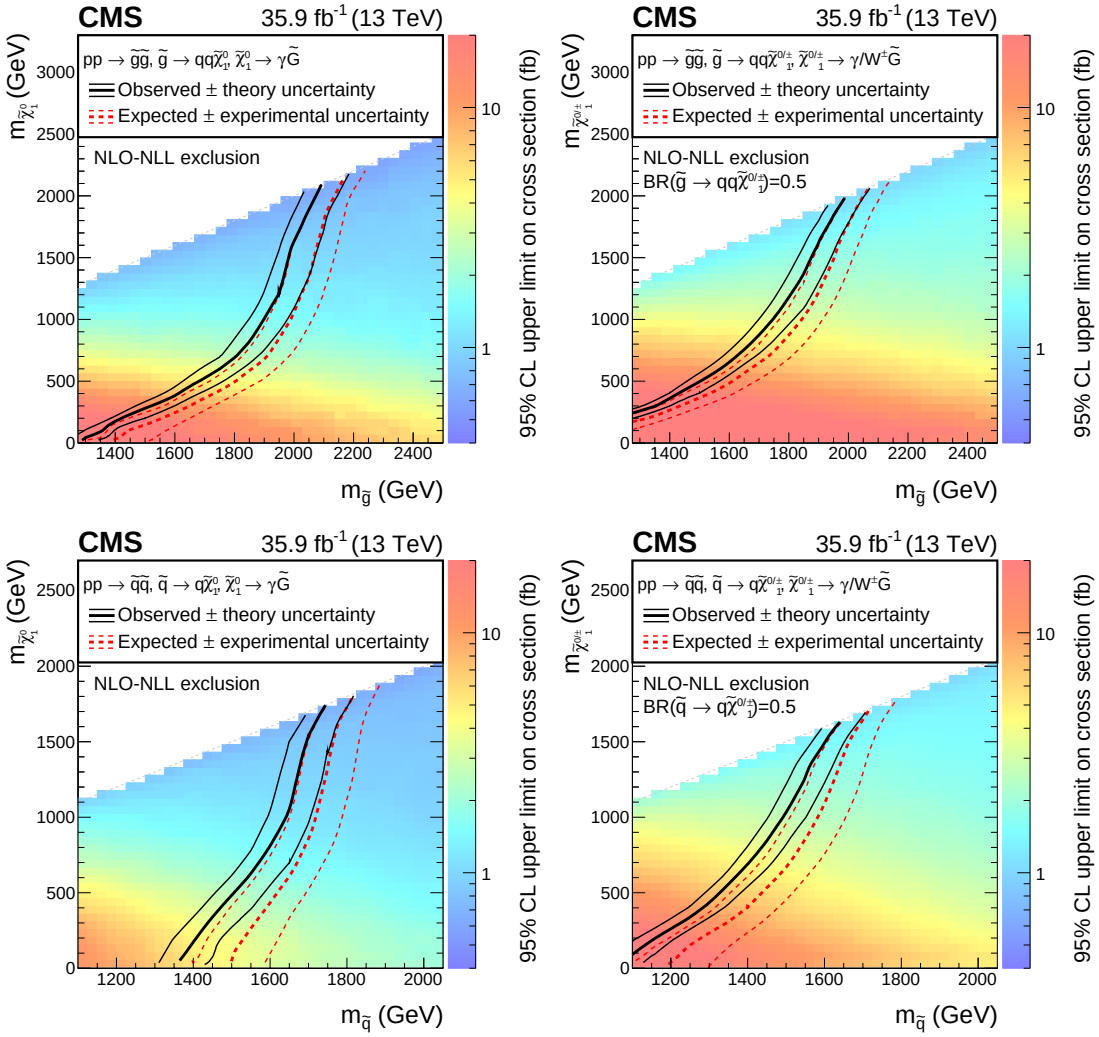

Figure 9.12: The 95% CL limits for the T5gg (top left) and T5Wg (top right), and the T6gg (bottom left) and T6Wg (bottom right) SMS models in the gluino/squark−neutralino/chargino mass plane. The color scale encodes the observed upper cross section limit for each point. The thick lines represent the observed (black) and expected (red) exclusion contours, where the phase space of lower masses is excluded by the analysis. The thin dotted red curves indicate the region containing 68% of the distribution of limits expected under the background-only hypothesis. The thin solid black curves show the change in the observed limit due to variation of the signal cross sections within their theoretical uncertainties. For the signal production cross section of squarks five accessible mass-degenerate squark flavors for $\tilde{q}_L$ and $\tilde{q}_R$ are assumed.

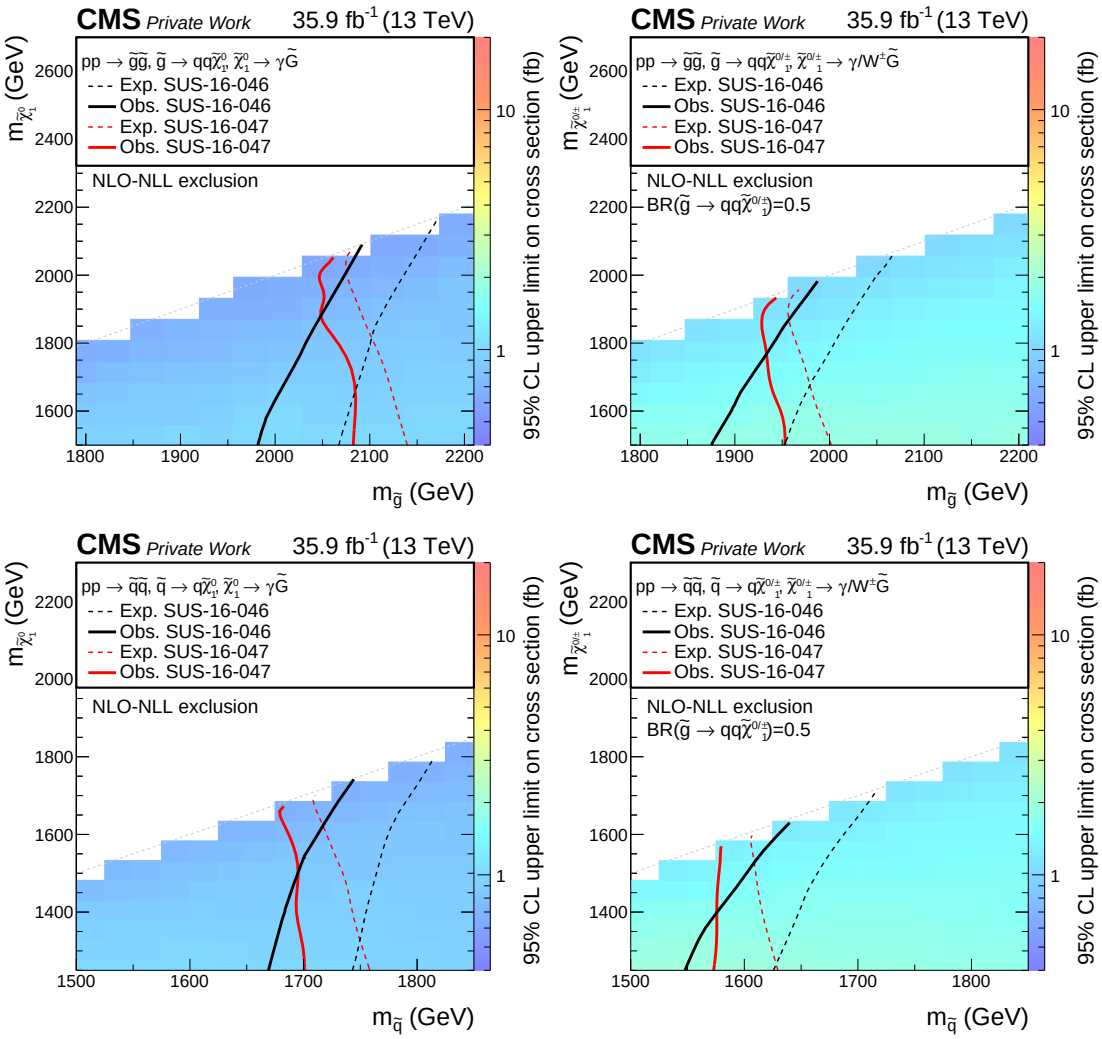

Figure 9.13: Expected (dashed) and observed (solid) exclusion limits at 95% CL set by SUS-16-046 (black) and SUS-16-047 (red) in the T5gg (top left), T5Wg (top right), T6gg (bottom right), and the T6Wg (bottom left) scenario. The color scale encodes the observed upper cross section limit for each point set by SUS-16-046.

9.3.3 Observed significances and reinterpretation of the results

Representative for EWK and strong production SUSY models, the observed significances are shown in Fig. 9.14 for the GGM and the T5Wg scenario, respectively. The observed significances for all other SUSY scenarios are provided in Fig. F.1 in the appendix. As already observed for the signal points defining the exclusion contours in the limits shown in the previous section, the observed limit is weaker compared to the expected limit, also reflected here by positive values of the observed significances. The largest observed significance is 1.6 standard deviations (s.d.). For the statistical interpretation, the analysis combines the yields of four signal region bins with adjacent phase spaces. Therefore, the transition of the significances for SUSY scenarios of similar mass configuration is smooth. In the phase space considered for the strong production scenarios, almost only the highest two S_T^γ bins are populated by signal events, resulting in similar significance values for all mass points. For the EWK scenarios, all signal region bins are populated by signal events with varying parts for different mass configurations. Therefore, the observed significances of the EWK scenarios show larger variations for different signal points, depending on which S_T^γ bin is driving the cross section limit.

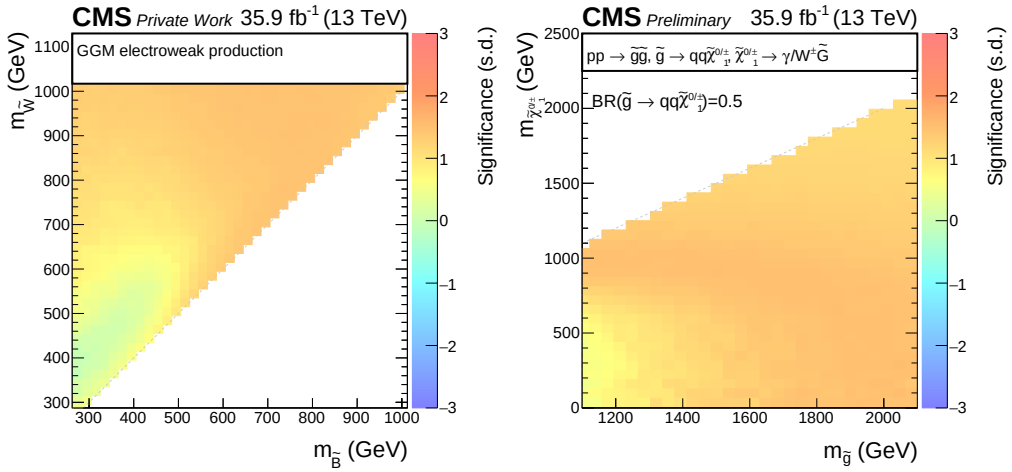

Figure 9.14: Observed significances in standard deviations (s.d.) for the GGM (left) and T5Wg (right) signal scenarios. The largest observed significance is 1.6 s.d., reflecting the slight excess of events measured in the highest S_T^γ bins.

The analysis uses several models to interpret the results in the light of SUSY. Besides these models, further SUSY or other BSM models expecting events in the signal region investigated by this analysis are conceivable. One key guidance of the analysis strategy was to enable the reinterpretation of the results by phenomenologists. In addition, the inclusive event selection provides results with a high generality. Therefore, also the covariance and correlation matrices [197], showing the correlation of the total SM background in the SR

bins, are provided in Fig. 9.15. Since all SR bins are dominated by the V(γ) background, large correlations are observed among the SR bins.

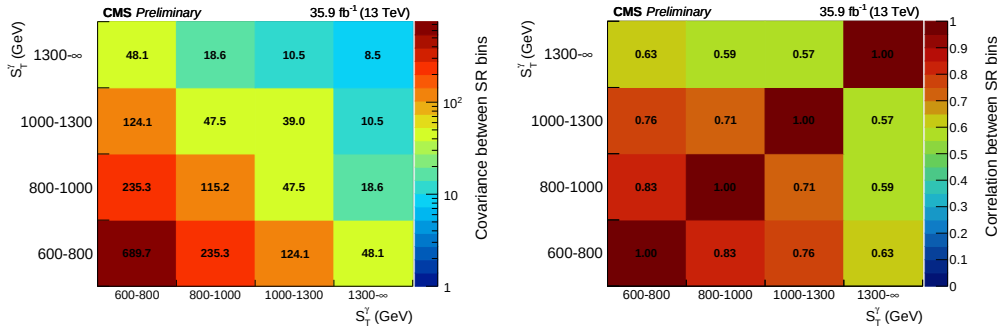

Figure 9.15: Covariance (left) and correlation (right) matrices for the SM background composition of the four signal region bins.

Chapter 10

Summary and Outlook

A search for electroweak (EWK) and strong production of supersymmetric particles in final states with photons and large missing transverse momentum has been presented in this document. A data set of proton-proton collisions at a center-of-mass energy of 13 TeV recorded by the CMS experiment was analyzed. The data set corresponds to an integrated luminosity of 35.9 fb^{-1}. Final states with photons and large missing transverse momentum are expected in scenarios with gauge-mediated supersymmetry (SUSY) breaking with high probability, if the next-to-lightest SUSY particle is a neutralino with bino or wino components and if the neutralino decays promptly.

The search was optimized for a transparent event selection that is inclusive with regard to EWK and strong production of SUSY particles to maximize the probability of discovery and to serve as inclusive analysis for the reinterpretation of the results in further models of new physics. The event selection almost only exploits the properties of photons and gravitinos, without any requirements on the presence or absence of jets or charged leptons.

With a contribution of 77% to the signal region, the most dominant standard model background comes from Z boson and $\text{W}^{\pm}$ boson production, especially with photon radiation, $\text{V}(\gamma)$, where the Z boson decays into two neutrinos and the $\text{W}^{\pm}$ boson decays into a charged lepton and a neutrino. The shape of these processes was estimated using Monte-Carlo simulation. The normalization of the $\text{V}(\gamma)$ background was determined in a signal-depleted fit control region. The background from $\gamma + \text{jets}$ events has a significant contribution to the fit control region, but is almost negligible in the signal and validation region. To determine scale factors with high precision, the $\text{V}(\gamma)$ and $\gamma + \text{jets}$ backgrounds were fitted simultaneously in the distribution $|\Delta\phi(\vec{p}_{\text{T}}^{\,\text{miss}}, \text{nearest jet}/\gamma)|$ in which the two fit components have different shapes. Prior to the fit, the $\text{V}(\gamma)$ and $\gamma + \text{jets}$ background contribute with a similar number of events to the fit control region. The remaining backgrounds include pair production of top quarks with and without photon radiation ($\text{t}\bar{\text{t}}(\gamma)$), electrons misidentified as photons ($\text{e} \to \gamma$), and diboson processes. In total these only make up for 18% of the backgrounds contributing to the fit control region prior to the fit and remain with a fixed normalization in the fit. The scale factors for $\text{V}(\gamma)$

and γ + jets were found to be 0.87 and 1.83 with a statistical precision of 6.9 and 3.3%, respectively. Several sources of systematic uncertainties affect the shape predicted from simulation and were determined for each bin in the signal region and both backgrounds separately. These systematic uncertainties vary from 7 to 11% for the dominant V(γ) background and result in a total uncertainty in the V(γ) background of $10.2 - 13.8\%$ depending on the signal region bin. The $\mathrm{t\bar{t}}(\gamma)$ and diboson backgrounds were estimated using Monte-Carlo simulations, while the contribution of the $\mathrm{e} \to \gamma$ background was estimated scaling electron control regions with the electron-to-photon misidentification probability determined with data. The total standard model background prediction was found to be stable in all cross checks.

The data were compared to the expectation based on the standard model in the signal region. No significant deviations were observed. Upper cross section and exclusion limits have been calculated at 95% confidence level for several SUSY models. The analysis is sensitive to EWK production of charginos and neutralinos and to strong production of gluinos and squarks in particular if the mass difference between gauginos and gluinos or squarks is small. A two-dimensional EWK signal scan in the framework of general gauge mediation was used to interpret the results. In the case of similar wino and bino masses, the analysis excludes masses below 980 GeV, improving on the former best limit by 270 GeV. Two EWK simplified models were also used for interpretation, in which the analysis excludes masses of the next-to-lightest supersymmetric particle up to 780 GeV and 950 GeV. Limits have been set for strong production simplified models based on gluino and squark pair production, excluding gluino (squark) masses up to 2100 (1750) GeV.

This analysis complements searches investigating photon final states with high jet activity, final states with at least two photons, and photon final states with one charged lepton. The analysis sets the most stringent limits to date in the EWK production models, and in the strong production models if gauginos and gluinos or squarks have similar masses.

The predecessor analysis and the search presented in this document are published in Physics Letters B 759 (2016) 479 and Physics Letters B 780 (2018) 118, respectively.

The data set recorded by CMS in 2012, which was analyzed by the predecessor analysis SUS-14-016, was significantly larger compared to the data sets recorded in the years before. This, and the remarkably lower trigger thresholds of the parked data set enabled the development of a new analysis with high sensitivity to EWK SUSY models. The analysis SUS-14-016 set the highest exclusion limits in all considered models and built the foundation for the successor analyses SUS-16-023 and SUS-16-046, developed using the data sets recorded in 2015 and 2016, respectively. From the beginning of the data taking in 2015, the center-of-mass energy was increased from 8 to 13 TeV, significantly increasing the production cross sections of SUSY particles. However, the impact on the cross section is much larger for (heavy) squarks and gluinos compared to lighter gauginos produced via electroweak interactions. The event selection for the analysis SUS-16-046 was changed to obtain sensitivity to both EWK and strong production SUSY scenarios

with photons in the final state. As, besides the large increase in the center-of-mass energy, also the integrated luminosity of the data set taken in 2016 was almost doubled compared to the 2012 data set, the results obtained in SUSY searches based on the 2016 data set represent a milestone in the quest for SUSY. The analysis SUS-16-046 reduced the complexity of the event selection compared to the predecessor analyses to enable the reinterpretation of the results in other models for new physics. In 2017, CMS recorded 46 fb^{-1} of data in pp collisions at 13 TeV, and approximately 70 fb^{-1} of data are expected for the run in 2018, before the LHC starts the second long shutdown period. As no significant deviations are observed in SUS-16-046, the data sets recorded in 2017 and 2018 could serve the development or improvement of the analysis methods. Figure 10.1 shows an extrapolation of the expected limit for 150 fb^{-1} in the TChiWg (left) and T5Wg (right) model under the assumption of similar relative uncertainties compared to the analysis presented in this document. No significant increase in the exclusion limits of SUSY particle masses is expected.

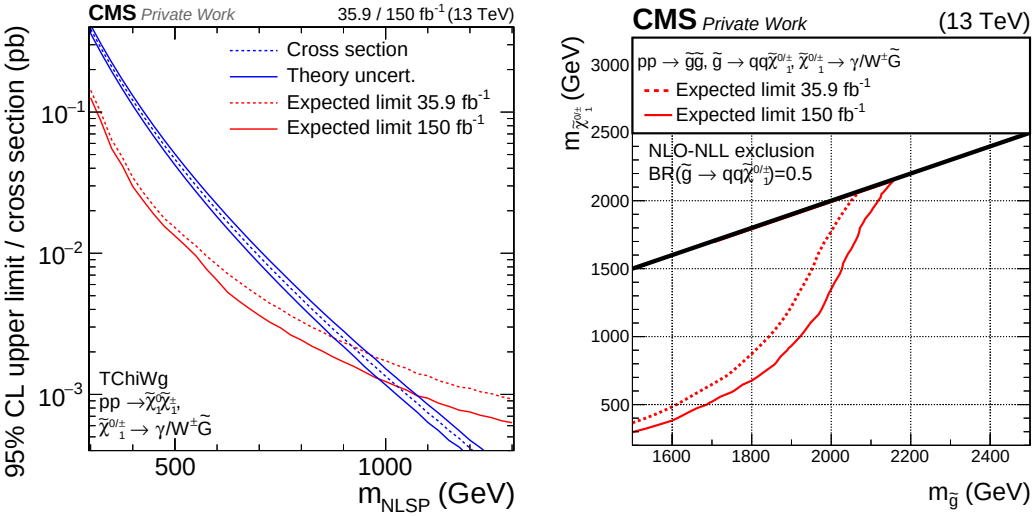

Figure 10.1: Extrapolation of the expected limits for 150 fb^{-1} (solid red lines) in the TChiWg (left) and T5Wg (right) model compared to the limits based on 35.9 fb^{-1} (dashed red lines). Similar relative uncertainties as determined in the analysis SUS-16-046 are assumed. The thick black line in the right plot indicates the diagonal for which the next-to-lightest SUSY particles and gluinos have same masses.

The SM background prediction methods developed in SUS-14-016 and applied in SUS-16-023 and SUS-16-046 are found to be stable as proven with three statistically independent data sets. A good precision is achieved in the prediction of the most dominant background V(γ), with a total uncertainty of 10.2 to 13.8%, depending on the signal region bin, with the systematic uncertainties dominating the total uncertainty. As the fit eliminates all uncertainties in the normalization up to a certain precision of statistical origin, the systematic uncertainties arise from the simulated shape of the Monte-Carlo samples. A

sophisticated data-driven approach might be able to further reduce the uncertainty in the V(γ) prediction, although data-driven methods are often accompanied by uncertainties in the extrapolation of the prediction to significantly different phase spaces. The stability would have to be checked in detailed studies. One possibility could be to use $Z(\rightarrow \mu\mu)\gamma$ data events to predict the most dominant background process $Z(\rightarrow \nu\nu)\gamma$ in the signal region. This method suffers from statistical precision but would gain from the combination of the 2017 and 2018 data sets with the 2016 data set. In case of improvement the total gain of developing new background prediction methods is expected to be small for this analysis.

One of the key ideas of this thesis was to provide a transparent analysis and comprehensive results, in contrast to several other SUSY searches employing complex selection methods and defining over 100 signal region bins. Nevertheless, to increase sensitivity to a specific signal scenario, more exclusive event selections might be applied or an expansion of signal regions binned in characteristic variables, e.g., the hadronic activity or number of leptons or photons, could be defined.

A plot summarizing the mass exclusion limits set by CMS SUSY analyses in the context of gauge-mediated SUSY breaking is shown in Fig. 10.2. The analysis at hand, in Fig. 10.2 abbreviated by "γ + ME_T: arXiv:1711.08008", makes an important contribution to the overall mass reach of CMS SUSY searches in scenarios with photons in the final state. Besides this analysis, there are other SUSY searches within the CMS collaboration targeting similar phase spaces with large missing transverse momentum, i.e., the analysis SUS-16-047 investigating final states with at least one photon and large hadronic activity and the analysis SUS-17-012 targeting signatures with at least one photon and one charged lepton. A sensible statistical combination of the results of these analyses might increase the overall sensitivity to SUSY scenarios with photons in the final state. There are efforts within the CMS collaboration to perform such a combination, possibly also including the results of the analysis SUS-17-011 targeting final states with two photons.

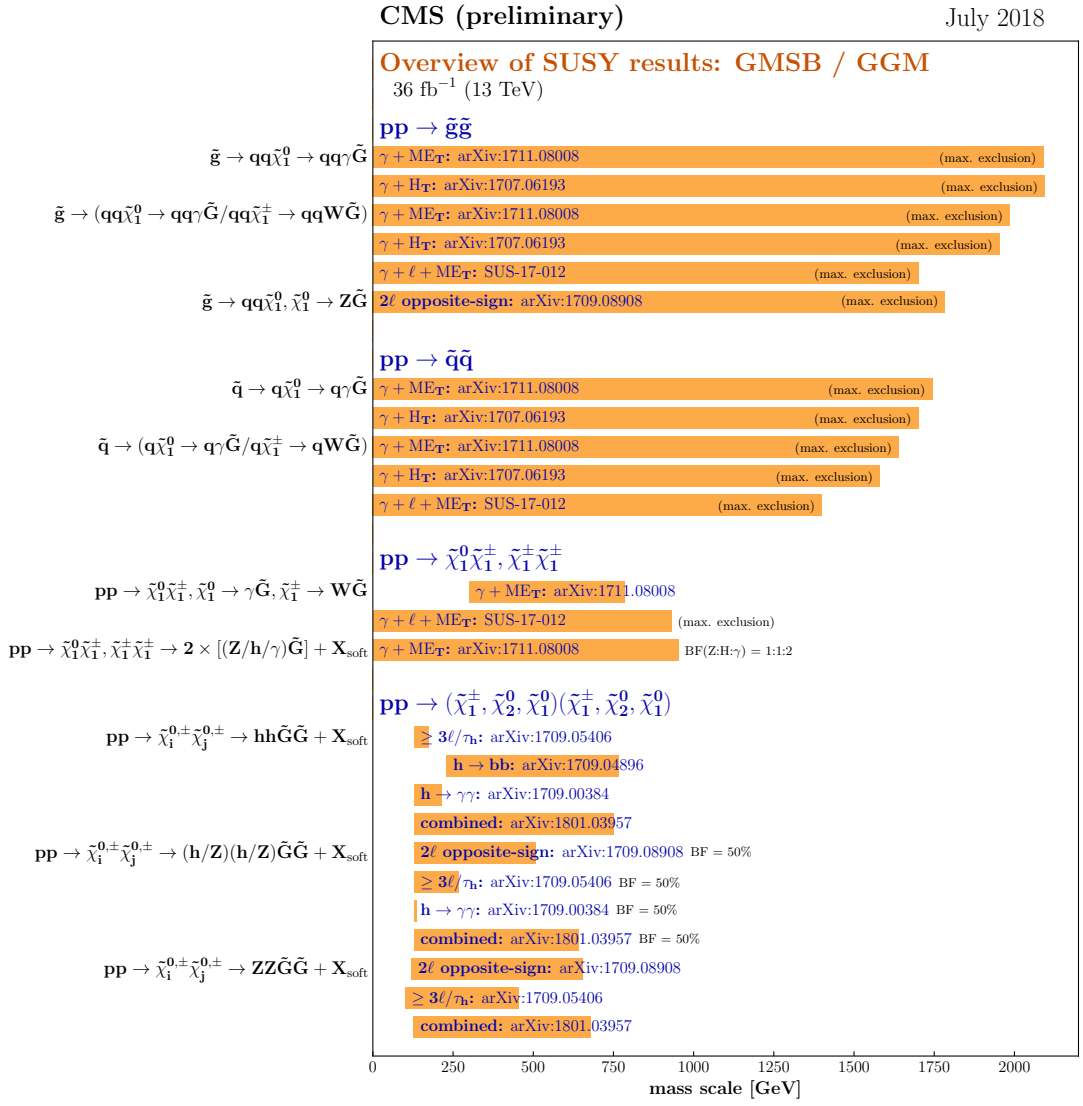

Figure 10.2: Summary plot of the mass reach of CMS SUSY searches in scenarios with gauge-mediated SUSY breaking [198]. The analysis at hand is abbreviated by "γ + ME$_T$: arXiv:1711.08008" and makes an important contribution to the overall mass reach of CMS SUSY searches in scenarios with photons in the final state.

Appendix A

Trigger efficiencies

The signal trigger requires one photon candidate reconstructed by an HLT-optimized particle-flow algorithm with $p_{\mathrm{T}} > 165\,\mathrm{GeV}$ and $H/E < 0.1$. The trigger efficiency is measured in dependency of $p_{\mathrm{T}}(\gamma)$ to ensure that the offline requirement of $p_{\mathrm{T}}(\gamma) > 180\,\mathrm{GeV}$ covers the systematic turn-on effect around the trigger threshold of 165 GeV so that the trigger efficiency is constant over the whole $p_{\mathrm{T}}(\gamma)$ phase space used in the analysis. To ensure that no systematic dependency on the trigger efficiency enters the analysis, also all other variables used in the event selection are checked, as shown in this appendix.

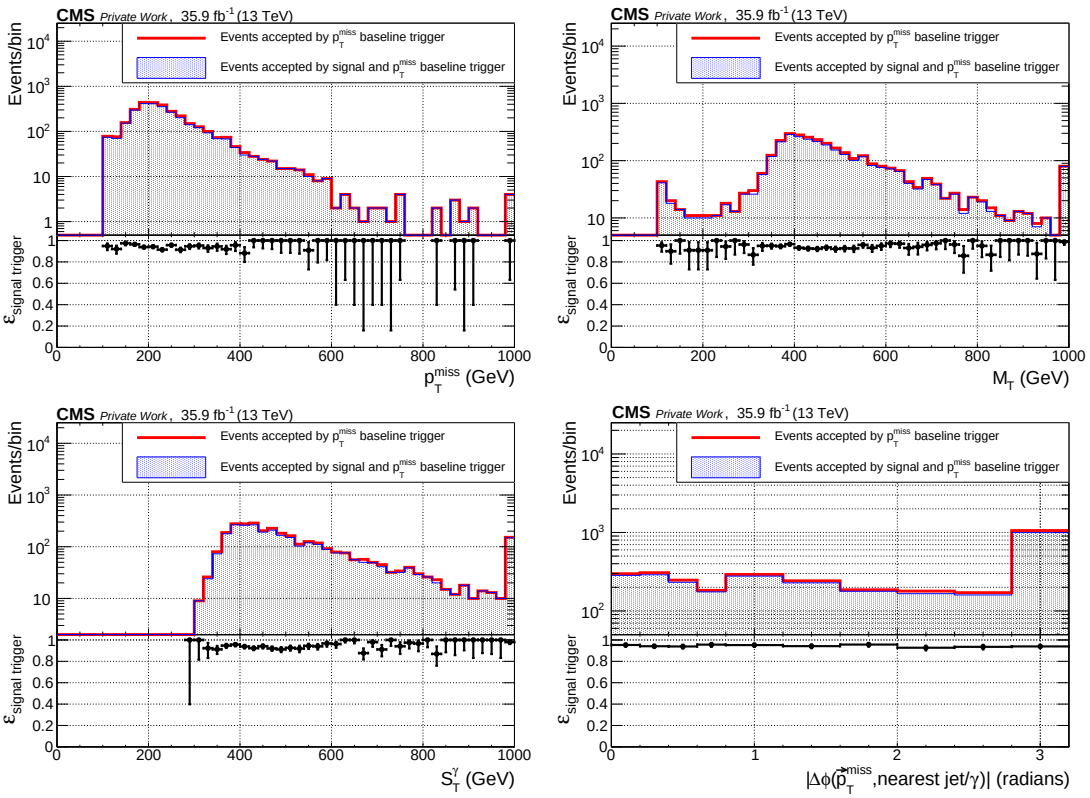

Figure A.1: Signal trigger efficiency as a function of $p_{\mathrm{T}}^{\mathrm{miss}}$ (top left), $\mathrm{M_T}$ (top right), $\mathrm{S_T^{\gamma}}$ (bottom left), and $|\Delta\phi(\vec{p}_{\mathrm{T}}^{\,\mathrm{miss}}, \text{nearest jet}/\gamma)|$ (bottom right). The measurement is performed using the `HLT_PFMET170` baseline trigger in the phase space defined by the preselection and requiring $p_{\mathrm{T}}^{\mathrm{miss}}$ and $\mathrm{M_T} > 100\,\mathrm{GeV}$.

Appendix B

Simulated data sets

DBS paths of all standard model background and signal Monte-Carlo samples used in the analysis are listed in Tables B.1 and B.2. Several standard model background samples are simulated for adjacent generator-based H_T or $p_T(\gamma)$ intervals to increase the statistical precision of the simulation.

Table B.1: DBS paths of the SM background MC samples used for the background prediction or studies. The cross sections are given to the order used by the generator.

/*/RunIISummer16MiniAODv2-PUMoriond17_80X_mcRun2_asymptotic_2016_TrancheIV_v6*/MINIAODSIM	σ[pb]
/GJets_HT-40To100_TuneCUETP8M1_13TeV-madgraphMLM-pythia8/*-v1/*	20790
/GJets_HT-100To200_TuneCUETP8M1_13TeV-madgraphMLM-pythia8/*-v4/*	9238
/GJets_HT-200To400_TuneCUETP8M1_13TeV-madgraphMLM-pythia8/*-v1/*	2305
/GJets_HT-400To600_TuneCUETP8M1_13TeV-madgraphMLM-pythia8/*-v1/*	274.4
/GJets_HT-600ToInf_TuneCUETP8M1_13TeV-madgraphMLM-pythia8/*-v1/*	93.46
/QCD_HT100to200_TuneCUETP8M1_13TeV-madgraphMLM-pythia8/*-ĭ/*	27990000
/QCD_HT200to300_TuneCUETP8M1_13TeV-madgraphMLM-pythia8/*_ext1-v1/*	1712000
/QCD_HT300to500_TuneCUETP8M1_13TeV-madgraphMLM-pythia8/*_ext1-v1/*	347700
/QCD_HT500to700_TuneCUETP8M1_13TeV-madgraphMLM-pythia8/*_ext1-v1/*	32100
/QCD_HT700to1000_TuneCUETP8M1_13TeV-madgraphMLM-pythia8/*_ext1-v1/*	6831
/QCD_HT1000to1500_TuneCUETP8M1_13TeV-madgraphMLM-pythia8/*_ext1-v1/*	1207
/QCD_HT1500to2000_TuneCUETP8M1_13TeV-madgraphMLM-pythia8/*_ext1-v1/*	119.9
/QCD_HT2000toInf_TuneCUETP8M1_13TeV-madgraphMLM-pythia8/*_ext1-v1/*	25.24
/ZNuNuGJets_MonoPhoton_PtG-130_TuneCUETP8M1_13TeV-madgraph/*-v1/*	0.223
/ZLLGJets_MonoPhoton_PtG-130_TuneCUETP8M1_13TeV-madgraph/*-v1/*	0.143
/WGJets_MonoPhoton_PtG-130_TuneCUETP8M1_13TeV-madgraph/*-v1/*	0.834
/ZJetsToNuNu_HT-100To200_13TeV-madgraph/*_ext1-v1/*	280.47
/ZJetsToNuNu_HT-200To400_13TeV-madgraph/*_ext1-v1/*	77.67
/ZJetsToNuNu_HT-400To600_13TeV-madgraph/*_ext1-v1/*	10.73
/ZJetsToNuNu_HT-600To800_13TeV-madgraph/*-v1/*	2.559
/ZJetsToNuNu_HT-800To1200_13TeV-madgraph/*-v3/*	1.1796
/ZJetsToNuNu_HT-1200To2500_13TeV-madgraph/*_ext1-v1/*	0.28833
/ZJetsToNuNu_HT-2500ToInf_13TeV-madgraph/*-v1/*	0.006945
/WJetsToLNu_HT-100To200_TuneCUETP8M1_13TeV-madgraphMLM-pythia8/*_ext1-v1/*	1345
/WJetsToLNu_HT-200To400_TuneCUETP8M1_13TeV-madgraphMLM-pythia8/*_ext1-v1/*	359.7
/WJetsToLNu_HT-400To600_TuneCUETP8M1_13TeV-madgraphMLM-pythia8/*_ext1-v1/*	48.91
/WJetsToLNu_HT-600To800_TuneCUETP8M1_13TeV-madgraphMLM-pythia8/*_ext1-v1/*	12.05
/WJetsToLNu_HT-800To1200_TuneCUETP8M1_13TeV-madgraphMLM-pythia8/*_ext1-v1/*	5.501
/WJetsToLNu_HT-1200To2500_TuneCUETP8M1_13TeV-madgraphMLM-pythia8/*_ext1-v1/*	1.329
/WJetsToLNu_HT-2500ToInf_TuneCUETP8M1_13TeV-madgraphMLM-pythia8/*_ext1-v1/*	0.03216
/TTGJets_TuneCUETP8M1_13TeV-amcatnloFXFX-madspin-pythia8/*-v1/*	3.697
/TTJets_TuneCUETP8M1_13TeV-amcatnloFXFX-pythia8/*-v1/*	831.76
/WWTo2L2Nu_13TeV-powheg/*-v1/*	12.178
/WWToLNuQQ_13TeV-powheg/*-v1/*	49.997
/ZZ_TuneCUETP8M1_13TeV-pythia8/*-v1/*	16.523
/WZ_TuneCUETP8M1_13TeV-pythia8/*-v1/*	47.13

Table B.2: DBS paths of the signal samples used in the analysis. Note that the T5gg and T6gg SMS are extracted from the T5Wg and T6Wg SMS, respectively.

/*_TuneCUETP8M1_13TeV-madgraphMLM-pythia8/ RunIISpring16MiniAODv2-PUSpring16Fast_80X_mcRun2_asymptotic_2016_miniAODv2_v0-v1/ MINIAODSIM
/SMS-TChiWG*/*/* /SMS-TChiNG_BF50N50G*/*/* /SMS-T5Wg*/*/* /SMS-T6Wg*/*/* /SMS-T5Wg_mGo2150To2500*/*/* /SMS-T6Wg_mSq1850To2150*/*/*
/GMSB_GravitinoLSP_N1decays_TuneCUETP8M1_13TeV_pythia8/ RunIISummer16MiniAODv2-PUSummer16Fast_80X_mcRun2_asymptotic_2016_TrancheIV_v6-v1/ MINIAODSIM

Appendix C

Validation plots for the prediction method for misidentified electrons

In addition to the e $\rightarrow \gamma$ validation plots depending on S_T^γ presented in Section 8.3.2, Fig. C.1 - C.3 show p_T^{miss}, M_T, and $p_T(\gamma)$ in the same phase spaces, namely after applying the preselection, but requiring $p_T(\gamma) > 100\,\text{GeV}$, additionally requiring $p_T^{miss} > 50\,\text{GeV}$ and $M_T > 50\,\text{GeV}$, and in the fit control region. Good agreement is observed within the uncertainties between the prediction obtained by applying the e $\rightarrow \gamma$ estimation method to simulation and the direct generator match.

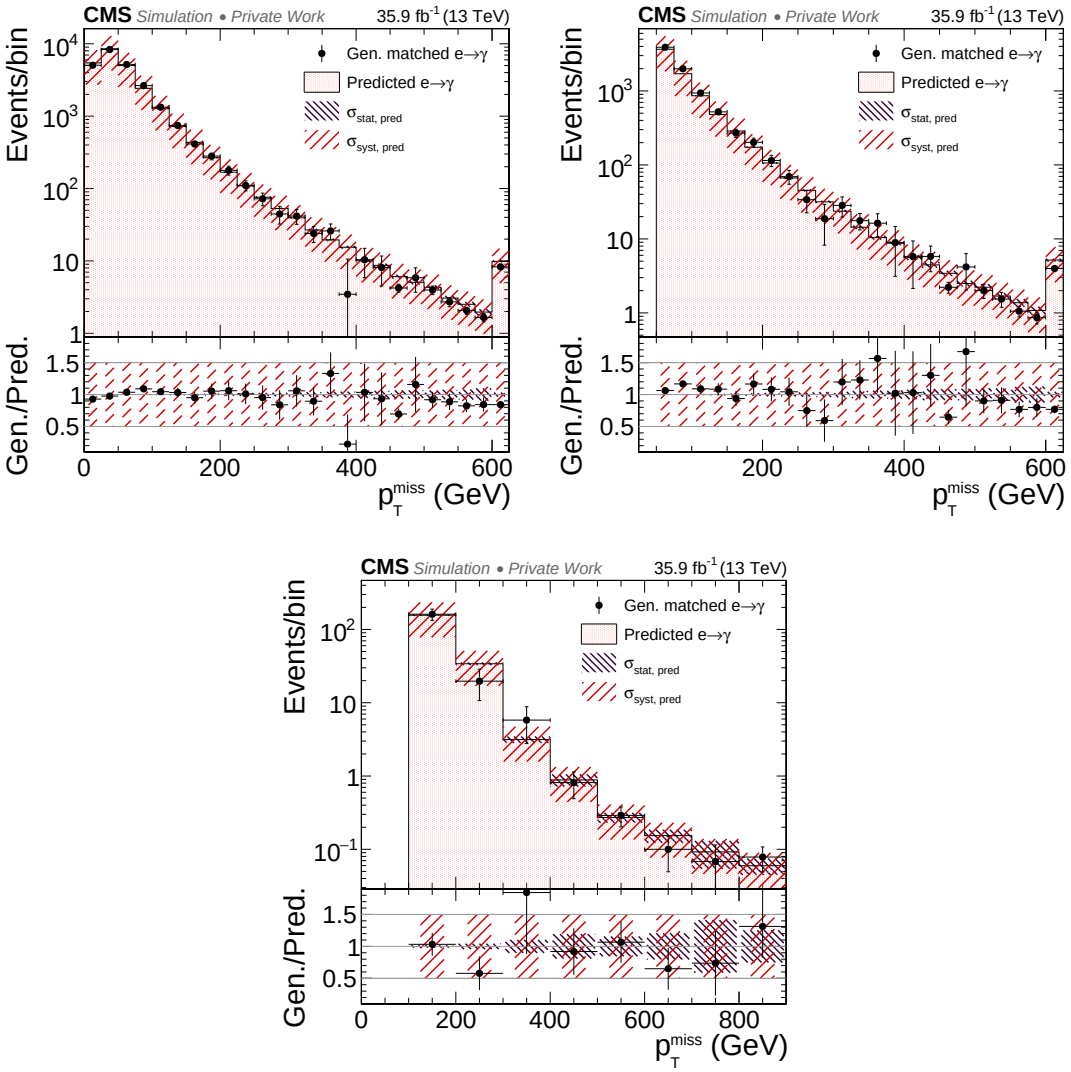

Figure C.1: Validation plots for the e $\rightarrow \gamma$ background estimation method for $p_{\mathrm{T}}^{\mathrm{miss}}$ after applying the preselection, but requiring $p_{\mathrm{T}}(\gamma) > 100\,\mathrm{GeV}$ (top left), additionally requiring $p_{\mathrm{T}}^{\mathrm{miss}} > 50\,\mathrm{GeV}$ and $\mathrm{M_T} > 50\,\mathrm{GeV}$ (top right), and in the fit control region (bottom).

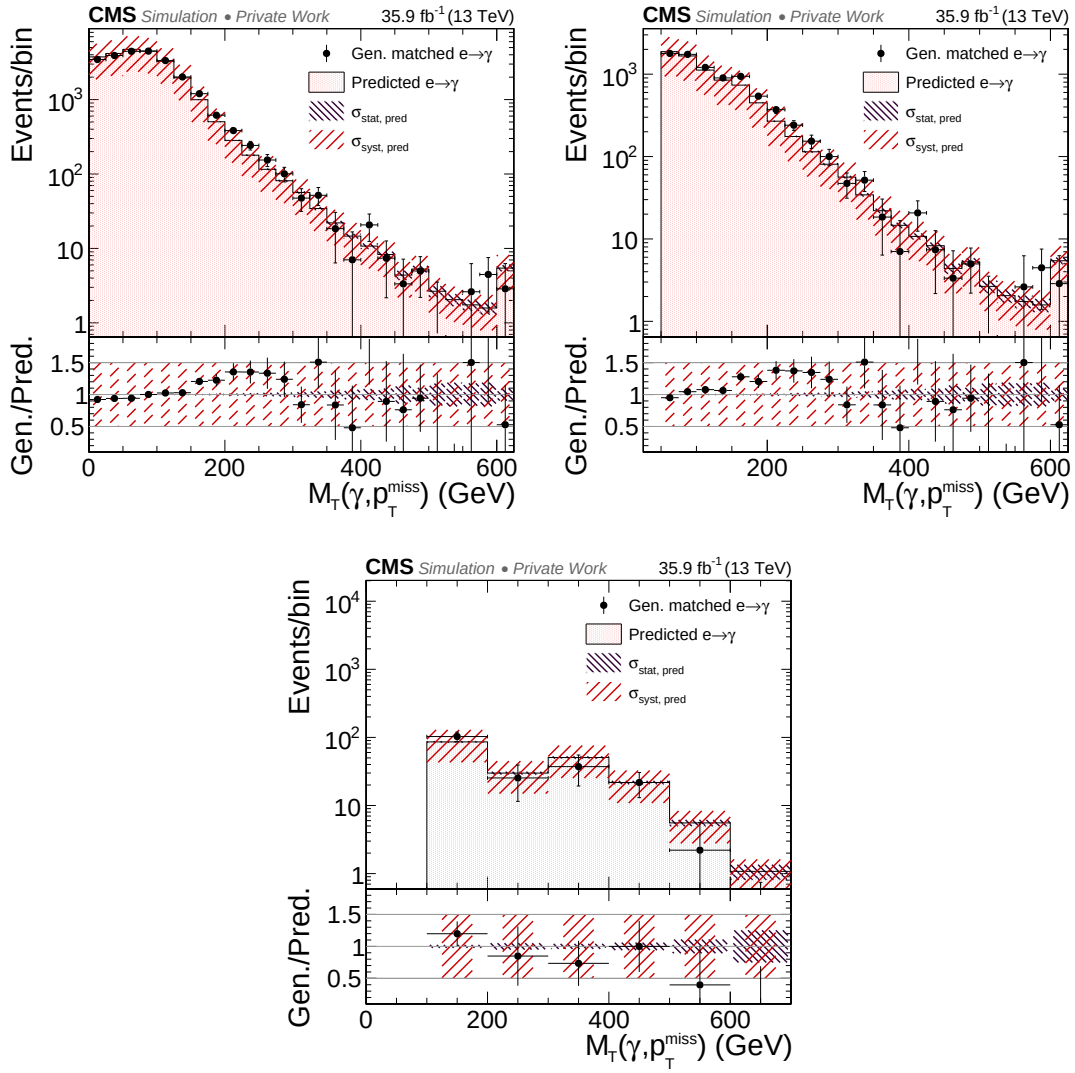

Figure C.2: Validation plots for the e $\rightarrow \gamma$ background estimation method for M_T after applying the preselection, but requiring $p_T(\gamma) > 100\,\text{GeV}$ (top left), additionally requiring $p_T^{\text{miss}} > 50\,\text{GeV}$ and $M_T > 50\,\text{GeV}$ (top right), and in the fit control region (bottom).

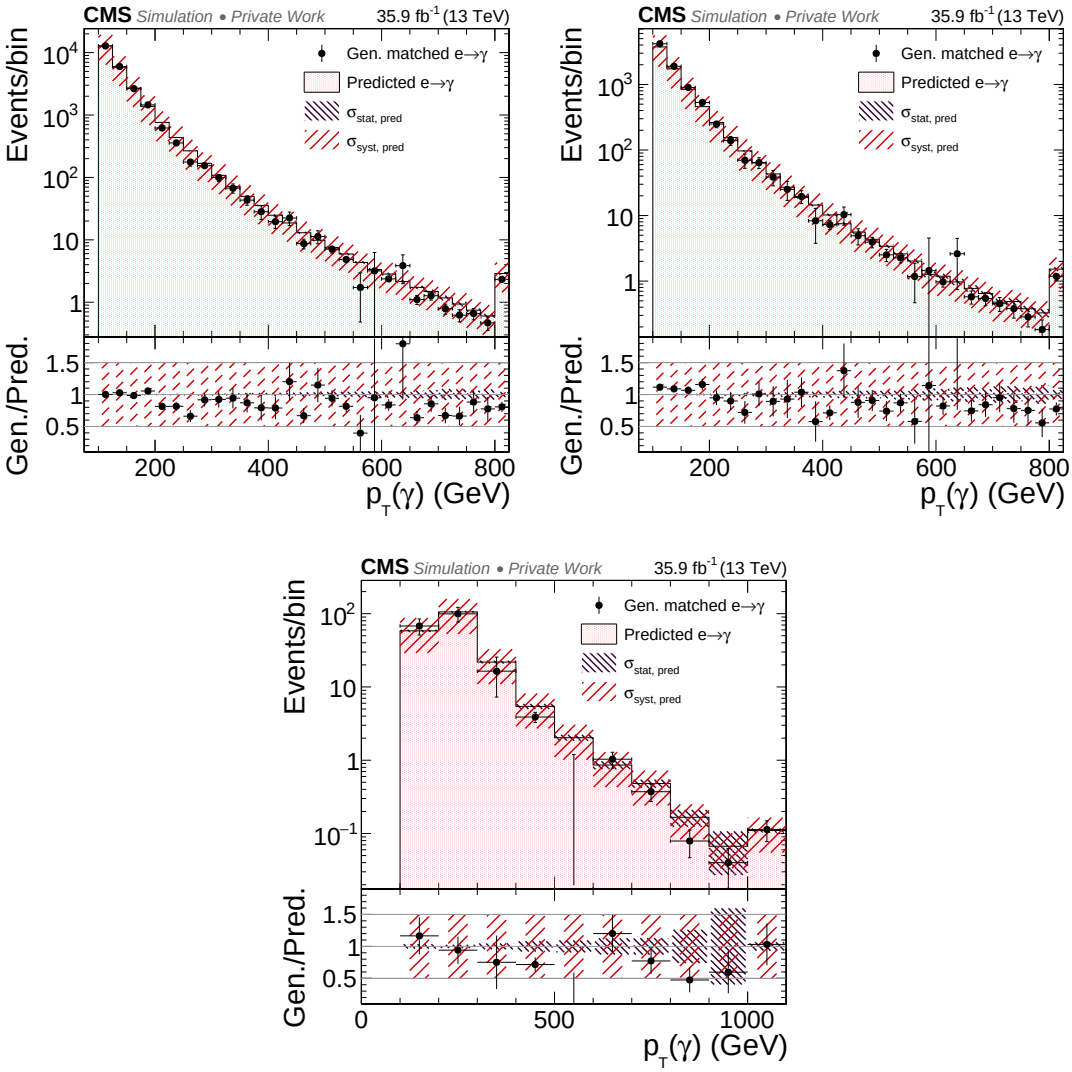

Figure C.3: Validation plots for the e $\rightarrow \gamma$ background estimation method for $p_{\mathrm{T}}(\gamma)$ after applying the preselection, but requiring $p_{\mathrm{T}}(\gamma) > 100\,\mathrm{GeV}$ (top left), additionally requiring $p_{\mathrm{T}}^{\mathrm{miss}} > 50\,\mathrm{GeV}$ and $\mathrm{M_T} > 50\,\mathrm{GeV}$ (top right), and in the fit control region (bottom).

Appendix D

Systematic uncertainties in the shape due to the choice of PDF sets

To determine the shape uncertainty in the simulation of the V(γ) and $\gamma+$jets background due to the choice of the PDFs, 100 replicas of each PDF are used to rescale the MC simulation [188]. The event selection, the fit, and the final prediction of the background contribution to the signal region are performed for each rescaling separately. The standard deviation with respect to the mean prediction of all 100 variations is determined bin-by-bin in the signal region and is taken as systematic uncertainty. Table 8.6 in Section 8.4.2 shows the absolute and relative deviations with respect to the mean determined based on the 100 replicas of the PDFs for V(γ) and $\gamma+$jets. The respective scale factors and deviations from the nominal prediction are shown in the main document to improve the readability but are listed in Tables D.1−D.9 for completeness.
The index given in the first column refers to the weight saved in the MC sample for the respective PDF replica. The indices $9-108$ correspond to the different PDF replicas, while the indices $0-8$ give the nominal value and variations of the renormalization and factorization scale.
The deviations from the nominal prediction in the signal region are listed in Tables D.4−D.9 and are visualized in Fig. 8.8 in the main document.
A visualization of the scale factors listed in Tables D.1−D.3 obtained by fitting the rescaled MC samples is provided in Fig. D.1, also showing the fit results for different renormalization and factorization scales.

Table D.1: Scale factor fit result for the V(γ) and $\gamma+$jets backgrounds using different replicas of the PDF sets.

Index	$\mathcal{SF}_{\mathrm{V}(\gamma)}$	$\mathcal{SF}_{\gamma+\mathrm{jets}}$
9	0.87	1.83
10	0.88	1.88
11	0.89	1.91
12	0.87	1.81
13	0.87	1.84
14	0.89	1.90
15	0.89	1.89
16	0.83	1.75
17	0.86	1.87
18	0.88	1.85
19	0.90	1.97
20	0.89	1.87
21	0.88	1.88
22	0.89	1.87
23	0.77	1.61
24	0.88	1.85
25	0.89	1.89
26	0.87	1.84
27	0.77	1.62
28	0.91	1.87
29	0.88	1.84
30	0.87	1.83
31	0.87	1.87
32	0.91	1.92
33	0.86	1.87
34	0.77	1.63
35	0.82	1.74
36	0.88	1.85
37	0.81	1.74
38	0.89	1.89
39	0.88	1.86
40	0.87	1.84
41	0.84	1.78
42	0.87	1.84

Table D.2: Scale factor fit result for the V(γ) and $\gamma+$jets backgrounds using different replicas of the PDF sets.

Index	$\mathcal{SF}_{\mathrm{V}(\gamma)}$	$\mathcal{SF}_{\gamma+\mathrm{jets}}$
43	0.88	1.89
44	0.87	1.87
45	0.88	1.89
46	0.89	1.90
47	0.87	1.87
48	0.88	1.86
49	0.87	1.83
50	0.87	1.89
51	0.87	1.86
52	0.88	1.85
53	0.87	1.86
54	0.87	1.85
55	0.81	1.70
56	0.88	1.87
57	0.87	1.86
58	0.86	1.88
59	0.76	1.62
60	0.88	1.86
61	0.86	1.87
62	0.88	1.87
63	0.70	1.50
64	0.87	1.85
65	0.73	1.54
66	0.88	1.89
67	0.80	1.73
68	0.89	1.87
69	0.88	1.85
70	0.87	1.84
71	0.85	1.84
72	0.87	1.82
73	0.87	1.86
74	0.88	1.86
75	0.88	1.86

Table D.3: Scale factor fit result for the V(γ) and $\gamma+$jets backgrounds using different replicas of the PDF sets.

Index	$\mathcal{SF}_{\mathrm{V}(\gamma)}$	$\mathcal{SF}_{\gamma+\mathrm{jets}}$
76	0.78	1.63
77	0.84	1.77
78	0.88	1.85
79	0.86	1.85
80	0.88	1.86
81	0.89	1.81
82	0.86	1.84
83	0.85	1.81
84	0.89	1.89
85	0.93	1.89
86	0.92	1.90
87	0.87	1.89
88	0.87	1.86
89	0.88	1.87
90	0.87	1.85
91	0.88	1.83
92	0.86	1.86
93	0.88	1.86
94	0.87	1.84
95	0.87	1.84
96	0.86	1.79
97	0.90	1.78
98	0.89	1.87
99	0.88	1.83
100	0.87	1.89
101	0.88	1.86
102	0.89	1.91
103	0.87	1.82
104	0.88	1.88
105	0.88	1.85
106	0.88	1.88
107	0.88	1.82
108	0.90	1.85

Table D.4: Absolute (abs.) and relative (rel.) deviations from the nominal prediction for V(γ) in the four signal region bins using different PDF replicas.

	S_T^γ :							
V(γ)	$600-800$ GeV		$800-1000$ GeV		$1000-1300$ GeV		>1300 GeV	
Index	abs.	rel.	abs.	rel.	abs.	rel.	abs.	rel.
9	0.43	0.2%	-0.07	-0.1%	-0.05	-0.1%	-0.04	-0.3%
10	3.12	1.5%	1.08	1.4%	0.60	1.7%	0.53	4.2%
11	1.97	0.9%	-0.36	-0.5%	-0.39	-1.1%	-0.71	-5.7%
12	-2.97	-1.4%	-1.70	-2.2%	-0.66	-1.9%	-0.57	-4.5%
13	-0.32	-0.1%	-0.08	-0.1%	-0.32	-0.9%	-0.26	-2.1%
14	1.57	0.7%	0.82	1.1%	0.08	0.2%	0.18	1.4%
15	1.12	0.5%	-0.47	-0.6%	-0.52	-1.5%	-0.63	-5.0%
16	0.89	0.4%	-0.04	-0.0%	0.12	0.4%	-0.01	-0.1%
17	4.48	2.1%	1.21	1.6%	0.40	1.2%	0.33	2.6%
18	-1.26	-0.6%	-0.48	-0.6%	0.12	0.4%	-0.11	-0.8%
19	0.46	0.2%	-0.73	-0.9%	-1.06	-3.0%	-0.74	-5.9%
20	-6.27	-2.9%	-3.17	-4.1%	-1.70	-4.9%	-0.79	-6.2%
21	2.54	1.2%	-0.12	-0.2%	-0.23	-0.6%	-0.13	-1.0%
22	-1.34	-0.6%	-0.71	-0.9%	-0.34	-1.0%	0.07	0.6%
23	-4.89	-2.3%	-1.90	-2.5%	-0.59	-1.7%	-0.53	-4.2%
24	4.48	2.1%	1.26	1.6%	1.13	3.2%	0.18	1.4%
25	2.17	1.0%	0.09	0.1%	0.14	0.4%	-0.06	-0.5%
26	2.43	1.1%	0.85	1.1%	1.51	4.3%	0.20	1.6%
27	-6.95	-3.2%	-2.87	-3.7%	-1.47	-4.2%	-0.73	-5.8%
28	-5.47	-2.6%	-2.38	-3.1%	-0.62	-1.8%	-0.86	-6.8%
29	10.53	4.9%	3.88	5.0%	2.17	6.2%	1.43	11.3%
30	1.02	0.5%	0.43	0.6%	0.32	0.9%	-0.05	-0.4%
31	0.99	0.5%	-0.33	-0.4%	-0.10	-0.3%	-0.08	-0.6%
32	-0.57	-0.3%	-0.39	-0.5%	-0.01	-0.0%	-0.37	-2.9%
33	1.47	0.7%	-0.03	-0.0%	-0.46	-1.3%	-0.06	-0.5%
34	-5.10	-2.4%	-2.22	-2.9%	-0.83	-2.4%	-0.36	-2.9%
35	-4.66	-2.2%	-2.03	-2.6%	-0.84	-2.4%	-0.16	-1.2%
36	1.41	0.7%	1.44	1.9%	0.89	2.5%	0.83	6.6%
37	-2.76	-1.3%	-1.02	-1.3%	-0.31	-0.9%	-0.31	-2.5%
38	-1.60	-0.8%	-0.71	-0.9%	0.03	0.1%	-0.14	-1.1%
39	3.00	1.4%	1.07	1.4%	0.20	0.6%	-0.02	-0.2%
40	-0.86	-0.4%	-0.86	-1.1%	-0.71	-2.0%	-0.27	-2.1%
41	-0.20	-0.1%	0.00	0.0%	0.13	0.4%	-0.23	-1.8%
42	1.33	0.6%	0.49	0.6%	0.09	0.3%	-0.10	-0.8%

Table D.5: Absolute (abs.) and relative (rel.) deviations from the nominal prediction for V(γ) in the four signal region bins using different PDF replicas.

	S_T^γ :							
V(γ)	$600-800$ GeV		$800-1000$ GeV		$1000-1300$ GeV		>1300 GeV	
Index	abs.	rel.	abs.	rel.	abs.	rel.	abs.	rel.
43	1.50	0.7%	0.27	0.3%	0.17	0.5%	0.39	3.1%
44	0.91	0.4%	-0.30	-0.4%	-0.52	-1.5%	-0.20	-1.6%
45	4.11	1.9%	0.46	0.6%	0.11	0.3%	0.11	0.9%
46	-0.47	-0.2%	-0.84	-1.1%	-0.85	-2.4%	-0.62	-4.9%
47	0.81	0.4%	-0.26	-0.3%	-0.68	-1.9%	-0.29	-2.3%
48	0.82	0.4%	-0.31	-0.4%	0.45	1.3%	-0.42	-3.3%
49	0.66	0.3%	0.34	0.4%	-0.17	-0.5%	-0.00	-0.0%
50	-0.68	-0.3%	-0.74	-1.0%	-0.85	-2.4%	0.15	1.2%
51	-1.05	-0.5%	-0.71	-0.9%	-0.35	-1.0%	-0.06	-0.5%
52	0.88	0.4%	0.14	0.2%	-0.01	-0.0%	-0.31	-2.4%
53	0.34	0.2%	-0.32	-0.4%	-0.38	-1.1%	-0.12	-0.9%
54	-0.92	-0.4%	-0.41	-0.5%	-0.10	-0.3%	-0.20	-1.6%
55	-1.59	-0.7%	-0.66	-0.9%	-0.17	-0.5%	-0.28	-2.2%
56	6.51	3.0%	2.53	3.3%	1.21	3.5%	1.00	8.0%
57	-0.95	-0.4%	-0.30	-0.4%	-0.51	-1.4%	-0.12	-1.0%
58	0.72	0.3%	-0.02	-0.0%	-0.54	-1.5%	0.18	1.4%
59	-3.46	-1.6%	-1.41	-1.8%	-0.67	-1.9%	-0.30	-2.4%
60	1.93	0.9%	0.85	1.1%	0.28	0.8%	0.34	2.7%
61	2.83	1.3%	0.56	0.7%	0.41	1.2%	0.77	6.1%
62	-1.89	-0.9%	-0.56	-0.7%	-0.36	-1.0%	0.16	1.3%
63	-9.28	-4.3%	-3.53	-4.6%	-1.54	-4.4%	-0.85	-6.7%
64	-0.55	-0.3%	-0.79	-1.0%	-0.84	-2.4%	-0.43	-3.4%
65	-7.90	-3.7%	-2.41	-3.1%	-1.06	-3.0%	-0.20	-1.6%
66	0.62	0.3%	-0.21	-0.3%	-0.19	-0.5%	0.04	0.3%
67	-3.48	-1.6%	-2.37	-3.1%	-1.24	-3.5%	-0.63	-5.0%
68	-1.00	-0.5%	-0.58	-0.8%	-0.57	-1.6%	-0.18	-1.4%
69	1.65	0.8%	-0.06	-0.1%	0.21	0.6%	-0.09	-0.7%
70	-2.62	-1.2%	-1.17	-1.5%	-1.14	-3.3%	-0.57	-4.5%
71	-0.89	-0.4%	-0.60	-0.8%	-0.58	-1.6%	-0.11	-0.9%
72	-1.91	-0.9%	-0.57	-0.7%	-0.23	-0.7%	-0.27	-2.2%
73	-1.13	-0.5%	-0.76	-1.0%	-0.57	-1.6%	-0.04	-0.3%
74	-1.20	-0.6%	-0.93	-1.2%	-0.52	-1.5%	-0.17	-1.3%
75	0.17	0.1%	-0.27	-0.4%	-0.02	-0.1%	0.18	1.4%

Table D.6: Absolute (abs.) and relative (rel.) deviations from the nominal prediction for V(γ) in the four signal region bins using different PDF replicas.

	S_T^γ :							
V(γ)	$600-800$ GeV		$800-1000$ GeV		$1000-1300$ GeV		>1300 GeV	
Index	abs.	rel.	abs.	rel.	abs.	rel.	abs.	rel.
76	-8.48	-4.0%	-3.33	-4.3%	-1.40	-4.0%	-0.27	-2.1%
77	-0.09	-0.0%	-0.69	-0.9%	-0.52	-1.5%	-0.25	-2.0%
78	-0.11	-0.0%	-0.30	-0.4%	-0.26	-0.7%	0.04	0.3%
79	0.11	0.0%	-0.76	-1.0%	-0.96	-2.7%	-0.67	-5.3%
80	-1.00	-0.5%	-0.60	-0.8%	-0.07	-0.2%	-0.09	-0.7%
81	-0.61	-0.3%	-0.38	-0.5%	0.89	2.5%	0.18	1.5%
82	-1.01	-0.5%	0.13	0.2%	0.06	0.2%	0.13	1.1%
83	1.81	0.8%	0.04	0.0%	-0.27	-0.8%	-0.34	-2.7%
84	-2.37	-1.1%	-1.39	-1.8%	-0.68	-1.9%	-0.45	-3.5%
85	-7.86	-3.7%	-2.82	-3.7%	-0.43	-1.2%	-0.62	-5.0%
86	7.81	3.7%	3.91	5.1%	1.85	5.3%	0.86	6.8%
87	2.22	1.0%	0.35	0.5%	-0.02	-0.1%	0.38	3.0%
88	1.42	0.7%	-0.11	-0.1%	0.52	1.5%	0.17	1.3%
89	0.70	0.3%	0.35	0.5%	-0.04	-0.1%	0.12	0.9%
90	-0.05	-0.0%	-0.53	-0.7%	-0.39	-1.1%	-0.18	-1.4%
91	2.60	1.2%	0.82	1.1%	0.34	1.0%	0.04	0.3%
92	-0.43	-0.2%	-0.16	-0.2%	-0.20	-0.6%	0.01	0.0%
93	0.95	0.4%	0.12	0.2%	-0.05	-0.2%	0.19	1.5%
94	-0.10	-0.0%	-0.26	-0.3%	0.03	0.1%	-0.03	-0.2%
95	-2.44	-1.1%	-1.63	-2.1%	-1.05	-3.0%	-0.65	-5.2%
96	0.70	0.3%	1.05	1.4%	0.76	2.2%	0.16	1.3%
97	8.21	3.8%	5.45	7.1%	3.61	10.3%	1.76	14.0%
98	2.33	1.1%	0.78	1.0%	0.48	1.4%	0.12	1.0%
99	12.61	5.9%	5.65	7.4%	3.02	8.6%	1.39	11.0%
100	2.66	1.2%	0.37	0.5%	-0.21	-0.6%	-0.06	-0.5%
101	3.62	1.7%	1.05	1.4%	0.45	1.3%	0.44	3.5%
102	-0.00	-0.0%	-1.00	-1.3%	-0.68	-1.9%	-0.49	-3.9%
103	1.06	0.5%	0.33	0.4%	0.57	1.6%	0.48	3.8%
104	0.71	0.3%	-0.15	-0.2%	-0.35	-1.0%	-0.30	-2.4%
105	2.40	1.1%	0.53	0.7%	0.52	1.5%	-0.05	-0.4%
106	0.47	0.2%	-0.39	-0.5%	-0.49	-1.4%	-0.15	-1.2%
107	3.56	1.7%	2.22	2.9%	1.45	4.1%	0.53	4.2%
108	1.21	0.6%	0.91	1.2%	0.13	0.4%	-0.03	-0.2%

Table D.7: Absolute (abs.) and relative (rel.) deviations from the nominal prediction for $\gamma + \text{jets}$ in the four signal region bins using different PDF replicas.

	S_T^γ :							
$\gamma + \text{jets}$	$600 - 800\,\text{GeV}$		$800 - 1000\,\text{GeV}$		$1000 - 1300\,\text{GeV}$		$> 1300\,\text{GeV}$	
Index	abs.	rel.	abs.	rel.	abs.	rel.	abs.	rel.
9	-0.01	-0.2%	-0.01	-0.2%	-0.01	-0.2%	-0.00	-0.2%
10	0.10	2.1%	-0.08	-1.8%	0.00	0.1%	0.05	5.0%
11	-0.64	-12.7%	-0.19	-4.3%	-0.07	-1.8%	-0.00	-0.1%
12	-0.28	-5.6%	-0.01	-0.3%	-0.11	-2.6%	-0.08	-7.3%
13	-0.18	-3.6%	0.03	0.7%	-0.01	-0.2%	-0.05	-4.3%
14	-0.41	-8.2%	-0.09	-2.0%	0.03	0.7%	0.07	6.7%
15	-0.61	-12.1%	-0.06	-1.3%	0.03	0.7%	0.01	1.4%
16	0.20	3.9%	0.09	2.1%	0.06	1.4%	-0.03	-2.9%
17	0.34	6.8%	-0.02	-0.4%	0.02	0.5%	0.09	8.3%
18	-0.12	-2.5%	0.07	1.6%	0.09	2.2%	0.02	2.1%
19	-0.74	-14.7%	-0.16	-3.6%	-0.03	-0.7%	0.04	3.8%
20	-0.66	-13.2%	-0.20	-4.5%	-0.17	-3.9%	-0.05	-4.7%
21	0.09	1.8%	-0.12	-2.7%	-0.08	-2.0%	-0.01	-0.6%
22	-0.29	-5.8%	-0.08	-1.7%	-0.07	-1.6%	0.01	1.3%
23	-0.23	-4.7%	0.04	0.9%	0.06	1.4%	-0.01	-1.0%
24	-0.09	-1.9%	-0.03	-0.6%	0.03	0.7%	0.07	6.7%
25	-0.20	-4.1%	-0.11	-2.5%	-0.09	-2.2%	0.03	2.5%
26	0.30	6.0%	0.10	2.3%	0.04	1.0%	-0.01	-0.9%
27	-0.14	-2.9%	-0.03	-0.7%	-0.07	-1.7%	-0.09	-8.7%
28	0.09	1.8%	-0.14	-3.2%	-0.15	-3.5%	-0.14	-13.1%
29	1.23	24.5%	-0.02	-0.4%	0.09	2.1%	0.11	10.5%
30	-0.01	-0.2%	0.08	1.9%	0.10	2.3%	0.01	0.5%
31	0.09	1.8%	-0.08	-1.8%	-0.04	-0.9%	0.04	3.3%
32	0.29	5.7%	-0.08	-1.8%	0.00	0.0%	-0.00	-0.3%
33	0.08	1.7%	-0.06	-1.3%	0.04	1.0%	0.05	5.0%
34	0.90	18.0%	0.09	2.1%	0.04	0.8%	-0.07	-6.8%
35	-0.07	-1.3%	-0.02	-0.6%	-0.05	-1.2%	-0.01	-1.1%
36	0.09	1.8%	0.06	1.4%	0.07	1.7%	0.02	2.0%
37	-0.20	-4.0%	0.02	0.5%	0.16	3.8%	0.06	5.7%
38	-0.07	-1.3%	-0.05	-1.1%	0.03	0.7%	0.03	2.9%
39	-0.17	-3.5%	0.03	0.6%	-0.00	-0.1%	0.00	0.1%
40	0.15	3.0%	-0.03	-0.8%	-0.05	-1.1%	-0.01	-1.1%
41	0.93	18.6%	0.05	1.2%	0.04	1.0%	-0.01	-0.5%
42	0.24	4.9%	0.10	2.4%	0.07	1.6%	-0.01	-0.5%

Table D.8: Absolute (abs.) and relative (rel.) deviations from the nominal prediction for $\gamma + \text{jets}$ in the four signal region bins using different PDF replicas.

	S_T^γ :							
$\gamma + \text{jets}$	$600 - 800\,\text{GeV}$		$800 - 1000\,\text{GeV}$		$1000 - 1300\,\text{GeV}$		$> 1300\,\text{GeV}$	
Index	abs.	rel.	abs.	rel.	abs.	rel.	abs.	rel.
43	-0.50	-10.1%	-0.07	-1.5%	-0.01	-0.3%	0.08	7.7%
44	-0.11	-2.2%	-0.07	-1.6%	-0.07	-1.7%	0.02	2.0%
45	0.12	2.4%	-0.06	-1.3%	-0.13	-3.1%	-0.01	-0.6%
46	-0.49	-9.7%	-0.08	-1.8%	-0.11	-2.6%	-0.05	-4.4%
47	-0.59	-11.7%	-0.08	-1.8%	-0.07	-1.7%	0.02	1.7%
48	0.31	6.1%	0.06	1.3%	0.02	0.4%	-0.02	-2.0%
49	0.00	0.0%	-0.02	-0.5%	-0.09	-2.1%	-0.04	-3.9%
50	-0.48	-9.6%	-0.06	-1.3%	-0.04	-0.9%	0.01	0.6%
51	0.17	3.3%	0.03	0.6%	0.01	0.3%	-0.00	-0.3%
52	-0.14	-2.8%	0.03	0.6%	0.01	0.3%	-0.03	-2.9%
53	-0.50	-9.9%	-0.08	-1.7%	0.04	1.0%	0.05	4.9%
54	-0.03	-0.7%	0.08	1.8%	0.04	0.9%	-0.02	-1.7%
55	-0.03	-0.5%	0.14	3.3%	0.08	1.9%	-0.05	-4.9%
56	0.69	13.8%	-0.07	-1.6%	-0.01	-0.2%	0.13	12.0%
57	-0.08	-1.6%	-0.01	-0.3%	-0.09	-2.2%	-0.07	-6.6%
58	-0.38	-7.5%	-0.19	-4.4%	-0.11	-2.6%	0.06	5.6%
59	-0.08	-1.7%	0.11	2.4%	0.04	1.1%	-0.02	-1.9%
60	-0.28	-5.5%	0.02	0.5%	0.04	0.9%	0.01	1.2%
61	1.06	21.2%	-0.11	-2.5%	0.00	0.0%	0.13	12.6%
62	-0.17	-3.4%	0.01	0.2%	0.02	0.5%	-0.01	-1.3%
63	0.18	3.5%	0.12	2.7%	0.07	1.7%	-0.07	-6.3%
64	-0.36	-7.1%	-0.02	-0.4%	-0.01	-0.1%	-0.02	-1.9%
65	0.17	3.4%	0.10	2.3%	0.06	1.4%	-0.05	-4.5%
66	-0.49	-9.8%	-0.07	-1.6%	0.03	0.8%	0.11	9.9%
67	0.26	5.2%	-0.05	-1.2%	-0.08	-1.9%	-0.04	-3.6%
68	-0.13	-2.6%	0.04	0.9%	-0.01	-0.2%	-0.08	-7.4%
69	-0.37	-7.3%	-0.05	-1.1%	-0.01	-0.2%	0.02	2.2%
70	-0.04	-0.7%	0.01	0.2%	-0.04	-0.9%	-0.09	-8.4%
71	-0.21	-4.2%	-0.01	-0.1%	0.02	0.4%	0.00	0.0%
72	-0.08	-1.6%	0.06	1.4%	0.05	1.1%	-0.03	-3.2%
73	0.08	1.6%	-0.05	-1.2%	-0.04	-0.9%	0.01	1.0%
74	-0.27	-5.3%	0.01	0.3%	-0.10	-2.3%	-0.04	-4.2%
75	0.21	4.1%	0.00	0.0%	-0.03	-0.7%	-0.01	-1.1%

Table D.9: Absolute (abs.) and relative (rel.) deviations from the nominal prediction for γ + jets in the four signal region bins using different PDF replicas.

	S_T^γ :							
γ + jets	600 − 800 GeV		800 − 1000 GeV		1000 − 1300 GeV		> 1300 GeV	
Index	abs.	rel.	abs.	rel.	abs.	rel.	abs.	rel.
76	0.00	0.0%	-0.00	-0.0%	-0.02	-0.4%	-0.07	-6.9%
77	-0.44	-8.8%	-0.02	-0.4%	-0.11	-2.7%	-0.03	-3.1%
78	-0.02	-0.3%	-0.03	-0.7%	-0.05	-1.1%	-0.01	-1.2%
79	-0.49	-9.9%	-0.03	-0.6%	-0.07	-1.6%	-0.04	-3.6%
80	0.31	6.3%	-0.02	-0.5%	0.06	1.3%	0.03	2.6%
81	0.56	11.1%	-0.03	-0.6%	0.01	0.3%	-0.04	-4.1%
82	-0.01	-0.1%	-0.03	-0.6%	0.02	0.5%	-0.01	-0.6%
83	-0.54	-10.7%	-0.13	-3.1%	-0.07	-1.7%	0.03	2.6%
84	-0.13	-2.5%	0.07	1.7%	0.01	0.1%	-0.06	-5.7%
85	0.02	0.4%	-0.12	-2.7%	-0.07	-1.7%	-0.10	-9.5%
86	-0.01	-0.2%	0.17	3.9%	0.04	1.1%	-0.03	-3.0%
87	0.46	9.2%	-0.10	-2.4%	-0.08	-1.8%	0.06	5.5%
88	1.33	26.6%	0.09	2.2%	0.07	1.7%	0.04	4.1%
89	-0.15	-3.0%	-0.04	-0.9%	0.02	0.6%	0.01	1.0%
90	0.81	16.1%	-0.04	-1.0%	-0.07	-1.7%	-0.01	-1.0%
91	-0.25	-4.9%	0.06	1.4%	-0.07	-1.7%	-0.07	-7.0%
92	-0.50	-9.9%	-0.09	-2.1%	0.12	2.9%	0.13	11.9%
93	1.03	20.5%	0.04	0.9%	-0.05	-1.1%	-0.03	-3.1%
94	-0.13	-2.6%	0.03	0.6%	-0.06	-1.3%	-0.05	-4.8%
95	0.30	6.0%	-0.05	-1.2%	-0.14	-3.4%	-0.11	-10.3%
96	0.23	4.6%	0.21	4.7%	0.21	4.9%	0.01	0.6%
97	0.59	11.9%	0.41	9.4%	0.44	10.5%	0.03	2.7%
98	0.12	2.3%	0.06	1.4%	0.02	0.6%	0.01	0.8%
99	0.53	10.5%	0.07	1.5%	0.09	2.0%	0.13	12.2%
100	-0.30	-5.9%	-0.07	-1.5%	0.01	0.3%	0.07	6.6%
101	0.22	4.4%	-0.07	-1.6%	0.02	0.4%	0.05	4.3%
102	0.09	1.8%	-0.09	-2.0%	-0.07	-1.7%	0.00	0.3%
103	0.15	2.9%	0.06	1.3%	0.03	0.7%	0.01	0.6%
104	-0.49	-9.8%	-0.04	-1.0%	-0.03	-0.8%	0.01	0.5%
105	-0.20	-3.9%	0.06	1.5%	0.03	0.6%	0.00	0.0%
106	-0.47	-9.4%	-0.05	-1.1%	-0.08	-2.0%	-0.01	-1.2%
107	0.04	0.7%	0.07	1.6%	0.08	1.9%	0.02	2.3%
108	-0.14	-2.8%	0.01	0.2%	-0.05	-1.2%	-0.07	-6.3%

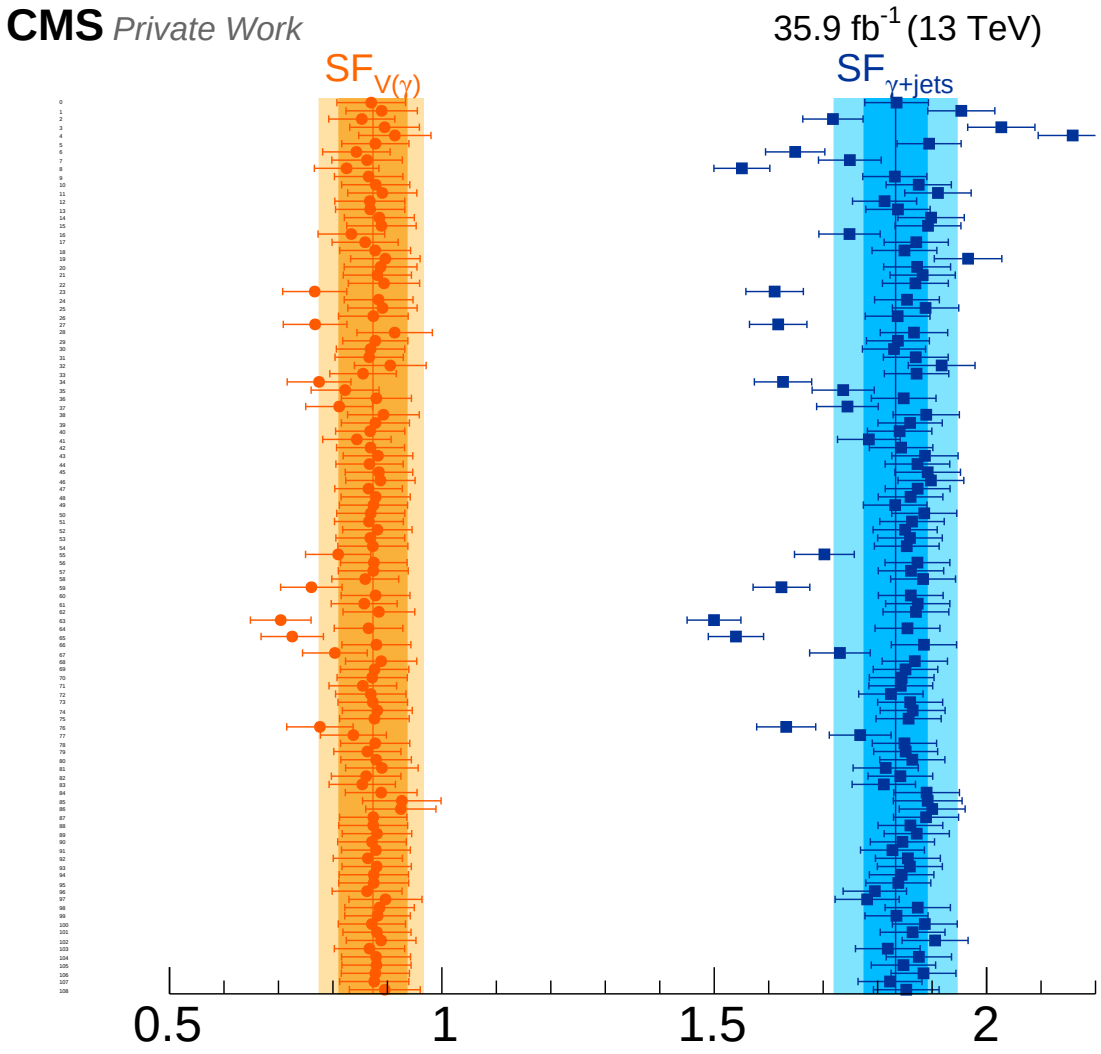

Figure D.1: Nominal fit results (first row, index 0) and fit results for different variations of the renormalization and factorization scale (index/row $1-8$) and for different PDF replicas (index/row $9-108$). The lines and darker, inner error bands correspond to the nominal fit results, the lighter, outer error bands correspond to the squared sum of the fit uncertainty and all other systematic uncertainties arising from the variation of the factorization and renormalization scale, using different PDF weights and shifting the JES by its uncertainty, as described in Section 8.4.2.

Appendix E

Signal uncertainties

Visualization of the uncertainties in the signal simulation as discussed in Section 9.2.3 for those signal scenarios not shown in the main document.

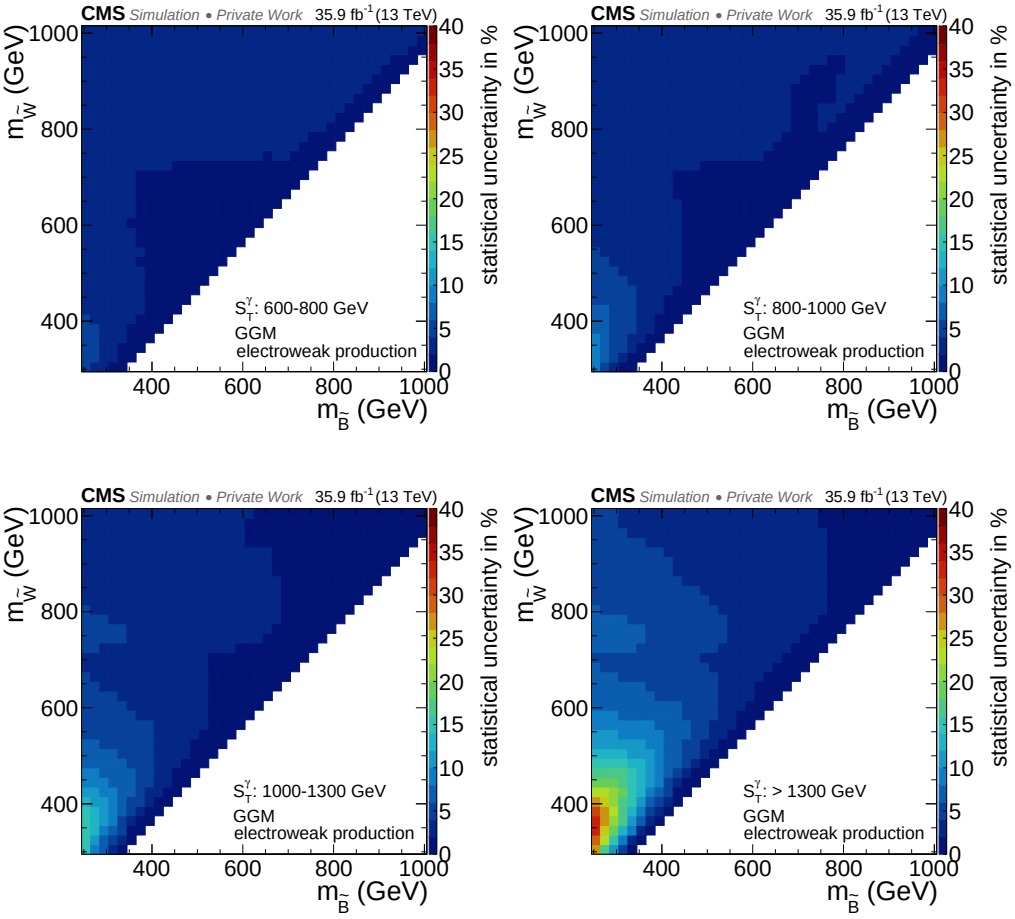

Figure E.1: Statistical uncertainty arising from the finite number of generated events in the signal MC simulation for the GGM EWK production model for the four signal region bins in S_T^γ with $600-800\,\text{GeV}$ (top left), $800-1000\,\text{GeV}$ (top right), $1000-1300\,\text{GeV}$ (bottom left), and more than $1300\,\text{GeV}$ (bottom right).

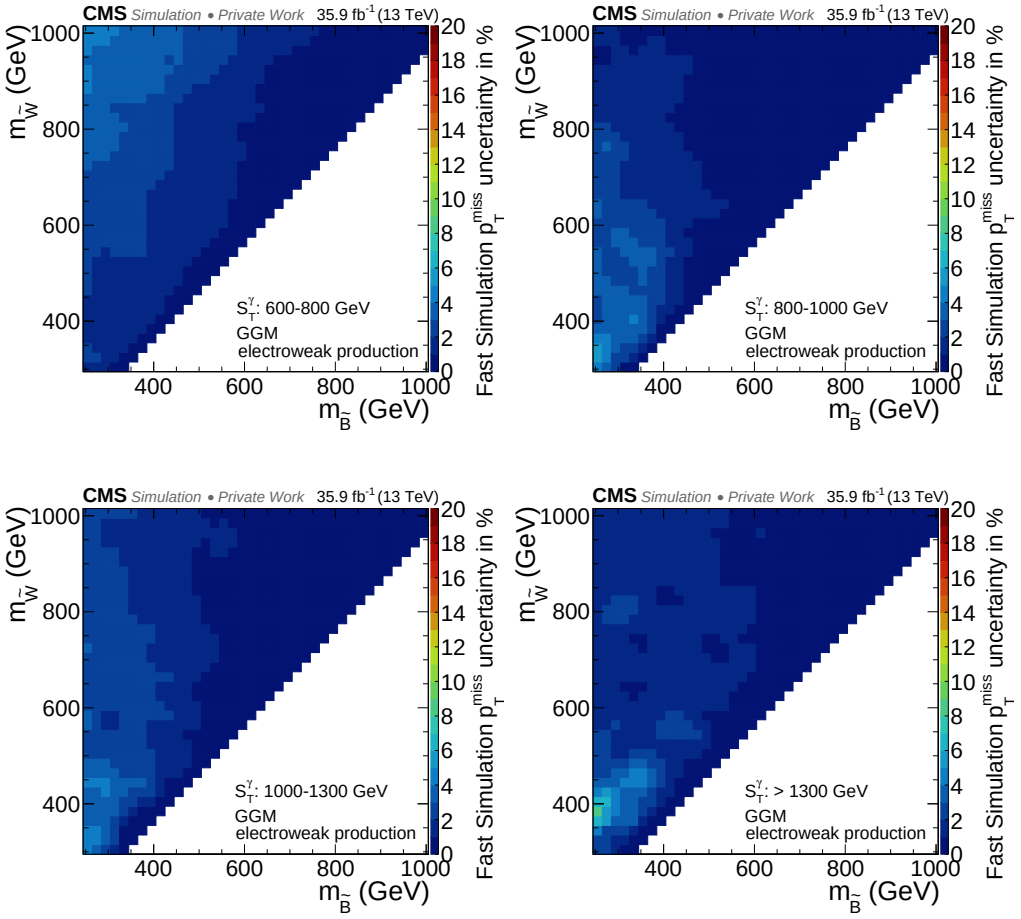

Figure E.2: Systematic uncertainties arising from $p_{\mathrm{T}}^{\mathrm{miss}}$ mismodelling due to the fast simulation of the CMS detector for the GGM EWK production model for the four signal region bins in S_{T}^{γ} with $600 - 800\,\mathrm{GeV}$ (top left), $800 - 1000\,\mathrm{GeV}$ (top right), $1000 - 1300\,\mathrm{GeV}$ (bottom left), and more than $1300\,\mathrm{GeV}$ (bottom right)..

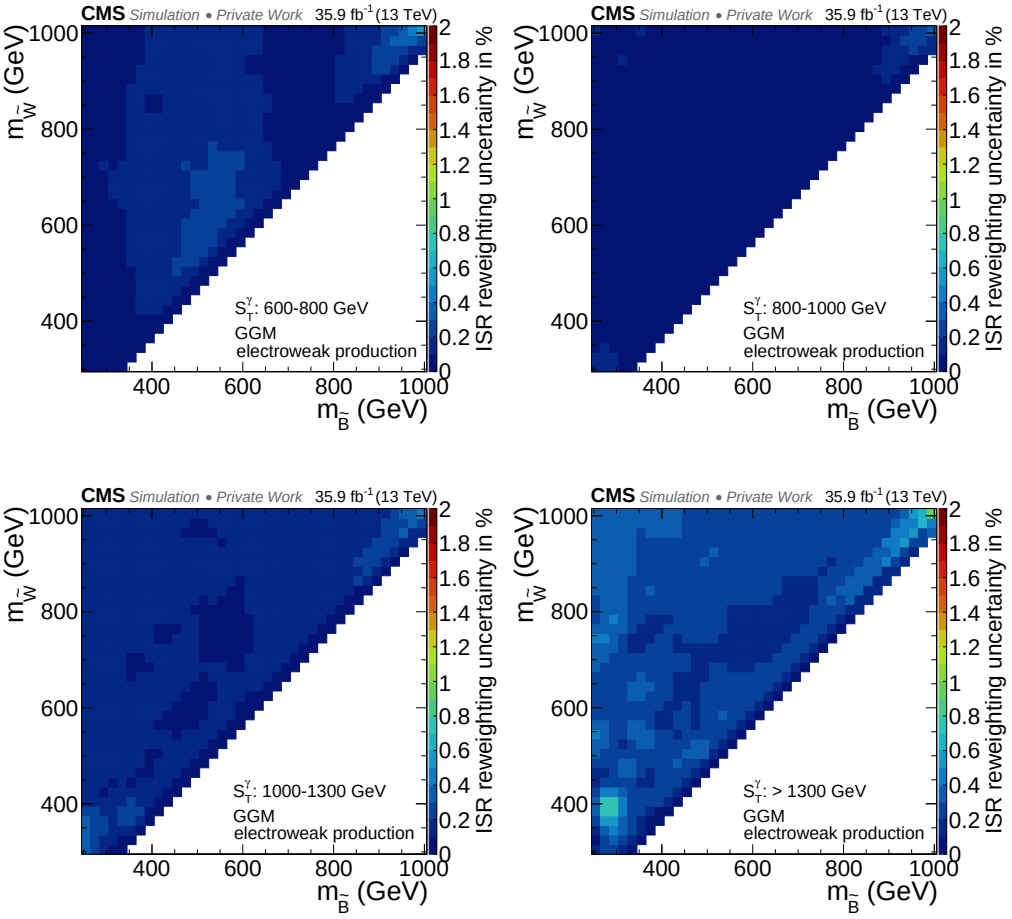

Figure E.3: Systematic uncertainties arising from the ISR reweighting of the $p_{\mathrm{T}}^{\mathrm{ISR}}$ distribution for the GGM EWK production model for the four signal region bins in $\mathrm{S}_{\mathrm{T}}^{\gamma}$ with $600 - 800\,\mathrm{GeV}$ (top left), $800 - 1000\,\mathrm{GeV}$ (top right), $1000 - 1300\,\mathrm{GeV}$ (bottom left), and more than $1300\,\mathrm{GeV}$ (bottom right)..

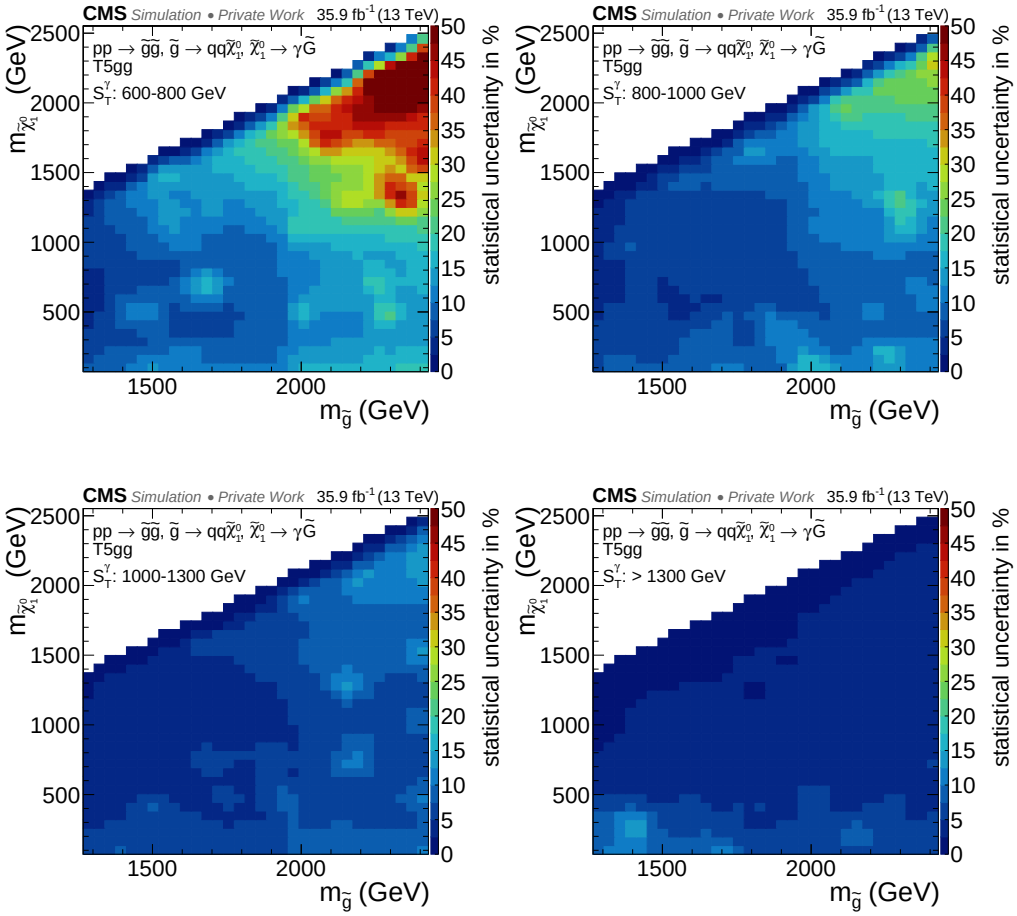

Figure E.4: Statistical uncertainty arising from the finite number of generated events in the signal MC simulation for the T5gg strong production SMS for the four signal region bins in S_T^γ with $600-800\,\text{GeV}$ (top left), $800-1000\,\text{GeV}$ (top right), $1000-1300\,\text{GeV}$ (bottom left), and more than $1300\,\text{GeV}$ (bottom right).

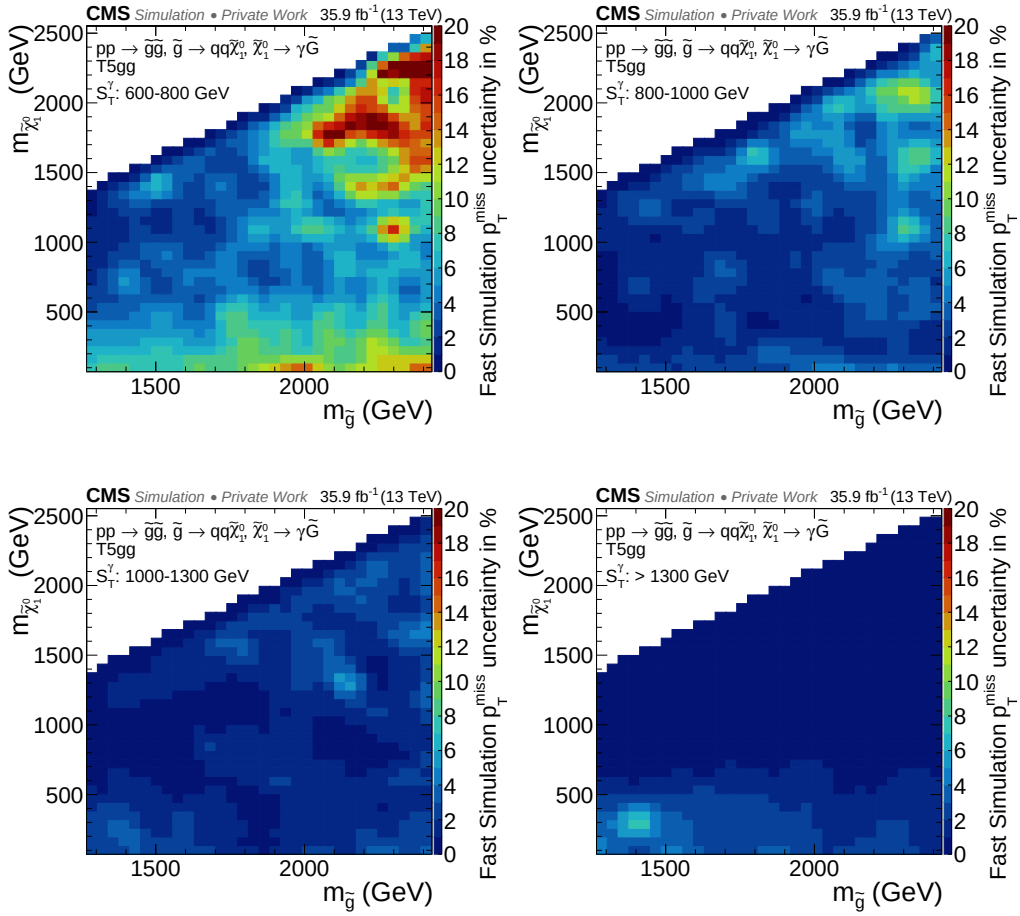

Figure E.5: Systematic uncertainties arising from $p_{\mathrm{T}}^{\mathrm{miss}}$ mismodelling due to the fast simulation of the CMS detector for the T5gg strong production SMS for the four signal region bins in S_{T}^{γ} with $600 - 800\,\mathrm{GeV}$ (top left), $800 - 1000\,\mathrm{GeV}$ (top right), $1000 - 1300\,\mathrm{GeV}$ (bottom left), and more than $1300\,\mathrm{GeV}$ (bottom right).

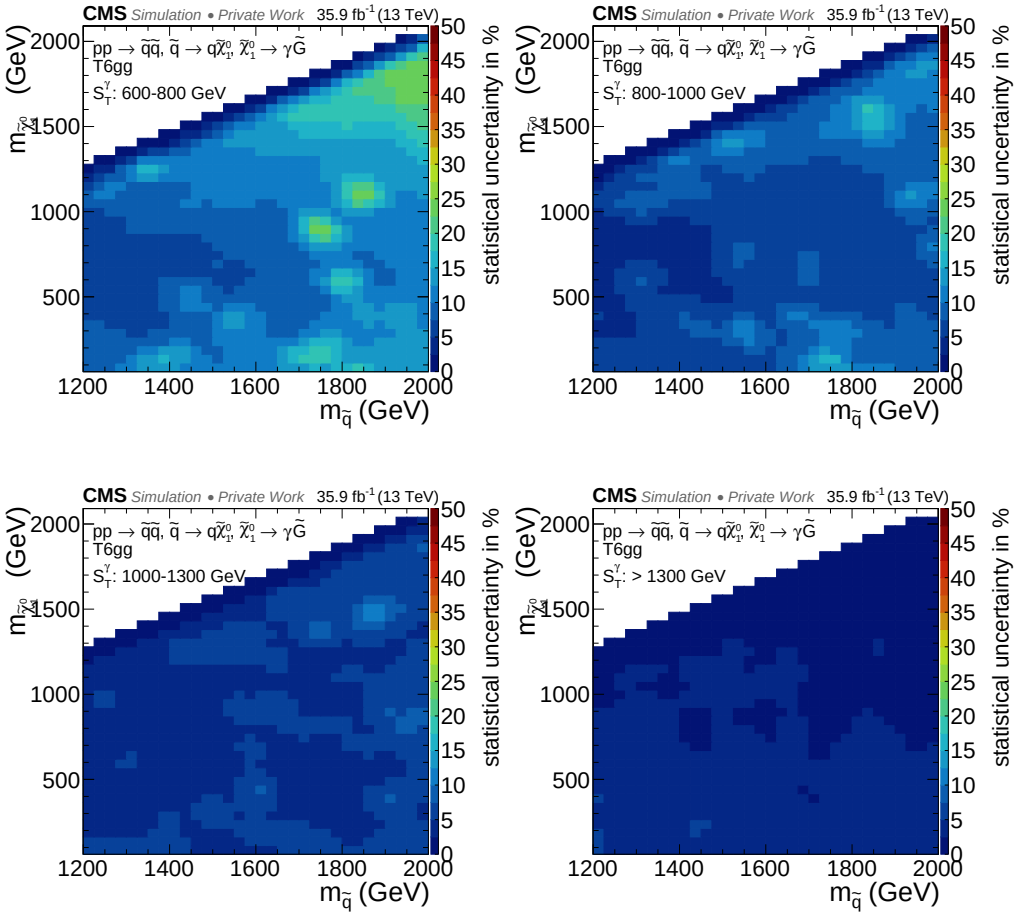

Figure E.6: Statistical uncertainty arising from the finite number of generated events in the signal MC simulation for the T6gg strong production SMS for the four signal region bins in S_T^γ with $600-800\,\text{GeV}$ (top left), $800-1000\,\text{GeV}$ (top right), $1000-1300\,\text{GeV}$ (bottom left), and more than $1300\,\text{GeV}$ (bottom right).

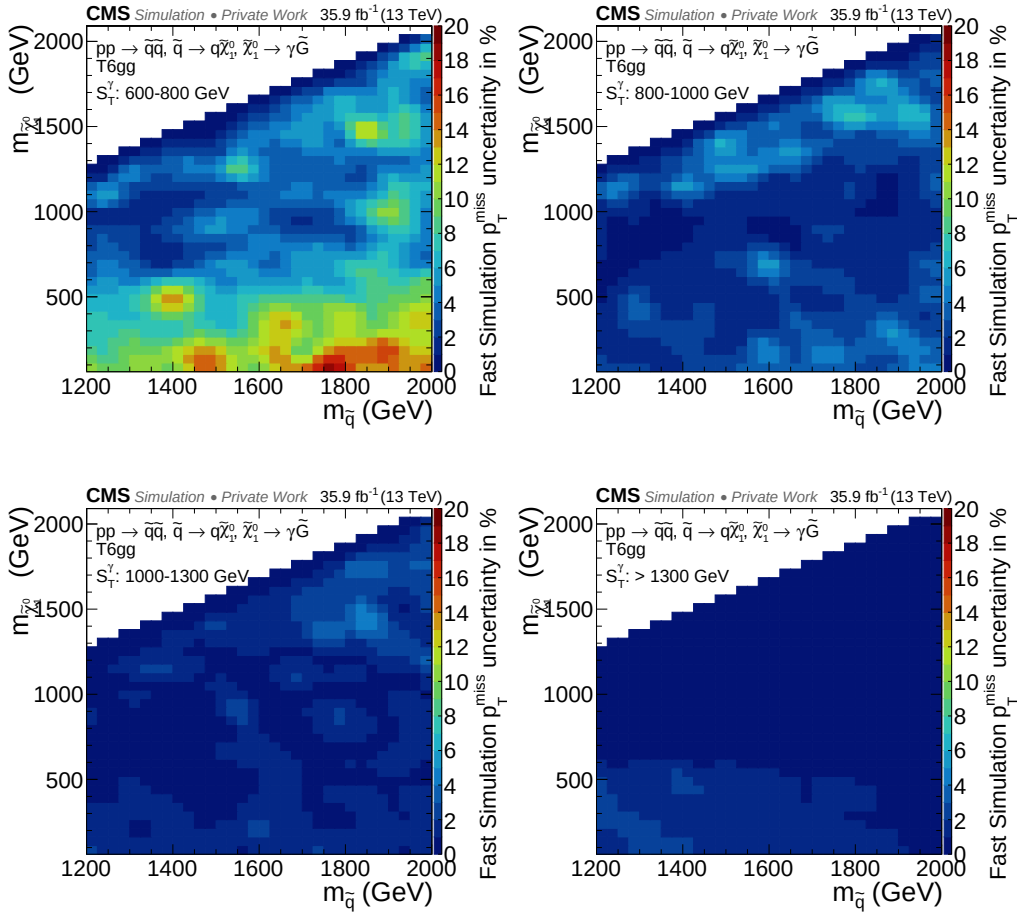

Figure E.7: Systematic uncertainties arising from $p_{\mathrm{T}}^{\mathrm{miss}}$ mismodelling due to the fast simulation of the CMS detector for the T6gg strong production SMS for the four signal region bins in S_{T}^{γ} with $600 - 800\,\mathrm{GeV}$ (top left), $800 - 1000\,\mathrm{GeV}$ (top right), $1000 - 1300\,\mathrm{GeV}$ (bottom left), and more than $1300\,\mathrm{GeV}$ (bottom right).

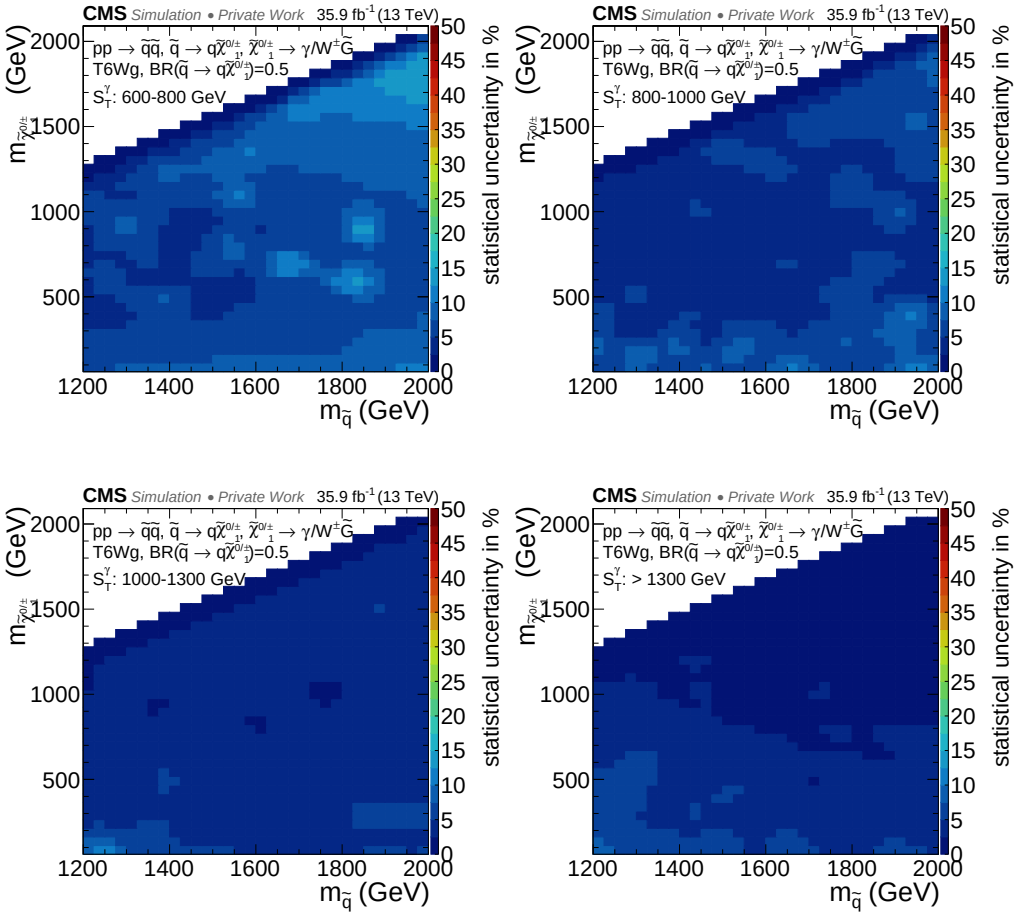

Figure E.8: Statistical uncertainty arising from the finite number of generated events in the signal MC simulation for the T6Wg strong production SMS for the four signal region bins in S_T^γ with $600-800\,\text{GeV}$ (top left), $800-1000\,\text{GeV}$ (top right), $1000-1300\,\text{GeV}$ (bottom left), and more than $1300\,\text{GeV}$ (bottom right).

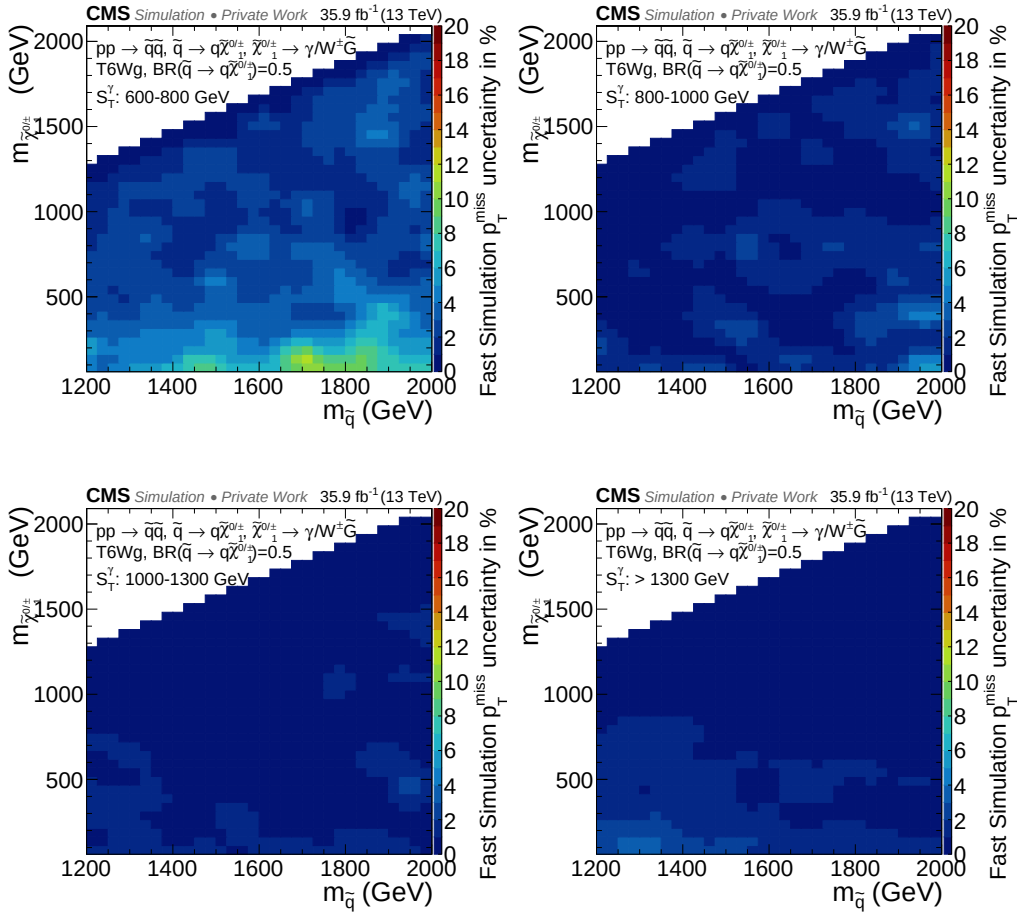

Figure E.9: Systematic uncertainties arising from $p_{\mathrm{T}}^{\mathrm{miss}}$ mismodelling due to the fast simulation of the CMS detector for the T6Wg strong production SMS for the four signal region bins in S_{T}^{γ} with $600 - 800\,\mathrm{GeV}$ (top left), $800 - 1000\,\mathrm{GeV}$ (top right), $1000 - 1300\,\mathrm{GeV}$ (bottom left), and more than $1300\,\mathrm{GeV}$ (bottom right).

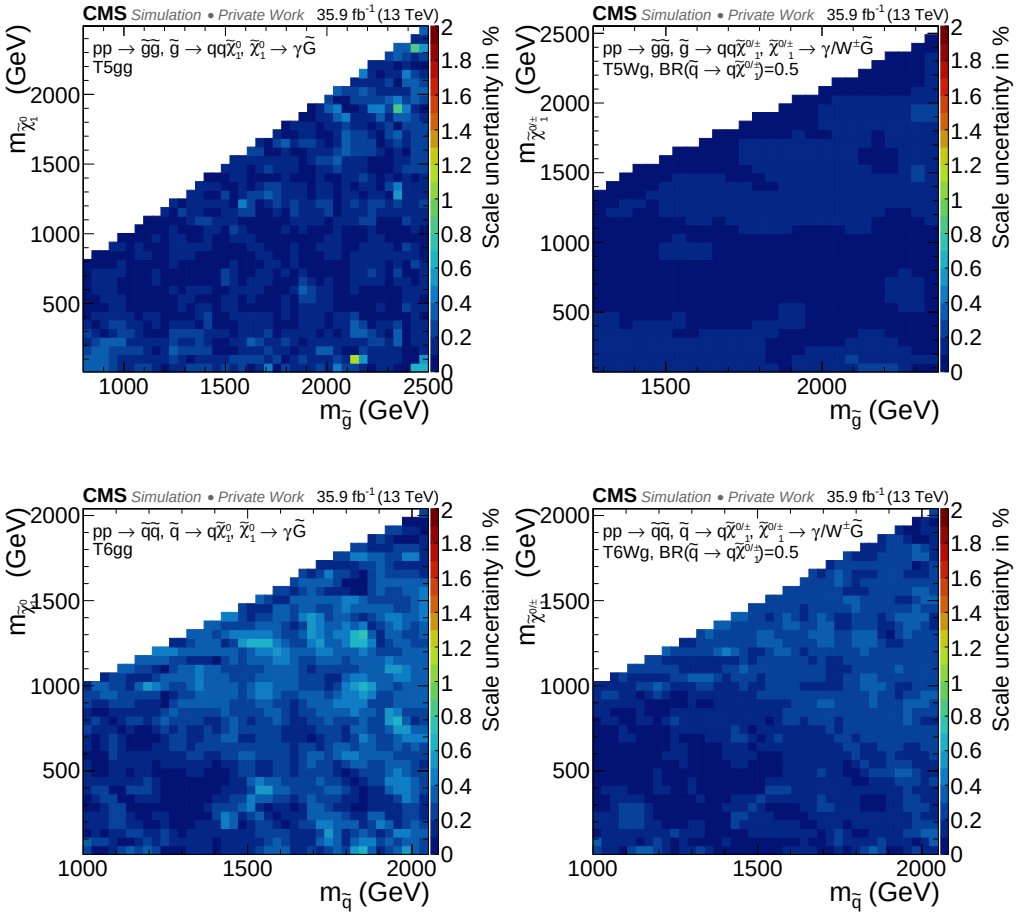

Figure E.10: Systematic uncertainty in the shape arising from the choice of the factorization and renormalization scales for the T5gg (top left), T5Wg (top right), T6gg (bottom left), and T6Wg (bottom right) scenarios.

Appendix F

Observed significances of the signal scenarios

Figure F.1 shows the observed significances for the TChiWg and TChiNg SMS (top left), as well as for the T5gg (top right), T6gg (bottom left), and T6Wg (bottom right) SMS.

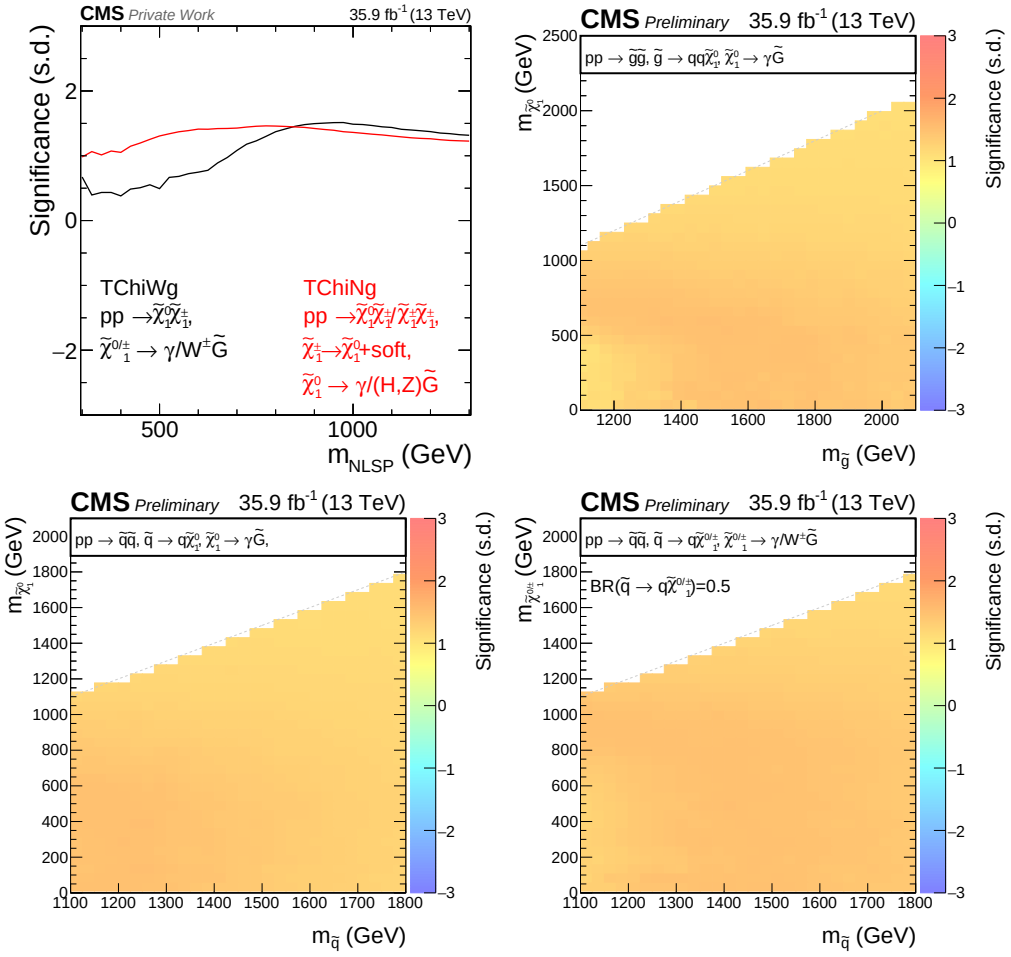

Figure F.1: Observed significances for the TChiWg and TChiNg (top left), T5gg (top right), T6gg (bottom left), and T6Wg (bottom right) scenarios.

Bibliography

[1] CMS Collaboration, "Search for supersymmetry in electroweak production with photons and large missing transverse energy in pp collisions at $\sqrt{s} = 8$ TeV", *Phys. Lett. B* **759** (2016) 479, doi:10.1016/j.physletb.2016.05.088, arXiv:1602.08772.

[2] CMS Collaboration, "Search for gauge-mediated supersymmetry in events with at least one photon and missing transverse momentum in pp collisions at $\sqrt{s} = 13$ TeV", *Phys. Lett. B* **780** (2018) 118, doi:10.1016/j.physletb.2018.02.045, arXiv:1711.08008.

[3] W. Hollik, "Quantum field theory and the Standard Model", 2010, arXiv:1012.3883.

[4] S. F. Novaes, "Standard model: An Introduction", 1999, arXiv:hep-ph/0001283.

[5] H. Spiesberger, M. Spira, and P. M. Zerwas, "The Standard model: Physical basis and scattering experiments", 2000, arXiv:hep-ph/0011255.

[6] Particle Data Group Collaboration, "Review of Particle Physics", *Chin. Phys. C* **40** (2016) 100001, doi:10.1088/1674-1137/40/10/100001.

[7] S. P. Martin, "A Supersymmetry primer", *Adv. Ser. Direct. High Energy Phys.* **21** (2010) 1, doi:10.1142/9789812839657_0001, arXiv:hep-ph/9709356v7.

[8] CMS Collaboration, "The CMS experiment at the CERN LHC", *JINST* **3** (2008) S08004, doi:10.1088/1748-0221/3/08/S08004.

[9] CMS Collaboration, "CMS Physics: Technical Design Report Volume 1: Detector Performance and Software", 2006, https://cds.cern.ch/record/922757.

[10] CMS Collaboration, "Technical proposal for the upgrade of the CMS detector through 2020", 2011, https://cds.cern.ch/record/1355706.

[11] CMS Collaboration, "Technical proposal for the Phase-II upgrade of the Compact Muon Solenoid", 2015, http://cds.cern.ch/record/2020886.

[12] LHC Study Group Collaboration, T. S. Pettersson and P. Lefèvre, "The Large Hadron Collider: conceptual design", 1995, http://inspirehep.net/record/402898.

[13] S. Ambrosanio et al., "Aspects of GMSB phenomenology at TeV colliders", 2000, arXiv:hep-ph/0002191v3.

[14] G. Giudice and R. Rattazzi, "Theories with gauge mediated supersymmetry breaking", *Phys. Rept.* **322** (1999) 419, doi:10.1016/S0370-1573(99)00042-3, arXiv:hep-ph/9801271.

[15] Y. Kats, P. Meade, M. Reece, and D. Shih, "The status of GMSB after 1/fb at the LHC", *JHEP* **02** (2012) 115, doi:10.1007/JHEP02(2012)115, arXiv:1110.6444.

[16] CMS Collaboration, "Data Parking and Data Scouting at the CMS Experiment", 2012, http://cds.cern.ch/record/1480607.

[17] CMS Collaboration, "Missing transverse energy performance of the CMS detector", *JINST* **6** (2011) P09001, doi:10.1088/1748-0221/6/09/P09001, arXiv:1106.5048.

[18] CMS Collaboration, "Search for supersymmetry in events with a photon, a lepton, and missing transverse momentum in pp collisions at $\sqrt{s} = 8$ TeV", *Phys. Lett. B* **757** (2016) 6, doi:10.1016/j.physletb.2016.03.039, arXiv:1508.01218.

[19] J. Schulz, "Search for electroweak production of supersymmetric gauginos with photons at CMS", Master's thesis, RWTH Aachen University, 2014. http://inspirehep.net/record/1339830/.

[20] CMS Collaboration, "Search for supersymmetry in final states with at least one photon and MET in pp collisions at $\sqrt{s}$=13 TeV", 2016, http://cds.cern.ch/record/2204917.

[21] F. Pisano and N. O. Reis, "Natural units, numbers and numerical clusters", 2001, arXiv:hep-ph/0112097.

[22] CMS Collaboration, "Observation of a new boson at a mass of 125 GeV with the CMS experiment at the LHC", *Phys. Lett. B* **716** (2012) 30, doi:10.1016/j.physletb.2012.08.021, arXiv:1207.7235.

[23] ATLAS Collaboration, "Observation of a new particle in the search for the Standard Model Higgs boson with the ATLAS detector at the LHC", *Phys. Lett. B* **716** (2012) 1, doi:10.1016/j.physletb.2012.08.020, arXiv:1207.7214.

[24] ATLAS and CMS Collaboration, "Combined Measurement of the Higgs Boson Mass in pp Collisions at $\sqrt{s} = 7$ and 8 TeV with the ATLAS and CMS Experiments", *Phys. Rev. Lett.* **114** (2015) 191803, doi:10.1103/PhysRevLett.114.191803, arXiv:1503.07589.

[25] CMS Collaboration, "Precise determination of the mass of the Higgs boson and tests of compatibility of its couplings with the standard model predictions using proton collisions at 7 and 8 TeV", *Eur. Phys. J. C* **75** (2015) 212, doi:10.1140/epjc/s10052-015-3351-7, arXiv:1412.8662.

[26] S. Glashow, "Partial Symmetries of Weak Interactions", *Nucl.Phys.* **22** (1961) 579, doi:10.1016/0029-5582(61)90469-2.

[27] S. Weinberg, "A Model of Leptons", *Phys. Rev. Lett.* **19** (1967) 1264, doi:10.1103/PhysRevLett.19.1264.

[28] A. Salam, "Weak and Electromagnetic Interactions", 1968, http://inspirehep.net/record/53083.

[29] Wikipedia, "Standard Model ", https://en.wikipedia.org/wiki/Standard_Model. Accessed on August 14, 2018.

[30] R. Alkofer and J. Greensite, "Quark Confinement: The Hard Problem of Hadron Physics", *J. Phys. G* **34** (2007) 3, doi:10.1088/0954-3899/34/7/S02, arXiv:hep-ph/0610365v2.

[31] K. G. Wilson, "Confinement of Quarks", *Phys. Rev. D* **10** (1974) 2445, doi:10.1103/PhysRevD.10.2445.

[32] E770, E744, CCFR Collaboration, "A Precision measurement of electroweak parameters in neutrino - nucleon scattering", *Eur. Phys. J. C* **1** (1998) 509, doi:10.1007/s100520050099, arXiv:hep-ex/9701010.

[33] CMS Collaboration, "Measurement of the weak mixing angle with the Drell-Yan process in proton-proton collisions at the LHC", *Phys. Rev. D* **84** (2011) 112002, doi:10.1103/PhysRevD.84.112002, arXiv:1110.2682.

[34] LHCb Collaboration, "Measurement of the forward-backward asymmetry in $Z/\gamma^* \to \mu^+\mu^-$ decays and determination of the effective weak mixing angle", *JHEP* **11** (2015) 190, doi:10.1007/JHEP11(2015)190, arXiv:1509.07645.

[35] X.-G. He, J. Tandean, and G. Valencia, "Penguin and Box Diagrams in Unitary Gauge", *Eur. Phys. J. C* **64** (2009) 681, doi:10.1140/epjc/s10052-009-1162-4, arXiv:0909.3638.

[36] LHCb Collaboration, "Measurement of the $B_s^0 \to \mu^+\mu^-$ branching fraction and effective lifetime and search for $B^0 \to \mu^+\mu^-$ decays", *Phys. Rev. Lett.* **118** (2017) 191801, doi:10.1103/PhysRevLett.118.191801, arXiv:1703.05747.

[37] M. Carena and H. E. Haber, "Higgs boson theory and phenomenology", *Prog. Part. Nucl. Phys.* **50** (2003) 63, doi:10.1016/S0146-6410(02)00177-1, arXiv:hep-ph/0208209.

[38] U. Amaldi, W. de Boer, and H. Furstenau, "Comparison of grand unified theories with electroweak and strong coupling constants measured at LEP", *Phys. Lett. B* **260** (1991) 447, doi:10.1016/0370-2693(91)91641-8.

[39] Super-Kamiokande Collaboration, "Review of Nucleon Decay Searches at Super-Kamiokande", 2016, arXiv:1605.03235.

[40] Super-Kamiokande Collaboration, "Search for proton decay via p→$e^+\pi^0$ and p→ $\mu^+\pi^0$ in 0.31 megaton · years exposure of the Super-Kamiokande water Cherenkov detector", *Phys. Rev. D* **95** (2017) 012004, doi:10.1103/PhysRevD.95.012004, arXiv:1610.03597.

[41] S. Pokorski, K. Rolbiecki, and K. Sakurai, "Proton decay testing low energy supersymmetry with precision gauge unification", *Phys. Rev. D* **97** (2018) 035027, doi:10.1103/PhysRevD.97.035027, arXiv:1707.06720.

[42] M. Gonzalez-Garcia and Y. Nir, "Neutrino masses and mixing: Evidence and implications", *Rev. Mod. Phys.* **75** (2003) 345, doi:10.1103/RevModPhys.75.345, arXiv:hep-ph/0202058v3.

[43] The Super-Kamiokande Collaboration, "Evidence for an Oscillatory Signature in Atmospheric Neutrino Oscillations", *Phys. Rev. Lett.* **93** (2004) 101801, doi:10.1103/PhysRevLett.93.101801, arXiv:hep-ex/0404034.

[44] Super-Kamiokande Collaboration, "Evidence for the Appearance of Atmospheric Tau Neutrinos in Super-Kamiokande", *Phys. Rev. Lett.* **110** (2013) 181802, doi:10.1103/PhysRevLett.110.181802, arXiv:1206.0328v2.

[45] F. P. An et al., "Observation of Electron-Antineutrino Disappearance at Daya Bay", *Phys. Rev. Lett.* **108** (2012) 171803, doi:10.1103/PhysRevLett.108.171803, arXiv:1203.1669.

[46] S. T. Petcov, "The Nature of Massive Neutrinos", *Adv. High Energy Phys.* **2013** (2013) 852987, doi:10.1155/2013/852987, arXiv:1303.5819.

[47] O. Cremonesi, "Neutrino masses", *PoS* **EPS-HEP** (2013) 146, doi:10.22323/1.180.0146.

[48] P. Minkowski, "$\mu \to e\gamma$ at a rate of one out of 109 muon decays?", *Phys. Lett. B* **67** (1977) 421, doi:10.1016/0370-2693(77)90435-X.

[49] G. Bertone, D. Hooper, and J. Silk, "Particle dark matter: Evidence, candidates and constraints", *Phys. Rept.* **405** (2005) 279, doi:10.1016/j.physrep.2004.08.031, arXiv:hep-ph/0404175.

[50] K. Garrett and G. Duda, "Dark Matter: A Primer", *Adv. Astron.* **2011** (2011) 968283, doi:10.1155/2011/968283, arXiv:1006.2483.

[51] N. Jarosik et al., "Seven-year Wilkinson Microwave Anisotropy Probe (WMAP) Observations: Sky Maps, Systematic Errors, and Basic Results", *The Astrophysical Journal Supplement Series* **192** (2011) 14, doi:10.1088/0067-0049/192/2/14, arXiv:1001.4744.

[52] G. Sharma, Anu, and B. C. Chauhan, "Dark Matter and Neutrinos", 2017, arXiv:1711.10564.

[53] K. G. Begeman, A. H. Broeils, and R. H. Sanders, "Extended rotation curves of spiral galaxies - Dark haloes and modified dynamics", *Monthly Notices of the Royal Astronomical Society* **249** (1991) 523, doi:10.1093/mnras/249.3.523.

[54] D. H. Weinberg et al., "Observational probes of cosmic acceleration", *Physics Reports* **530** (2013) 87, doi:10.1016/j.physrep.2013.05.001, arXiv:1201.2434.

[55] R. Hodson, "The dark Universe", *Nature* **537** (2016) 193, doi:10.1038/537S193a.

[56] L. Bergstrom, "Dark Matter Evidence, Particle Physics Candidates and Detection Methods", *Annalen Phys.* **524** (2012) 479, doi:10.1002/andp.201200116, arXiv:1205.4882.

[57] M. Mordehai, "MOND theory", *Canadian Journal of Physics* **93** (2015) 107, doi:10.1139/cjp-2014-0211, arXiv:1404.7661.

[58] L. Blanchet and L. Heisenberg, "Dark matter via massive bigravity", *Phys. Rev. D* **91** (2015) 103518, doi:10.1103/PhysRevD.91.103518, arXiv:1504.00870v2.

[59] L. Bernard and L. Blanchet, "Phenomenology of dark matter via a bimetric extension of general relativity", *Phys. Rev. D* **91** (2015) 103536, doi:10.1103/PhysRevD.91.103536.

[60] C. Beskidt, W. de Boer, D. Kazakov, and F. Ratnikov, "Constraints on Supersymmetry from LHC data on SUSY searches and Higgs bosons combined with cosmology and direct dark matter searches", *Eur. Phys. J. C* **72** (2012) 2166, doi:10.1140/epjc/s10052-012-2166-z, arXiv:1207.3185.

[61] C. Autermann, "Experimental status of supersymmetry after the LHC Run-I", *Prog. Part. Nucl. Phys.* **90** (2016) 125, doi:10.1016/j.ppnp.2016.06.001, arXiv:1609.01686.

[62] J. March-Russell and S. West, "A simple model of neutrino masses from supersymmetry breaking", *Phys. Lett. B* **593** (2004) 181, doi:https://doi.org/10.1016/j.physletb.2004.04.050, arXiv:hep-ph/0403067.

[63] J. E. Kim and J. S. Lee, "Neutrino mass and lepton number violation with charged scalars", arXiv:hep-ph/9907452.

[64] R. Barbier et al., "R-parity violating supersymmetry", *Phys. Rept.* **420** (2005) 1, doi:10.1016/j.physrep.2005.08.006, arXiv:hep-ph/0406039.

[65] M. Dine, "Supersymmetry and String Theory". Cambridge University Press, 2016.

[66] G. Degrassi et al., "Towards high-precision predictions for the MSSM Higgs sector", *The European Physical Journal C - Particles and Fields* **28** (2003) 133, doi:10.1140/epjc/s2003-01152-2, arXiv:hep-ph/0212020.

[67] P. Meade, N. Seiberg, and D. Shih, "General Gauge Mediation", *Prog. Theor. Phys. Suppl.* **177** (2009) 143, doi:10.1143/PTPS.177.143, arXiv:0801.3278.

[68] P. Meade, M. Reece, and D. Shih, "Prompt Decays of General Neutralino NLSPs at the Tevatron", *JHEP* **1005** (2010) 105, doi:10.1007/JHEP05(2010)105, arXiv:0911.4130.

[69] M. Buican, P. Meade, N. Seiberg, and D. Shih, "Exploring general gauge mediation", *JHEP* **03** (2009) 016, doi:10.1088/1126-6708/2009/03/016, arXiv:0812.3668.

[70] Shih, David et al, "Simple SUSY spectra for photons + MET searches", http://www.physics.rutgers.edu/~kats/binoNLSP/. Accessed on August 14, 2018.

[71] H. Pagels and J. R. Primack, "Supersymmetry, Cosmology, and New Physics at Teraelectronvolt Energies", *Phys. Rev. Lett.* **48** (1982) 223, doi:10.1103/PhysRevLett.48.223.

[72] F. Staub, W. Porod, and J. Niemeyer, "Strong dark matter constraints on GMSB models", *JHEP* **01** (2010) 058, doi:10.1007/JHEP01(2010)058, arXiv:0907.0530.

[73] V. Iršič et al., "New Constraints on the free-streaming of warm dark matter from intermediate and small scale Lyman-α forest data", *Phys. Rev. D* **96** (2017) 023522, doi:10.1103/PhysRevD.96.023522, arXiv:1702.01764.

[74] L. Covi, "Gravitino Dark Matter confronts LHC", *Journal of Physics: Conference Series* **485** (2014) 012002.

[75] L. Covi et al., "Supersymmetric mass spectra for gravitino dark matter with a high reheating temperature", *JHEP* **01** (2011) 033, doi:10.1007/JHEP01(2011)033, arXiv:1009.3801.

[76] G. Cottin, M. A. Díaz, M. J. Guzmán, and B. Panes, "Gravitino Dark Matter in Split Supersymmetry with Bilinear R-Parity Violation", *Eur. Phys. J. C* **74** (2014) 3138, doi:10.1140/epjc/s10052-014-3138-2, arXiv:1406.2368.

[77] CMS Collaboration, "Interpretation of Searches for Supersymmetry with simplified Models", *Phys. Rev. D* **88** (2013) 052017, doi:10.1103/PhysRevD.88.052017, arXiv:1301.2175.

[78] J. T. Ruderman and D. Shih, "General Neutralino NLSPs at the Early LHC", *JHEP* **1208** (2012) 159, doi:10.1007/JHEP08(2012)159, arXiv:1103.6083.

[79] Y. Kats and M. J. Strassler, "Probing Colored Particles with Photons, Leptons, and Jets", *JHEP* **11** (2012) 097, doi:10.1007/JHEP11(2012)097,10.1007/JHEP07(2016)009, arXiv:1204.1119. [Erratum: JHEP07,009(2016)].

[80] P. Grajek, A. Mariotti, and D. Redigolo, "Phenomenology of general gauge mediation in light of a 125 GeV Higgs", *JHEP* **07** (2013) 109, doi:10.1007/JHEP07(2013)109, arXiv:1303.0870.

[81] CMS Collaboration, "Search for supersymmetry in events with at least one photon, missing transverse momentum, and large transverse event activity in proton-proton collisions at $\sqrt{s} = 13$ TeV", *JHEP* **12** (2017) 142, doi:10.1007/JHEP12(2017)142, arXiv:1707.06193.

[82] CMS Collaboration, "Searches for electroweak production of charginos, neutralinos, and sleptons decaying to leptons and W, Z, and Higgs bosons in pp collisions at 8 TeV", *Eur. Phys. J. C* **74** (2014) 3036, doi:10.1140/epjc/s10052-014-3036-7, arXiv:1405.7570.

[83] CMS Collaboration, "Combined search for electroweak production of charginos and neutralinos in proton-proton collisions at $\sqrt{s} = 13$ TeV", *JHEP* **03** (2018) 160, doi:10.1007/JHEP03(2018)160, arXiv:1801.03957.

[84] ATLAS Collaboration, "Search for photonic signatures of gauge-mediated supersymmetry in 13 TeV pp collisions with the ATLAS detector", *Phys. Rev. D* **97** (2018) 092006, doi:10.1103/PhysRevD.97.092006, arXiv:1802.03158.

[85] ALICE Collaboration, "The ALICE experiment at the CERN LHC", *JINST* **3** (2008) S08002, doi:10.1088/1748-0221/3/08/S08002.

[86] ALICE Collaboration, "Performance of the ALICE Experiment at the CERN LHC", *Int. J. Mod. Phys. A* **29** (2014) 1430044, doi:10.1142/S0217751X14300440, arXiv:1402.4476.

[87] ATLAS Collaboration, "The ATLAS Experiment at the CERN Large Hadron Collider", *JINST* **3** (2008) S08003, doi:10.1088/1748-0221/3/08/S08003.

[88] ATLAS Collaboration, "Performance of the ATLAS Detector using First Collision Data", *JHEP* **09** (2010) 056, doi:10.1007/JHEP09(2010)056, arXiv:1005.5254.

[89] LHCb Collaboration, "The LHCb Detector at the LHC", *JINST* **3** (2008) S08005, doi:10.1088/1748-0221/3/08/S08005.

[90] LHCb Collaboration, "LHCb Detector Performance", *Int. J. Mod. Phys. A* **30** (2015) 1530022, doi:10.1142/S0217751X15300227, arXiv:1412.6352.

[91] Wikipedia, "Proton Synchrotron Booster ", https://en.wikipedia.org/wiki/Proton_Synchrotron_Booster. Accessed on August 14, 2018.

[92] W. Herr and B. Muratori, "Concept of luminosity", 2006, https://cds.cern.ch/record/941318.

[93] R. Bruce et al., "LHC Run 2: Results and challenges", 2016, https://cds.cern.ch/record/2201447.

[94] J. Wenninger, "Approaching the Nominal Performance at the LHC", 2017, http://cds.cern.ch/record/2289717.

[95] R. R. Wilson, "The Tevatron", *Phys. Today* **30N10** (1977) 23, doi:10.1063/1.3037746.

[96] V. Papadimitriou, "Luminosity determination at the Tevatron", 2011, arXiv:1106.5182.

[97] A. Valishev, "Tevatron accelerator physics and operation highlights", *Conf. Proc. C* **110328** (2011) 37, arXiv:1202.5525.

[98] CMS Collaboration, "Public CMS Luminosity Information", https://twiki.cern.ch/twiki/bin/view/CMSPublic/LumiPublicResults. Accessed on August 14, 2018.

[99] CMS Collaboration, "CMS Conventions", https://twiki.cern.ch/twiki/bin/viewauth/CMS/CMSConventions. Accessed on August 14, 2018.

[100] CMS Collaboration, "The Phase-1 Upgrade of the CMS pixel detector", *Nuclear Instruments and Methods in Physics Research Section A: Accelerators, Spectrometers, Detectors and Associated Equipment* **845** (2017) 101, doi:10.1016/j.nima.2016.06.039. Proceedings of the Vienna Conference on Instrumentation 2016.

[101] CMS Collaboration, "Phase 1 upgrade of the CMS pixel detector", *JINST* **12** (2017) C02033, doi:10.1088/1748-0221/12/02/C02033.

[102] CMS Collaboration, "Description and performance of track and primary-vertex reconstruction with the CMS tracker", *JINST* (2014) P10009, doi:10.1088/1748-0221/9/10/P10009, arXiv:1405.6569.

[103] CMS Collaboration, "CMS Tracker Detector Performance Results ". Accessed on August 14, 2018.

[104] CMS Collaboration, "Alignment of the CMS tracker with LHC and cosmic ray data", *JINST* **9** (2014) P06009, doi:10.1088/1748-0221/9/06/P06009, arXiv:1403.2286.

[105] A. Benaglia, "The CMS ECAL performance with examples", *JINST* **9** (2014) C02008, doi:10.1088/1748-0221/9/02/C02008.

[106] V. D. Elvira, "Measurement of the Pion Energy Response and Resolution in the CMS HCAL Test Beam 2002 Experiment", 2004, http://cds.cern.ch/record/800406.

[107] S. Abdullin et al., "The CMS barrel calorimeter response to particle beams from 2 to 350 GeV/c", *The European Physical Journal C* **60** (2009) 359, doi:10.1140/epjc/s10052-009-0959-5.

[108] CMS Collaboration, "The performance of the CMS muon detector in proton-proton collisions at $\sqrt{s} = 7\,\text{TeV}$ at the LHC", *JINST* **8** (2013) P11002, doi:10.1088/1748-0221/8/11/P11002, arXiv:1306.6905.

[109] CMS Collaboration, "The CMS trigger system", *JINST* **12** (2017) P01020, doi:10.1088/1748-0221/12/01/P01020, arXiv:1609.02366.

[110] CMS Collaboration, "Performance and upgrade of the CMS electron and photon trigger for Run 2", *J. Phys. Conf. Ser.* **587** (2015) 012021, doi:10.1088/1742-6596/587/1/012021.

[111] G. Bauer et al., "The CMS High Level Trigger System: Experience and Future Development", *Journal of Physics: Conference Series* **396** (2012) 012008.

[112] CMS Collaboration, M. Tosi, "The CMS trigger in Run 2", 2017, https://cds.cern.ch/record/2290106.

[113] CMS Collaboration, "Run 2 Upgrades to the CMS Level-1 Calorimeter Trigger", *JINST* **11** (2016) C01051, doi:10.1088/1748-0221/11/01/C01051, arXiv:1511.05855.

[114] G. Bauer et al., "Operational experience with the CMS Data Acquisition System", *Journal of Physics: Conference Series* **396** (2012) 012007.

[115] CMS Collaboration, V. Daponte, "HLT configuration management system", 2015, https://cds.cern.ch/record/2061510.

[116] I. Bird et al., "Update of the Computing Models of the WLCG and the LHC Experiments", 2014, https://cds.cern.ch/record/1695401.

[117] I. Bird, "Computing for the Large Hadron Collider", *Annual Review of Nuclear and Particle Science* **61** (2011) 99, doi:10.1146/annurev-nucl-102010-130059.

[118] CMS Collaboration, "Worldwide LHC Computing Grid", http://wlcg.web.cern.ch/. Accessed on August 14, 2018.

[119] J. Alwall et al., "The automated computation of tree-level and next-to-leading order differential cross sections, and their matching to parton shower simulations", *JHEP* **07** (2014) 079, doi:10.1007/JHEP07(2014)079, arXiv:1405.0301.

[120] J. Alwall et al., "MadGraph 5: going beyond", *JHEP* **06** (2011) 128, doi:10.1007/JHEP06(2011)128, arXiv:1106.0522.

[121] J. Alwall et al., "Comparative study of various algorithms for the merging of parton showers and matrix elements in hadronic collisions", *Eur. Phys. J. C* **53** (2008) 473, doi:10.1140/epjc/s10052-007-0490-5, arXiv:0706.2569.

[122] T. Sjöstrand, S. Mrenna, and P. Z. Skands, "PYTHIA 6.4 physics and manual", *JHEP* **05** (2006) 026, doi:10.1088/1126-6708/2006/05/026, arXiv:hep-ph/0603175.

[123] K. Bloom, "CMS software and computing for LHC Run 2", *PoS* **ICHEP2016** (2016) 185, arXiv:1611.03215.

[124] G. Petrucciani, A. Rizzi, and C. Vuosalo, "Mini-AOD: A New Analysis Data Format for CMS", *Journal of Physics: Conference Series* **664** (2015) 072052.

[125] CMS Collaboration, "CMSSW Application Framework ", https://twiki.cern.ch/twiki/bin/view/CMSPublic/WorkBookCMSSWFramework. Accessed on August 14, 2018.

[126] D. Spiga et al., "The CMS Remote Analysis Builder (CRAB)", in *Proceedings of the 14th International Conference on High Performance Computing*, HiPC'07, p. 580. Springer-Verlag, 2007.

[127] R. Brun and F. Rademakers, "ROOT: An object oriented data analysis framework", *Nucl. Instrum. Meth. A* **389** (1997) 81, doi:10.1016/S0168-9002(97)00048-X.

[128] I. Antcheva et al., "ROOT: A C++ framework for petabyte data storage, statistical analysis and visualization", *Comput. Phys. Commun.* **180** (2009) 2499, doi:10.1016/j.cpc.2009.08.005, arXiv:1508.07749.

[129] P. S. Foundation, "Python", https://www.python.org/. Accessed on August 14, 2018.

[130] CMS Collaboration, "The CMS dataset bookkeeping service", *J. Phys. Conf. Ser.* **119** (2008) 072001, doi:10.1088/1742-6596/119/7/072001.

[131] T. Kinoshita, "Mass Singularities of Feynman Amplitudes", *Journal of Mathematical Physics* **3** (1962) 650, doi:10.1063/1.1724268.

[132] T. D. Lee and M. Nauenberg, "Degenerate Systems and Mass Singularities", *Phys. Rev.* **133** (1964) B1549, doi:10.1103/PhysRev.133.B1549.

[133] R. Akhoury, M. G. Sotiropoulos, and V. I. Zakharov, "The KLN theorem and soft radiation in gauge theories: Abelian case", *Phys. Rev. D* **56** (1997) 377, doi:10.1103/PhysRevD.56.377, arXiv:hep-ph/9702270.

[134] T. Sjöstrand, "A model for initial state parton showers", *Phys. Lett. B* **157** (1985) 321, doi:https://doi.org/10.1016/0370-2693(85)90674-4.

[135] M. Bengtsson and T. Sjostrand, "Coherent Parton Showers Versus Matrix Elements: Implications of PETRA - PEP Data", *Phys. Lett. B* **185** (1987) 435, doi:10.1016/0370-2693(87)91031-8.

[136] A. Buckley et al., "General-purpose event generators for LHC physics", *Phys. Rept.* **504** (2011) 145, doi:10.1016/j.physrep.2011.03.005, arXiv:1101.2599.

[137] W. T. Giele, D. A. Kosower, and P. Z. Skands, "Higher-Order Corrections to Timelike Jets", *Phys. Rev. D* **84** (2011) 054003, doi:10.1103/PhysRevD.84.054003, arXiv:1102.2126.

[138] S. Catani, F. Krauss, R. Kuhn, and B. R. Webber, "QCD matrix elements + parton showers", *JHEP* **11** (2001) 063, doi:10.1088/1126-6708/2001/11/063, arXiv:hep-ph/0109231.

[139] S. Frixione and B. R. Webber, "Matching NLO QCD computations and parton shower simulations", *JHEP* **06** (2002) 029, doi:10.1088/1126-6708/2002/06/029, arXiv:hep-ph/0204244.

[140] R. Frederix and S. Frixione, "Merging meets matching in MC@NLO", *JHEP* **12** (2012) 061, doi:10.1007/JHEP12(2012)061, arXiv:1209.6215.

[141] J. Alwall et al., "A Standard format for Les Houches event files", *Comput. Phys. Commun.* **176** (2007) 300, doi:10.1016/j.cpc.2006.11.010, arXiv:hep-ph/0609017.

[142] P. Z. Skands et al., "SUSY Les Houches accord: Interfacing SUSY spectrum calculators, decay packages, and event generators", *JHEP* **07** (2004) 036, doi:10.1088/1126-6708/2004/07/036, arXiv:hep-ph/0311123.

[143] B. Andersson, G. Gustafson, G. Ingelman, and T. Sjöstrand, "Parton fragmentation and string dynamics", *Physics Reports* **97** (July, 1983) 31, doi:10.1016/0370-1573(83)90080-7.

[144] A. Kupco, "Cluster hadronization in HERWIG 5.9", 1998, arXiv:hep-ph/9906412.

[145] CMS Collaboration, "Event generator tunes obtained from underlying event and multiparton scattering measurements", *Eur. Phys. J. C* **76** (2016) 155, doi:10.1140/epjc/s10052-016-3988-x, arXiv:1512.00815.

[146] NNPDF Collaboration, "Parton distributions for the LHC Run II", *JHEP* **04** (2015) 040, doi:10.1007/JHEP04(2015)040, arXiv:1410.8849.

[147] GEANT4 Collaboration, "GEANT4: A Simulation toolkit", *Nucl. Instrum. Meth. A* **506** (2003) 250, doi:10.1016/S0168-9002(03)01368-8.

[148] S. Abdullin et al., "The fast simulation of the CMS detector at LHC", *J. Phys. Conf. Series* **331** (2011) 032049.

[149] CMS Collaboration, "Recent Developments in CMS Fast Simulation", *PoS* **ICHEP2016** (2016) 181, arXiv:1701.03850.

[150] P. Nason, "A new method for combining NLO QCD with shower Monte Carlo algorithms", *JHEP* **11** (2004) 040, doi:10.1088/1126-6708/2004/11/040, arXiv:hep-ph/0409146.

[151] S. Frixione, P. Nason, and C. Oleari, "Matching NLO QCD computations with Parton Shower simulations: the POWHEG method", *JHEP* **11** (2007) 070, doi:10.1088/1126-6708/2007/11/070, arXiv:0709.2092.

[152] S. Alioli, P. Nason, C. Oleari, and E. Re, "A general framework for implementing NLO calculations in shower Monte Carlo programs: the POWHEG BOX", *JHEP* **06** (2010) doi:10.1007/JHEP06(2010)043, arXiv:1002.2581.

[153] T. Melia, P. Nason, R. Rontsch, and G. Zanderighi, "W^+W^-, WZ and ZZ production in the POWHEG BOX", *JHEP* **11** (2011) 078, doi:10.1007/JHEP11(2011)078, arXiv:1107.5051.

[154] P. Nason and G. Zanderighi, "W^+ W^- , WZ and ZZ production in the POWHEG-BOX-V2", *Eur. Phys. J. C* **74** (2014) 2702, doi:10.1140/epjc/s10052-013-2702-5, arXiv:1311.1365.

[155] G. Bozzi et al., "Production of Drell-Yan lepton pairs in hadron collisions: Transverse-momentum resummation at next-to-next-to-leading logarithmic accuracy", *Phys. Lett. B* **696** (2011) 207, doi:10.1016/j.physletb.2010.12.024, arXiv:1007.2351.

[156] T. Gehrmann et al., "W^+W^- Production at Hadron Colliders in Next-to-Next-to Leading Order QCD", *Phys. Rev. Lett.* **113** (2014) 212001, doi:10.1103/PhysRevLett.113.212001, arXiv:1408.5243.

[157] W. Beenakker, R. Hopker, M. Spira, and P. M. Zerwas, "Squark and gluino production at hadron colliders", *Nucl. Phys. B* **492** (1997) 51, doi:10.1016/S0550-3213(97)80027-2, arXiv:hep-ph/9610490.

[158] A. Kulesza and L. Motyka, "Threshold resummation for squark-antisquark and gluino-pair production at the LHC", *Phys. Rev. Lett.* **102** (2009) 111802, doi:10.1103/PhysRevLett.102.111802, arXiv:0807.2405.

[159] A. Kulesza and L. Motyka, "Soft gluon resummation for the production of gluino-gluino and squark-antisquark pairs at the LHC", *Phys. Rev. D* **80** (2009) 095004, doi:10.1103/PhysRevD.80.095004, arXiv:0905.4749.

[160] W. Beenakker et al., "Soft-gluon resummation for squark and gluino hadroproduction", *JHEP* **12** (2009) 041, doi:10.1088/1126-6708/2009/12/041, arXiv:0909.4418.

[161] W. Beenakker et al., "Squark and Gluino Hadroproduction", *Int. J. Mod. Phys. A* **26** (2011) 2637, doi:10.1142/S0217751X11053560, arXiv:1105.1110.

[162] C. Borschensky et al., "Squark and gluino production cross sections in pp collisions at $\sqrt{s} = 13$, 14, 33 and 100 TeV", *Eur. Phys. J. C* **74** (2014) 3174, doi:10.1140/epjc/s10052-014-3174-y, arXiv:1407.5066.

[163] W. Beenakker et al., "Production of Charginos, Neutralinos, and Sleptons at Hadron Colliders", *Phys. Rev. Lett.* **83** (1999) 3780, doi:10.1103/PhysRevLett.83.3780,10.1103/PhysRevLett.100.029901, arXiv:hep-ph/9906298. [Erratum: *Phys. Rev. Lett.* **100** (2008) 029901].

[164] B. Fuks, M. Klasen, D. R. Lamprea, and M. Rothering, "Gaugino production in proton-proton collisions at a center-of-mass energy of 8 TeV", *JHEP* **10** (2012) 081, doi:10.1007/JHEP10(2012)081, arXiv:1207.2159.

[165] B. Fuks, M. Klasen, D. R. Lamprea, and M. Rothering, "Precision predictions for electroweak superpartner production at hadron colliders with Resummino", *Eur. Phys. J. C* **73** (2013) 2480, doi:10.1140/epjc/s10052-013-2480-0, arXiv:1304.0790.

[166] C. Lippmann, "Particle identification", *Nucl. Instrum. Meth. A* **666** (2012) 148, doi:10.1016/j.nima.2011.03.009, arXiv:1101.3276v4.

[167] CMS Collaboration, "POG recipes for Run 2", https://twiki.cern.ch/twiki/bin/view/CMS/POGRecipesICHEP2016. Accessed on August 14, 2018.

[168] CMS Collaboration, "Particle-flow reconstruction and global event description with the CMS detector", *JINST* **12** (2017) P10003, doi:10.1088/1748-0221/12/10/P10003, arXiv:1706.04965.

[169] W. Adam, B. Mangano, T. Speer, and T. Todorov, "Track Reconstruction in the CMS tracker", 2006, https://cds.cern.ch/record/934067.

[170] W. Adam, R. Frühwirth, A. Strandlie, and T. Todorov, "Reconstruction of electrons with the Gaussian-sum filter in the CMS tracker at the LHC", *Journal of Physics G: Nuclear and Particle Physics* **31** (2005) N9.

[171] CMS Collaboration, "Performance of Photon Reconstruction and Identification with the CMS Detector in Proton-Proton Collisions at sqrt(s) = 8 TeV", *JINST* **10** (2015) P08010, doi:10.1088/1748-0221/10/08/P08010, arXiv:1502.02702.

[172] CMS Collaboration, "Jet energy scale and resolution in the CMS experiment in pp collisions at 8 TeV", *JINST* **12** (2017) P02014, doi:10.1088/1748-0221/12/02/P02014, arXiv:1607.03663.

[173] CMS Collaboration, "Cut Based Photon ID for Run 2", https://twiki.cern.ch/twiki/bin/view/CMS/CutBasedPhotonIdentificationRun2.

[174] M. Cacciari and G. P. Salam, "Pileup subtraction using jet areas", *Phys. Lett. B* **659** (2008) 119, doi:10.1016/j.physletb.2007.09.077, arXiv:0707.1378.

[175] CMS Collaboration, "Electron and photon performance in CMS with the full 2016 data sample", 2017, https://cds.cern.ch/record/2255497.

[176] M. Cacciari, G. P. Salam, and G. Soyez, "The anti-k_t jet clustering algorithm", *JHEP* **04** (2008) 063, doi:10.1088/1126-6708/2008/04/063, arXiv:0802.1189.

[177] M. Cacciari, G. P. Salam, and G. Soyez, "FastJet user manual", *Eur. Phys. J. C* **72** (2012) 1896, doi:10.1140/epjc/s10052-012-1896-2, arXiv:1111.6097.

[178] CMS Collaboration, "Determination of jet energy calibration and transverse momentum resolution in CMS", *JINST* **6** (2011) 11002, doi:10.1088/1748-0221/6/11/P11002, arXiv:1107.4277.

[179] CMS Collaboration, "Jet Identification for the 13 TeV data Run2016", https://twiki.cern.ch/twiki/bin/view/CMS/JetID13TeVRun2016. Accessed on August 14, 2018.

[180] CMS Collaboration, "Cut based electron ID for Run 2", https://twiki.cern.ch/twiki/bin/view/CMS/CutBasedElectronIdentificationRun2. Accessed on August 14, 2018.

[181] CMS Collaboration, "Baseline muon selections for Run 2", https://twiki.cern.ch/twiki/bin/viewauth/CMS/SWGuideMuonIdRun2. Accessed on August 14, 2018.

[182] M. Cacciari, G. P. Salam, and G. Soyez, "FastJet user manual", *Eur. Phys. J. C* **72** (2012) 1896, doi:10.1140/epjc/s10052-012-1896-2, arXiv:1111.6097.

[183] CMS Collaboration, "Performance of missing energy reconstruction in 13 TeV pp collision data using the CMS detector", 2016, http://cds.cern.ch/record/2205284.

[184] CMS Collaboration, "Measurement of the Inclusive W and Z Production Cross Sections in pp Collisions at $\sqrt{s} = 7$ TeV", *JHEP* **10** (2011) 132, doi:10.1007/JHEP10(2011)132, arXiv:1107.4789.

[185] K. S. Cranmer, "Kernel estimation in high-energy physics", *Comput. Phys. Commun.* **136** (2001) 198, doi:10.1016/S0010-4655(00)00243-5, arXiv:hep-ex/0011057.

[186] M. K. Kiesel, "Search for supersymmetry in events with at least one photon, missing transverse momentum, and large transverse event activity in proton-proton collisions at 13 TeV with the CMS detector in 2016". Dissertation, RWTH Aachen University, Aachen, 2018. doi:10.18154/RWTH-2018-225245.

[187] N. D. Gagunashvili, "Comparison of weighted and unweighted histograms", 2006, arXiv:physics/0605123.

[188] J. Butterworth et al., "PDF4LHC recommendations for LHC Run II", *J. Phys. G* **43** (2016) 023001, doi:10.1088/0954-3899/43/2/023001, arXiv:1510.03865.

[189] CMS Collaboration, "CMS Luminosity Measurements for the 2016 Data Taking Period", 2017, http://cds.cern.ch/record/2257069.

[190] CMS Collaboration, "Search for top-squark pair production in the single-lepton final state in pp collisions at $\sqrt{s} = 8$ TeV", *Eur. Phys. J. C* **73** (2013) 2677, doi:10.1140/epjc/s10052-013-2677-2, arXiv:1308.1586.

[191] T. Junk, "Confidence level computation for combining searches with small statistics", *Nucl. Instrum. Meth. A* **434** (1999) 435, doi:10.1016/S0168-9002(99)00498-2, arXiv:hep-ex/9902006.

[192] A. L. Read, "Presentation of search results: the CLs technique", *J. Phys. G* **28** (2002) 2693, doi:10.1088/0954-3899/28/10/313.

[193] ATLAS, CMS, and LHC Higgs Combination Group Collaborations, "Procedure for the LHC Higgs boson search combination in Summer 2011", 2011, https://cds.cern.ch/record/1379837.

[194] G. Cowan, K. Cranmer, E. Gross, and O. Vitells, "Asymptotic formulae for likelihood-based tests of new physics", *Eur. Phys. J. C* **71** (2011) 1554, doi:10.1140/epjc/s10052-011-1554-0,10.1140/epjc/s10052-013-2501-z, arXiv:1007.1727. [Erratum: Eur. Phys. J. C 73 (2013) 2501].

[195] J. Neyman and E. S. Pearson, "On the problem of the most efficient tests of statistical hypotheses", *Philosophical Transactions of the Royal Society of London A: Mathematical, Physical and Engineering Sciences* **231** (1933) 289, doi:10.1098/rsta.1933.0009.

[196] A. Wald, "Tests of Statistical Hypotheses Concerning Several Parameters when the Number of Observations is Large". American Mathematical Society, 1943.

[197] CMS Collaboration, T. C. Collaboration, "Simplified likelihood for the re-interpretation of public CMS results", 2017, http://cds.cern.ch/record/2242860.

[198] CMS Collaboration, "CMS Supersymmetry Physics Results ", https://twiki.cern.ch/twiki/bin/view/CMSPublic/PhysicsResultsSUS. Accessed on August 14, 2018.